PROTON NMR RELAXATION INVESTIGATIONS OF PARTICLE EXFOLIATION AND DISTRIBUTION IN POLYMER/CLAY NANOCOMPOSITES

A Dissertation
Presented to
The Academic Faculty

by

BO XU

In Partial Fulfillment
of the Requirements for the Degree
Doctor of Philosophy in the
School of Materials Science and Engineering

Georgia Institute of Technology
December 2010

PROTON NMR RELAXATION INVESTIGATIONS OF PARTICLE EXFOLIATION AND DISTRIBUTION IN POLYMER/CLAY NANOCOMPOSITES

Approved by

Dr. Haskell W. Beckham, Advisor
School of Materials Science and Engineering
Georgia Institute of Technology

Dr. Johannes Leisen, Advisor
School of Chemistry and Biochemistry
Georgia Institute of Technology

Dr. David G. Bucknall
School of Materials Science and Engineering
Georgia Institute of Technology

Dr. Sankar Nair
School of Chemical and Biomolecular Engineering
Georgia Institute of Technology

Dr. Yoshiaki Kawajiri
School of Chemical and Biomolecular Engineering
Georgia Institute of Technology

Date Approved: November 1, 2010

To my dear wife — Sophia Guo, for believing in my dream

To my unborn daughter — Molly Keyi Xu, for exhilarating me being a father

To my parents—Yongcai Xu and Kexiu Yang, for inspiring and supporting me

I love you all

ACKNOWLEDGEMENTS

There have been many people who went above and beyond helping me with my studies at Georgia Tech. as well as my life in the States. My advisors, Dr. Haskell Beckham and Dr. Johannes Leisen have been with me from the start of my work. I want to thank them for their inspiration, encouragement, support and wisdom, without which this work would never have been done. I am also grateful for their guidance in leading me to the spin world and for their patience in teaching me.

I want to extend my sincere thanks to all of my committee members, Dr. David Bucknall, Dr. Sankar Nair and Dr. Yoshiaki Kawajiri for their valuable time and constructive suggestions. I want to also thank Dr. David Bucknall and Dr.Yonathan Thio for their invaluable source of fruitful discussion and support. My sincere gratitude goes to Dr. Eileen Harkin-Jones and Dr. Rund Abu-Zurayk of Queen's University Belfast for their samples and helpful discussion. Special thanks to Dr. Ulrich Scheler and Dr. Böhme Ute of Leibniz Institute of Polymer Research Dresden for supporting my stay in Germany.

My work at Georgia Tech. would not have been a good time without working with my research group. I would like to thank all group members, Dr. Sunghyun Nam, Dr. Marcus Foston, Dr. Chris Hubbell, Dr. Rudra Choudhury, Ryan Kincer, Gulfem Ipek Nasuf, and Doh-Yeon Park for all their cooperation in sharing instruments, helpful scientific inputs and wonderful friendships.

Last but not least, my heartfelt thanks go to my wife, Sophia Guo for her patience, love, inspiration and encouragement. I cannot thank my parents enough for all of their

tremendous support and guidance in my life. This dissertation is especially dedicated to my soon-to-be-born daughter. All her kicks and moves excite me in becoming a father. In addition, my deepest thanks go to my brother and sister-in-law, who always take care of my parents and support me at all the time. I would also like to thank my two lovely nieces for accompanying my parents and help them have a great time.

To all of my family and friends, I am eternally grateful.

TABLE OF CONTENTS

LIST OF TABLES

LIST OF FIGURES

LIST OF ABBREVIATIONS

C15A	Cloisite 15A
C20A	Cloisite 20A
C30B	Cloisite 30B
CEC	Cation exchange capacity
DSC	Differential scanning calorimetry
EMA	Ethylenemethyl acrylate copolymer
EPR	Electron paramagnetic resonance
FH	Fluorohectorite
FIBT	Foused ion beam tomography
FID	Free induction decay
FTIR	Fourier transform infrared spectroscopy
MAS	Magic-angle spinning
MMT	Montmorillonite
NMR	Nuclear magnetic resonance
OM	Optical microscopy
PBT	Poly(butylene terephthalate)
PCL	poly(ε-caprolactone)
PCN	Polymer/clay nanocomposites
PET	Poly(ethylene terephehalate)
PLA	Poly(lactic acid)
LMW PLA	Low molecular weight PLA
HMW PLA	High molecular weight PLA
PMMA	Poly(methyl methacrylate)
PP	Polypropylene
PP-*g*-MA	PP-g-maleic anhydride
PRE	Paramagnetic relaxation enhancement
PS	Poly(styrene)
PVA	Poly(vinyl alcohol)
SAXS	Small angle X-ray scattering
SEM	Scanning electron microscopy
SS NMR	Solid-state nuclear magnetic resonance

LIST OF SYMBOLS

α	Quality of clay dispersion
α_0	Quality of clay dispersion in a reference material
A_s	Polymer/clay interfacial area per unit volume
$A_{s,i}$	Ideal interfacial area of montmorillonite, ~ 750 m^2/g
$A_{s,NMR}$	Interfacial area measured by the initial slope from NMR
b	Thickness of undetectable protons on clay surface
B_0	Magnetic field strength
C	Electron-nucleus coupling constant
C_{Fe}	Fe^{3+} concentration, as Fe_2O_3 wt%
D	Spin-diffusion coefficient
δ	Spin-diffusion barrier radius
Δ	Face-to-face interparticle spacing
D_0	Diffusivity of protons at the surface of a sink
d_{001}	Basal spacing
Δ_{app}	Apparent interplatelet separation
d_c	Lateral dimension of stacks
d_i	Fractal dimension of solids
Δ_{ideal}	Ideal interparticle spacing
D_{mobile}	Spin-diffusion coefficient of mobile phase
d_p	Average impurity separation
D_{rigid}	Spin-diffusion coefficient of rigid phase
D_s	Spin diffusion coefficient of surface protons
$D_{s,eff}$	Effective diffusivity
Δ_{TEM}	TEM interparticle separation
ε	Homogeneity of clay dispersion
ϕ	Volume fraction

f	Degree of exfoliation
g	Edge-to-edge interparticle spacing
H	Planck's constant
h_0	Thickness of a single platelet, ~ 1 nm
h_c	Average cumulative thickness of a stack
h_{clay}	Height or thickness of a clay particle
I	Spin number
k	Coupling constant
K A	Prefactor in our model ($\propto \alpha^2$)
k_{Curie}	Coupling constant due to the Curie relaxation
λ	Stretch ratio
L	Half thickness of detectable protons between particles
M	Bulk magnetization
m	Polarization per nucleus
m_0	Equilibrium polarization per nucleus
M_c^n	Normalized and corrected magnetization
M^n	Normalized magnetization
M_o	Equilibrium magnetization
N_{ps}	Average number of platelets per stack
N_0	Number density of protons per unit volume
N_p	Number of paramagnetic centers per unit volume
$N_{p,eff}$	Effective number of paramagnetic centers
p	Magnetization of a nuclear spin
p_o	Equilibrium magnetization of a nuclear spin
r	Electron-nucleus distance
ρ	Density
$R_{1,para}$	Paramagnetic contribution to the spin-lattice relaxation rate
S, S_i	Initial slope
S_{ref}	Initial slope of a reference material

S_v	Interfacial surface per unit volume
T	Absolute temperature
T_1	Spin-lattice relaxation time
$T_{1,m}$	Intrinsic spin-lattice relaxation time
$T_{1,para}$	Paramagnetic contribution to the spin-lattice relaxation time
$T_{1,PCN}$	Spin-lattice relaxation time of polymer/clay nanocomposites
$T_{1,polymer}$	Spin-lattice relaxation time of polymer
T_1^H	Proton spin-lattice relaxation time
T_2	Spin-spin relaxation time
T_c	Crystallization temperature
τ_c	Correlation time of impurity centers
T_m	Melting temperature
τ_r	Rotational correlation time of molecular motion
τ_s	Spin-spin relaxation time of impurity centers
V_{clay}, V_c	Volume fraction of clay
V_d	Volume fraction of detectable protons per unit volume
$V_{polymer}$, V_p	Volume fraction of polymer
W_c	Weight fraction of clay
ξ^2	Fractional area occupied by clay particles in a plane
β	Exponential power of impuirty concentration
γ	Gyromagnetic ratio
ΔB_{pp}	peak-to-peak line-width
Δ_f	Apparent NMR spacing
$\Delta\nu_{1/2}$	Line-width at half intensity
Ω	Domain of nuclei around particles
ω_0	Larmor frequency

SUMMARY

In the past two decades polymer/clay nanocomposites (PCNs) have emerged as promising materials that exhibit remarkably improved properties when compared to conventional composites and pristine polymers. Such improvements strongly depend on the dispersion of clay nanoparticles in the polymer matrix. In spite of great efforts expended in characterizing clay dispersion, effective, simple and quantitative techniques are still needed. This work addresses this challenge by presenting new aspects of ^{1}H solid-state NMR for quantifying clay dispersion in PCNs filled with clay containing paramagnetic ions. Employing these ^{1}H solid-state NMR methods, some structure-processing-deformation relationships of PCNs were derived, and basic insights into nuclear relaxation and spin diffusion in PCNs were gained as well.

Detailed models and analyses were described for ^{1}H spin-lattice relaxation in the presence of paramagnetic clays in PCNs. Relaxation recovery was analytically correlated to clay dispersion in two ways: one is the initial relaxation recovery which is related to clay surface area, and the other is the spin-lattice relaxation time which is related to interparticle spacing. These two NMR observables were employed to quantitatively observe the evolution of clay morphology in poly(propylene)/clay (PP/MMT) nanocomposites upon equibiaxial stretching, as well as upon *in situ* uniaxial deformation. The initial relaxation recovery was independently utilized to determine the polymer-clay interfacial surface area and the degree of clay exfoliation. We demonstrated the capabilities of our models in quantitatively characterizing several materials, including poly(vinyl alcohol), nylon 6, poly(ε-caprolactone) (PCL), poly(lactic acid) (PLA) and PP

nanocomposites. These results were used to examine the dependence of clay morphology upon processing (strain ratio, strain rate, temperature), deformation (extension), component characteristics (polymer molecular weight, clay surface modification) and clay content. Effects of paramagnetic Fe^{3+} concentration and external magnetic field strength on ^{1}H spin-lattice relaxation in PCNs were also investigated and discussed. In particular, low field separates the initial relaxation recovery into two stages: one related to clay content and the other related to the polymer-clay interfacial surface area. The low field was observed to enhance the paramagnetic contribution to the spin-lattice relaxation rate, increasing its sensitivity to clay morphology. In addition, measurements of long-distance spin diffusion coefficients for a variety of polymers and paramagnetic characteristics of organically modified clay were explored. Overall, the utility of NMR relaxometry in characterizing PCNs has been significantly expanded and successfully demonstrated in this dissertation.

CHAPTER 1

General Introduction

1.1. Background- Motivation and Objectives

Novel polymer/nanoparticle compounds, so-called nanocomposites are increasingly attracting interest in industry and academia.[1-18] Typically, conventional composites are filled with micrometer-scale materials, such as particles (e.g. carbon black[19-22]), fibers (e.g. glass fibers[23-25]), or layered particles (e.g. graphene,[26-27] mica or talc[28-32]) in order to improve polymer properties, or simply to reduce cost. These materials have been widely used in a diversity of areas, such as transportation, construction, electronics, and consumer products. However, these composites to some extent exhibit drawbacks, such as weight increase, brittleness and opacity. These disadvantages are mainly due to the existence of agglomerates of the particulate fillers on a micrometer scale. In contrast, the incorporation of nanoparticles into a polymer matrix introduces nanocomposites with remarkable improvements in mechanical, optical, thermal, barrier, even electrical properties when compared to conventional composite and the pure matrix.[4,6,8,33-36]

Based on dimensions of nanoparticles, one can distinguish them into three types (Figure 1.1): (1) three dimensions: carbon black, polyhedral oligomeric silsesquioxane (POSS), fullerene (C60), gold, silver, copper, Fe_2O_3, ZnO, SiO_2,CdS, PbS, $CaCO_3$, $BaSO_4$, etc.; (2) two dimensions: carbon nanotube, halloysite nanotubes , palygorskite, cellulose whisker, DNA, etc.; (3) one dimension: montmorillonite, saponite, hectorite, fluoromica, laponite, graphite, MoS_2, layered double hydroxide, etc.

3D nanosize	carbon black, polyhedral oligomeric silsesquioxane, fullerene, gold, silver, Fe_2O_3, ZnO, SiO_2,CdS, PbS, $CaCO_3$, $BaSO_4$
2D nanosize	carbon nanotube, halloysite nanotubes , palygorskite, cellulose whisker, DNA
1D nanosize	montmorillonite, saponite, hectorite, fluoromica, laponite, graphite, MoS_2, Layered double hydroxide

Figure 1.1. Schematic representatives of typical nanoparticles with three shapes: sphere (isodimensional nano-scale, 3D), rod (2D) and platelet (1D), and related examples of particles filled in polymeric nanocomposites.

Polymer/clay nanocomposites (PCNs), as one of most investigated nanomaterials, offer excellent materials to address economic issue and potential answers to fundamentally scientific questions.[6-7,9,14-17,37-39] To date PCNs have been increasingly applied in daily products such as automotive parts, package, beer bottles, cables, paper coating, shoes, medical device, etc.[15-17,40] In general, incorporating finely dispersed clay particles in polymer at low loadings (typically, ~ 5 wt%) enhances materials performance, such as stiffness, toughness, hardness, abrasion resistance, dimensional stability, heat resistance, gas barrier and fire resistance. These remarkable enhancements are primarily correlated with the large interfacial area per unit weight of the exfoliated clay (e.g., 750 m^2/g) as well as the large aspect ratio (~ 50 up to 1000). These two important features of clay nanoparticles strongly depend on their dispersion and exfoliation which is influenced not only by the nature of components but also by preparation and processing. In addition,

PCNs can also serve as model systems to study chain conformation and dynamics of polymer chains confined by clay platelets.[11-14,39] Hence, a good understanding of clay morphology will not only benefit the design and applications of these nanomaterials but also provide great insights into how the 'nano-effect' causes the remarkable enhancements in properties of these nanocomposites.

Although manufacturing a variety of PCNs has been made a great progress, some basic questions still remain challenging, such as why nanoclay of very low loadings (~ 5 wt%) can produce such a remarkable improvement in properties, and how micrometer-scale clay particles can be homogeneously exfoliated down to the nano-scale. Besides the nature of polymer/clay interaction, the details of clay morphology will be of great help to a good understanding of PCNs. Thus, there is a great need to develop simple, effective and quantitative techniques to characterize PCNs in two important characters: clay distribution and exfoliation.

Quantification of clay dispersion in PCNs is a great challenge, because there are a variety of possibilities in nanostructures. Various techniques have been developed to characterize the structure of PCNs.[6-7,9,37] As a complement to other tools, solid-state nuclear magnetic resonance (SS NMR) was recently explored to quantify clay dispersion in PCNs.[41-46].[47-52] Proton spin-lattice relaxation time (T_1^H) has been explored to correlate with the clay morphology in PCNs filled with clay containing paramagnetic Fe^{3+} ions. The lack of the analytical relation between nuclear spin-lattice relaxation and clay dispersion, however, limits this function of SS NMR.

The primary aim of the present work is to better understand nuclear spin-lattice relaxation in paramagnetic PCNs with respect to clay morphology and the nature of clay

and polymer. Although nuclear spin-lattice relaxation under the influence of paramagnetic centers has been extensively investigated,[53-59] few work has been done to elucidate the proton spin-lattice relaxation in polymer/paramagnetic clay nanocomposites.[41-45] The paramagnetic contribution to the spin-lattice relaxation rate ($R_{1,para} = 1/T_{1,para}$) was introduced to be the difference in the spin-lattice relaxation rate between PCNs ($1/T_{1,PCN}$) and the pristine polymer ($1/T_{1,polymer}$); namely, $R_{1,para} = 1/T_{1,PCN} - 1/T_{1,polymer}$.[41-44] It has been observed that $R_{1,para}$ is dependent not only upon the dispersion of paramagnetic clay particles (e.g., dispersion, content) but also Fe^{3+} concentration (type of clays).[41-44] However, these observations have not been fully understood. For example, it has been conjectured that the dispersion of clay does not change up to 50 wt% clay in polymer based on $R_{1,para}$ as a function of clay content.[43,46] However, the aggregation becomes worse with increasing clay content by the observation from other techniques.[60-61] The goals of this present work are to analytically correlate proton spin-lattice relaxation with clay morphology, and to apply these connections to examine effects of processing and deformation on the structure of PCNs.

The main objectives of the present study are as follows:

- Develop a combination of ^1H SS NMR and TEM approach to observe the evolution of clay morphology in polypropylene/montmorillonite nanocomposites upon equibiaxial stretching.
- Correlation of ^1H spin-lattice relaxation process with clay dispersion in paramagnetic PCNs: correlate the initial relaxation with interfacial surface and correlate $R_{1,para}$ with interparticle spacing; develop these analytical relationships into quantifying clay dispersion.

- Examine the effects of Fe^{3+} concentration and fields on the proton spin-lattice relaxation.
- Explore ^{1}H SS NMR to investigate PCNs upon uniaxial deformation.

1.2. Clay Structure and Nanocomposite Structures

1.2.1. Clay Structure

One of clay minerals, montmorillonite widely filled in nanocomposites, belongs to the structural family of the 2:1 phyllosilicates. It is essentially composed of a central octahedral sheet of alumina or magnesia sandwiched between two external silica tetrahedral sheets (Figure 1.2). The platelet thickness is ~ 1 nm and the lateral dimensional of these platelets varies from 30 nm up to several microns which depends on the sources of clays.[9,62-63] These platelets pack themselves together to form stacks with a regular van de Waals gap which is called the gallery. The gallery and a platelet consist of the basal spacing, d_{001} measured by X-ray diffraction.

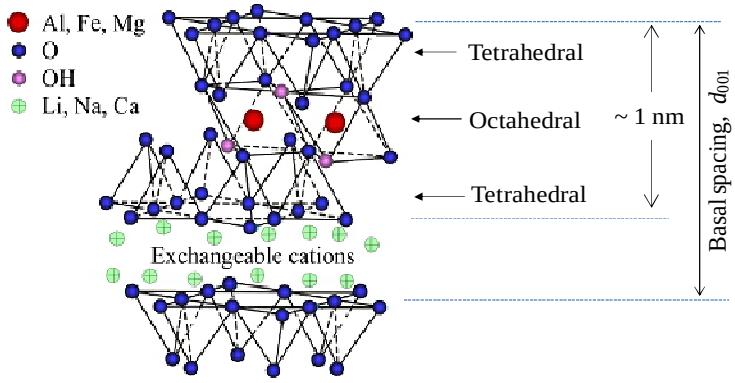

Figure 1.2. Schematics for structural characteristics of 2:1 phyllosilicates[9,37,62]

Isomorphic substitution within the layers (for example, Al^{3+} replaced by Mg^{2+} or by Fe^{3+} in the central sheet) generates negative charges that are counterbalanced by alkali or alkaline earth cations (Na^{+}, Ca^{2+}, K^{+}) in galleries. The important feature of these clays is that these cations can be exchanged with other cation molecules. The amount of exchange is known as cation exchange capacity (CEC), generally expressed as meq/100 g (milli-equivalents per 100 grams of clay). In order to render these hydrophilic platelets more hydrophobic, the cations of the interlayer can be substituted by cationic surfactants such as alkylammonium or alkylphosphonium (onium).[64-67] These organic cations lower the surface energy and expand the galleries, and improve the wetting and intercalation of the polymer matrix.[68-69] In addition, the organic cations may provide functional groups that can react or interact with monomer or polymer to enhance interfacial adhesion between the clay platelets and polymer matrix. The physical and chemical modification of clay facilitates clay dispersion and exfoliation in polymer matrices.

1.2.2. Nanocomposite Structure

In conventional composites, micro-scale clay particles, as a separated inorganic phase (Figure 1.3a), are dispersed in polymer matrix since the polymer is unable to wet the silicate platelets. When exfoliated down to the nano-scale, clay particles exhibit complicated clay morphology.[70] But two main types of nanostructures are mostly found. One is the intercalated structure where clay particles are intercalated by polymer (as the intercalated structure as shown in Figure 1.3b). The other is the exfoliated structure where clay particles are fully exfoliated into single platelets dispersed in a continuous polymer matrix (as the exfoliated structure in Figure 1.3c). In the intercalated structure, a

single (and sometimes more than one) extended polymer chain intercalates into the galleries of clay particles, leading to a well ordered multilayer morphology. In exfoliated nanocomposites, the individual clay platelets are distributed in the polymer matrix. The exfoliated structures can be further distinguished into two situations associated with the distribution of single platelets: uniform distribution with single interparticle spacing, and poor distribution with large ranges of interparticle spacing.

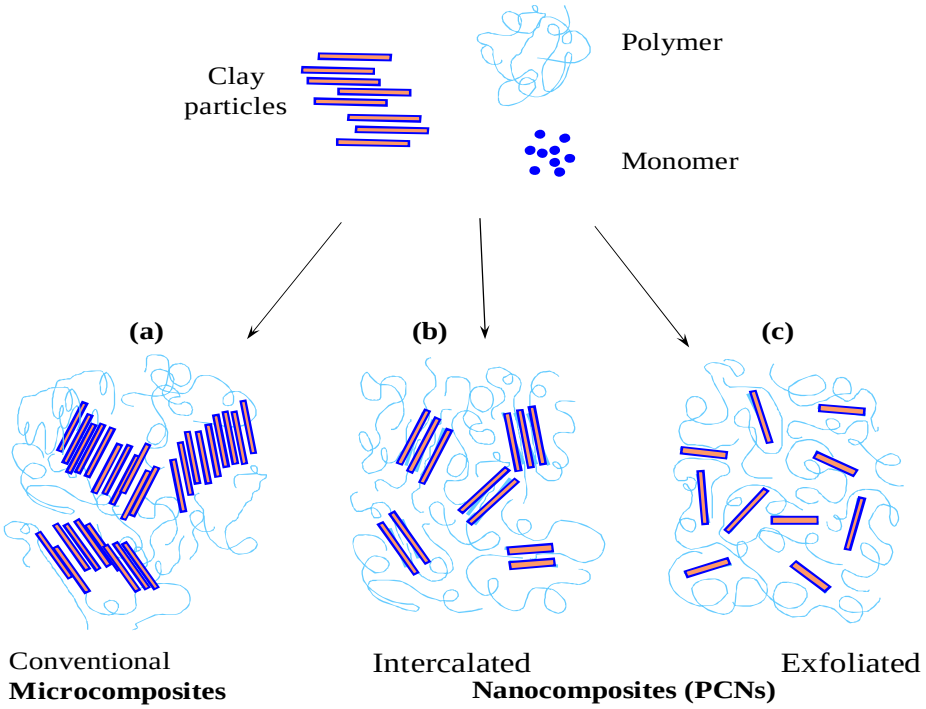

Figure 1.3. Schematic illustration of three types of structures in polymer/clay composites prepared from the starting polymer or monomer, which is associated with methods described in the next section. Conventional microcomposite: micro-scale clay particles (a); nanocomposites: intercalated particles (b) and exfoliated platelets(c).[9,37]

1.3. Fabrication and Properties of Polymer/clay Nanocomposites

1.3.1. Method and Process

So far polymer/clay nanocomposites have been prepared mainly by three methods:

Exfoliation-absorption from solution. This is based on a solvent solution in which the polymer or pre-polymer is soluble and the clay particles are swellable. The clay platelets are first swollen and exfoliated in a solvent, such as water, chloroform, or toluene. The polymer then adsorbs onto the exfoliated platelets, and PCN nanocomposites are finally obtained upon solvent removal. Polyvinyl alcohol (PVA)[71-74] and polyethylene oxide (PEO)[75-77] nanocomposites were successfully prepared using this method.

In-situ intercalative Polymerization. At present, the majority of commercial PCN materials are fabricated by this method, such as nylon 6/clay nanocomposites from Ube, Ltd.[78-79] In this technique, clay particles are swollen within the liquid monomer (or a monomer solution) such that the polymerization forming the polymer can occur inside the galleries.[61,80-83]

Melt intercalation. Clay particle powder is mixed into the polymer melts. During this process, the polymer can migrate into clay galleries, thereby expanding galleries and reducing the platelet-platelet interaction. At the same time, under the external force from extruders,[84-85] mixer,[86] ultrasound,[87-88] microwave,[89] etc., the clay particles are broken into smaller stacks and further individual platelets are peeled apart, producing either an intercalated and/or exfoliated nanocomposite. The resultant nanocomposite morphology is strongly dependent not only upon the nature of components such as clay surface

modification and molecular weight of polymer, but also upon a variety of processing conditions such as the screw design, compounding temperature, shear stress, residual time inside barrels. For the industry, this technique is quite appealing. Melt processing is compatible with conventional and readily available processing machines; it is also environmentally benign since no solvents are required.

1.3.2. Morphology-dependent Performance in Nanocomposites

Performances of polymer/clay nanocomposites in mechanical performance, flame retardancy, barrier and thermal stability and thermal expansion have been intimately related to clay morphology. For instance, considerable increase in stiffness and strength has been achieved at rather low clay platelet concentrations. However, improvements in the composite strength at higher platelet loadings (> 5 wt %) are often not as good as that expected from theoretical models for reinforced polymers, and even decrease with increasing clay loading over 5 wt %. This has been attributed to difficulties in achieving complete exfoliation and dispersion of platelets within the polymer. Simply speaking, this is caused by aggregation of clay particles. Thus, the details of clay morphology will be of benefit to an understanding of material properties and further to the design and development of nanocomposites.

One of the first demonstrations of PCNs was by the Toyota research groups[81-82] who showed that adding just 5% of nanoclay to nylon-6 resulted in a 40% increase in tensile strength, 68% increase in flexural modulus, an 80 °C increase in heat distortion temperature (HDT), and significant enhancement of barrier properties over pure nylon-6. Different types of composites as depicted in Figure 1.3 have been found to display

notably different properties. Figure 1.4 (a) indicates that a decrease in the elongation at break for a conventional composite is observed, while an intercalated nanocomposite shows slight enhancement of this property. Especially, the exfoliated nanocomposite exhibits a large increase of the elongation at break. Polyimide nanocomposites demonstrate both an increase in stress and elongation at break up to < 5 wt% MMT content. At higher filler content, both properties experience a sharp drop towards values lower than those recorded for the pristine polyimide (Figure 1.4b). This behavior is related to the formation of aggregates at higher filler content, which makes these composites much weaker.

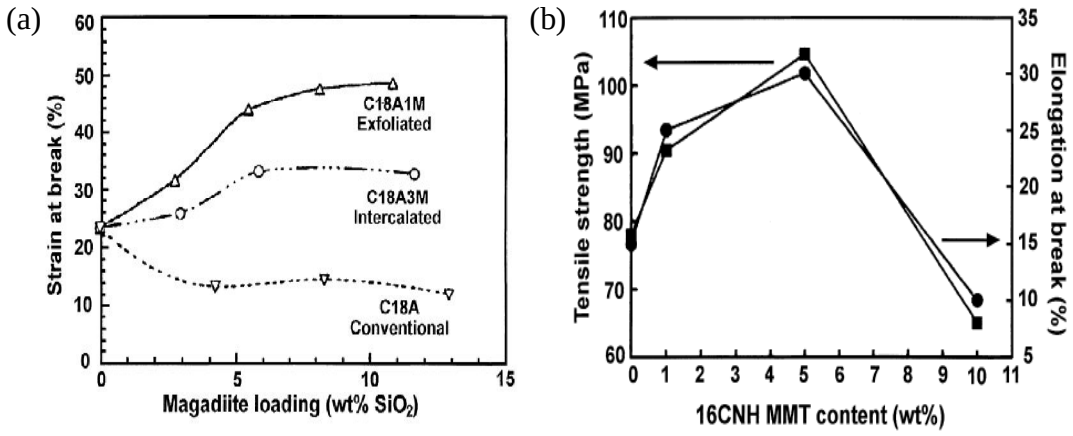

Figure 1.4. (a) Comparison of the strain-at-break values for an exfoliated epoxy nanocomposite prepared from magadiite modified with methyl-octadecylammonium ion (C18A1M), an intercalated nanocomposite prepared from magadiite modified with trimethyloctadecylammonium ion (C18A3M) and a conventional composite prepared from magadiite modified with octadecylammonium ion (C18A);[90] (b) Tensile strength and elongation at break as a function of MMT content for poly(imide) nanocomposites filled with MMT modified with hexadecylammonium ion.[91]

1.4. Characterization Techniques for Nanocomposite Structure

A key to understand nanomaterials is first to develop techniques for characterizing nanostructures in order to establish the relationships between their performance and structural morphology. So far a variety of methods have been used to overcome this challenging task, which were grouped into four categories by Vaia et al.:[92] real space (microscopy), reciprocal space (scattering), interfacial surface (NMR, optical spectroscopy, dielectric spectroscopy), and physical effects (mechanical properties, barrier properties). The real space techniques, including transmission electron microscopy (TEM), scanning electron microscopy (SEM), atomic force microscopy (AFM) and optical microscopy (OM), can visualize clay morphology on multi-scales. Reciprocal space scattering techniques are informative and somewhat quantitative since they typically detect bulk materials. These scattering techniques, however, have issues with proper data interpretation. Spectroscopy techniques like dielectric, Fourier transform infrared spectroscopy (FTIR), NMR and electron paramagnetic resonance (EPR) can probe polymer/clay interfacial area in nanocomposites by detecting changes in structure and dynamics at the interface. Indirect physical effect methods have been used to deduce clay morphology from barrier performance, mechanical properties, thermal behavior or rheology. All of the above characterization techniques have their own limits, but they can be complementary to each other. The morphology characterization via different techniques contributes to gaining a precise picture of nanostructures. With regard to advantages and limits, several techniques and the relative morphological descriptors are briefly reviewed.

1.4.1. Imaging

Imaging can be used to directly visualize details of material microstructure on multiple length scales. A variety of imaging techniques have been developed to characterize clay dispersion in polymeric nanocomposites, such as optical microscopy (OM),[93-95] scanning electron microscopy (SEM),[96-97] atomic force microscopy (ATM),[97-101] and transmission electron microscopy (TEM).[81,93,102-104] More recently, some imaging techniques used for characterization of clay dispersion, include transmission electron microtomography (TEMT)[92,105-106], scanning transmission X-ray microscopy (STXM)[107-108] and focused ion beam tomography(FIBT)[109].

SEM provides images of clay surface features in nanocomposites. Usuki et al.[110] treated the surface of nanocomposite films with oxygen plasma to remove the nylon 6 on the surface layer. Their SEM photographs revealed 'nano wall' of a single platelet in 1 nm thickness standing on the surface. Also, to observe the surface of nanocomposites after physical and chemical treatments, AFM can catch the features of clay particles such as the thickness, lateral length and the resulting aspect ratio, as well as the features of polymer crystals.[97-101,111-112]

So far conventional two-dimensional transmission electronic microscopy (2D TEM) is widely used as an essential tool for characterizing the nanocomposite morphology. TEM provides real-space analysis on the spatial distribution of silicate crystals. Visualizing clay platelets or particles as dark lines (reflecting the distribution in absorption of electrons between organic polymer and silicate clay) in nanocomposites offers a far more direct way to observe the clay dispersion when compared to other

techniques. TEM images for classical morphologies presented in polymer/clay composites are illustrated in Figure 1.5.

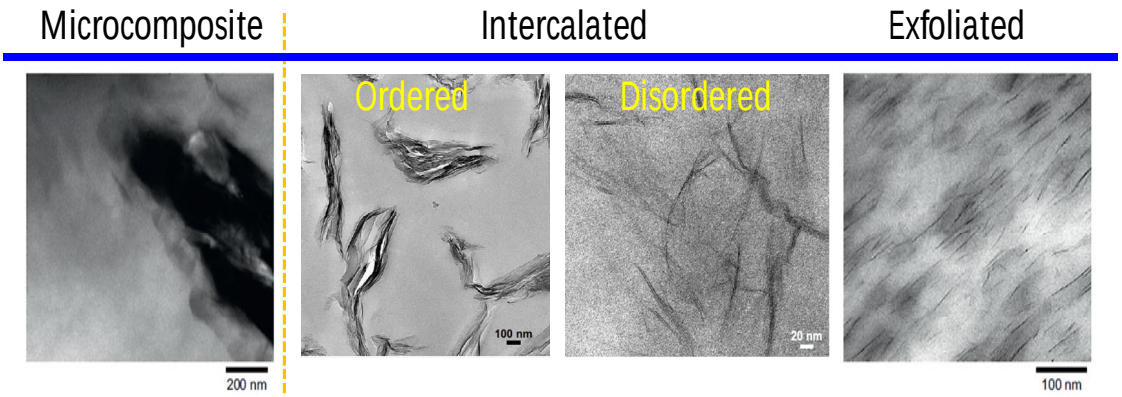

Figure 1.5. 2D TEM images for polymer/clay composites: conventional microcomposite; three nanocomposites- ordered/ disordered intercalated, and exfoliated.[8,37,113]

Semi-quantitative statistics based on TEM images have been computed to summarize details of clay morphology, such as particles density per area of images, interparticle spacing, particle length and particle thickness as well as the average number of platelets per stack. For example, Dennis et al.,[114] Fornes et al.[115-116] and VanderHart et al.,[42,45] measured the clay particle density to compare the quality of clay dispersion in terms of the extruder screw design, nature of components and processing conditions. Higher particle density at a specific clay loading indicates larger degree of the clay exfoliation, and thus better dispersion. Bertmer et al.[41] and van Es[117] evaluated the interparticle spacing by drawing an array of parallel lines over the TEM images, and then dividing the total length of the lines by the number of the clay particles intersecting the lines. If a stack or single platelet is counted as an entity, smaller interparticle spacing suggests better dispersion. With regard to the parameters of particle size, Nam and co-

workers [118] proposed to measure the clay particle length and thickness of dispersed clay stacks, and the correlation length between these stacks. Vermogen et al.[93] used the same parameters as well as aspect ratio to understand the mechanism of clay dispersion and changes of clay structure associated with the screw profiles. Owing to a small space probed by normal 2D TEM, OM or low magnification electron microscopy (bright-field TEM) at the macroscopic scale can be used as a complementary tool to reveal an overview of clay dispersion/distribution of clay particles. Normally, optical microscopy observations allow one to observe large clay agglomerates which could be beyond the observation range of normal 2D TEM. Vermogen et al.[93] developed an image analysis procedure based on OM/TEM for evaluating the clay dispersion in a polypropylene matrix; they found that the proportion of micron-size agglomerates could not be neglected, which is of help to understand macroscopic properties of nanocomposites.

Under the science of stereology, Basu et al.[119] proposed two independent TEM-based parameters, exfoliation number and interparticle spacing for dispersion in nanocomposites using integral geometry and spatial statistics. The exfoliation number is defined as the fraction of the polymer/clay interfacial area over total clay surface area per unit volume; the spacing is defined as the mean of face-to-face distances between particle-projected line traces, which can be evaluated by the relation of clay volume fraction and polymer/clay interfacial area fraction derived from TEM image analysis. Particle aspect ratio and orientation, however, are not captured by these two parameters. Their cases of polypropylene/MMT nanocomposites demonstrate the advantages of these two quantifiers in clay dispersion. In a more recent study, Xie et al.[95] modified these two quantifiers by including OM information on macroscopical dispersions of micrometer

agglomerates. It could add more insights into the 'real' clay dispersion using a combination of both microscopical and macroscopical aspects.

Technically speaking, the 2D TEM approach requires considerable skill and experience for complicated sample preparation and TEM operation as well. Also, utility of TEM is often criticized for lacking statistical accuracy because it visualizes the very local morphology. Taking images at different locations for TEM samples probably yields different morphology information. The reliable way is to take images at different locations on the multiple length scales and from different orientations until a whole picture of the morphology is achieved. The most difficulty in obtaining good TEM images is to obtain ultrathin samples (typically 50 – 90 nm) in microtoming sections. Moreover, meaningful statistics require capturing a large number of representative and high quality images and analyzing several hundreds of particles. In addition, orientation and alignment of clay particles in nanocomposites are helpful to quantitative analysis on TEM images. Otherwise, a silicate platelet lying with its surface parallel to the viewing direction will exhibit much bigger projected thickness; a curled platelet could present multiple black lines in a two-dimensional projected image, leading to additional platelets mistakenly accounted. In certain cases, precise TEM analysis is impossible, owing to random dispersion of clay particles and low phase contrast in nanocomposite. To TEM observation itself, damage of organic polymer by electron irradiation could change morphology and ultimately limit the measurement accuracy.

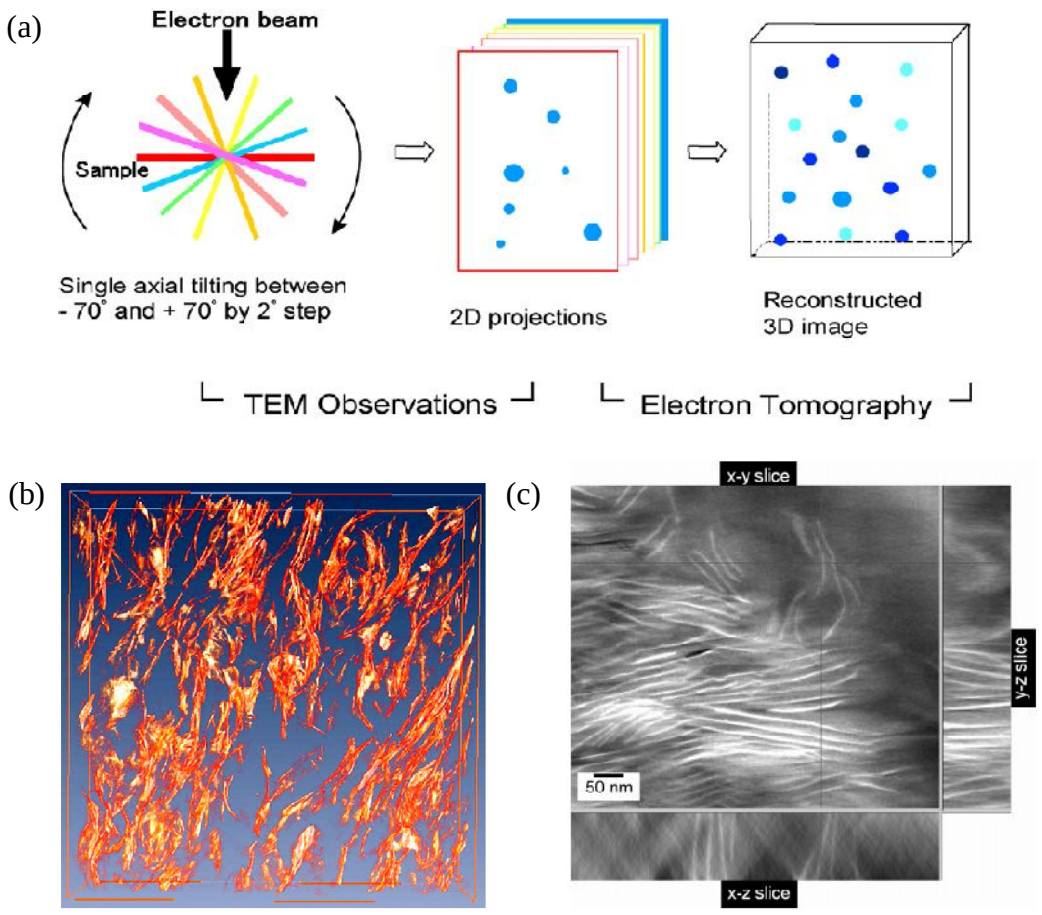

Figure 1.6. (a) Representative procedure for 3D-TEM measurements;[120] (b) 3D-TEM image with the volume of 1.6 × 1.6 × 0.1 μm^3 for ethylene-vinyl-acetate/MMT nanocomposites;[106] (c) Three slices along three orthogonal planes (x-y, x-z and y-z) from 3D-TEM image using the simultaneous iterative reconstruction techniques for epoxy/MMT nanocomposites.[92]

Nowadays three-dimensional microscopy technique, based on tomography and TEM, so-called TEMT or 3D-TEM is increasingly attractive in characterizing three-dimensional micro-/nano-structure of materials.[121] 3D structural observation on nanometer scale would offer the most accurate results with few assumptions in image interpretation, when compared to 2D images with the limitations stated above. Figure 1.6(a) outlines a typical process of 3D-TEM/electron tomography,[120] during which a series of 2D TEM images at various angles is obtained by single axis or conical tilting of

a sample, followed by backprojection of 2D TEM images using a technique of computerized tomography. The reconstruction of 3D images in real space by these two steps is designated as 3D-TEM. Two examples are presented for ethylene vinyl acetate (EVA)/MMT nanocomposites[106] and epoxy/MMT[92] in Figures 1.6(c) and (b), respectively. The 3D TEM view of extracted clay phase shows that clay stacks were not completely exfoliated in the EVA nanocomposite, which is in accordance with the SAXS data indicating the existence of the complex intercalated/exfoliated structure. In contrast to SAXS, the tomographic reconstruction (see Figure 1.6c and b) provides precise details of the distribution of morphological features, in addition to statistical averages over the sample volume.

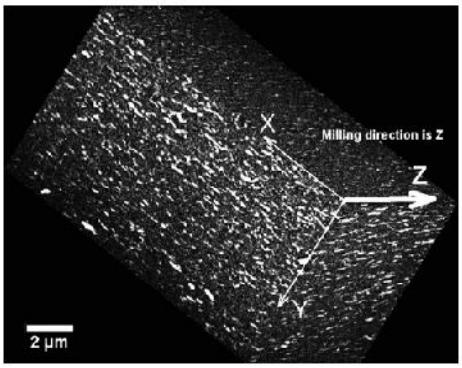

Figure 1.7. 3D image of layered silicate dispersion (white parts) in poly[(butylene succinate)-co-adipate] matrix (PBSA) using focused ion beam (FIB)-tomography. The reconstructed volume after data processing was 14.85 × 8.55 × 9.51 μm^3. FIB Milling direction, 'Z' refers to the direction of slicing scanned by 2D high-resolution SEM (HR-SEM).[109]

Ray et al.[109] developed focused ion beam (FIB)-tomography as a high-resolution three-dimensional (3D) technique to study the morphology of polymer/clay nanocomposites. The FIB 3D-tomography of a material is built up using computer

reconstruction of 2D images scanned by high-resolution SEM (HR-SEM) for the 2D cross sections which are prepared by milling steps using the Gallium ion beam. The spatial dispersion of clay particles in 3D-space in Figure 1.7 displays that the silicate particles dispersed in the polymer matrix form a network structure; this structure and particle size in 4.5 -7.5 nm thickness are in good agreement with SAXS results.

In a polymeric multiphase clay nanocomposite system, the detailed chemical distribution could offer much more information on phase transformation than clay dispersion. Recently, Martin et al. demonstrated scanning transmission X-ray microscopy (STXM) as a very powerful tool to characterize the detailed nanocomposite morphology.[107-108] STXM spectromicroscopy allows a complete chemical and compositional analysis with excellent chemical sensitivity and a high spatial resolution, providing direct information on the presence of different polymer components at the polymer-clay interfaces. Experimental details relevant to STXM of structured soft condensed matter nanomaterials may be found in the literature. Figure 1.8 shows the STXM images (b) with contrast on the basis of the elemental differential X-ray absorption through components of the composite material (a).[107] In the case of the nanocomposite with the three components, polypropylene, PP-*g*-maleic anhydride (PP-*g*-MA) and organoclay (C20A), the STXM image clearly shows the distribution of these three components represented with different colors. The important morphological features of this system were revealed directly in Figure 1.8(b): (i) the PP matrix and the compatibilizer, PP-*g*-MA are blended homogeneously; (ii) the compatibilizer surrounds preferentially the nanoclay due to polar interactions; (iii) there are several MMT particles that appear completely in purple color, e.g. in the bottom-left part of the image, which

correspond to clay particles fully intercalated by the compatibilizer, but there are no MMT particles fully in yellow or orange color. In this way, STXM could provide more information on morphologies in the nanocomposite with multi-phases, in which regular TEM could not identify the chemical details.

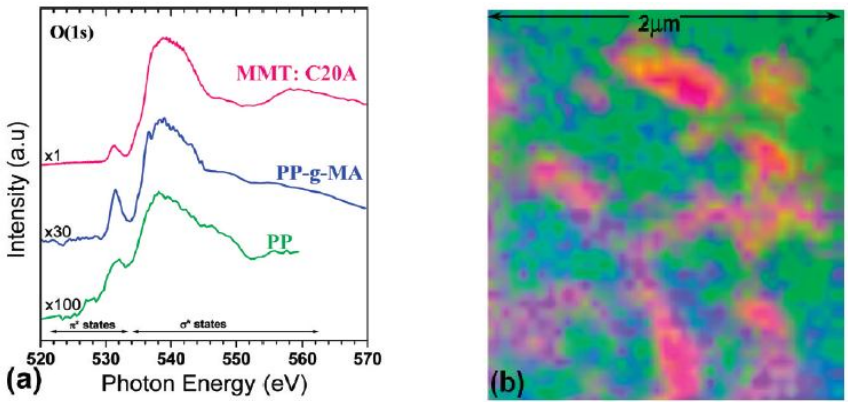

Figure 1.8. (a) X-ray absorption near edge spectroscopy (XANES) spectra at the O(1s) edge of pristine components: polypropylene (PP), PP-*g*-maleic anhydride (PP-*g*-MA) and organoclay (C20A). (b) 2 μm by 2 μm STXM composition map of PP/C20A/PP-*g*-MA (80/5/15) recorded from 500 eV up to 570 eV. The green line or regions is corresponding to PP phase, blue to PP-*g*-MA, and magenta to C20A.[107]

1.4.2. Diffraction and Scattering

It is feasible to utilize diffraction (e.g. XRD[69]) and scattering (e.g., WAXS,[122] SAXS,[123] SANS[124]) as a rapid tool, or for in-situ, real time studies in characterizing clay morphology or observing the relative evolution during deformation. Different from microscopy, X-ray technique is the reciprocal-space analysis for elucidating nanoscale morphologies. That is, this technique provides averaged morphological information in this space. By observing the position, full-width-at-half-maximum (FWHM), and

intensity of the basal reflections in XRD [125]or WAXS [126] patterns from the dispersed clay, a rough picture of the nanocomposite structure (intercalated or exfoliated) can be gained.

Figure 1.9 summarizes the corresponding X-ray spectra for four possible types of polymer/clay composites: conventional microcomposite and three nanocomposites.[69] Polymer/clay microcomposites display the same XRD spectrum as that of the starting clay particles, indicating that the clay structure is not affected upon mixing with the polymer. On the other hand, in intercalated nanocomposites, the basal reflection shifts to the lower angle relative to that of the starting clay, indicative of expanding the clay galleries by intercalation of polymer chains (angle value and gallery height being related through the Bragg's relation: $\lambda = 2\ d_{001} \sin(\theta_{001})$, where λ corresponds to the wave length of the X-ray radiation used in the diffraction experiment, d_{001} the basal spacing and θ_{001} is the measured basal reflection angle). A decrease in the order degree of platelet stacking results in a broad and weak basal peak, while preserved multi-layer structure allows a sharp basal peak detectable as well as subsequent reflection peaks in XRD profiles. On the other hand, in the exfoliated structure, no more diffraction peaks are visible either because of a much too large spacing between the layers beyond the scanning angle window of XRD instruments, or because the nanocomposite does not present ordering.[8] However, conclusive XRD information on clay morphology in some cases can be to some degree misleading. In case of low sensitivity or counting time of scan, the peak could be undetectable. In the absence of internal order or alignment in clay platelets, the basal peak becomes quite weak or broad, and may be unobservable.

Detailed modeling of the XRD profiles was attempted to yield structural data, such as clay particle size, extent of disorder and interlayer composition. For instance,

directly applying the Scherrer equation, the particle size was obtained in polypropylene/MMT nanocomposites.[127] However, this XRD information is in disagreement with the TEM observations, because many factors contributing to the peak breadth must be considered separately. In addition, although XRD can roughly offer information on clay structures, relatively little is known about the spatial distribution of the particles in nanocomposites.

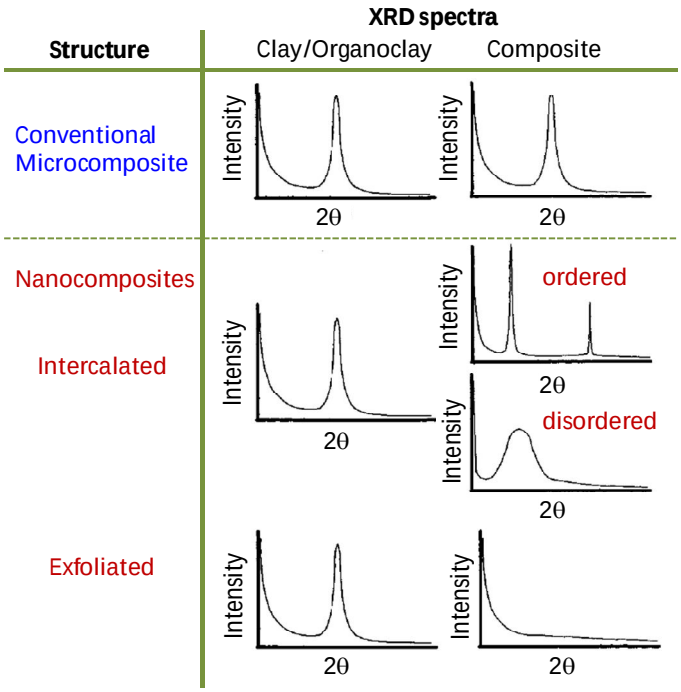

Figure 1.9. Comparison of X-ray diffraction spectra expected in four types of polymer/clay composites.[69]

Another X-ray technique, SAXS has been proved to be a powerful tool to determine the size, shape, and internal structure of the clay particles in nanocomposites with particle sizes ranging from 1 to 50 nm.[128] The 3D study using 2D SAXS and 2D WAXD developed by Bafna, et al.[122] allows one to directly compare 3D orientations of

different structural features in high density polyethylene/MMT nanocomposites. The relative clay morphological parameters were also identified, such as size of clay particles in thickness, the number of platelets per stack, lateral width and gallery height. In this point, it is conceptually more useful than a single WAXD reflection. Masenelli-Varlot et al.[129] used SAXS to determine a thickness distribution. By fitting the scattering signal, the proportion of each particle in a certain thickness obtained by optical microscopy/TEM images was determined and compared to those distributions from image analysis. It turns out a good agreement between SAXS and image analysis (see Figure 1.10). Ray et al.[130] proposed a new approach for quantifying the quality of clay dispersion in a polymer matrix by SAXS combined with TEM. They studied the effect of clay content on the nanocomposite morphology such as the probability of finding nearby clay particles and their thickness calculated using the Generalized Indirect Fourier Transformation technique and the modified Caillé theory. In the case of all nanocomposites investigated, SAXS results were in good agreement with TEM observations. These results indicate that the clay content is the key factor in controlling the network structure of dispersed clay particles in nanocomposites.

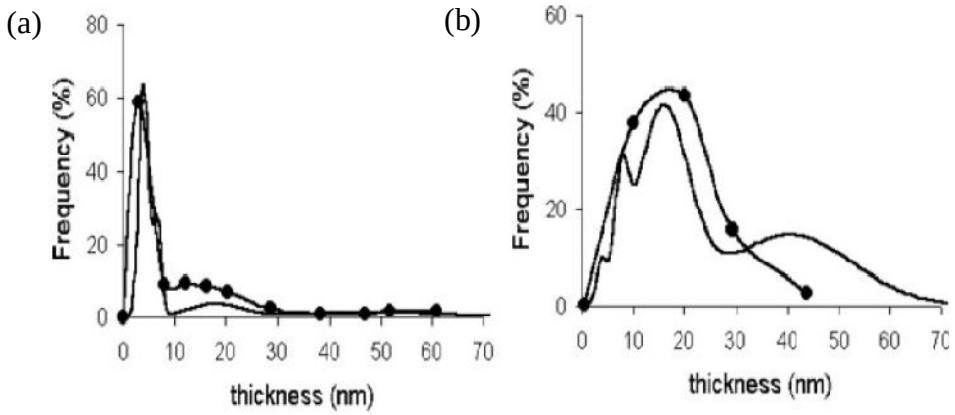

Figure 1.10. Comparison of SAXS (–•–) and microscopy (—) techniques for quantifying the clay dispersion in nylon 6/clay (a) and in polyethylene/clay (b) nanocomposites.[129]

For in-situ, real time studies, diffraction and scattering techniques have been used to study how clay morphology forms and develops when annealing a clay/polymer system in a molten state[131-136] or deforming nanocomposites.[104,124,126,137-138] Vaia et al.[134] first used XRD to study the kinetics of melt intercalation by tracing the time evolution of XRD diffraction patterns in statically annealed polystyrene/organically modified fluorohectorite. Kinetics of intercalation of polymer into organoclay was correlated with the change in intensity of the pristine and intercalated diffraction peaks with time. These investigations suggest that formation of intercalation structure requires no additional processing time when compounding polymer/clay system using conventional processing techniques like extrusion. In a further study,[136] this in-situ XRD method was validated by SANS measurements, the mechanism of which is based on conformation change of PS chains when experiencing from 3D random walk to confined 2D walk in nano-galleries of clay. The conformation change leads to the slope evolution of the low q SANS intensity as a function of annealing time. Various factors play an important role in the formation of intercalated structure, such as the molecular weight of a polymer matrix, chemical treatment of clay surface, and polymer/silicate interfacial interaction. Time-resolved high-temperature-XRD was also used to probe the expansion behavior of clay during intercalative polymerization.[139] The details of the evolution of clay gallery height were observed to investigate effects of clay loadings, polymerization conditions (e.g. temperature, solution, initiator, etc.) on the formation of nanocomposites.

Under external forces (e.g. thermal or mechanical), the formation of the nanostructure in a polymer/clay system is attractive since such information will benefit an understanding of structure-processing relationship.[104,124,126,137-138] In order to investigate

the formation of intercalated nanocomposites compounded by a corotating twin-screw extruder, Zheng et al.[140] monitored the gallery height of organoclay in samples taken from different positions along a screw using XRD. The basal peak of XRD spectra shift into a low angle for samples taken from the hopper to the die, suggesting that polymer chains can diffuse into the galleries of the organoclay within a few minutes during mixing. Bousmina et al.[131-132] followed up structure evolution in polymer/clay system under shear stress through concurrent XRD and rheometry. They found pretty slow polymer diffusion into clay galleries, during which more intercalated structure forms and the resulting intercalated stacks become more homogeneous and smaller in size. Interestingly, reversible de-intercalation and intercalation processes in the polyethylene oxide/organoclay nanocomposites[133] were detected during secondary crystallization and subsequent melting of secondary crystals by temperature-dependent synchrotron wide-angle X-ray diffraction (WAXD).

In a study on deformation of the brittle nylon 6-MMT nanocomposites, SAXS results were used to complement TEM in confirming that the role of the clay platelets apparently was to trigger the formation of numerous crazes.[123] In another study,[124] for tough thermoplastic polyurethanes (TPU) nanocomposites filled with synthetic fluoromica under uniaxial deformation, initially isotropic 2D SAXS pattern becomes anisotropic with increase of strain (see Figure 1.11a. The formation of the stripe along transverse direction suggests platelet alignment in the direction of strain. Since the scattering signal results predominately from the silicates rather than the matrix, TPU (see Figure 1.11b), scattering at q = 0.003 Å^{-1} and q = 0.005 Å^{-1} (e.g., Figure 1.11c) is finally used to calculate the Hermans orientation parameter, f for assessing the orientation of

silicates. The Hermans orientation parameter, *f*, as a function of strain in Figure 1.11(d) reflects the orientation of the silicates during uniaxial deformation. It was found that the orientation is dependent of a complex manner involving not only size but also dispersion state and spatial restrictions encountered from the nearby particles. Recently, Tang et al.[137] used 2D SAXS to study polyethylene/MMT nanocomposites with synchronously improved strength and toughness after tensile deformation. They compared different composites with different polymer/clay interfacial interaction as well as clay dispersion state, and found that the high degree of orientation of clay platelets results from the synergistic movements of polymer chains and silicates, owing to the formation of a network-like structure by strong polymer/clay interfacial interaction. As comparison, PE/MMT composite with no strong interfacial interaction and poor clay dispersion displays the relatively weak orientation of MMT platelets, and a strong cavitation during deformation.

To sum up, in order to fully understand the complicated morphological picture of nanocomposites in the static state or under deformation, diffraction and scattering will be necessary to combine with other techniques such as imaging, spectroscopy (discussed later) and indirect methods. Each technique exerts its unique advantages as a check on the others by complementing other's deficiencies.

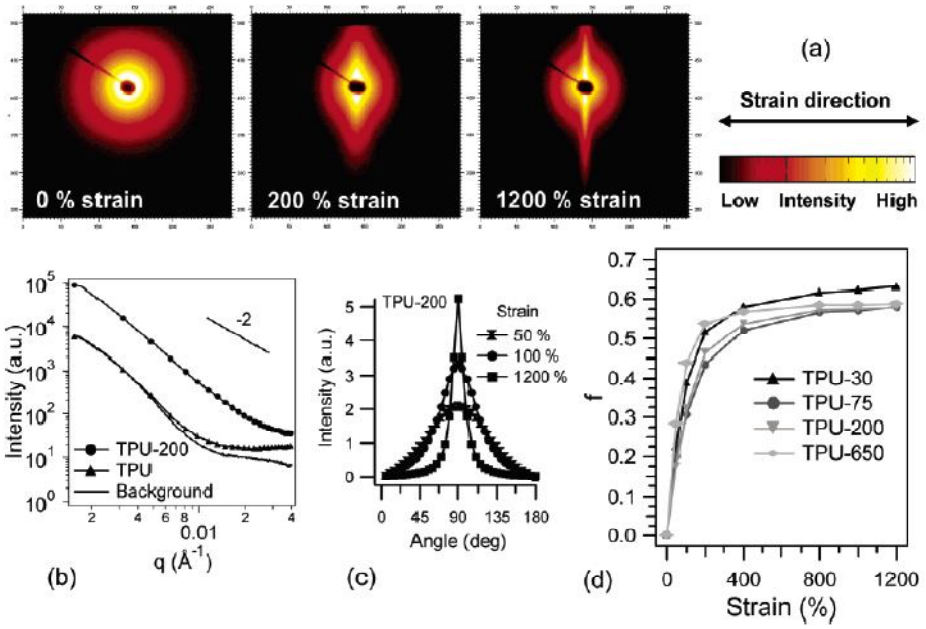

Figure 1.11. (a) 2D SAXS patterns at selected strains for thermoplastic polyurethanes nanocomposite with synthetic fluoromica particles of ~ 30 nm diameter, (b) 1D SAXS profiles illustrating the dominant silicate scattering and power-law behavior, (c) azimuthal scan of scattered intensity at q = 0.003 Å^{-1} for thermoplastic polyurethanes nanocomposite with synthetic fluoromica particles of ~ 200 nm diameter at selected strains, and (d) Hermans orientation parameter as a function of strain in nanocomposites with the particles of the thickness size as the number behind of TPU in the inset captions.[124]

1.4.3. Spectroscopy

Spectroscopic techniques have been also developed to detect the nanocomposite morphology. These techniques include Fourier transform infrared spectroscopy (FTIR), dielectric spectroscopy, solid-state nuclear magnetic resonance (SS NMR), etc.

Loo et al.[141] first studied the orientation distribution of exfoliated MMT platelets in nylon 6 by developing a FTIR method which shows several advantages over TEM, such as a larger sampling volume and simple sample preparation. The 1018 and 1046 cm^{-1} peaks attributed solely to the Si–O vibrations of the nanocomposite were used to analyze the nanoclay orientation relative to the transition dipole moment of angles of

these two vibrations in clay, which is in agreement with laborious TEM statistics. Recently, Fu et al.[142-143] used micro-FTIR measurements to in situ observe the molecular orientation in a small region ahead of the crack tip in nylon 6 nanocomposites. There is lower molecular orientation observed in the nanocomposite relative to the pure nylon 6 during crack initiation and propagation, indicative of the lower plastic deformation. The observation was finally attributed to the brittleness of the nanocomposite. Witschnigg et al.[144] reported that near infrared (NIR) spectroscopy could be quantitatively correlated with the interlayer distance.

Davis et al.[145] correlated dielectric spectroscopy with clay exfoliation during extrusion processing of nylon 6 and clay nanocomposites. The clay morphology can be primarily revealed by a combination of the Maxwell–Wagner characteristic relaxation frequency value (f_{mw}), the conductive resistance and segmental mobility of these polymers. For example, the intercalated and exfoliated nanocomposites have a f_{mw} value of about 5.1 Hz, but the exfoliated nanocomposites have much larger resistance and segmental mobility values than the intercalated nanocomposites.

SS NMR

NMR methods increasingly become attractive as an effective technique for quantifying the level of clay dispersion.[41-46,146] SS NMR methods show some advantages over traditional tools, such as simple sample preparation, nondestructive examination, and bulk information (e.g. sample detected in a 7 mm diameter NMR rotor is roughly 10^{10} times in volume that of a TEM ultrathin film).

Clay minerals, in particular MMT filled in nanocomposites often contain Fe^{3+} ions in small amounts (typically, 0-5 wt% as Fe_2O_3) substituting Al^{3+} in the octahedral plane (Figure 1.2). The important feature of the Fe^{3+} ion is that it is paramagnetic due to its unpaired electrons (I = 5/2). The paramagnetic Fe^{3+} ions inside clay can produce magnetic fluctuations and further perturb NMR parameters, such as significant line broadening, partial signal loss, and a notable shortening of the spin-lattice relaxation time (T_1) for the neighboring nuclei on clay surface. By building up the magnetization gradient around clay particles, the polarization will propagate from the neighboring nuclei into the remote ones via spin diffusion. Here, these paramagnetic Fe^{3+} ions acting as powerful relaxation centers largely enhance the ^1H and ^{13}C spin-lattice relaxation throughout composites.[42,146] These enhancements in the initial relaxation and the relaxation rate ($1/T_1$) will be more significant when there is more polymer/clay interfacial surface area, or smaller average interparticle spacing. For a given clay content, more interfacial area indicates higher degree of clay exfoliation, and smaller interparticle spacing indicates more homogeneous clay distribution. As a result, these changes in the nuclear spin-lattice relaxation are correlated with two important features of clay morphology: interfacial surface area and interparticle spacing (as discussed in the last Section 1.4.1).

More detailed and quantitative information on morphology of paramagnetic nanocomposites has been gained from a simple picture of T_1^H shortening in a polymer matrix mentioned above. Bertmer et al.[41] correlated the paramagnetic contribution to the spin-lattice relaxation rate ($R_{1,para}$) with the clay/nylon 6 surface-to-volume ratio. The average number of platelets per stack (N_{ps}) was estimated for nanocomposites containing different clay contents by scaling with two of them with known values of N_{ps} from TEM

data. The experimental data are in good agreement with the values calculated in the hypothesis of two platelets per stack (see Figure 1.12). However, it should be noted that the experimental data points for samples at the two highest contents exhibit between the line for the perfect exfoliation (solid line) and the line for N_{ps} = 2 (dashed line). It indicates that the degree of exfoliation apparently becomes better with the addition of clay. In this point, this method is in disagreement with TEM data. Furthermore, given the direct proportionality to surface area, the mean interparticle spacings were estimated, which, however, were significantly larger than those obtained by TEM analysis (see Section 1.4.1).

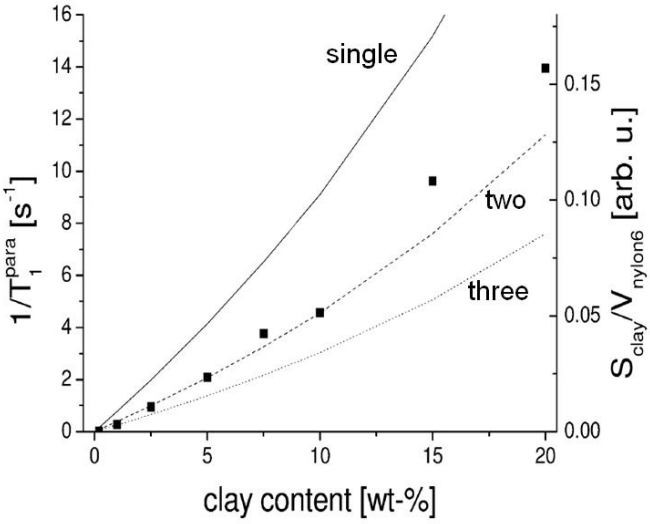

Figure 1.12. Paramagnetic contribution to the proton spin-lattice relaxation rate (left axis) and surface-to-volume ratio (right axis) as a function of clay content for a nylon-6/montmorillonite nanocomposite.[41] The lines refer to the surface-to-volume ratios in the case of single platelet (solid line) and of two (dashed line) and three platelets (dotted line) per stack, which are scaled from 2.5 and 5 wt% MMT nanocomposites with two platelets per stack.

Calberg et al.[43] observed that $R_{1,para}$ increases faster with an increase of clay content in the plot of $R_{1,para}$ as a function of clay content (W_c). This observation is unexpected, because the aggregation of clay particles causes a decrease in interfacial surface area per unit clay weight. Thus, the increase of $R_{1,para}$ should become slow with W_c, when the aggregation take place. This unexpected observation was attributed to no serious aggregation until the MMT content up to 50 wt%. However, their conjecture is not in accordance with XRD and TEM data.[60-61]

VanderHart et al.[42,44-45] developed NMR relaxometry as a means to characterize morphology of MMT nanocomposites with nylon 6, polystyrene (PS), and styrene-acrylonitrile copolymer (SAN). Spin-diffusion models were proposed to describe spin-lattice relaxation under the influence of paramagnetic centers. Two paramagnetic effects on nuclear spin-lattice relaxation are utilized: the initial slope of $M_c^n \sim t^{1/2}$ is related to the interfacial surface area; $R_{1,para}$ is related to average interparticle spacing. The fraction of the interfacial surface area was calculated by scaling the initial slopes with that of a reference material with the fully exfoliated structure. $R_{1,para}$ could be related to the apparent mean interparticle spacing. This apparent spacing was used to calculate the homogeneity of clay distribution. Combined with qualitative XRD and TEM data, the results of the fraction of the interfacial surface area and the dispersion homogeneity allow one to characterize clay morphology of a nanocomposite in a complete way.

The initial relaxation strongly depends on the ability in the build-up of magnetization by paramagnetic clay particles and the neighboring nuclei. Surface modification or interaction between polymer chains and modifiers change the densities of the neighboring nuclei in different PCNs. Different clays contains different Fe^{3+}

concentrations. These factors could vary the initial relaxation behavior. Therefore, the initial slope can be changed not only by polymer/clay interfacial area but also by the nature of components such as paramagnetic clay, modifier and polymer.

From the foregoing discussions, the conclusion on nanocomposite morphology from NMR methods is sometimes contradictory to that from other techniques. As a consequence, the detailed exploration of NMR methods for characterizing nanocomposite morphology is still needed, in order to define their abilities and limitations. Moreover, the certain relationship between relaxation and morphology need to be established. To be specific, there are many fundamental questions that have not been answered, which limits the functions of SS NMR in characterizing clay dispersion:

(1) *What is the real picture for impurities to change the nuclear spin-lattice relaxation of the neighboring nuclei around clay particles?* How is the magnetization gradient built up around clay particles following saturation? The picture will be depicted in Chapters 2, 6 and 9.

(2) *What factors could affect the nuclear spin-lattice relaxation besides clay morphology?* The spin-lattice relaxation is not only sensitive to clay morphology but also to impurity concentration inside clay, clay surface modification and the static field. These will be addressed in Chapters 4, 5 and 6.

(3) *What is the analytical relation of the clay dispersion to the nuclear spin-lattice relaxation?* Although some explorations have been done to correlate clay dispersion d the nuclear spin-lattice relaxation, their analytical relationships still remain unknown. The detailed models and thorough analysis will be presented in Chapters 3 and 4.

Other Spectroscopy Techniques

1.4.4. Other Techniques

The so-called '3D clay network structure' was investigated based on the indirect response to clay morphology from the macroscopic properties of the polypropylene/MMT nanocomposites tested by dynamic mechanical thermal analysis (DMTA), differential scanning calorimetry (DSC), thermogravimetric analysis (TGA) and rheometry.[135] They found that the formation of percolating clay network at the turning point of 1 wt% organoclay could dramatically change the macroscopic properties. In another study,[147] the size of the cooperatively rearranging region evaluated from DSC can be related to composite morphology: a larger size found in the exfoliated PCNs and an unchanged size found in the intercalated PCNs.

Other indirect methods for nanocomposite morphology are being developed with regard to the macroscopic properties. For example, as indicated in Figure 1.13, the theories of Halphi-Tsai and Mori-Tanaka based on the stiffness data for nylon6-MMT nanocomposites could predict platelet aspect ratio and the number of platelets per stack, which are roughly in agreement with the TEM data.[8,115] The Halpin–Tsai equations for the aspect ratio slightly underestimate the experimental data, while the Mori–Tanaka theory overestimates the experimental data. Figure 1.13(b) and (c) show the predictions of the number of platelets per stack (particle size in thickness) from the equations of Halphi-Tsai and Mori-Tanaka by fitting the experimental relative moduli data. The Halpin–Tsai equation gives a good estimation that the experimental value of 1.4 fall between curves corresponding to 1 and 2 platelets per stack (Figure 1.13b), whereas the

Mori–Tanaka theory overestimates the experimental data to predict a completely exfoliated morphology. These two important parameters for clay morphology are also assessed by the relative permeability data in nanocomposites. Xu et al.[148] proposed a lamella-based model to predict the relative permeability theory, and applied their model to evaluate clay morphology in several nanocomposites, which is consistent with results from XRD or TEM data.

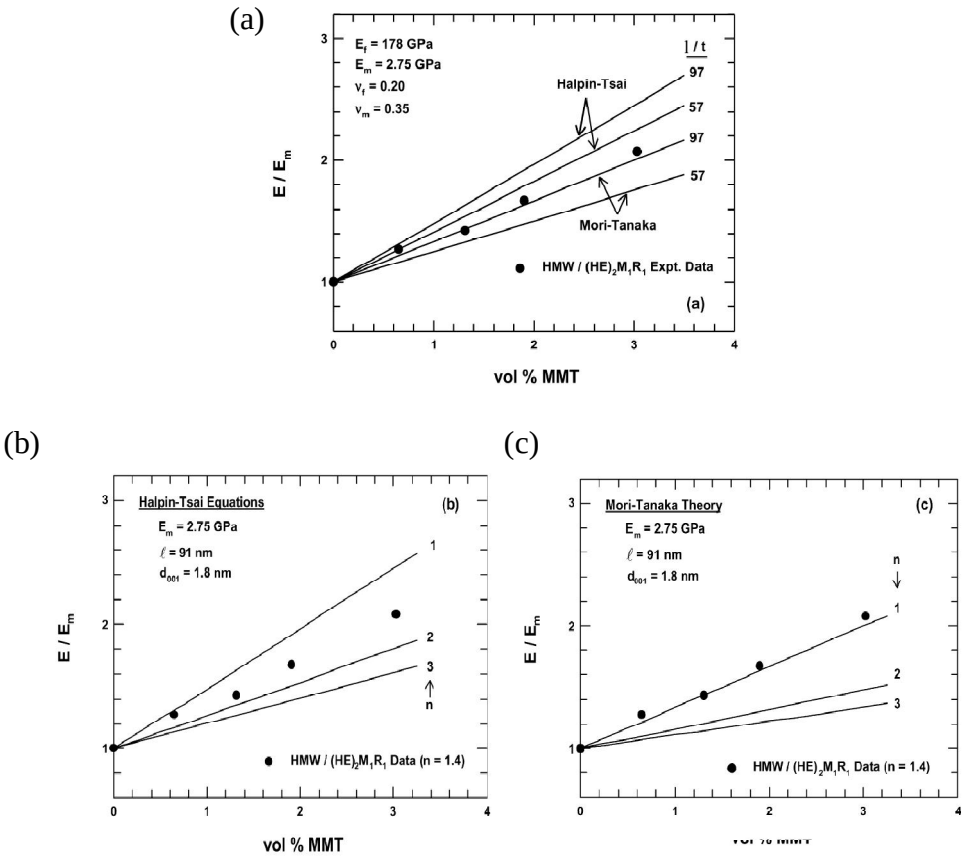

Figure 1.13. Experimental and theoretical modulus data for high molecular weight nylon 6 nanocomposites; model predictions are based on unidirectional reinforcement of (a) pure MMT having a filler modulus of 178 GPa and aspect ratio of 57 (experimentally determined number average value) and 97, corresponding to complete exfoliation, and (b,c) stacks of clay intercalated with polymer having one or more platelets per stack.[107] Note that experimental modulus data is plotted versus volume fraction (vol%) of MMT, since MMT is the reinforcing silicate.

1.4.5. Summarization of Nanocomposite Morphology

Based on the foregoing discussions, various techniques have been employed to characterize the clay morphology of polymer nanocomposites. A variety of morphological descriptors were introduced to present clay morphology. Table 1.1 summarizes these descriptors and the relative techniques.

1.5. Short Introduction to Proton Spin-lattice Relaxation (T_1)

In this section, some basic knowledge about nuclear relaxation, in particular the spin-lattice relaxation will be briefly introduced so that one can better understand the solid-state NMR experiments that were conducted on the nanocomposites. The details relevant to NMR spectroscopy may be found in the books.[53-59,149]

In the classical Newtonian model, the nuclear magnetic moment, $\boldsymbol{\mu}$ is related to angular momentum $\mathbf{L}$ by

$$\boldsymbol{\mu} = \gamma \mathbf{L} \tag{1.1}$$

where γ is the gyromagnetic ratio (the gyromagnetic ratio is characteristic for each nucleus, e.g., ^{1}H γ is 2.6752×10^7 rad $T^{-1}s^{-1}$; an electron, 1.76×10^{11} rad $T^{-1}s^{-1}$). The intrinsic angular momentum of a nucleus possessing a spin can be written in terms of basic quantum mechanics as

Table 1.1. Summary of reported parameters for clay morphology in nanocomposites obtained by various techniques

Parameter	Details	Technique	Refs.
Basal spacing, d_{001}	Calculated by the Bragg's law	XRD, TEM, SAXS	69,92,150-151
Proportion of micron-size agglomerates	Volume fraction of all micron-size agglomerates divided by total vol% of clay	OM, TEM	92-93,95
Particle length	Curved or straight length along black lines in TEM images; calculated from XRD patterns using the Scherrer equation	TEM, XRD	85,116,125
Particle thickness	Single platelet, 1 nm; size of stacks	TEM, XRD, FIBT, SAXS	85,109,116,125,130,152
Particle aspect ratio	Length divided by thickness	TEM, modulus data,	85,115-116,148,93, 145
Average number of platelets/stack	Directly estimated by TEM or calculated by thickness of stacks	TEM, Rheometry, modulus data, SAXS	85,116,125,153-154
Idealized interparticle spacing	Directly calculated from a repeating polymer/clay lamellar structure	'Ideal' model	70,155-156
face-to-face interparticle distance	Interparticle distance in the direction perpendicular to that of the lengths of the stacks	TEM, SAXS, NMR	41,44,95,113,117,157
lateral edge particle distance	Interparticle distance in the direction parallel to the stack orientation	TEM	93
Apparent interparticle spacing	Simulated from NMR relaxation data	NMR	44
Mean interparticle distance per unit volume of clay	Mean of all possible straight-line distances in 3D, at arbitrary angles, between arbitrary points on the surface of clay particle	OM, TEM	44,93,95,119
Polymer/clay interfacial area	clay surface area touched by polymer chains	TEM	95,119
Exfoliation number	Polymer/clay interfacial area divided by the total clay surface per unit volume of the samples	TEM	119
TEM particle density	Average number of particles per unit area in images	TEM	85,116,125
Degree of dispersion	Percentage of exfoliated platelets in the total clay content	TEM, NMR	44,119
Homogeneity	Clay distribution; quantitative data from NMR;	NMR, images	44 95
Orientation of particles	Preferred direction of particles in specimens	FTIR, TEM, SAXS	126,137,142-143
Clay Network	Interconnected clay particle	SAXS, images, rheometry	120,135,137

$$\mathbf{L} = \hbar\mathbf{I} \tag{1.2}$$

where **I** is called the spin quantum number or simply "the spin", and $\hbar = h/2\pi$, Planck's constant divided by 2π. That is, the spin quantum number is the maximum experimentally observable component of **L** multiplyied by $h/2\pi$, which can be a half-integer, or an integer. For proton, **I** = 1/2; the possible spins (m) are +1/2 and –1/2, corresponding to two nuclear ground states in which the nuclear moment is aligned with and against the external magnetic field, B_0, respectively. In an external magnetic field B_0, the energy of a spin can be expressed by

$$E = -\mu \cdot B_0 = \hbar\, \gamma\, m\, B_0 \tag{1.3}$$

For protons, the difference in two energy levels (m = -1/2 and m = +1/2) is

$$\Delta E = \hbar\, \gamma\, B_0 \tag{1.4}$$

Clearly, the bigger B_0, the larger ΔE. The population ratio of these two levels at an absolute temperature T is governed by the Boltzmann distribution:[59]

$$\frac{N(-1/2)}{N(+1/2)} = \frac{N_-}{N_+} = \exp\left(-\Delta E / kT\right) \tag{1.5}$$

where N is the population at a energy level. Transition between two levels generates radiation which releases the energy as $\Delta E = \hbar \gamma B_0$, as shown in eq 1.4. The energy of radiation is related to the frequency, v_0 by $\Delta E = hv_0$. The frequency of radiation due to this transition is

$$\omega_0 = 2\pi v_0 = \gamma B_0 \tag{1.6}$$

If the frequency of radio pulse is matched to the frequency of radiation due to transitions between the two levels, the resonance phenomenon, so-called nuclear magnetic resonance can be observed. This frequency is the well-known Larmor frequency.

Bloch Equations

Simply speaking, the observable magnetization is the sum of the angular momentum of all spins in nuclei of a sample at a static magnetic field, B_0. The magnetization (M_0) of a sample in an NMR spectrometer is displayed in Figure 1.14(a). The static field, B_0 is in the z-direction. In equilibrium, the magnetization of the sample (M_0) is always parallel to the direction of B_0. Application of a radio pulse with the Larmor frequency perturbs this equilibrium by exciting transitions between the energy levels. Figure 1.14(b) displays the precession of the magnetization, M. about z with an angular frequency, ω_0. A 90° pulse with a certain duration can create net magnetization, M_{xy} (the transverse magnetization) in the (xy) plane. After turning off the radio pulse, the projection of magnetization in the (xy) plane ($M\perp$) will decay to zero at the rate defined by the transverse relaxation time (T_2), while the projection of magnetization parallel to

the z direction ($M_{//}$) will grow up to M_0 at the rate defined by the longitudinal relaxation time (T_1). We call the observed NMR signal in these processes as Bloch decay (sometimes, called free-induction decay, FID), which can be described by the Bloch equation:[59]

$$\frac{d\mathbf{M}}{dt} = \gamma \mathbf{M} \times \mathbf{B} - \frac{\mathbf{M}_{\perp}}{T_2} + \frac{(\mathbf{M}_0 - \mathbf{M}_{//})}{T_1} \tag{1.7}$$

In the process from Figure 1.14(c) to (a) at equilibrium, the first term on the right hand of eq 1.7 drops out, and then we have

$$\frac{d\mathbf{M}}{dt} = -\frac{\mathbf{M}_{\perp}}{T_2} + \frac{(\mathbf{M}_0 - \mathbf{M}_{//})}{T_1} \tag{1.8}$$

If we observe z-component and x- or y-component of magnetization, we have

$$\frac{M_x(t)}{M_0} (\text{or } \frac{M_y(t)}{M_0}) = e^{-t/T_2} \tag{1.9}$$

$$\frac{M_z(t)}{M_0} = 1 - e^{-t/T_1} \tag{1.10}$$

In pulsed NMR, we can detect z-component and x- or y-component of magnetization, and analyze the experimental data to obtain the relaxation times. In practice, the NMR

signal is influenced by many possible time-dependent and time-independent interactions. By probing the evolution of the signal, NMR can gain information about the molecular structure and dynamics.

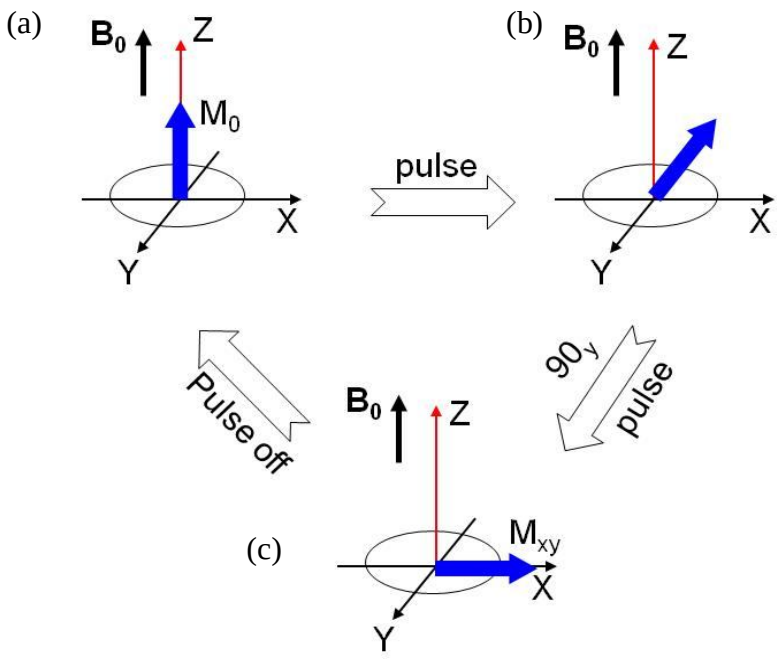

Figure 1.14. Magnetization of a sample in a NMR spectrometer: (a) at equilibrium; (b) after perturbation by a radio pulse; magnetization precesses with an angular frequency ω_0 about the z-axis; (c) 90^o pulse to achieve the transverse magnetization, M_{xy} on the (xy) plane.

Hahn Spin Echo

In practice, the free induction decay is due to nuclear relaxation via the inhomogeneous magnetic field. To overcome this issue, we utilize the Hahn spin echo experiment elegantly designed by Hahn: a 90° pulse produces the regular FID, followed

by a 180^0 pulse, which refocuses the spins with slightly different precession frequencies due to their experienced inhomogeneous field, as illustrated in Figure 1.15.

In certain cases, spin echo techniques can be of help to measurement of T_1. In the normal saturation-recovery experiment, a series of 90° pulses saturate z-component, namely, $M_z = 0$. Immediately following these pulses, the z-component will grow with the time constant, T_1. In order to observe the recovered magnetization intensity, one flips the z-magnetization into the x-y plane. In a very inhomogeneous field, it may be difficult to observe an FID following the 90° pulse, because olymer solids have short T_2 times. Hence, a spin echo is utilized to observe magnetization intensity.

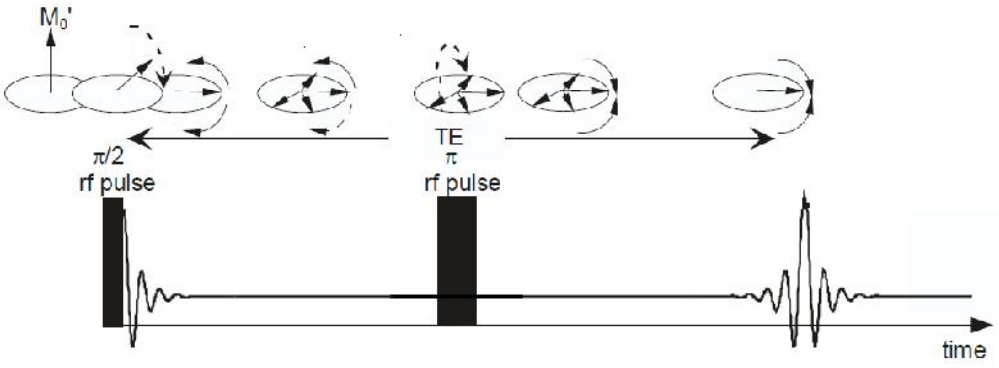

Figure 1.15. The Hahn spin echo experiment. The upper pictures depict spin vectors to describe the magnetization flip by a 90° pulse, magnetization dephasing, and refocusing by a 180° pulse. The bottom illustrates the Hahn echo pulse sequence.

Experiments for Spin-lattice Relaxation Time

There are two primary techniques used to measure the spin-lattice relaxation time: inverse recovery and saturation recovery. The former employs a 180 pulse to flip magnetization to the -z axis, while the latter uses a train of the 90 pulses to equalize populations of spins, that is, $M_z = 0$. Besides the molecular structure and dynamics, there

are two possible contributing causes to spin-lattice relaxation which may occur under some conditions. Spin-lattice relaxation is remarkably shortened by interaction with unpaired electrons in the paramagnetic impurity-containing compounds, because the magnetic moment of an unpaired electron is much stronger on the order of 1000 time (the gyromagnetic ratio, $\gamma_e/\gamma_H \sim 1000$) than the local fields from the neighboring nuclei. The strong fluctuating electron field will induce transitions between energy levels, and results in the short longitudinal relaxation time. Another factor is that the strong dipole-dipole interaction between nuclei may average out the relaxation times of all nuclei at different environments and a single relaxation time is usually obtained. This average-out process is called spin-diffusion. These two factors on the spin-lattice relaxation were recognized in the early stage of NMR development. In 1949, Bloembergen proposed and investigated the relaxation in paramagnetic ion-doped crystals.[53] He combined the two factors as a complete transport equation for the changes of nuclear magnetization, and discussed the relaxation mechanism.

1.6. Scope of Present Work

The specific purpose for this work presented in the following chapters was to demonstrate the potential of ^{1}H SS NMR as an essential tool in studying polymer/clay nanocomposites. A comprehensive review of polymer/clay nanocomposites, in particular the characterization of clay structure and morphology is given in Chapter 1. A detailed description of the ^{1}H solid-state NMR method is described in Chapter 2 to study the evolution of clay morphology in polypropylene/montmorillonite nanocomposites as a function of processing conditions such as the stretch ratio, strain rate and stretch

temperature. Specific models were proposed in Chapters 3 and 4 to describe the spin-lattice relaxation process in nanocomposites: initial relaxation behavior at short times related to effective clay surface and spin-lattice relaxation rate related to a whole picture of clay dispersion. Several cases of PCNs were investigated using our models. In Chapter 5, impurity-concentration dependence of paramagnet relaxation rate was found. A field-dependence of proton spin-lattice relaxation process was investigated in Chapter 6. Chapter 7 addresses an application of the relation of nuclear relaxation to clay morphology in measuring spin diffusion coefficient of polymer over a large distance (> 10 nm). In Chapter 8, observing structural evolution of PCNs upon uniaxial deformation by nuclear relaxation behavior is started up. Chapter 9 provides a study on proton spin-lattice relaxation in the essential component, organically modified clay filled in nanocomposites, in order to gaining better insights into proton nuclear relaxation behavior of PCNs. Table 1.2 summarizes the investigated polymer/clay nanocomposites and the SS NMR methods.

Table 1.2. Summary of investigated polymer/clay nanocomposites

Polymer/clay nanocomposites	Effect studied	method	Figure	Page number
PP/MMT with different stretch ratios	stretch ration, stretch strain, temperature	Initial slope	Figure 2.3 Figure 2.6 Figure 3.4	p 63 p 72 p 94
		$T_{1,para}$	Figure 2.4	p 67
PP/MMT with different clay contents	clay content	Initial slope	Figure 4.11 Figure 6.5	p 131 p 154
		$T_{1,para}$	Figure 4.9 Figure 6.11	p 127 p 162
PP/MMT with different clay contents	uniaxial deformation	Initial slope	Figure 8.5	p 204
		$T_{1,para}$	Figure 8.4	p 203
PP/MMT	processing	Initial slope, $T_{1,para}$	Figure 4.11	p131
PVA/MMT	clay content	Initial slope, $T_{1,para}$	Figure 4.10	p 129
		$T_{1,para}$	Figure 4.3 Figure 5.1	p 116 p 138
PVA/MMT with different MMTs	type of clays	$T_{1,para}$	Figure 4.4	p 117
Nylon6/MMT	clay content	$T_{1,para}$	Figure 4.5	p 119
PCL/MMT	surface modification	$T_{1,para}$	Figure 4.7	p 123
PLA/MMT	clay content	Initial slope, $T_{1,para}$	Figure 4.12	p 133
		Initial slope	Figure 6.8 Figure 6.9 Figure 6.10	p 158 p 159 p 160
	molecular weight	$T_{1,para}$	Figure 4.8 Figure 6.2	p 126 p 163

CHAPTER 2

Evolution of Clay Morphology in Polypropylene/Montmorillonite Nanocomposites upon Equi-biaxial Stretching: A Solid-State NMR and TEM Approach

Bo Xu, Johannes Leisen, Haskell W. Beckham,[*] Rund Abu-Zurayk,[‡] Eileen Harkin-Jones, [‡] Tony McNally[‡]
School of Polymer, Textile and Fiber Engineering, Georgia Institute of Technology, Atlanta, Georgia 30332-0295, USA
[‡] Polymers Research Cluster, School of Mechanical and Aerospace Engineering, Queen's University Belfast, Belfast BT9 5AH, UK

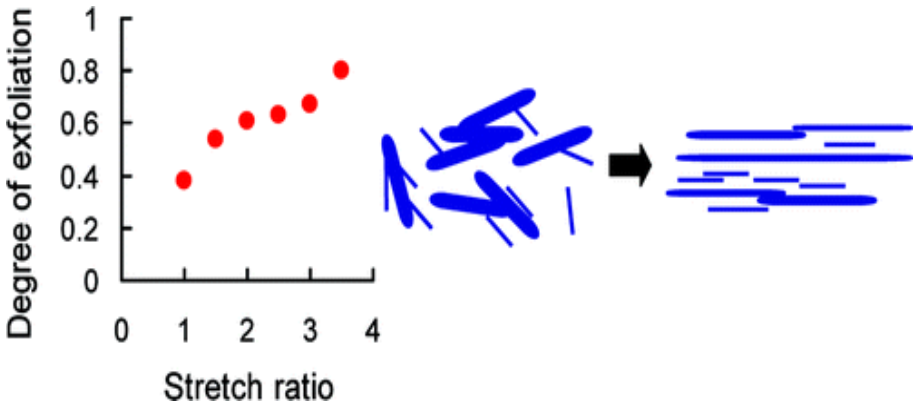

As published in Macromolecules, **2009**, Vol.42, p.8959-8968

2.1. Abstract

Solid-state NMR and TEM were used to quantitatively examine the evolution of clay morphology upon equi-biaxial stretching of polypropylene/montmorillonite (PP-MMT) nanocomposites up to a stretch ratio (λ = final length/initial length) of 3.5. ^{1}H spin-lattice relaxation times were measured by the saturation-recovery sequence. For the nanocomposites, initial portions of the magnetization recovery curves ($\leq$ ~20 ms) were found to depend on $\sqrt{t}$, indicative of diffusion-limited relaxation and in agreement with calculations based on estimates of the spin-diffusion barrier radius surrounding the paramagnetic centers in the clay, the electron-nucleus coupling constant, and the spin-diffusion coefficient. Initial slopes of these magnetization recovery curves directly correlated with the fraction of clay/polymer interface. New clay surface was exposed as a near linear function of strain. Long-time portions of the magnetization recovery curves yielded information on the average interparticle separations, which decreased slowly before reaching a plateau at λ = ~ 2.5 as particles aligned. TEM images supported these findings and were used to define and quantify degrees of exfoliation and homogeneity from the NMR data. Exfoliation, defined as $(\text{platelets/stack})^{-1}$, increased from 0.38 (unstretched) to 0.80 at λ = 3.5 for PP-MMT nanocomposites stretched at 150 °C and 16 s^{-1}. A lower stretch temperature, 145 °C which is slightly below melting onset, led to an exfoliation degree of 0.87 at λ = 2.8, consistent with the ability of higher melt viscosities to allow for higher shear stress transfer. Exposure of new clay surface is attributed to aggregate break-up and orientation at low strains ($\lambda \leq$ ~2) and to platelets sliding apart at higher strains.

2.2. Introduction

Performance in polymer/clay nanocomposites (PCNs) depends on the nature of the interaction between polymer and clay and on details of the clay dispersion, which is affected by processing or deformation.[124,158-159] Relationships between processing conditions and clay morphology need to be firmly established to prepare PCNs with targeted properties. Some processing/structure and deformation/structure relationships have been reported for PCNs, mostly prepared by extrusion and injection molding,[93,114,160] or deformed by uniaxial stretching.[124] On the other hand, little has appeared on the effect of multi-axial deformation of PCNs,[161-162] which is relevant for such processes as blow molding. A recent study of poly(ethylene terephthalate)/clay nanocomposites revealed how equi-biaxial stretching aligned tactoids and increased exfoliation by sliding platelets apart.[163] Here we report on the evolution of clay morphology in polypropylene/montmorillonite nanocomposites that have been equi-biaxially stretched. Mechanical properties have been reported for these materials[164] and will be connected with the quantitative descriptions of clay morphology presented below. We employed a combination of tools, but our analysis is based primarily on results from solid-state nuclear magnetic resonance (NMR) and transmission electron microscopy (TEM). The advantages and limitations of TEM and NMR, along with X-ray diffraction (XRD), have been well documented for characterizing clay dispersion in PCNs.[44,70,150,158,165-167] Here we use NMR and TEM in a complementary and integrated manner, for example, by defining some morphology descriptors that depend on both NMR and TEM data. The clay morphology as a function of strain is quantified and qualitatively correlated with the clay orientation.

PCNs containing homogeneously dispersed, completely exfoliated clay particles are rarely fabricated. For polyolefins, the production of such systems becomes increasingly difficult with high clay loadings and the clay morphology is commonly characterized by a distribution of particle types and sizes including exfoliates, intercalates, and flocculated aggregates composed of two or more stacked platelets. This is certainly the case for polypropylene/clay nanocomposites,[135,152,160,168-170] the focus of the studies reported here. The clay that we used was montmorillonite (MMT), a naturally occurring layered silicate that contains small quantities of paramagnetic Fe^{3+} impurities. While these impurities do not affect most properties of nanocomposites containing MMT, they have a tremendous effect on the NMR relaxation characteristics, which is the basis of using NMR to characterize clay morphology.[44] The details and consequences of this paramagnetic effect are described in the following section.

2.3. Background on NMR Spin-lattice Relaxation in Paramagnetic Materials

2.3.1. NMR Spin-Lattice Relaxation via Paramagnetic Centers

From the earliest days of NMR, it has been known that paramagnetic impurities in materials enhance spin-lattice relaxation.[53] Theoretical models that describe this enhanced relaxation were developed and tested, particularly on crystalline inorganic solids doped with known quantities of paramagnetic ions such as Cr^{3+}, Mn^{2+}, or Ce^{3+}.[53-59] Paramagnetic species enhance spin-lattice relaxation in two ways: (1) direct interaction with neighboring nuclei, and (2) spin diffusion from remote nuclei to the paramagnetic centers. Thus, following a perturbation of the nuclear spin system (e.g., by placing a

sample in a static magnetic field, or saturating it with rf pulses), the total rate at which the magnetization, M, changes with time, t, is

$$\left(\frac{\partial M}{\partial t}\right)_{\text{total}} = \left(\frac{\partial M}{\partial t}\right)_{\text{direct}} + \left(\frac{\partial M}{\partial t}\right)_{\text{diff}} + \left(\frac{\partial M}{\partial t}\right)_{\text{intrinsic}} \tag{2.1}$$

where $(\partial M/\partial t)_{\text{direct}}$ is the rate of magnetization change due to direct interaction with paramagnetic species, $(\partial M/\partial t)_{\text{diff}}$ is the rate of magnetization change resulting from spin diffusion to the paramagnetic relaxation sinks, and $(\partial M/\partial t)_{\text{intrinsic}}$ is the intrinsic rate of magnetization change due to interaction of the sample lattice with the static magnetic field (B_o). When relaxation intrinsic to the sample lattice is very slow, $(\partial M/\partial t)_{\text{intrinsic}}$ can be ignored.

The direct relaxation term has been given by

$$\left(\frac{\partial M}{\partial t}\right)_{\text{direct}} = \left(\frac{C}{r^6}\right)(M_0 - M) \tag{2.2}$$

where M_0 is the equilibrium magnetization, r is the distance from the paramagnetic center, and C is a constant describing the strength of the interaction between paramagnetic center and nucleus. After angular averaging, C can be expressed as

$$C = \frac{2}{5} I(I+1)(\gamma_p \gamma_n \hbar \frac{\mu_o}{4\pi})^2 \frac{\tau_c}{1+\omega_n^2 \tau_c^2} \tag{2.3}$$

where γ_p and γ_n are the magnetogyric ratios of the paramagnetic electron and observed nucleus, respectively, μ_o is the magnetic constant ($4\pi \times 10^{-7}$ N/A^2), I is the spin number of the paramagnetic center (5/2 for Fe^{3+}), τ_c is the correlation time for the interaction of the paramagnetic center with the lattice, and ω_n is the Larmor frequency of the observed nucleus ($\gamma_n B_o$). As the distance from a paramagnetic center increases, nuclear relaxation due to direct interaction diminishes rapidly (note r^{-6} dependence in eq 2.2).

The spin diffusion term in eq 2.1 has been given by $(\partial M/\partial t)_{diff} = D\nabla^2 M$, where D is the average spin-diffusion coefficient.[53] In the direct vicinity of paramagnetic centers, spin diffusion is suppressed due to the large local magnetic fields of unpaired electrons. For a surrounding spherical region with radius δ, the spin-diffusion coefficient is considered to be zero and δ is called the spin-diffusion barrier radius.[53-55,59,171] If the average distance between two paramagnetic centers (d_p) is much larger than the spin-diffusion barrier radius, and the direct relaxation rate is sufficiently high, the rate-limiting step in the overall relaxation is spin diffusion to the paramagnetic centers.[54-56] This is referred to as diffusion-limited relaxation and is characterized by magnetization growth following saturation that obeys a square-root-of-time dependence:

$$\frac{M(t)}{M_0} = \frac{4}{3}\pi^{3/2} C^{1/2} N_p t^{1/2} \tag{2.4}$$

where N_p is the number of paramagnetic centers per unit volume. Equation 2.4 holds in the following range of recovery times:[54,172]

$$\frac{\delta^6}{C} < t < C^{1/2} D^{-3/2} \tag{2.5}$$

Immediately following saturation of the spin system, no magnetization gradients exist in a sample. These gradients build up rapidly where relaxation by direct interaction with paramagnetic centers is most prevalent. As magnetization gradients develop, magnetization recovery is diffusion-limited and characterized by an initial square-root-of-time dependence for a finite time period defined by eq 2.5. Once gradients are established throughout the matrix, magnetization grows exponentially with time toward equilibrium:

$$\frac{M(t)}{M_0} = 1 - \exp(-t / T_1) \tag{6}$$

Since the transition from diffusion-limited to exponential magnetization growth is gradual, it could be beneficial to estimate the time limits of the diffusion-limited regime for a given sample according to eq 2.5.

2.3.2. Polymer-Clay Nanocomposites

Natural clays like montmorillonite contain paramagnetic impurities such as Fe^{3+} ions located within a central octahedral alumina layer sandwiched between two sheets of tetrahedral silica; the total thickness of this clay platelet is ~ 1 nm (see Figure 1.2). When incorporated into a polymer to make a nanocomposite, these clays provide a source of enhanced NMR spin-lattice relaxation for the surrounding chain segments. In analogy to the paramagnetic impurities in crystalline compounds discussed above, the Fe^{3+} ions in

the clay can shorten the T_1s of nuclei near the surface of the clay by direct interaction, and of nuclei remote from the clay surface through spin diffusion. However, before analyzing data using the approach described above, some differences between inorganic crystals doped with paramagnetic impurities and polymer-clay nanocomposites (PCNs) should be considered. For example, in the doped inorganic crystals, the paramagnetic centers are homogeneously dispersed with typical concentrations (N_p) between 10 and 0.1 $\times 10^{19}/cm^3$, which leads to average impurity separations, $d_p = 2 \times (3/4\pi N_p)^{1/3}$, between 2 and just over 12 nm, respectively.[58] In clays used for PCNs, the paramagnetic centers are present in similar and even slightly higher concentrations of 10^{19} to $10^{21}/cm^3$ (calculated from structural formulas and either density or unit-cell dimensions obtained from X-ray diffraction), but the clays are then dispersed, very often inhomogeneously, in polymeric matrices at concentrations typically of 1 to 5 wt %. The minimum separation between clay platelets can be estimated for an "idealized" nanocomposite (Δ_{ideal}), that is, one in which the clay is completely exfoliated and homogeneously dispersed:

$$\Delta_{ideal} = V_{polymer}/(V_{clay}/h_{clay}) \tag{2.7}$$

where $V_{polymer}$ is the volume fraction of polymer, V_{clay} is the volume fraction of clay, and h_{clay} is the clay platelet height or thickness. Using densities of 0.91 and 2.6 g/cm^3 for polypropylene and montmorillonite, respectively, and h_{clay} = 1 nm, eq 2.7 was used to calculate interplatelet spacings between 290 and 50 nm for 1 to 5 wt % clay, respectively. These dimensions would be even larger for clay aggregates that are not fully exfoliated. Thus, in PCNs, a greater majority of organic nuclei lie outside the spherical regions

around the paramagnetic centers with radius d_p. Furthermore, the paramagnetic centers in PCNs are not in direct contact with the nuclei of the polymeric matrix, but are embedded in the central layer of a three-layer platelet and therefore separated by a minimum of 0.5 nm from the nearest organic nuclei on the platelet surfaces. As the clay commonly exists as stacks of platelets, many of the paramagnetic centers can be even farther away from the nearest organic nuclei. A consequence of the very dilute nature of the paramagnetic centers in PCNs is that the intrinsic ^{1}H T_1s of the samples must be taken into account (see eq 2.1) as the T_1 differences between pure polymer and PCN may not be that great.

VanderHart, et al. have discussed the influence of clay-embedded paramagnetic impurities on the NMR properties of polymers in PCNs, [42,45,146] and showed how ^{1}H T_1 relaxation data can be used to quantify the degrees of exfoliation and dispersion homogeneity of the nanoscopic clay.[44] Working from a diffusion model that included both spin diffusion and longitudinal relaxation, they simulated the evolution of magnetization during a saturation recovery experiment. Their model consisted of two regions, the bulk polymer and a thin layer (0.4 nm wide) near the clay surface that served as an interfacial relaxation sink. They simulated relaxation curves using finite element methods and representative T_1, D, and interplatelet spacing values (estimated using eq 2.7 for a well exfoliated sample) for some polystyrene/montmorillonite nanocomposites. They then tried to approximate the calculated relaxation curves with a biexponential. The exponential fits very well for long recovery times, but not so well for short times after saturation. The short-time behavior, specifically 5 – 50 ms, was better fit using a square-root-of-time dependence. Thus their data are consistent with diffusion-limited relaxation. Most importantly, they described how the short-time portion of the recovery curves

plotted versus $\sqrt{t}$ yielded straight lines with slopes that were directly proportional to the polymer-clay interfacial area, hence, amount of exfoliated clay. They used these initial slopes (S), corrected point-by-point for the intrinsic relaxation of the pure polymer, to calculate a degree of exfoliation, f. For a given clay and clay concentration,

$$f = (\text{platelets/stack})^{-1} = S/[S_{\text{ref}} \times (\text{platelets/stack})_{\text{ref}}] \tag{2.8}$$

where S is the corrected initial slope for the sample and S_{ref} is the corrected initial slope for a reference material. Using a reference material known from TEM to be very well exfoliated, $(\text{platelets/stack})_{\text{ref}} = 1$ and the degree of exfoliation is simply calculated as a ratio of slopes. Furthermore, they also noted that the overall relaxation curves, approximately the exponential long-time portion of the magnetization recovery curves, yielded relaxation rates related to the quality of the clay dispersion.[42,45] They defined an overall paramagnetic contribution to the spin-lattice relaxation rate ($1/T_{1,\text{para}}$), which could be calculated simply by subtracting the rate due to the pure polymer ($1/T_{1,\text{polymer}}$) from the measured rate for the PCN ($1/T_{1,\text{PCN}}$):

$$\frac{1}{T_{1,\text{para}}} = \frac{1}{T_{1,\text{PCN}}} - \frac{1}{T_{1,\text{polymer}}} \tag{2.9}$$

While $1/T_{1,\text{para}}$ provides a relative measure of the homogeneity of the average interparticle separation, they also introduced a more quantitative measure. They calculated apparent interplatelet separations (Δ_{app}) using their model by matching the T_1s from the long-time portion of the magnetization recovery curves with experimental

values. This apparent average separation was then compared to an "ideal" interplatelet spacing (Δ_{ideal} from eq 2.7) scaled by the degree of exfoliation (f from eq 2.8) to yield a quantitative measure of the homogeneity, ε:[44]

$$\varepsilon = (\Delta_{ideal}/f)/\Delta_{app} \tag{2.10}$$

where $\varepsilon = 1$ characterizes a sample with good homogeneity.

2.4. Experimental

Materials. Organically modified montmorillonite (MMT) was obtained from Southern Clay Products as their commercial product Cloisite 15A. Organically modified fluorohectorite (FH) was obtained from UniCO-OP Chemicals Japan as Somasif MAE. Samples were dried under vacuum at 110 °C for 48 hours and cooled for 72 hours at room temperature before all measurements. Structural characteristics of both clays are detailed in Table 2.1.

The polypropylene-montmorillonite nanocomposite was fabricated by melt compounding 5 wt % Cloisite 15A and isotactic polypropylene (PP, M_w = 250 kg/mol, M_w/M_n = 4.1) blended with 3 wt % PP-*g*-maleic anhydride (DuPont, Fusabond® P, denoted as PP-MA). A PP/PP-MA blend without clay was also prepared using the same procedures as that used for the nanocomposite. In the following, the polymeric matrix is simply referred to as 'polypropylene' or 'PP', and the nanocomposite is referred to as 'PP-MMT'.

The PP and PP-MMT were compression-molded at 190 °C to form sheets with a thickness of 1 mm. This was followed by equi-biaxial stretching in a home-built apparatus[173] for both PP and nanocomposite sheets. A series of samples with stretch ratios (λ = final length/initial length) of 1.5 to 3.5 were prepared by stretching at 150 °C (~ 5 °C below the peak melt temperature) with a strain rate of 16 s^{-1}. Some samples were also prepared at 145 °C (16 s^{-1}) and with a strain rate of 32 s^{-1} (150 °C). Prior to stretching, samples were held at their respective deformation temperature for 3 min.

Table 2.1. Structural characteristics of organically modified clays[a]

	Montmorillonite (MMT)	Fluorohectorite (FH)
Mean formula unit[b]	$Na_{0.65}[Al,Fe]_4Si_8O_{20}(OH)$	$Na_{0.66}Mg_{2.68}(Si_{3.98}Al_{0.02})O_{10.02}F_{1.96}$
Fe_2O_3 content (wt %)	2.83[c]	0
CEC (meq/100 g)[d]	125	85 ~ 120
Weight loss on ignition (%)	43	42
Basal spacing (nm)	3.2	3.4
Organic modifier[e]	2C18	2C18
Area per cation (nm^2)[f]	~1.51	~1.35
T_1^H (ms)[g]	10	300

[a] Unless stated otherwise, information on MMT was obtained from technical literature provided by Southern Clay Products, Inc., while information on FH taken from McNally, et al.[97] [b] Taken from Xie et al.[174] for MMT and from Yang et al. for FH.[175] [c] This value from Southern Clay Products was determined by elemental analysis and corresponds to 4.96 wt % Fe_2O_3 or 3.47 wt % Fe in the pure clay (assuming all Fe^{3+}). [d] Cation exchange capacity; value depends on layer and edge charges; range for FH taken from Yang et al.[175] and Schmidt et al.[176] [e] Tallow-sourced dimethyl dialkyl ammonium chlorides in which the alkyl tails consist of ~65 wt % C_{18}, ~30 wt % C_{16} and ~5 wt % C_{14} for MMT; and ~25 wt % C_{18}, ~74 wt % C_{16} and ~1 wt % other for FH. [f] For FH, calculated from average layer charge of 0.33 mol per half unit cell (Si_4O_{10})[177] using method similar to Osman et al.;[175] for MMT, calculated beginning from typical surface area of ~750 m^2/g.[178] [g] Measured using saturation recovery.

Measurements. Solid-state NMR measurements were performed using a Bruker DSX-300 NMR spectrometer operating at 7.05 T and a double-resonance CP/MAS probe. The

organically modified clays were packed as powders into 7-mm (outside diameter) ceramic rotors for magic-angle spinning (MAS). Solid-state ^{13}C NMR spectra (10k scans) were measured using ^{13}C single-pulse excitation with ^{1}H high-power decoupling during detection. A recycle delay of 4 s, sample spinning speed of 5 kHz, and 90° pulse durations of 5 μs were employed.

For the polymer and nanocomposites, circles with diameters of ~6.8 mm were punched from the sheets using a leather hole punch and stacked into the 7-mm MAS rotors. All spin-lattice (T_1) relaxation experiments were conducted using the CP/MAS probe but on static samples without MAS. A saturation-recovery sequence was employed for recording the ^{1}H T_1 data.[44] For a given sample, 64 different relaxation delays from 0.5 ms to 10 s were measured with 16 averages each. The resulting ^{1}H spectra contained single peaks that were integrated to yield $M(t)$ where t is the respective delay time. Background signal was measured using an empty rotor and subtracted from each spectrum. Equilibrium magnetization (M_o) was obtained as the average integrated intensity from the spectra for t = 7, 8, 9, and 10 s (which are > 5 × T_1). Plots of $M(t)/M_o$ versus t yielded the saturation recovery curves. The overall ^{1}H T_1 was obtained by fitting to eq 2.6.

Due to lower signal-to-noise ratios for spectra at short recovery delays, the initial portions of the magnetization recovery curves (up to 50 ms) were measured using 64 scans for 32 separate relaxation delays. As described above, the resulting ^{1}H spectra were integrated to yield $M(t)$ and normalized by M_o. The normalized magnetization, $M(t)/M_o$, for the nanocomposites was corrected by subtracting point-by-point the $M(t)/M_o$ for the

identically deformed pure polymer which was then plotted versus $\sqrt{t}$. The resulting initial magnetization build-up curves were fitted by linear regression.

High resolution TEM images were recorded on a Phillips CM100 instrument using an accelerating voltage of 100 kV on ultra-thin samples (typically 60 nm). For each stretching condition a total of 5 – 7 representative images were analyzed manually with respect to the average particle density, length, thickness and separation using the software package ImageJ version 1.24o (NIH). All particles, including platelets, intercalates, and aggregates were sampled.

Wide-angle X-ray diffraction patterns were recorded on a PANalytical X'Pert Pro diffractometer using Cu $K_{\alpha 1}$ radiation generated at 45 kV and 40 mA (wavelength = 1.5406 Å). Samples were scanned at 0.02°/s in the range of 2θ = 1-15°. The d_{001} basal spacing was calculated using the Bragg equation.

Differential scanning calorimetry (DSC) measurements were performed on a Seiko 220C at a heating rate of 10 °C/min to 200 °C. Thermogravimetric analysis (TGA) was conducted on a Seiko TG/DTA 320 in N_2. Samples were heated at 15 °C/min to 600 °C and held there for 10 min. Following this heat treatment, residual mass was taken as the pure clay content.

2.5. Results and Discussion

Solid-state ^{1}H NMR spin-lattice relaxation data were collected using the saturation recovery method for all PP and PP-MMT samples. Representative data are shown in Figure 2.1 for the PP-MMT and corresponding PP biaxially stretched to λ = 2.5. Solid-state ^{1}H NMR spectra (Fig 2.1a) were integrated and plotted versus recovery time

to yield relaxation curves (Fig 2.1b) that are fit well with exponentials (eq 2.6) to yield single T_1s. While it is straightforward to observe that the relaxation rate for the nanocomposite is greater, it would be easy to overlook information that can be gleaned from the very initial portions of these recovery curves. Bourbigot et al. have shown the initial slopes of magnetization recovery curves are proportional to the clay-polymer interfacial area.[44] Here we apply the theories of Blumberg[54] and others[55-56,172] to calculate the time regime over which we should analyze the recovery curves for extracting this information. In other words, we want to apply eq 2.4, which describes the magnetization recovery in terms of N_p, so we would like an estimate of the time period, defined by eq 2.5, over which this equation is valid. For clays, N_p is analogous to the effective surface area and therefore should provide information on the degree of exfoliation.

To make this determination, we need estimates of the spin-diffusion barrier radius (δ), electron-nucleus coupling constant (C), and spin-diffusion coefficient (D). The barrier radius was estimated using the structure of the organically modified MMT (cf. Table 2.1) and some information obtained from its solid-state ^{13}C NMR spectrum. Figure 2.2 displays ^{13}C direct polarization MAS spectra of two organoclays: MMT, which contains paramagnetic species, and fluorohectorite, which is void of these impurities. Otherwise, FH is quite comparable to MMT. In particular the packing densities and structures of the ammonium surfactant modifiers are similar for these two clays.

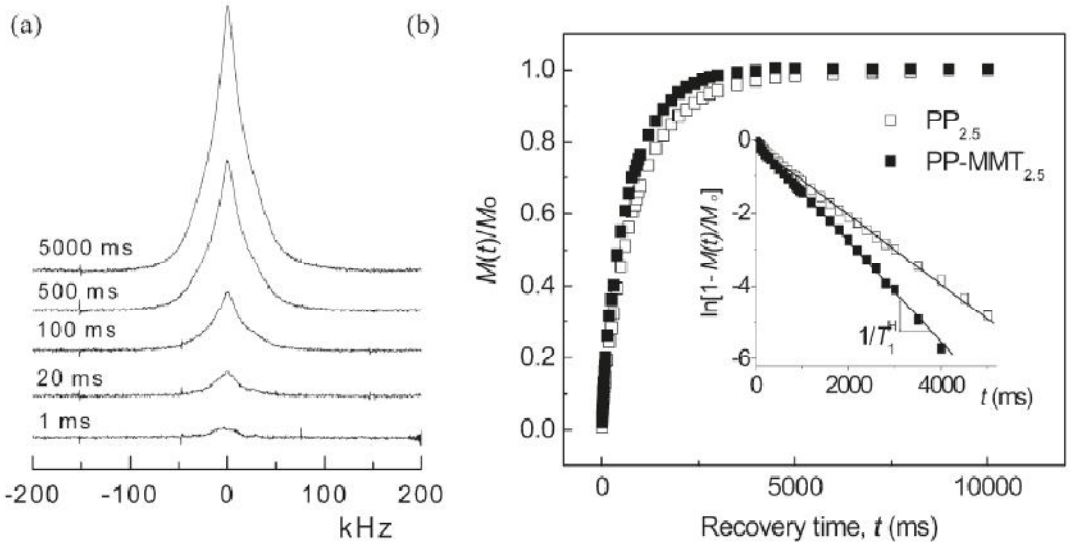

Figure 2.1. ^{1}H NMR magnetization recovery following saturation: (a) spectra, labeled with respective recovery time, for PP-MMT nanocomposite with stretch ratio $\lambda = 2.5$ (PP-MMT$_{2.5}$), and (b) normalized magnetization, $M(t)/M_o$, versus recovery time obtained by integrating ^{1}H spectra for PP-MMT$_{2.5}$ and the polypropylene with the same stretch ratio (PP$_{2.5}$). The inset in (b) displays the same data plotted as $\ln[1 - M(t)/M_o]$ versus recovery time, the slopes of which reflect the inverse T_1s. The nanocomposite exhibits faster relaxation (shorter T_1^{H}) than the corresponding polymer.

The spectra were recorded under MAS and at 70 °C, above the transition to a liquid-like phase for dimethyldioctadecylammonium cations adsorbed onto mica surfaces,[177] to mitigate broadening due to residual dipolar couplings. The major peak at 30 ppm is due to conformationally disordered methylene chains, all-trans methylenes appear at 33 ppm, the chain-end methylene and methyl carbons appear at 23 and 15 ppm, respectively, and the ammonium head-group methylene and methyl carbons appear centered around 53 ppm. While all peaks are broader for MMT than for FH, the head-group carbons are broadened beyond detection. Thus, we propose that the head-group

carbons are within the sphere of direct relaxation by the paramagnetic impurities in MMT. This observation was used to estimate the spin-diffusion barrier radius, δ, for our samples. The cross-sectional diameter of the head group is ~0.4 nm[179] and the paramagnetic centers are located within clay platelets at a minimum distance of 0.5 nm from the nearest surface, leading to an estimate for the barrier radius of $\delta \leq 0.9$ nm. This estimate is consistent with ^{1}H NMR data on pure MMT (no organic modifier, 3.35 wt % Fe_2O_3),[180] where the absence of observable ^{1}H resonance peaks for surface hydroxyls indicates that δ is at least 0.5 nm. Our estimate is also consistent with a ^{29}Si NMR study on pure clay samples (0.1 – 5 wt % Fe_2O_3) in which the authors reported a δ of the order of 1 nm.[181]

VanderHart et al. measured ^{1}H Bloch decays at 300 MHz for commercial MMT and reported that 36% of the available protons were not detected.[146] We estimated that the spin-diffusion barrier radius extends about 0.4 nm into the gallery space from the surface of each platelet. The average gallery height for our clay is 2.2 nm (basal spacing of 3.2 nm minus platelet thickness of 1 nm). Assuming a homogeneous distribution of ^{1}Hs in the gallery space, 0.8/2.2 = 36% of the ^{1}Hs in the galleries fall within the region ≤ δ and should not be detectable, which is completely consistent with the data of VanderHart et al.[146]

The estimated spin-diffusion barrier radius δ gives us an idea of the extent to which direct relaxation by the paramagnetic centers reaches into the bulk sample from the center of the clay platelets. This is depicted in Figure 2.2(c) along with other relative distances within the organically modified MMT (i.e., Cloisite 15A) platelet. The magnitude of δ means that for stacked or layered platelets only the exposed outer surfaces

play a role in shortening the nuclear T_1s in the organic matrix. The average separation between paramagnetic centers (d_p), estimated at 1.2 nm from the N_p (~10^{21}/cm^3) which was calculated from the Fe^{3+} content and structural formula (see Table 1.1), is comparable in size to δ thereby ensuring the entire exposed clay surface is rendered paramagnetic. Conceptually, the exposed clay surface is proportional to an effective number of paramagnetic centers, $N_{p,eff}$. With increasing exfoliation, $N_{p,eff}$ will increase.

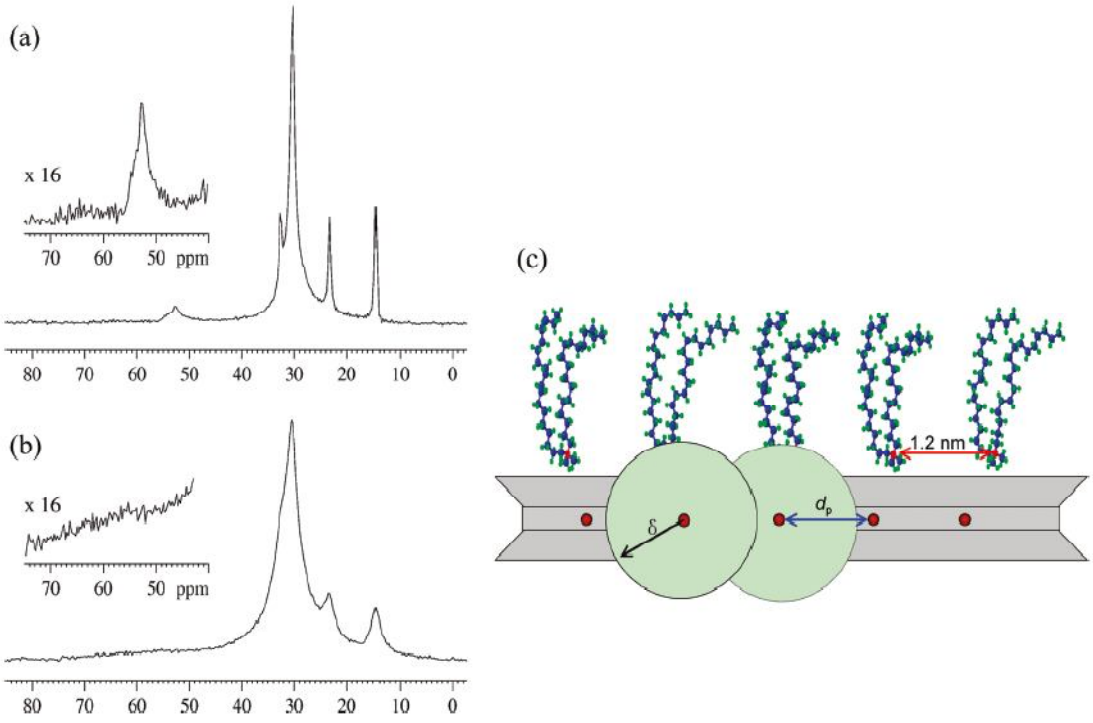

Figure 2.2. Solid-state ^{13}C direct polarization MAS spectra collected at 70 °C of organically modified (a) fluorohectorite, and (b) montmorillonite which contains paramagnetic Fe^{3+} in the octahedral interlayer. The insets depict expanded regions for the methyl and methylene peaks of the ammonium head group. (c) Cartoon illustrating relative distances within an organically modified Cloisite 15A clay platelet. Paramagnetic Fe^{3+} centers are shown as spheres fixed in the middle plane and located on average d_p = 1.2 nm apart, estimated from N_p (~10^{21}/cm^3) calculated from Fe^{3+} content and structural formula (see Table 2.1). Lateral packing of surface modifiers estimated at 1.2 nm from the area per cation assuming a cubic array. Surfactants are shown on only one surface of platelet as other surface may be stacked against other platelets. The spin-diffusion barrier radius δ is estimated to be 0.9 nm.

The electron-nucleus coupling constant is given by eq 2.3. For a given sample, the only unknown is the electron spin-lattice correlation time, τ_c. We estimated this value for our clay from the measured ^{1}H spin-lattice relaxation time and structure of the organically modified clay (see Table 2.1). At 300 MHz, the average T_1 for the observable ^{1}Hs in Cloisite 15A is 10 ms. The observable ^{1}Hs are located 0.9 to 1.1 nm from a clay surface, with the lower boundary being the estimated spin-diffusion barrier and upper boundary calculated as half the distance to the neighboring clay surface: basal spacing, 3.2 nm, minus the platelet thickness, 1 nm, divided by 2. We assume that relaxation in these materials occurs primarily by direct interaction with the paramagnetic centers and is described by eq 2.2; thus, $1/T_1 = Cr^{-6}$. However, this equation is valid for interaction between a single electron and nucleus, and Figure 2.2(c) suggests that the nuclei nearer the surface can directly interact with multiple centers. Thus, we ignore the ^{1}Hs closest to the clay surface and consider the ones at 1.1 nm, which must have T_1s longer than the measured average of 10 ms. Using r = 1.1 nm and T_1 > 10 ms, we calculated a lower bound of $\tau_c > 10^{-9}$ s. This is consistent with T_1 data measured on the organically modified clay as a function of temperature (data not shown) at 300 MHz: With increasing temperature, T_1 decreases indicating that $\omega_o\tau_c > 1$ and $\tau_c > 1/(2\pi \times 300 \text{ MHz}) > 5 \times 10^{-10}$ s. Our τ_c is also consistent with another reported τ_c estimate for commercial MMT.[146] Using $\tau_c > 10^{-9}$ s, we calculate the coupling constant using eq 2.3 to be $C < 2 \times 10^{-52}$ m^6/s.

The spin diffusion coefficient for polypropylene has been reported to be as high as 0.5 nm^2/ms.[182-183] For estimating the time window for diffusion-limited relaxation, we used a D of 0.1 nm^2/ms, the room-temperature value for the D of amorphous polypropylene and polyethylene.[184-185] This smaller value was chosen to reflect the

structure of the region immediately adjacent to the paramagnetic centers, in which surfactant tails are similar to polyethylene segments and conformationally disordered according to the ^{13}C solid-state NMR spectrum (see Figure 2.2). We also estimated the spin-diffusion coefficient from the ^{1}H linewidth of the organically modified FH, which is structurally analogous to the Cloisite 15A but without the line-broadening paramagnetic impurities, using an approach described by Hedesiu et al.[184] Since the lineshape contained a rigid and amorphous component, two Ds were calculated and averaged to obtain a single effective D of 0.1 nm^2/ms.[186],

Using $\delta \sim 0.9$ nm, $C < 2 \times 10^{-52}$ m^6/s, and $D \sim 0.1$ nm^2/ms, we estimated the time window for diffusion-limited relaxation to be 3 to 14 ms (see eq 2.5). Figure 2.3(a) shows a plot of normalized and corrected magnetization, $[M(t)/M_o]_{PP\text{-}MMT} - [M(t)/M_o]_{PP}$, against the square root of recovery time for a series of PP-MMT nanocomposites with different stretch ratios. From 3 to 20 ms the data can be fit well with straight lines ($R^2 > 0.99$), which is a strong indication of diffusion-limited relaxation. Above 20 ms, the data slowly deviate from linearity as the transition to exponential magnetization growth occurs. However, even up to 50 ms the data are reasonably linear with $\sqrt{t}$ ($R^2 = 0.95$). Data were also measured for recovery times below 3 ms, but they deviated significantly from the straight lines shown in Figure 2.3(a). Thus, the lower boundary for diffusion-limited relaxation was estimated quite precisely, while the upper boundary could be extended due to the gradual nature of the transition to exponential magnetization growth.

Crystallinity, although it increases slightly with stretch ratio, is identical for the PP and PP-MMT at a given stretch ratio.[164] The pure clay content was found by TGA to be 2.7% for all samples. Thus differences in the normalized and corrected magnetization-

recovery slopes of Figure 2.3 can not be attributed to differences in polymer crystallinity or clay concentration. The slopes of the straight lines increase with increasing stretch ratio, which reflects the increase in the effective number of paramagnetic centers, $N_{p,eff}$, as new clay surface is exposed due to the shearing that occurs during the stretching process. The amount of new clay surface exposed for a given stretch ratio has been quantified by normalizing the slopes of Figure 2.3(a) by the slope for the sample that has not been stretched ($\lambda = 1$). This is shown in Figure 2.3(b) as clay surface versus stretch ratio. The amount of new clay surface exposed increases over 2-fold and is a near linear function of the equi-biaxial stretch ratio up to $\lambda = 3.5$.

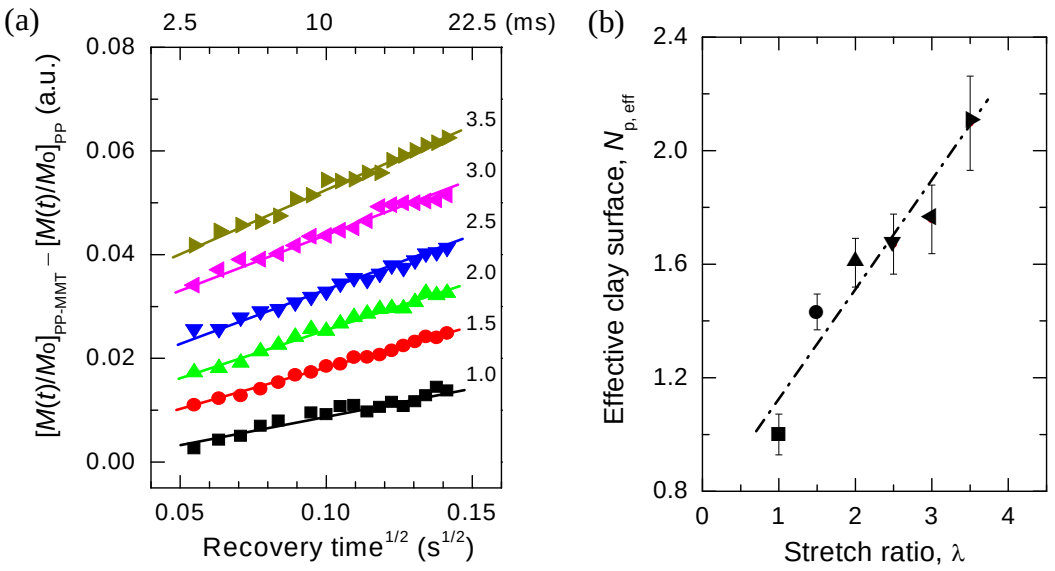

Figure 2.3. (a) Normalized and corrected magnetization, $[M(t)/M_o]_{PP\text{-}MMT} - [M(t)/M_o]_{PP}$, versus the square root of recovery time for PP-MMT nanocomposites with different stretch ratios (λ). PP-MMT and PP films were equi-biaxially stretched at 16 s^{-1} and 150 °C. For a given λ, PP-MMT data were corrected using data from an identically deformed PP. Stretch ratios, from 1 (unstretched) to 3.5, are shown above the respective data for a given sample, which are vertically displaced to prevent overlap. Lines are linear least-square fits. Slopes of these lines, normalized to the slope of the line for $\lambda = 1$ and proportional to the exposed clay surface or effective number of paramagnetic centers $N_{p,eff}$, are plotted in (b) as a function stretch ratio.

While the initial magnetization recovery provides information on the amount of exposed clay surface, the spin-diffusion-mediated long-time relaxation behavior provides information on the average interparticle spacing. As described by Bourbigot et al.,[44] the long-time relaxation behavior is quantitatively captured in the overall ^{1}H spin-lattice relaxation time of the nanocomposite, $T_{1,PCN}$. These values were measured and corrected for relaxation due to the pure polymer (cf. eq 2.9) to yield the paramagnetic contribution to the spin-lattice relaxation time, $T_{1,para}$, which is plotted in Figure 2.4(a) as a function of stretch ratio. In this plot, $T_{1,para}$ decreases at first slowly and then steeply from $\lambda = 1.5$ to 2.5, after which an apparent plateau is reached. These data contrast the initial-slope data of Figure 2.3 which increase nearly linearly for all stretch ratios, signifying an increase in the amount of exposed clay surface for all stretch ratios. If the $T_{1,para}$ data simply reflected the amount of exposed clay surface, then they should decrease linearly as well. The $T_{1,para}$ data of Figure 2.4(a) indicate the average interparticle spacing decreases slowly at first, more rapidly up to $\lambda = 2.5$, and then levels off for higher stretch ratios. Decreasing $T_{1,para}$ values are characteristic of decreasing average interparticle separations since $T_{1,para}$ values are governed by the distances over which spin diffusion must occur to the paramagnetic relaxation sinks. These results are consistent with those obtained from TEM data. Average interparticle separations were measured by image analysis and are shown in Figure 2.4(b) as a function of stretch ratio. The TEM interparticle separations (Δ_{TEM}) decrease up to $\lambda = 2.5$, after which they plateau in agreement with the $T_{1,para}$ data. The slightly slower decrease from $\lambda = 1$ to 1.5 for the $T_{1,para}$ data is attributed to aggregate break-up without significant separation of the resulting daughter particles, which would

not lead to a large decrease in $T_{1,para}$. The data are consistent with this explanation, especially considering the particle density increases rather significantly from 17 ± 4 at λ = 1 to 39 ± 7 at λ = 1.5. Average interparticle separations, particle densities and other results obtained from analysis of TEM data are summarized in Table 2.2 and discussed below.

Representative TEM images are shown in Figure 2.5 for each stretch ratio. The unstretched PP-MMT film contains nanoparticles that are reasonably well-dispersed and randomly oriented (cf. Figure 2.5a). Most of the clay exists in aggregates of 2 to 3 platelets while some single layers are found. Aggregates of stacked and skewed platelets exist; examples are marked with circles in the TEM image of Figure 2.5(a). These aggregates are broken up and the platelets are aligned with increasing stretch ratio. By λ = 2 to 2.5 (cf. Figs. 2.5c and d), platelets are mostly aligned but the existence of some thick particles suggest that further exfoliation can take place with increasing stretch ratio, which is consistent with the NMR data of Figures 2.3 and 2.4. Shearing of aligned clay particles leads to further exfoliation for stretch ratios of 3 and 3.5 (cf. Figs. 2.3, 2.5e and 2.5f).

A single orientation direction, marked with arrows, is evident in the micrographs of Figure 2.5. The nanocomposite sheets were stretched biaxially in the *x*-*y* plane while the TEM images are views of either *x*-*z* or *y*-*z* cross-sections. The appearance of single primary orientation directions for the clay particles, which are essentially discs, indicates the particles orient parallel to the *x*-*y* plane of the sheet. TEM projections in the *x*-*y* plane would more clearly illustrate the effect of biaxial stretching on clay particle orientation, however, microtoming samples in this plane is very difficult as the sheets are so thin.

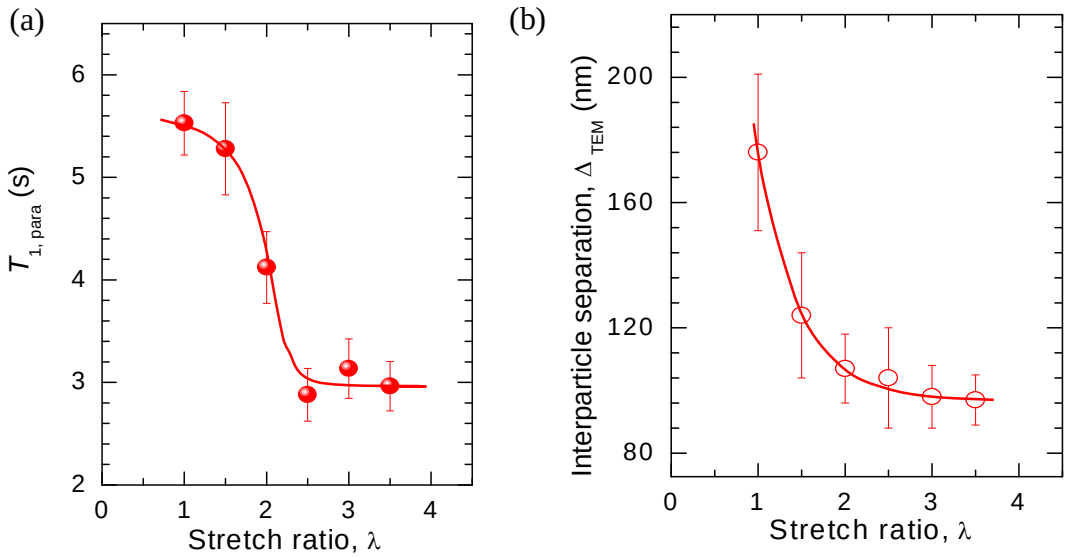

Figure 2.4. (a) Paramagnetic contribution to the overall NMR spin-lattice relaxation time, $T_{1,para}$ (from eq 2.9), and (b) average interparticle separation, Δ_{TEM}, from TEM data as functions of stretch ratio, λ, for PP-MMT films equi-biaxially stretched at 16 s^{-1} and 150 °C. Unstretched sample has λ = 1. Dash-dot lines are guides.

Quantitative image analysis of the TEM data provided a wealth of information that is summarized in Table 2.2. With increasing stretch ratio, interparticle separation (Δ_{TEM}) is decreased, particle length increases, and particle thickness decreases. The particle density increases significantly for λ = 1.5, then remains mostly constant, given the error ranges, for higher stretch ratios. These findings are consistent with shear-induced disintegration and exfoliation of clay aggregates. Wide-angle X-ray diffraction (WAXD) data (not shown) reveal the d_{001} basal spacing for the organically modified MMT expands from 3.19 nm to 3.27 nm in the unstretched PP-MMT nanocomposite, suggesting that some PP chains have intercalated into the clay galleries. These chain

segments can effectively transfer stress to the platelets, weaken interplatelet interactions, and thereby facilitate separation and exfoliation.[114,160]

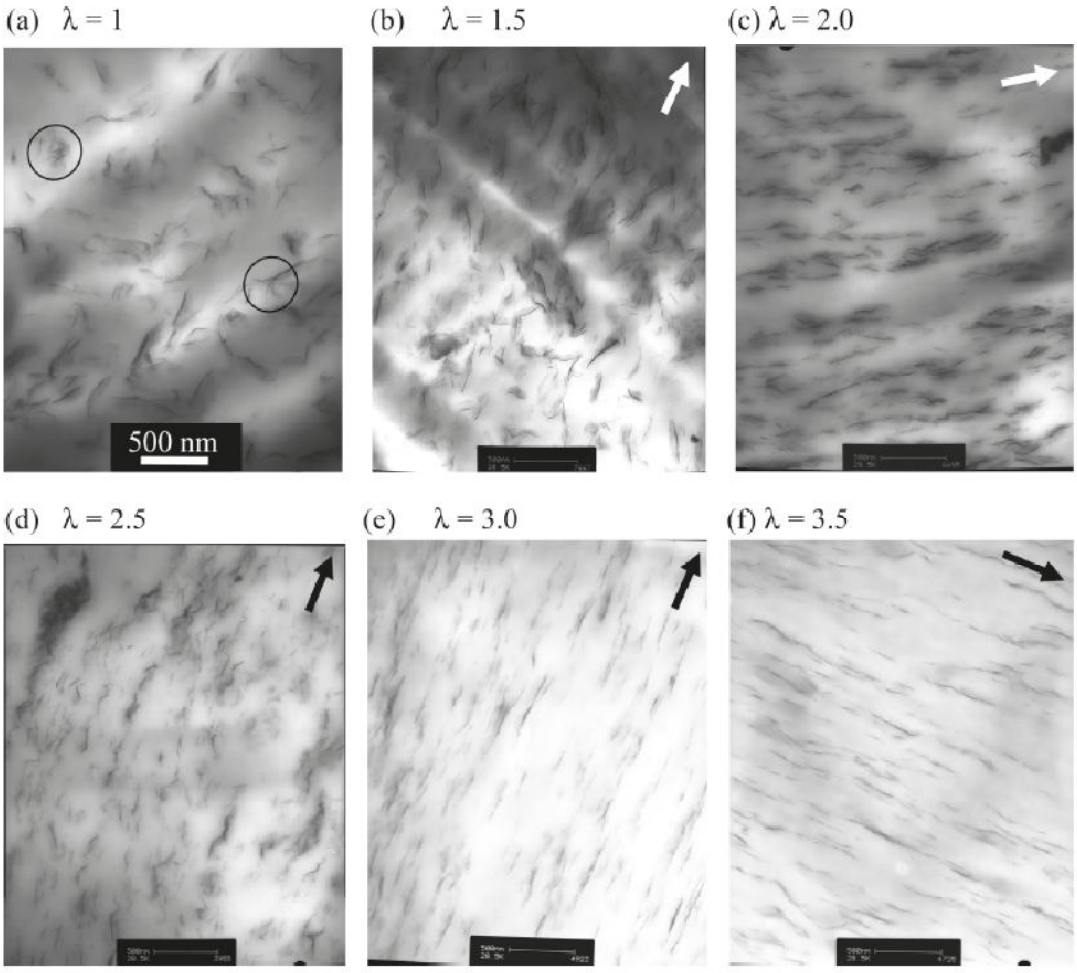

Figure 2.5. Representative TEM images of PP-MMT films with stretch ratios from λ = 1 (unstretched) (a) to λ = 3.5 (f). Samples were biaxially stretched at 150 °C and 16 s^{-1}. Scale shown in (a), 500 nm, is the same for each image. Circles shown in (a) mark the presence of stacked and skewed clay platelets. Arrows indicate the primary direction of orientation of clay particles. Sections for TEM were sliced along the direction normal to the film surface, and therefore normal to the stretch direction.

Table 2.2. Clay morphology from TEM.

stretch ratio, λ	interparticle separation, Δ_{TEM} (nm)[a]	particles/μm^2	length (nm)[b]	thickness (nm)[c]
1	176 ± 25	17 ± 4	189 ± 86	6.4 ± 1.7
1.5	124 ± 20	39 ± 7	170 ± 70	5.8 ± 1.3
2	107 ± 11	45 ± 11	216 ± 95	4.9 ± 1.1
2.5	104 ± 16	41 ± 7	210 ± 84	4.5 ± 0.8
3	98 ± 10	40 ± 6	275 ± 126	3.1 ± 0.5
3.5	97 ± 8	30 ± 13	283 ± 191	2.0 ± 0.5

[a]measured using method introduced by van Es;[117] [b]two particles considered one when separated by < 2 nm in direction normal to platelet plane; [c]single particle thickness determined as average of three positions along its length: middle and each of 2 ends.

The TEM and WAXD data can be used to extract more information from the NMR data. The initial-slope data of Figure 2.3 showed that the exposed clay surface more than doubled when the unstretched film was equi-biaxially stretched to $\lambda = 3.5$. This relative change can be converted into absolute information by estimating the average number of platelets per particle (N_{ps}) in the unstretched PP-MMT from the average particle thickness of 6.4 ± 1.7 nm (see Table 2.2). From WAXD data, we know the interplatelet spacing is 3.27 nm. Since this value reflects the mid-platelet to mid-platelet spacing, and a platelet is 1-nm thick, the corresponding thickness for a 2-platelet stack in a TEM image is taken to be 4.27 nm. Similarly, a 3-platelet stack should be 7.54 nm. Thus, the average particle in the unstretched PP-MMT contains between 2 and 3 platelets; interpolating between 4.27 and 7.54 nm yields an average number of platelets per particle of $N_{ps} = 2.64$. We can now calculate a degree of exfoliation, f, using eq 2.8 since $N_{p,eff} = S/S_{ref}$ and the number of platelets/stack is 2.64 for the reference material: $f = N_{p,eff}/2.64$. Results are summarized in Table 2.3 and plotted in Figure 2.6(a) as a function of stretch ratio. The degree of exfoliation increases roughly linearly from 0.38 at $\lambda = 1$ to 0.8 at $\lambda = 3.5$. From TEM, the average particle thickness at $\lambda = 3.5$ is 2.0 ± 0.5 nm, which means

that the average clay particle is between 1 and 2 platelets thick, that is, between 1 and 4.27 nm thick. Interpolating as before, the average number of platelets/stack at $\lambda = 3.5$ is 1.3, so the degree of exfoliation determined from TEM data alone is 0.77 (see eq 2.8), entirely consistent with the 0.8 value determined from NMR. After equi-biaxial stretching to $\lambda = 3.5$, the PP-MMT nanocomposite maintains some potential for further exfoliation; the degree of exfoliation has not yet leveled off in the plot of f versus λ (see Figure 2.6a).

Table 2.3. Clay morphology from NMR.

stretch ratio, λ	effective clay surface, $N_{p,eff}$	degree of exfoliation,[a] f	Δ_{ideal} / f (nm)[b]	homogeneity,[c] ε'
1	1	0.38	273	0.65
1.5	1.43 ± 0.07	0.54 ± 0.03	190 ± 5	0.65 ± 0.10
2	1.61 ± 0.09	0.61 ± 0.04	170 ± 6	0.63 ± 0.07
2.5	1.67 ± 0.11	0.63 ± 0.05	163 ± 7	0.64 ± 0.11
3	1.76 ± 0.12	0.67 ± 0.05	155 ± 7	0.63 ± 0.09
3.5	2.10 ± 0.16	0.80 ± 0.06	130 ± 8	0.75 ± 0.10

[a] $f = N_{p,eff}/2.64$, where 2.64 is platelets/stack in unstretched sample (i.e. reference material); [b] scaled ideal interparticle separation where $\Delta_{ideal} = 103$ nm (see eq 2.7);[41,44] [c] $\varepsilon' = \Delta_{TEM} /(\Delta_{ideal} / f)$.

The degree of exfoliation was used to scale the idealized interparticle separation of 103 nm calculated from the clay and polymer volume fractions using eq 2.7 (2.7 wt % clay, 2.6 g/cm^3 MMT, 0.91 g/cm^3 PP). The scaled ideal interparticle separations were calculated as Δ_{ideal}/f and are summarized in Table 2.3. These Δ_{ideal}/f values, which obviously decrease with increasing exfoliation, were calculated using the definition of Bourbigot et al.[44] They used these values to determine a homogeneity index by

comparing them with apparent interparticle spacings (cf. eq 2.10) that they extracted from modeling the long-time behavior of magnetization-recovery curves. Here we calculate a slightly different homogeneity index, ε'. We use the same ideal interparticle spacing scaled by the NMR-determined degree of exfoliation (Δ_{ideal}/f), but instead of an NMR-determined apparent interparticle spacing, we compare Δ_{ideal}/f with the interparticle spacings determined from TEM (Δ_{TEM}):

$$\varepsilon' = \Delta_{TEM} /(\Delta_{ideal}/f) \tag{2.11}$$

Homogeneity values were calculated for the PP-MMT samples using eq 2.11, are listed in Table 2.3 and plotted in Figure 2.6(b) as a function of stretch ratio. The ε' values are constant from λ = 1 to 3, but then increase slightly for λ = 3.5 as the degree of exfoliation jumps from 0.67 to 0.8 at this stretch ratio. Thus, homogeneity of the unstretched sample is not affected by stretching until higher strain levels are reached. It is interesting to note that the Δ_{TEM} values are nearly identical to the calculated Δ_{ideal} of 103 nm from λ = 2 to 3.5 (see Table 2.2 and Figure 2.4b), but the homogeneity increases slightly from λ = 3 to 3.5. Calculation of the ideal interparticle separation from component volume fractions only accounts for the height or thickness of a single clay platelet, not its lateral dimensions (cf. eq 2.7). Finite lateral dimensions should result in reduced actual interparticle separations, while aggregation should increase actual interparticle separations. The increase in homogeneity from λ = 3 to 3.5 is attributed to the increase in exfoliation due to sliding platelets apart that results in an increase in lateral particle dimensions.

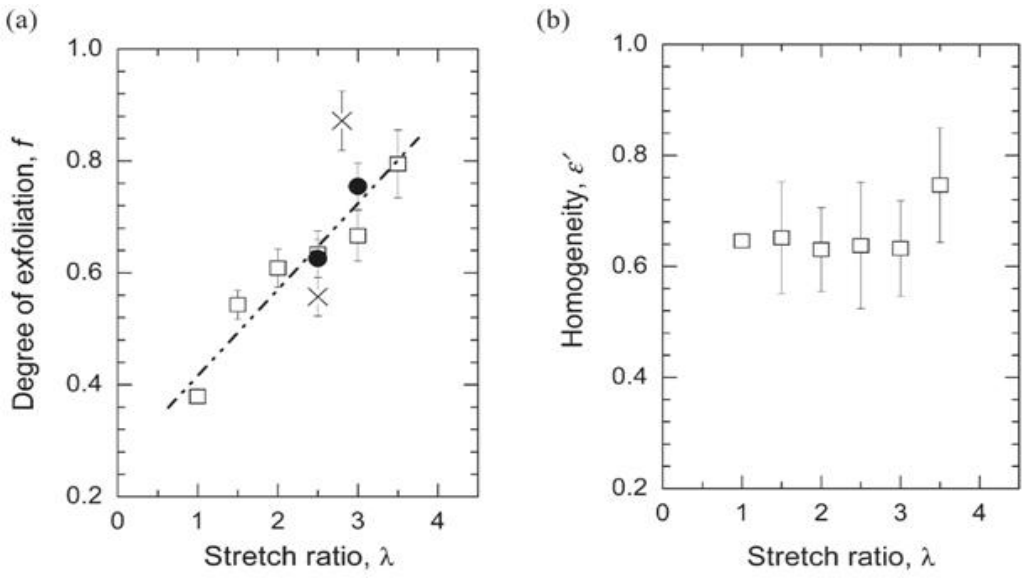

Figure 2.6. Degree of exfoliation, f (a) and homogeneity, ε' of clay dispersion (b) as a function of stretch ratio, λ, for PP-MMT films. Samples were equi-biaxially stretched at 150 °C and 16 s^{-1} (□), 150 °C and 32 s^{-1} (●), or 145 °C and 16 s^{-1} (×). Unstretched sample has λ = 1.

The PP-MMT nanocomposites described thus far were equi-biaxially stretched at 150 °C and 16 s^{-1}. The effect of strain rate was examined by stretching two samples at 32 s^{-1} (and 150 °C) to stretch ratios of λ = 2.5 and λ = 3. The degrees of exfoliation for these two samples are included in Figure 2.6(a) and reveal that doubling the shear rate at this deformation temperature does not significantly affect the clay morphology. On the other hand, a small decrease in the deformation temperature to 145 °C does have a significant effect. Two samples were stretched at 145 °C (and 16 s^{-1}) to stretch ratios of λ = 2.5 and λ = 2.8. The degrees of exfoliation for these two samples are also included in Figure 2.6(a): The PP-MMT stretched to λ = 2.8 exhibits the highest exfoliation degree (f = 0.87) of all the samples in this study. We attribute this result to a higher melt viscosity at 145 °C, which leads to more effective stress transfer from polymer to clay particles. Indeed, onset of melting for these nanocomposites was observed by DSC at around

150 °C. Higher melt viscosities and larger shear stresses have been shown to facilitate exfoliation.[84,93,116] Thus, although the strain rate has seemingly little effect on exfoliation at 150 °C, we expect the strain rate will affect results more significantly at lower temperatures, where the transfer of shear stress from polymer to clay is improved.

A schematic depicting the evolution of clay morphology upon equi-biaxial stretching PP-MMT nanocomposites is shown in Figure 2.7. This schematic summarizes the major findings from the NMR and TEM data. New clay surface is exposed throughout the stretching process (see Figures 2.3b and 2.6a), initially by break-up of large and skewed aggregates and lastly by sliding of platelets apart from each other. The average particle thickness decreases and the length increases (see Table 2.2), while the interparticle separation decreases to a plateau for the higher stretch ratios as the particles are aligned (see Figure 2.4).

With the exception of elastic modulus, the mechanical properties reported by Abu-Zurayk et al.[164] were shown to be diminished in the unstretched and low stretch ratio PP-MMT sheets but improved in a linear manner as stretch ratio increased. The reduction in yield and break stress is attributed to the presence of large clay tactoids which act as stress concentrators and initiate failure at large strains (but would not detrimentally influence low strain properties such as elastic modulus). As the stretch ratio increases it has been shown that the degree of exfoliation increases in a near linear manner (Figure 2.6) as the clay stacks are exfoliated and this reduction in tactoid size is reflected in a linear increase in yield and break stress. The elastic modulus of the PP-MMT sheet was unchanged relative to the pure PP in the unstretched sheet and at low stretch ratios. Modulus enhancement was not evident until a stretch ratio of 2.5 was achieved after

which modulus increased linearly with increasing stretch ratio. This is the ratio at which there is a large change in clay particle alignment from random to oriented as shown in Figure 2.4 where the interparticle separation reaches a plateau region. After this point the stretch ratio begins to have an influence on modulus such that modulus increases linearly with increasing degree of exfoliation (it should be noted that the changes in mechanical properties upon the addition of clay were shown not to be a consequence of changes in crystallinity).[164]

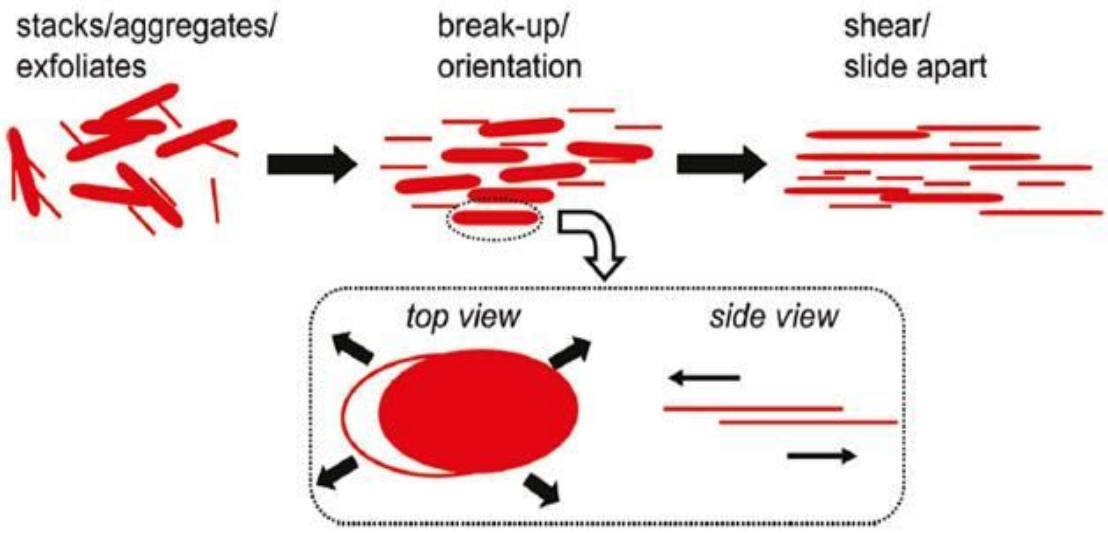

Figure 2.7. Schematic depicting the evolution of clay morphology under the action of equi-biaxial stretching of PP-MMT nanocomposites. According to NMR data, new clay surface emerges for all stretch ratios up to $\lambda = 3.5$. For stretch ratios $\lambda < 2.5$, large aggregates are broken up and oriented. At larger stretch ratios $\lambda \geq 2.5$, particles are highly oriented and new clay surface emerges by sliding platelets apart, lengthening and thinning the clay particles. This latter process is illustrated at the bottom of the schematic by the top and side views of an oriented stack.

We calculated a degree of exfoliation (f) from NMR data using a reference sample for which the number of platelets per stack was estimated from an average particle thickness measured by TEM. The f value at $\lambda = 3.5$ is approximately 0.8 whether it is calculated from the TEM-scaled NMR data or from the TEM data alone. Degrees of exfoliation were also computed for the other four samples ($\lambda = 1.5$, 2, 2.5 and 3) from their TEM-determined average particle thicknesses (cf. Table 2.2). The value for the sample at $\lambda = 3$ is 0.61, sufficiently similar to 0.67 computed from NMR data (cf. Table 2.3). However, the values for the remaining three samples ($\lambda = 1.5$, 2, and 2.5) are all lower by a factor of 3/4 from the ones determined from NMR data. We attribute this difference to the nature of the data collected using two separate techniques and the assumptions we used to determine the average number of platelets per stack. The TEM data provides distributions of particle thicknesses from which an average is calculated. This average is then placed discretely between two possible platelet stacks (e.g., 2-platelet and 3-platelet) and then interpolation leads to an average number of platelets per stack. Thus, we essentially throw out the actual distribution and replace it with a distribution consisting of two stacks. The NMR method directly provides the change in the total effective clay surface, $N_{p,eff}$. Consideration of particle distributions is unnecessary when quantifying the relative differences seen in Figure 2.3b. To convert the NMR-determined $N_{p,eff}$ values to degrees of exfoliation, a reference material must be selected; given the assumptions involved in determining the average number of platelets/stack from TEM data, the best reference sample is probably one that is fully exfoliated.[44] The real advantage to using NMR and TEM in the integrated manner

described in this report is that it eliminates the need for conducting labor-intensive TEM on all samples.

According to eq 2.5, the time window for diffusion-limited relaxation can be expanded by increasing the electron-nucleus coupling constant. Examination of eq 2.3 reveals that this is easily accomplished by simply making measurements at lower magnetic fields (ω_n in eq 2.3). We tested this by conducting saturation-recovery experiments on a bench-top NMR spectrometer operating at 23 MHz and discovered that the portion of the magnetization recovery curve that is linear with $\sqrt{t}$ did indeed increase by a factor of ~2. As low-field benchtop NMR spectrometers are common in industrial environments, this NMR methodology may have applications for process control and development.

2.6. Conclusions

Nanocomposites of polypropylene (PP) and 5 wt % organically modified montmorillonite (MMT), which contains ~3.5 wt % Fe^{3+} based on the pure clay, exhibit solid-state ^1H saturation recovery curves that are exponential for long times but linear with $\sqrt{t}$ for very short times ($\leq \sim 20$ ms). The $\sqrt{t}$-dependence for the short-time portions of these magnetization recovery curves is indicative of diffusion-limited relaxation. Considering the structure and NMR properties of the MMT, estimates of the spin-diffusion barrier radius (0.9 nm), electron-nucleus coupling constant ($< 2 \times 10^{-52}$ m^6/s), and spin-diffusion coefficient (0.1 nm^2/ms) were used to calculate the time window for diffusion-limited relaxation as 3 to 14 ms. Thus, the initial slopes of these relaxation curves were directly proportional to the number of paramagnetic centers, effectively a

measure of the exposed clay surface, or degree of exfoliation. Spin-lattice relaxation times, determined from the entire relaxation curves, could be corrected to yield the paramagnetic contribution to the overall relaxation time ($T_{1,para}$), which provided information on the average interparticle separation.

The PP-MMT nanocomposites were equi-biaxially stretched at 150 °C and 16 s^{-1}. The exposed clay surface increased with stretch ratio up to $\lambda = 3.5$ while the interparticle separation decreased until reaching a plateau at $\lambda \sim 2.5$. These NMR data were consistent with TEM images which revealed the particle thickness decreased continuously with stretch ratio up to $\lambda = 3.5$, while the interparticle separation decreased until reaching a plateau for $\lambda > 2$. TEM also revealed the average particle length increased with increasing stretch ratio, but most significantly for the largest strains ($\lambda \geq 3$). Evolution of clay morphology proceeds by aggregate break-up and orientation at lower strains followed by sliding aligned platelets apart at higher strains. Stretching at a slightly lower temperature of 145 °C led to a higher degree of exfoliation at $\lambda = 2.8$ but not at $\lambda = 2.5$ when compared to the samples stretched at 150 °C to the same or similar stretch ratios. We attribute this to more effective shear transfer in higher viscosities.

The TEM and NMR data were integrated to yield quantitative morphology descriptors for degree of exfoliation and homogeneity. The degree of exfoliation increased from 0.38 to 0.8 upon equi-biaxial stretching to $\lambda = 3.5$, while the homogeneity was constant around 0.65 up to $\lambda = 3$ and increased slightly to 0.75 at $\lambda = 3.5$. The degree of exfoliation (f) is defined exactly as Bourbigot et al.[44] have defined it; although we used a different reference, full exfoliation still means $f = 1$. The homogeneity, defined differently from Bourbigot et al.,[44] is simply a measure of how TEM interparticle

separations compare with *f*-scaled interparticle separations calculated from component volume fractions for an "ideal" nanocomposite in which the clay is fully exfoliated and perfectly layered. In addition to interparticle separations, calculated homogeneity values reflect finite particle lengths.

CHAPTER 3

Modeling Initial Spin-lattice Relaxation in Paramagnetic Polymer/clay Nanocomposites

3.1. Abstract

In this chapter, an analytical method based on a lamella-based model is presented to correlate the initial spin-lattice relaxation behavior with the clay morphology in paramagnetic polymeric nanocomposites. First, a general view is given to the development of the theoretical models for describing nuclear spin-lattice relaxation via paramagnetic centers. Next, a specific model is proposed for describing the initial spin-lattice relaxation behavior in PCNs due to the unique clay structure. Our analysis based on the model reveals that the paramagnetic contribution to magnetization recovery (M_c^n) is analytically correlated to the square root of the recovery time ($t^{1/2}$). This is in accord with experimental observations in Chapter 2. The relation of M_c^n with $t^{1/2}$ is found to be associated with the polymer/clay interfacial area (A_s) per unit volume as well as the spin diffusion coefficient (D_s). Our NMR method directly provides information about polymer/clay interfacial surface area and the degree of exfoliation in biaxially stretched polypropylene/ montmorillonite nanocomposites with different stretch ratios. The NMR results are completely comparable to TEM data. This demonstrates that our finding extends the utility of NMR relaxometry in independently quantifying clay dispersion in polymer nanocomposites without the aid of any other complementary techniques.

3.2. Theories and Models for Spin-lattice Relaxation via Paramagnetic Centers

Section 2.3.1 briefly described the nuclear spin-lattice relaxation via paramagnetic centers. In this section, theories and models of growth of the nuclear magnetization in the presence of paramagnetic impurities in solids are reviewed. Extensive discussion of the theoretical and practical aspects of spin relaxation in impurity-doped crystals may be found in the literature[53,59,171,187-189]

The predominant role played by paramagnetic impurity centers in nuclear spin-lattice relaxation in inorganic crystals was observed as early as 1947.[190] Great progress to explain the abnormally short spin-lattice relaxation times observed in nonmetallic diamagnetic solids was made by Bloembergen in 1949.[53] He introduced the concept of nuclear relaxation via spin diffusion to paramagnetic impurities and wrote the transport equation governing the evolution of the nuclear magnetization in time and space:

$$\frac{\partial m}{\partial t} = D_s \nabla^2 m - C(m - m_0)\sum_n |r - r_n|^{-6} - 2A_p \qquad (3.1)$$

where $m(\mathrm{r}, t)$ is the magnetization of a nuclear spin located at a point r and a time t, m_o is the thermal equilibrium magnetization, and D_s is the spin-diffusion coefficient. The term $C(\mathrm{r} - \mathrm{r}_n)^{-6}$ represents the probability of a transition due to the n^{th} impurity. The last term, $2A_p$ is the probability of transition due to a *rf* pulse. The electron-nucleus coupling constant C is defined as eq 2.3 in Section 2.3.1. Later, an analytical solution of this equation was found by Khutsishvili.[187] de Gennes[171] also developed an elegant solution to this equation, and his expression for T_1 can be simplified as

$$1 / T_1 \propto N_p \tag{3.2}$$

where N_P is the impurity concentration (see Chapter 2). Blumberg[54] later derived the $t^{1/2}$ law for the growth of the observed total magnetization at short times in the case of spin-diffusion limited relaxation, as described by eq 2.4 (Section 2.3.1). Diffusion-limited relaxation means that the relaxation process is controlled by the rate at which magnetization can diffuse to the paramagnetic centers.[55] The other case is rapid diffusion in which the direct relaxation through the electron-nucleus interaction is small compared to spin diffusion. Rorschach[55] derived a general expression for T_1, which links these two limiting cases by the competition between spin diffusion and direct interaction. Lowe and Tse[56] developed a single paramagnetic center model and solved Bloembergen's equation. Table 3.1 lists their results on the dependence of T_1 upon the magnetic field strength (B_0), the electron-nucleus coupling constant (C), impurity concentration (N_p), and spin diffusion coefficient (D_s) in the condition of $\omega_0\tau_c >> 1$ (see ω_0 and τ_c in eq 2.4).

Table 3.1. The dependence of the limiting cases of relaxation time upon B_0, C, N_p, and spin diffusion coefficient in the condition of $\omega_0\tau_c >> 1$[56]

Cases	Exponent dependence of T_1			
	B_0	τ_c	N_p	D_s
Rapid diffusion	2	1	-1	0
Diffusion-limited	1/2	1/4	-1	-3/4
Diffusion-vanishing	1	1/2	-4/3	-1/2

Now the concepts of spin diffusion, exponential recovery of magnetization and expressions for T_1 are well understood and developed. Devreux et al.[191] showed that, in

the case of no spin diffusion, the initial magnetization recovery due to the direct relaxation is given by

$$M(t) \propto t^{d_i/6} \tag{3.3}$$

where d_i is the fractal dimension of solids doped with the impurities. They measured the fractal dimension of aerogels based on ^{29}Si relaxation, which is in agreement with that determined by SAXS. Furman et al.[188-189] further developed this idea to correlate the magnetization growth of some impurity-doped solids with arbitrary spacings (e.g. clay, $V_2O_5 \cdot 16H_2O$, WO_3). They found that growth of the magnetization can be described by

$$M(t) \propto \exp[-(t/T_1^H)^n] \tag{3.4}$$

where n is associated with the dimensionality of the sample and the distribution of impurity centers; the value of n ranges between 1/3 and 1. In fact, eq 3.4 is generally known as a stretched exponential function, which has been successfully used to fit the spin-lattice relaxation of solids containing paramagnetic centers.

Simplify the transport equation, most of the developments of the theory are based on some assumptions, such as dilute paramagnetic centers for single center model, no spin diffusion (by selective nuclei and experimental methods) and pretty slow intrinsic relaxation (considering no impurity). As Section 2.3.1 in Chapter 2 suggests, taking the intrinsic relaxation into account, we have the exact transport equation without considering the *rf* pulse term as

$$\frac{\partial m}{\partial t} = D\nabla^2 m - C(m - m_0)\sum\nolimits_n \left|r - r_n\right|^{-6} - \frac{m - m_0}{T_{1,m}} \tag{3.5}$$

where $1/T_{1,m}$ is the intrinsic relaxation rate due to the interaction of the sample with the static magnetic field.

3.3. Modeling Initial Spin-lattice Relaxation

3.3.1. Introduction

In Chapter 2, it was shown that, in polypropylene/montmorillonite nanocomposites the paramagnetic contribution to the initial magnetization (first 20 ms) was $M_c^n \sim t^{1/2}$, where t is the recovery time.[44] We attributed this observation to the diffusion-limited case defined by its theoretical time boundaries. Based on a direct analogy between impurities in crystal solids and clay platelets covered by polymer, we correlated the prefactor of $t^{1/2}$ with the polymer/clay interfacial area. Furthermore, we quantitatively observed the evolution of polymer-clay surface during biaxially stretched PP/MMT nanocomposites, which was qualitatively consistent with TEM data.

VanderHart et al. connected the prefactor of $M_c^n \sim t^{1/2}$ with the surface area of paramagnetic sources partly from a theoretical point of view and partly from a numerical calculation.[44,192] The solution of the common diffusion equation indicates that the flux of the diffusant is initially linear in the square root of the diffusion time in the two phases A and B. The initial slope of the $M(t) \sim t^{1/2}$ law, S is[192]

$$S = S_v \left(\frac{\rho_{HA}\phi_A + \rho_{HB}\phi_B}{\phi_A \phi_B} \right) \frac{2}{\sqrt{\pi}} \frac{\sqrt{D_A D_B}}{\rho_{HA}\sqrt{D_A} + \rho_{HB}\sqrt{D_B}} \tag{3.6}$$

where S_v is the interfacial surface per unit volume; ϕ_A and ϕ_B, ρ_A and ρ_B, and D_A and D_B are the volume fractions, proton densities, proton spin diffusion coefficients of the phases A and B, respectively. If`$\rho_A = \rho_B$, $D_A = D_B = D$, then

$$S = S_v \frac{1}{\phi_A \phi_B} \frac{\sqrt{D}}{\sqrt{\pi}} \tag{3.7}$$

However, Clauss et al.[193] and VanderHart et al.[192] derived two solutions, eqs 3.6 and 3.7 for the common diffusion theory in the model of A/B phases. There are two differences between paramagnetic PCNs and the A/B phase model. One is that, the sharp magnetization gradient is produced under the influence of the paramagnetic clay and saturation pulses, while the sharp magnetization gradient can be achieved by *rf* pulses for phase selection in the A/B phase model. The other is that, the relaxation sources of surface protons in PCNs can be assumed to be always at equilibrium during the relaxation process. This is reasonable because these protons have extremely short relaxation times when compared to those of the bulk polymer protons. In contrast, the magnetization of one domain in the A/B model flows into another and the total magnetization remains constant. Thus, paramagnetic polymer/clay materials cannot be described by those models. Although we could relate the initial slope to the interfacial surface area, their quantitative relation in PCNs remains unknown. As a result, thorough analyses for ^{1}H

initial relaxation in paramagnetic PCNs will give an analytical relation of the initial slope with clay morphology.

3.3.2. Modeling

In this section, we propose an analytical model describing the initial relaxation in paramagnetic PCNs in saturation-recovery experiments. In this model, we consider the clay nanoparticles as relaxation centers, and view spin diffusion as one dimensional flux of magnetization between adjacent clay nanoparticles, as shown in Figure 3.1. Direct electron-nucleus interaction produces a diffusion barrier (the red frame, Figure 3.1) within which protons have extremely fast relaxation. The high magnetization of spins in this barrier will propagate into the remote nuclei via spin diffusion, which significantly shortens the overall T_1 of PCNs.

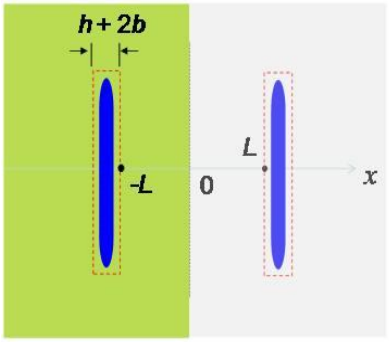

Figure 3.1. Schematic of a single clay particle in two well-stratified clay particles as a unit having the spacing of $2L+2b$ and the particle thickness of h in PCNs. The unobservable protons are in the $h + 2b$ region around the particle. A domain (Ω) around a particle is marked by the light green region.

Here we view a relaxation center consisting of a clay particle of h thickness plus a barrier of unobservable protons. These spectrally undetectable nuclei exhibit short

relaxation times, a few milliseconds or even shorter, which depend on the magnetic field, iron content of clay and sometimes temperatures as well as the electron-nucleus distance (see Chapters 2 and 9). Taking into account the time scale, these nuclei can be justifiably assumed to be at equilibrium immediately following the saturation of the system when compared to the relaxation time of the bulk nuclei, hundreds of milliseconds or up to seconds. Such a 0.4-nm-thick layer was found in organically modified MMT of 2.83 wt% Fe^{3+} (as Fe_2O_3) by ^{13}C spectra in a 7.04 T magnetic field (Chapter 2). We are interested in the detectable nuclei in the vicinity of particles but out of the barrier, *b*. The direct relaxation due to the electron-nucleus interaction sharply decreases with the electron-nucleus distance ($\sim r^{-6}$). The sharp magnetization gradient built around the relaxation centers immediately allows spin diffusion following saturation. To describe the magnetization change of these protons, we follow de Degennes[59,171] and adopt his approximation to eq 3.1 by neglecting the direct interaction term, which for one dimension can be expressed as

$$\begin{cases} \dfrac{\partial m(r,t)}{\partial t} = D_s \nabla^2 m(r,t) & |r - r_0| \geq b \\ m = m_0 & |r - r_0| \leq b \end{cases} \tag{3.8}$$

where $m(r, t)$ is the polarization per nucleus at the position r and the diffusion time, t; m_0 is the polarization per nucleus in thermal equilibrium; D_s is the spin diffusion coefficient (spatially constant diffusivity), m_0 is the equilibrium nuclear magnetization, and r_0 is the position of platelet surface. Spin diffusion is restricted in the one dimensional model to a domain between two adjacent clay nanoparticles, $- L \leq x \leq + L$ (cf., Figure 3.1).

Now let us focus on nuclear relaxation in the domain between particles. Consider a saturation-recovery experiment: m ($-L < x < +L$, $t = 0$) = 0 before recovery, while magnetization of the boundary spins on the relaxation center surface remain m ($-L$ or $+L$, t) = m_0 (eq 3.9, bottom) for all times. The symmetrical geometry of the one-dimensional model in Figure 3.1 provides $\partial m(x, t)/\partial x = 0$ at $x = 0$. In order to find a solution for the spin diffusion, we apply the Laplace transformation to eq 3.8 (upper) and then obtain the Laplace transform of the function m (t)

$$\overline{m} = \frac{m_0 \cosh(qx)}{p \cosh(qL)} \tag{3.9}$$

where p is a number sufficiently large to make $\overline{m}$ finite and $q = (p/D_s)^{1/2}$.

We wish to find an expression for the initial magnetization growth of the whole sample, measured by NMR. At short times following saturation, the total magnetization of the detectable protons grows by two mechanisms: magnetization flux from the relaxation sinks into the bulk protons via spin diffusion and the intrinsic relaxation due to the static magnetic field. The latter contribution is given by the Bloch equation as

$$\left(\frac{\partial M(t)}{\partial t}\right)_{\text{intrinsic}} = \frac{M_0 - M(t)}{T_{1,m}} \tag{3.10}$$

where $M(t)$ is the magnetization per unit volume, M_0 is the equilibrium value of the magnetization per unit volume and $T_{1,\text{m}}$ is the intrinsic relaxation time of the matrix in PCNs. The z-magnetization per unit volume is given by $M_0 = N_0 m_0 V_\text{d}$ at equilibrium, and

$M(t) = N_0 m(t)$ at a time, t, where N_0 is the number density of protons and V_d is the detectable volume fraction per unit volume. The magnetization of the protons within the region of a $A_s dx$ volume around a relaxation sink (A_s is the surface area of a sink, dx is the thickness of proton layer around a sink) can be written as $dM(t) = N_0 A_s m(t) dx$. Thus, another factor is the flux of magnetization from a relaxation source, expressed as $f_{flux} = D_0(\partial^2 M/\partial x^2)$,

$$f_{\text{flux}} = N_0 D_0 A_s \left(\frac{\partial m}{\partial x} \right)_{x=-L,+L} \tag{3.11}$$

where D_0 is defined as the apparent diffusion coefficient of protons at the surface of an object with surface area, A_s. Thus, we have the rate of magnetization recovery of all nuclei in a domain (Ω) around the object at short times as $\partial M/\partial t = f_{flux} + (\partial M/\partial t)_{intrinsic}$, namely,

$$\frac{\partial M(t)}{\partial t}\Big|_{\Omega} = N_0 D_0 A_s \frac{\partial m(x,t)}{\partial x}\Big|_{L,-L} + \frac{M_0 - M(t)}{T_{1,m}} \tag{3.12}$$

To obtain an analytical solution of eq 3.12, we first express the Laplace transform of eq 3.12 in terms of $\overline{m}$ in eq 3.9, and further derive the initial magnetization using the inverse Laplace transform (i.e., Carslaw and Jaeger[194]):

$$\frac{M(t)}{M_0} = \frac{2D^{1/2} A_s}{V_d} \left\{ \pi^{-1/2} + 2\sum_{n=1}^{\infty} (-1)^n i erfc\left(\frac{nL}{\sqrt{D_s t}} \right) \right\} t^{1/2} + \frac{1}{T_{1,m}} \left(t - \frac{1}{M_0} \int_0^t M(x) dx \right) \tag{3.13}$$

where $D = D_0^2/D_s$. the derivative of eq 3.13 can be written as

$$\frac{dY}{dt} = \frac{1}{2}C_1 t^{-1/2} + (-C_2)t^{-3/2} + \frac{1}{T_{1,m}}(1-Y) \tag{3.14a}$$

Here ,

$$Y = \frac{M(t)}{M(\infty)}$$

$$C_1 = \frac{2AD^{1/2}}{V_d}\left\{\pi^{-1/2} + 2\sum_{n=1}^{\infty}(-1)^n ierfc\left(\frac{nL}{\sqrt{D_s t}}\right)\right\};$$

$$C_2 = \frac{2AD^{1/2}}{V_d}\left\{\sum_{n=1}^{\infty}(-1)^n\left(\frac{nL}{\sqrt{D_s}}\right)erfc\left(\frac{nL}{\sqrt{D_s t}}\right)\right\}.$$

In our case, we can neglect the error function terms of C_1 and C_2 in eq 3.14. Mathematically, the functions of ierfc(x) and erfc(x) in the expressions of C_1 and C_2 in eq 3.14a converge quickly to zero as x goes to > 3, even at n = 1 (see Appendix C). In general, a half of the ideal interparticle spacing in PCNs, (L + b) is 650 nm – 5 nm for 0.2 ~ 20 wt% silicate, and the spin-diffusion coefficient, D_s is lower than 1.0 nm^2/ms. For example, we simply consider the typical case of the nanocomposite with 5 wt% ($L \approx 25$ nm) and $D_0 \approx 0.5$ nm^2/ms. Given that the interested range of recovery time is the first 50 ms, $L/(D_0 t)^{1/2}$ is > 5, and thus the function of ierfc(x) and erfc(x) is close to zero at x > 5

(see Appendix C). Note that, the smaller value of L at high clay loadings can lead to nonzero contribution for ierfc(x) and erfc(x) in eq 3.14a. In this case, the contribution from the error functions must be considered. If we observe the initial slope, the smaller interparticle spacing would result in diverging faster from the $t^{1/2}$ law. More will be discussed later. As a result, in some cases it is justified to neglect the error function terms in the following calculations. Then, eq 3.14a can be simplified:

$$\frac{dY}{dt} = \frac{\sqrt{D}}{\sqrt{\pi}} \frac{A_s}{V_d} t^{-1/2} + \frac{1}{T_{1,m}} (1 - Y) \tag{3.14b}$$

To check the accuracy of this approximation, we numerically calculate eqs 3.14(a) and 3.14(b) (see Figure 3.2) for the first 50 ms, and find that both numerical simulations are in complete agreement using the given specific parameters. Numerical simulations of eqs 3.14(a) and 3.14(b) also reveal no difference in the short-time relaxation behavior when A_s = 0.002 ~ 0.02 nm^2/nm^3, D_0 = 0.1 ~ 0.8 nm^2/ms, L = 10 ~ 500 nm and $T_{1,m}$ > 50 ms. Therefore, neglecting the error function terms in eq 3.14(a) is justified at short times. Solving eq 3.14(b), we finally obtain

$$\frac{M(t)}{M_0} = 2\frac{\sqrt{D}}{\sqrt{\pi}} \frac{A_s}{V_d} t^{1/2} + \frac{1}{T_{1,m}} t - \frac{4}{3} \frac{\sqrt{D}}{\sqrt{\pi}} \frac{1}{T_{1,m}} A_s t^{3/2} - \frac{1}{2} \frac{1}{T_{1,m}^2} t^2 + \ldots \tag{3.15a}$$

$$\frac{M(t)}{M_0} \approx 2\frac{\sqrt{D}}{\sqrt{\pi}} \frac{A_s}{V_d} t^{1/2} + \frac{1}{T_{1,m}} t \tag{3.15b}$$

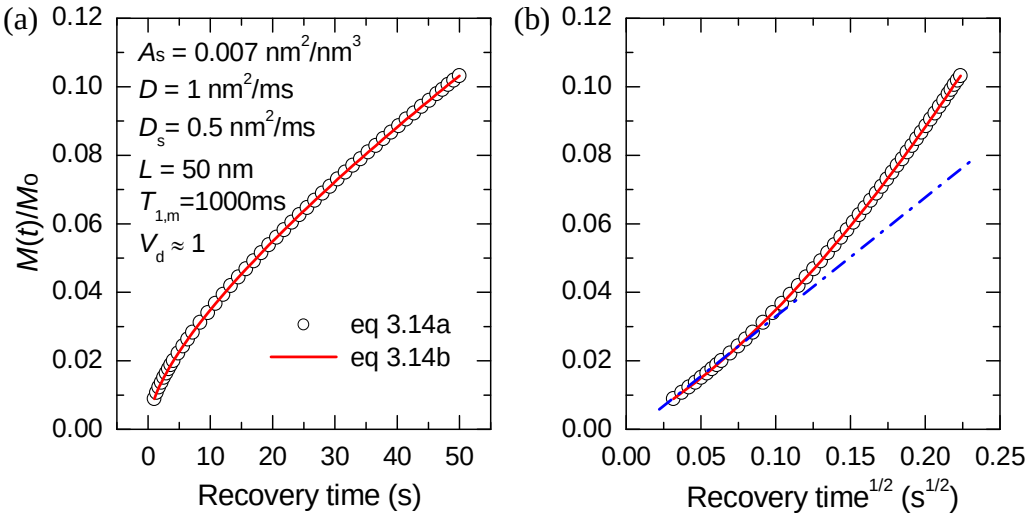

Figure 3.2. Magnetization recovery at the times from 1 ms to 50 ms from numerical approaches using eq 3.14(a) and eq 3.14(b), and A_s= 0.007 nm^2/nm^3, D = 1 nm^2/ms, D_s = 0.5 nm^2/ms, L = 50 nm, and $T_{1,m}$=1000 ms: (a) $M(t)/M_0$ vs recovery time, and (b) $M(t)/M_0$ vs the square root of recovery time. The dash-dotted line in (b) is the initial slope. $V_d \approx 1$ for typical PCNs with large interparticle spacings, $L >> b$.

Here, eq 3.15 suggests that the initial magnetization recovery is independent of the separation of clay nanoparticles, L. Equation 3.15(b) is approximated from eq 3.15(a), when $t << T_{1,m}$. For a polymer having the smaller $T_{1,m}$, the initial magnetization can be described by eq 3.15(a) rather than eq 3.15(b). We also compare the numerical solution of eq 3.14(b) with eq 3.15 for the first 50 ms. Figure 3.3 shows that these equations are consistent with each other at short times, with a slight divergence observed at > 35 ms,.

We arbitrarily assume that $T_{1,m}$ at short times is close to $T_{1,\text{polymer}}$, namely, $T_{1,m} \approx T_{1,\text{polymer}}$, where $T_{1,\text{polymer}}$ is the relaxation time of the corresponding pure polymer. In general, the exponential function describing the magnetization recovery curve is expressed by

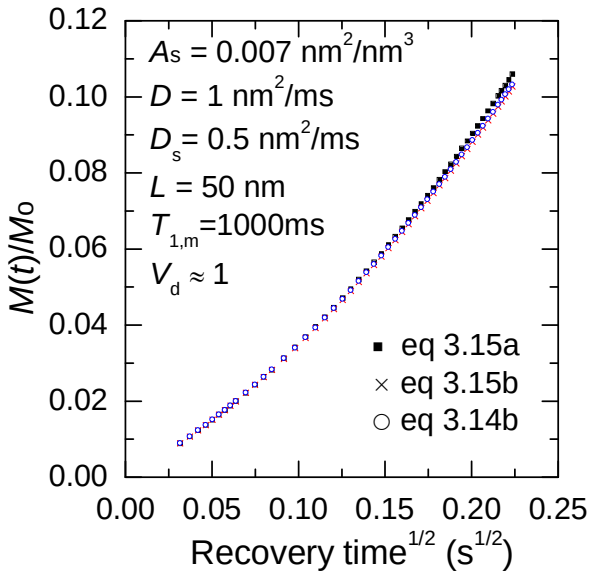

Figure 3.3. Magnetization recovery at the times from 1 ms to 50 ms from the numerical solution of eq 3.14(b) (○) and analytical solutions of eq 3.15(a) (■) and 3.15(b) (×), A_s = 0.007 nm^2/nm^3, D = 1 nm^2/ms, D_s = 0.5 nm^2/ms, L = 50 nm, and $T_{1,m}$ = 1000 ms.

$$\frac{M(t)}{M_0} = 1 - \exp\left(-\frac{t}{T_{1,\,polymer}}\right) \tag{3.16a}$$

At a short times, $t << T_{1,\,\mathrm{polymer}}$, we can obtain

$$\frac{M(t)}{M_0} \approx \frac{t}{T_{1,\,polymer}} \approx \frac{t}{T_{1,m}} \tag{3.16b}$$

Combining eqs 3.15 and 3.16, we finally have

$$\left(\frac{M(t)}{M_0}\right)_{PCN} - \left(\frac{M(t)}{M_0}\right)_{polymer} \propto 2\frac{\sqrt{D}}{\sqrt{\pi}}\frac{A_s}{V_d}t^{1/2} \tag{3.17}$$

Here, $(M(t)/M_0)_{PCN}$ and $(M(t)/M_0)_{polymer}$ are the magnetizations of a nanocomposite and the corresponding unfilled polymer, respectively. The term, $(M(t)/M_0)_{PCN} - (M(t)/M_0)_{polymer}$ on the left hand side of equation 3.17 is the paramagnetic contribution to the initial magnetization growth (M_c^n). Obviously, eq 3.17 indicates that $M_c^n \sim t^{1/2}$, which gives an analytical explanation for experimental observations in Chapter 2. Moreover, it can be seen in eq 3.17 that the initial slope is related to the surface area, A_s, the volume fraction, V_d as well as the diffusion coefficient, D (= D_0^2/D_s).

The initial relaxation behavior in the PP-MMT film with the stretch ratio of λ = 2.5 is analyzed using two methods suggested by eqs 3.17 and 3.15b. Figure 3.4(a) shows M_c^n as a function of $t^{1/2}$ (the same data for this sample as shown in Figure 2.3), whereas the initial relaxation data of this sample without correction are fitted by eq 3.15(b) (Figure 3.4b). The prefactor of $t^{1/2}$, 0.195 ± 0.020 $s^{-1/2}$ is obtained in Figure 3.4(b). By eq 3.17, M_c^n gives the initial slope, 0.190 ± 0.005 $s^{-1/2}$. These two approaches are consistent within the calculation error. It is worth noting that the prefactor of $t^{1/2}$ in eq 3.15(b) strongly depend on the chosen range of recovery time. Thus, it is important to have a priori knowledge about the time range for the diffusion-limited case, which is specifically discussed in Chapter 2. It should be emphasized that the initial slope could be affected not only by polymer/clay interfacial surface area, but also by other factors such as magnetic field, iron content of clay, and interfacial surface situation (e.g., proton packing density).

Although we specifically describe the initial magnetization recovery of PCNs containing paramagnetic clay nanoparticles, the method introduced above can also be applied to a variety of systems filled with paramagnetic centers in different geometrical shapes, such as spheres and rods (see Figure 1.1). For example, following the calculation stated above, we have derived the $t^{1/2}$ law for systems with spherical and rod-like paramagnetic centers (see Appendix B). Most importantly, the prefactors of the $t^{1/2}$ law for these cases are the same, reflecting that it is linearly proportional to the surface area of these centers. Thus, the $t^{1/2}$ law can be generalized to characterize the surface area in such a system in which paramagnetic centers have irregular shapes. Our results to some extent consolidates the argument by VanderHart, et al.[192] that the initial magnetization recovery follows the $t^{1/2}$ law, regardless of the spatial dimensionality of a relaxation sink.

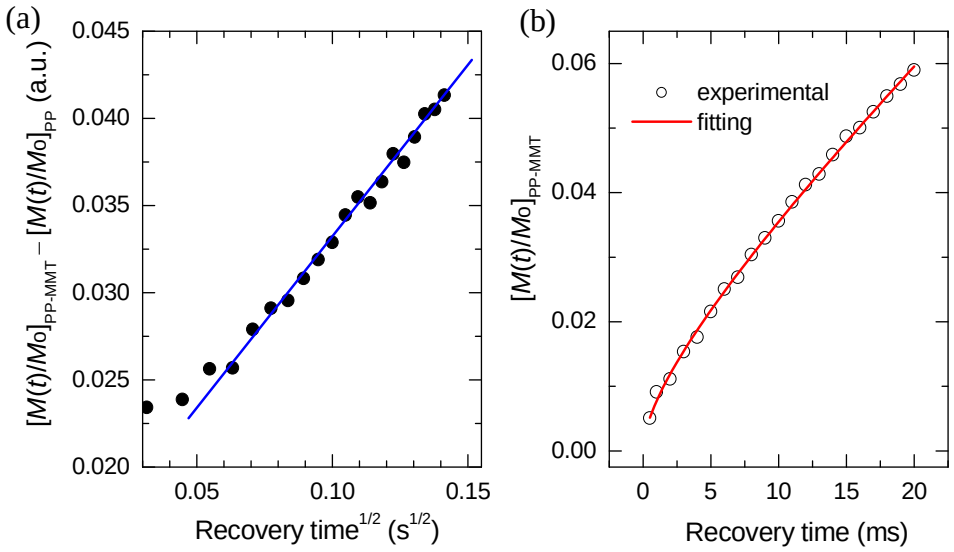

Figure 3.4. (a) Normalized and corrected magnetization, $[M(t)/M_o]_{PP\text{-}MMT} - [M(t)/M_o]_{PP}$, versus the square root of recovery time for PP-MMT nanocomposites with the stretch ratio of $\lambda = 2.5$. eq 3.17 describes this analysis to obtain the initial slope. The initial slope is 0.190 $s^{-1/2}$. (b) Normalized magnetization recovery $[M(t)/M_o]_{PP\text{-}MMT}$ curve fitted by eq 3.15(b) in the first 20 ms for the same sample as (a). The experimental data (○) and the fit (red line) are well overlapped. The prefactor of $t^{1/2}$ is calculated to be 0.195 $s^{-1/2}$.

3.3.3. Estimation of Interfacial Area in PP/MMT Nanocomposites

Surface area of clays was obtained by absorption methods and a theoretical formula proposed by Blum, et al.[178] For a typical montmorillonite, a specific surface area is estimated to be ~ 750 m^2/g. After adding into a polymer matrix, the polymer/clay interfacial area strongly depends upon clay exfoliation. If clay particles are assumed to be rectangular, TEM can be used to provide information about the interfacial surface area, A_s per unit volume using the following equation (see Appendix D):

$$A_s = \frac{2W_c\left(1/h_c + 2/d_c\right)}{\rho_c/\rho_p + W_c(1-\rho_c/\rho_p)} \tag{3.18}$$

where W_c is the mass fraction of MMT in a nanocomposite, h_c is average cumulative thickness per stack ($h_c = N_{ps} \times h_0$,where h_{ps} is average number of platelets/stack and h_0 is the thickness of a single platelet, ~ 1 nm), d_c is the lateral dimension of stacks, and ρ_c and ρ_p are clay and polymer densities, respectively. If $d_c >> 2\ h_c$, eq 3.18 can be simplified into

$$A_s = \frac{2W_c/h_c}{\rho_c/\rho_p + W_c(1-\rho_c/\rho_p)} \tag{3.19}$$

In fact, eq 3.19 can be generalized to particles with different shapes, if the lateral dimension of a particle is much larger than the average cumulative thickness (see Appendix D).

The average number of platelets per stack, N_{ps} can be calculated as

$$N_{ps} = A_{s,i} \ / A_{s,NMR} \tag{3.20}$$

where $A_{s,i}$ is the calculated surface area of MMT platelets, ~ 750 m^2/g surface area, and $A_{s,\,NMR}$ is the interfacial surface area of clay particles in PCNs. $A_{s,\,NMR}$ can be calculated using the following equation rearranged from eq 3.17:

$$A_s \approx \frac{\pi^{1/2}}{2D^{1/2}} S \tag{3.21}$$

Here, S is the initial slope (e.g., eq 2.8) , and the diffusion coefficient for polypropylene is assumed to be D = 0.3 nm^2/ms. We assume the bulk spin diffusion coefficient, D_s, and the diffusivity on the surface of the relaxation sinks, D_0 are the same as that of the bulk PP which exhibits the spin diffusion coefficients of 0.3 ~ 0.5 nm^2/ms.[195] We choose the lower boundary for D. The value of D = 0.2 nm^2/ms and 0.5 nm^2/ms are also considered to see how they affect the estimation of clay morphology.

Table 3.2 summarizes the interfacial surface area and particle morphology obtained by NMR and TEM for biaxially stretched films reported in Chapter 2. Figure 3.5 compares estimations of clay morphology from NMR and TEM. Using D = 0.3 nm^2/ms, NMR estimates clay morphology are consistent with TEM data. Hence, our NMR method can independently provide information about clay morphology, including the interfacial surface area and degree of exfoliation (f = 1/ N_{ps}). It is worth noting that a priori knowledge for the choice of the spin diffusion coefficient plays a key role. For example, using D = 0.5 nm^2/ms gives smaller interfacial areas and larger N_{ps}, leading to

underestimations of clay exfoliation with comparison to TEM data. On the other hand, using the smaller D = 0.2 nm^2/ms provides the opposite estimations.

Table 3.2. Interfacial surface area and particle morphology obtained by NMR and TEM for biaxially stretched films[a]

Stretch ratio, λ	NMR			TEM [b]			
	slope S	$A_{s,NMR}$ [c]	N_{ps} [d]	length d_c	thickness	h_c [e]	$A_{s,TEM}$ [f]
	$s^{-1/2}$	**10^{-3} nm^2/nm^3**		nm	nm		**10^{-3} nm^2/nm^3**
1.0	0.114	**5.83 ± 0.40**	3.20	189 ± 86	6.4 ± 1.7	2.64	**7.25 ± 0.42**
1.5	0.163	**8.34 ± 0.15**	2.24	170 ± 70	5.8 ± 1.3	2.47	**7.75 ± 0.55**
2.0	0.183	**9.36 ± 0.28**	1.99	216 ± 95	4.9 ± 1.1	2.19	**8.73 ± 0.70**
2.5	0.190	**9.72 ± 0.32**	1.92	210 ± 84	4.5 ± 0.8	2.07	**9.24 ± 0.69**
3.0	0.200	**10.23 ± 0.36**	1.82	275 ± 126	3.1 ± 0.5	1.64	**11.65 ± 1.29**
3.5	0.239	**12.23 ± 0.34**	1.53	283 ± 191	2.0 ± 0.5	1.31	**14.65 ± 2.52**

[a] error of NMR data is within 5%; densities of PP and MMT are 0.905 and 2.6 g/cm^3, respectively; nanocomposite films contain 2.7 wt% neat MMT. [b] see details in Table 2.2; [c] calculated by eq 3.21 using the rectangular clay platelets and spin diffusion coefficient, D = 0.3 nm^2/ms. [d]calculated by eq 3.20. [e] h_c, calculated by the method described in Section 2.5 of Chapter 2; we arbitrarily assume majority of particles in films contain 3 and 2 platelets for λ = 1.0 to 2.5, and 2 and 1 platelets for λ = 3.0 and 3.5. [f] $A_{s,TEM}$ calculated by eq 3.18.

A PP-MMT nanocomposite filled with 0.57 wt% pure silicates (PP-MMT0.57) was also investigated using our NMR method. The XRD curve of this sample shows a very broad and weak basal peak (see Appendix A), suggestive of a well exfoliated structure; TEM imaging shows that exfoliation is nearly complete and only a few stacks consist of 2 platelets (not shown here). When fully exfoliated, PP-MMT0.57 exhibits $A_{s,i}$ = 3.88 nm^2/nm^3 (calculated using 750 m^2/g and 0.57 wt% MMT). The NMR initial slope, S = 0.071 $s^{-1/2}$ of PP-MMT0.57 (Chapter 4) can be used to calculate $A_{s,\ NMR}$ = 3.63 nm^2/nm^3.Thus, N_{ps} =3.88 / 3.63 = 1.07 (f = 1/ N_{ps} = 0.94), using D = 0.3 nm^2/ms. These

quantitative NMR results on clay morphology are also in good agreement with other techniques.

In addition, it should be emphasized that the initial slope could be affected not only by polymer/clay interfacial surface area, but also by other factors such as magnetic field and iron content of clay (possibly also by interfacial surface situation (e.g., proton packing density)) (see Chapters and 4 and 6). Taking into account these factors, the initial slope needs to be justified before used to directly calculate the surface area. In our case, the iron content of pure silicates in Cloisite 15A, ~ 5 wt% Fe_2O_3 is high enough to form the relaxation sink as described in our model. Also, the magnetic field, 7.05 T is high to detect the initial relaxation recovery of the surface protons which contributes to the initial slope related to spin diffusion (see Chapter 6).

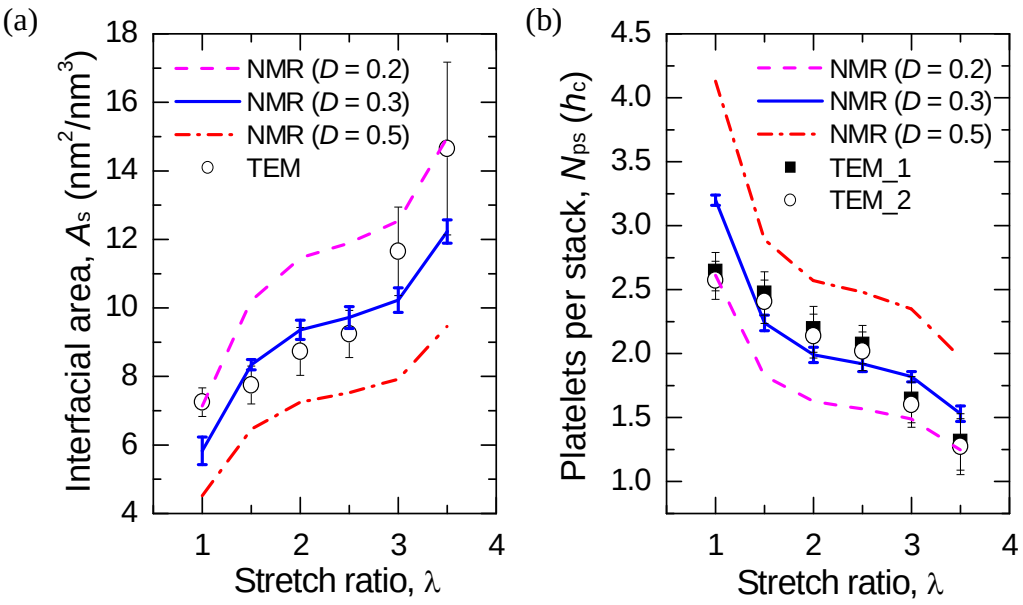

Figure 3.5. Comparison of clay morphology obtained by NMR and TEM: interfacial area, A_s (a) and average number of platelets/stack, N_{ps} (h_c) (b) as a function of stretch ratio in PP-MMT nanocomposite films. Note that three values of D, 0.2 (dashed line), 0.3 (solid line) and 0.5 nm^2/ms (dash-dotted line) are used to calculate $A_{s,\,NMR}$ and N_{ps}. TEM_1 data are calculated from the thickness of TEM data, whereas TEM_2 data are calculated by $N_{ps} = A_s(TEM)/A_{s,i}$.

3.4. Conclusions

We have proposed a model describing the initial magnetization recovery for polymer nanocomposites containing paramagnetic clay nanoparticles in the saturation recovery experiment. In this model we have derived analytical solutions to the magnetization flux equation. We have shown that the growth of magnetization at short times depends not only on the polymer/clay interfacial surface area but also on the spin diffusion coefficient. Clay morphology in a series of biaxially stretched polypropylene/montmorillonite nanocomposite films was investigated using our NMR model as well as TEM. The interfacial area and the degree of exfoliation from our model are well consistent with TEM data. Thus, the NMR method developed here has been demonstrated to independently provide quantitative information about clay morphology in nanocomposites.

CHAPTER 4

Clay Dispersion in Polymer Nanocomposites by Spin-Diffusion-Averaged Paramagnetic Enhanced NMR Relaxometry: Model Development and Scaling Relations

4.1. Abstract

A lamella-based model was developed for describing NMR longitudinal relaxation in polymer/paramagnetic clay nanocomposites. From this model, an analytical relationship was found to connect enhanced relaxation rate with clay morphology. The paramagnetic contribution to the NMR relaxation rate ($R_{1,para}$) is inversely proportional to the square of clay interparticle separation, and directly proportional to clay weight fraction squared. These relationships directly provide relative clay dispersion for a given series of polymer/clay nanocomposites (PCNs). With independent knowledge of clay dispersion in a single sample from either X-ray diffraction or transmission electron microscopy, clay dispersion in a given series of polymer/clay nanocomposites may be predicted. This is demonstrated for the following PCNs: poly(vinyl alcohol)/montmorillonite (PVA/MMT), nylon6/MMT, poly(ε-caprolactone)/MMT, poly(lactic acid)/MMT (PCL/MMT), polypropylene/MMT (PP/MMT) nanocomposites. These quantitative results are of great help to identify dependence of clay dispersion upon types of MMT, clay content, clay surface modification, molecular weight of a polymeric matrix, preparation method and processing conditions. The initial relaxation behavior and

$R_{1,para}$ were compared in characterizing clay morphology. The results reveal that the initial slope is related to the degree of exfoliation, and $R_{1,para}$ is related to the quality of dispersion involved with clay exfoliation and distribution. These findings offer new insights into the application of NMR relaxometry for characterizing clay dispersion in polymeric nanocomposites.

4.1. Introduction

In Chapter 3, a model was proposed for describing the initial spin-lattice relaxation behavior in polymer/clay nanocomposites. We have analytically found that the initial magnetization grows with time t, as $t^{1/2}$. This analytical relation can be utilized to provide clay morphology, such as interfacial surface area and average number of platelets per stack, N_{ps} (= the inverse degree of exfoliation, $1/f$ as defined in Chapter 2). The degree to which platelet stacks are exfoliated and dispersed in matrices is governed by interfacial interactions and processing, which in turn influences ultimate physical properties of polymer/clay nanocomposites (PCNs). Characterization of clay particle morphology in terms of degree of exfoliation and dispersion homogeneity can be accomplished by solid-state NMR relaxometry when clay platelets contain paramagnetic impurities that increase spin-lattice relaxation rate, $1/T_1$, of the matrix polymer (Chapter 2).

So-called paramagnetic relaxation enhancement (PRE) by direct interaction has been extensively employed to assist structure determination of biomacromolecules.[196] For these applications, site-resolved information is required and paramagnetic centers

must be deliberately incorporated at defined locations within macromolecules. Spin diffusion can be suppressed by focusing on weakly coupled nuclei (e.g., ^{15}N),[197] maintaining samples in solution[198] or by deuteration.[199] In rigid PCNs containing naturally paramagnetic clays, ^{1}H spin diffusion averages paramagnetic-enhanced relaxation throughout a sample.

Spin-diffusion-averaged paramagnetic enhancement of NMR relaxation has been used to quantitatively probe PCN morphology in two ways.[42,44,200] Chapter 3 addresses the first one that initial slopes of magnetization recovery curves are quantitatively related to surface/volume ratios of clay to polymer. The second is that paramagnetic contributions to overall spin-lattice relaxation rates, $R_{1,para}$, are directly proportional to clay interparticle spacing. Bourbigot et al.[44] developed a one-dimensional model consisting of perfectly stratified clay/polymer layers to simulate magnetization growth via relaxation and spin diffusion. They numerically simulated relaxation recovery curves but were not able to reproduce experimental curves across the entire range of recovery times. In this chapter, beginning with the same one-dimensional model and expression for magnetization growth via relaxation and spin diffusion, an analytical solution will be derived from which the dependence of $R_{1,para}$ on clay interparticle spacing is established. Some scaling relations will be then derived from this solution and their applicability will be also demonstrated using published experimental data on different sets of PCNs containing paramagnetic montmorillonite (MMT).[41,43,201] In doing so, we introduce a new plot for visualizing the quality of clay dispersion in PCNs with respect to average interparticle spacing and platelets/stack, reflecting a combination of clay exfoliation and distribution.

4.2. Experimental Details

Materials. See Chapter 2 for full details about preparation of polypropylene nanocomposites filled with different loadings of montmorillonite.

Poly(vinyl alcohol) (PVA)/montmorillonite nanocomposites (PVA-MMT) were prepared at the weight ratio (PVA/MMT) of 100/1, 100/2, 100/4, 100/6, 100/8, and 100/10 by the solution-intercalation film-casting method as described by other researchers.[73,201] The samples were dried at under vacuum at 80 ^{o}C for 48 hours before any measurements. Montmorillonite, STX-1b filled in PVA here was obtained from the Source Clays Repository, Purdue University, Indiana.

Poly(lactic acid) (PLA)/ Cloisite 30B nanocomposite as cast-films were provided by Dr. Mukerrem Cakmak of University of Akron.[202] Two different molecular weights of PLA, lower MW PLA2002D (LMW PLA) and higher MW PLA4032D (HMW PLA) (NatureWorks® Company) were filled with Cloisite 30B by melt compounding. Cloisite 30B containing 3.11 wt% Fe_2O_3 as Fe^{3+}, is an organically modified montmorillonite (Southern Clay Products, Inc.).

Poly(ε-caprolactone)/MMT nanocomposites prepared by melt compounding were reported by Lepoittevin et al.[60]

NMR Relaxometry. See Chapter 2 for full details about ^{1}H saturation-recovery NMR experiments at 7.05 T. ^{1}H saturation-recovery NMR experiments on PLA-MMT nanocomposites were performed on a magnetic resonance analyzer (MARAN 23 Ultra) using a permanent magnet of 0.54 T. At 0.54 T, 1024 scans were repeated for each relaxation delay.

TGA Analysis. See Chapter 2 for full details about measurements of the neat MMT content using thermogravimetric analysis (TGA).

WAXD measurements. See Chapter 2 for full details about Wide-angle X-ray Diffraction scanning. The d_{001} basal-spacing was calculated using the Bragg equation.

Systems in Literature. NMR relaxometry and X-ray diffraction data were taken from the literature for three series of PVA-MMT.[73,201] These three series contain MMTs with 2.7 wt%, 3.5 wt%, and 4.4 wt% Fe_2O_3 as Fe^{3+} provided by KUNIMINE Co. Ltd., Japan, respectively.

NMR relaxometry and TEM data were taken from the literature for nylon 6/montmorillonite nanocomposites prepared by melt compounding.[41,117] The organically modified montmorillonite in nylon 6 is Cloisite 20A (3.11 wt% Fe_2O_3 as Fe^{3+}) from Southern Clay Products, Inc. The Fe_2O_3 content in Cloisite 20A was determined using elemental analysis by Southern Clay Products.

NMR relaxometry, XRD and TEM data were taken from the literature for poly(ε-caprolactone) nanocomposites filled with Cloisite 25A and Cloisite 30B. The organically modified montmorillonite, Cloisite 20A (from Southern Clay Products, TX) contains 3.41 wt% Fe_2O_3 as Fe^{3+}.

Densities. Volume fractions of clay were calculated using specific densities of 0.905, 1.24, 1.15, 1.3, 1.13, and 2.6 g/cm^3 for PP, PLA, PCL, PVA, nylon 6 and neat MMT, respectively.

4.3. Results and Discussions

4.3.1. Modeling Magnetization Growth in Polymer/Clay Nanocomposites

Consider a regular, repeating lamellar structure of alternating clay particles with polymer (see Figure 4.1a), characterized by four parameters: Δ = face-to-face interparticle spacing, g = edge-to-edge interparticle spacing, d_c = lateral dimension of particle, and h = particle height or thickness. Note that a single particle can be characterized by one or more platelets per stack. Geometrically, assuming the uncorrelated adjacent platelets in the positioning of clay particles, the interparticle spacing Δ can be given by

$$\Delta = V_p/(V_c/\xi^2 h) \tag{4.1}$$

where V_p is the polymer volume fraction, V_c is the clay volume fraction, and ξ^2 is the fractional area occupied by particles in a plane: $\xi = d_c/(g + d_c)$ and $0 \leq \xi \leq 1$. For a given clay volume fraction, eq 4.1 indicates that interparticle spacing increases as h or ξ increase. Particle thickness, $h = (N_{ps} - 1)\, d_{001} + h_0$, where N_{ps} is average number of platelets per stack, d_{001} is the interplatelet basal spacing, and h_0 is the thickness of a single platelet. In cases of particles with large aspect ratios or PCNs with high clay loadings, ξ tends toward 1 (i.e., $g << d_c$), while ξ could be close to zero in PCNs with very low clay loadings or poor clay dispersion. For idealized PCNs containing fully exfoliated clay in which $h = h_0 \approx 1$ nm and $\xi = 1$, polymer and clay are perfectly stratified so that minimum interparticle spacings, Δ_i, are given simply by the clay volume fraction:

$$\Delta_i = h_0 (1 - V_c)/V_c \tag{4.2}$$

For the more commonly employed clay weight fraction, W_c:

$$\Delta_i = h_0 (\rho_c/\rho_p) (1 - W_c)/W_c \tag{4.3}$$

where ρ_c and ρ_p are clay and polymer densities, respectively. Such idealized interparticle spacings represent average interplatelet spacings in PCNs containing fully exfoliated and homogeneously dispersed clay. In our model, such PCNs would be characterized by large face-to-face matrix polymer domains (Ω_1 in Figure 4.1b) and small edge-to-edge matrix polymer domains (Ω_2 in Figure 4.1b).

We start with dynamics of polarization transfer under the influence of paramagnetic relaxation sinks. Let M be the z-component of the magnetization per unit volume, and M_o the equilibrium bulk magnetization per unit volume. In PCNs, the total rate of change of M is given by eq 2.1[200]

$$\left(\frac{\partial M}{\partial t}\right)_{\text{total}} = \left(\frac{\partial M}{\partial t}\right)_{\text{direct}} + \left(\frac{\partial M}{\partial t}\right)_{\text{diff}} + \left(\frac{\partial M}{\partial t}\right)_{\text{intrinsic}} \tag{4.4}$$

where $(\partial M/\partial t)_{\text{direct}}$ is the rate of magnetization change due to direct interaction with paramagnetic centers, $(\partial M/\partial t)_{\text{diff}}$ is the rate of magnetization change resulting from spin diffusion to the paramagnetic relaxation sinks, and $(\partial M/\partial t)_{\text{intrinsic}}$ is the intrinsic rate of

magnetization change due to interaction of the sample lattice with the static magnetic field (B_o). The paramagnetic relaxation sinks are the clay particles plus a layer (*b* in Figure 4.1c) of unobservable nuclei around them that remain polarized due to extremely fast relaxation via direct interaction (r^{-6} dependence) with paramagnetic centers near the particle surface. The nuclei within this barrier region are maintained at equilibrium and not observed. In fact, this assumption on the infinitely fast relaxation of protons in this barrier region is justified even for these protons exhibiting finitely fast relaxation (e.g., a few milliseconds). Thus, we follow de Gennes[171] and adopt an approximation to eq 4.4 by neglecting the direct interaction term, $(\partial M/\partial t)_{\text{direct}}$, to give $(\partial M/\partial t)_{\text{total}} = (\partial M/\partial t)_{\text{diff}} + (\partial M/\partial t)_{\text{intrinsic}}$, which for one dimension can be expressed as

$$\frac{\partial m(x,t)}{\partial t} = D_s \frac{\partial^2 m(x,t)}{\partial x^2} - \frac{1}{T_{1,m}}[m(x,t) - m_o] \tag{4.5}$$

where D_s is the bulk spin diffusion coefficient (uniform, not a function of x), m_o is the equilibrium nuclear magnetization per spin, and $1/T_{1,m}$ is the bulk spin relaxation rate. It is worth noting that, eq 4.5 and eq. 3.12 are eventually same but they have different focuses. Eq 4.5 describes the change of magnetization in the bulk polymer, whereas eq 3.12 focuses on depicting the change of overall magnetization due to the surface flux and the intrinsic relaxation.

Saturation insures that $m(-L < x < +L,\ t = 0) = 0$ before magnetization transport begins via spin diffusion and relaxation recovery; nuclei within a distance *b* from the clay surface maintain equilibrium, that is, $m(-L \text{ or } +L,\ t) = m_o$ for all times. The symmetry of

the one-dimensional model of Figure 4.1c means that $\partial m(0,t)/\partial x = 0$ at $x = 0$, equidistant between two clay particles. Under these conditions, an analytical solution to equation 4.5 can be written for transport of nuclear magnetization via diffusion and relaxation following saturation:

$$m = m_o - m_o \sum_{n=0}^{\infty} \frac{4(-1)^n}{(2n+1)\pi} \exp\left\{-\left[\frac{(2n+1)^2 \pi^2 D_s}{4L^2} + \frac{1}{T_{1,m}}\right] t\right\} \cos\left(\frac{2n+1}{2L}\pi x\right) \qquad (4.6)$$

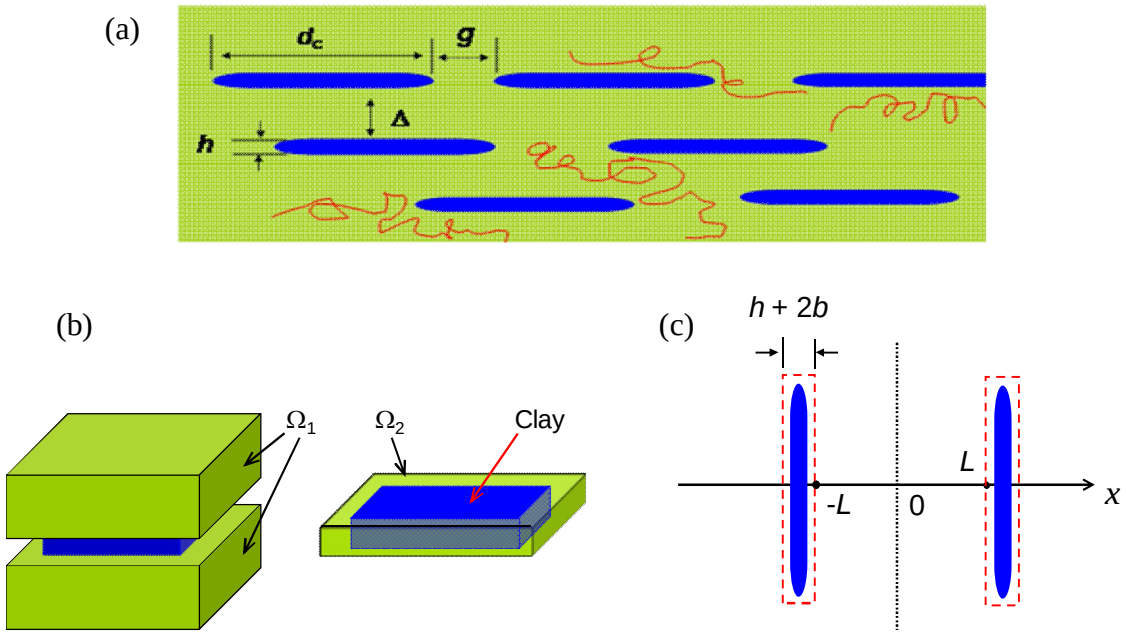

Figure 4.1. (a) Schematic of polymer-clay nanocomposite with stratified clay particles characterized by face-to-face interparticle separation Δ, thickness h, lateral dimension d_c, and edge-to-edge separation g. (b) Polymer matrix surrounding clay particle is divided into two different domains, Ω_1 and Ω_2. (c) One-dimensional lamellar model for the face-to-face domains (Ω_1) between a pair of clay particles where b is the thickness (~ 0.4 nm) of the thin layer of nuclei relaxed directly by the paramagnetic centers in the clay. Note that clay particles can be single platelets or stacks of platelets depending on the degree of exfoliation.

The detected signal is magnetization from all domains, $M(t) = \int m(x,t)d\Omega$ (see Figure 4.1b). Given the very large aspect ratio (d_c/h ~ 30 to 1000)[6,9,37,148,156,158] and surface area (~750 m^2/g)[178] of montmorillonite, magnetization transport in the face-to-face domains (Ω_1) is of prime relevance (see Figure 4.1c). The total magnetization in the Ω_1 domains, $M_1(t) = \Sigma \int m \, d\Omega$, is

$$M_1(t) = M_{o,1} - m_o N_0 \sum_{n=0}^{\infty} \frac{16V_1}{(2n+1)^2 \pi^2} \exp\left\{ -\left[\frac{(2n+1)^2 \pi^2 D_s}{4L^2} + \frac{1}{T_{1,m}} \right] t \right\} \tag{4.7}$$

where $M_{o,1}$ is the equilibrium magnetization, N_0 is the packing density of spins (number of spins per unit volume), and $V_1 = L\,(g + d_c)^2$ is the volume of Ω_1. Following the same approach as above, $m(x,t)$ and the total magnetization, $M_2(t)$, for the Ω_2 domain with volume V_2 are derived to give expressions similar to equations 4.6 and 4.7, respectively. The total magnetization of the unit cell comprised of one Ω_2 and two Ω_1 domains is $M(t) = M_1(t) + M_2(t)$, and the corresponding total equilibrium magnetization is $M_o = M_{o,1} + M_{o,2} = m_o N_0 (2V_1 + V_2)$. Finally, we obtain a complete solution using our one-dimensional model:

$$\frac{M(t)}{M_o} = 1 - \sum_{n=0}^{\infty} \beta_n^{-1} \left\{ \phi_1 \exp\left[-\left(\frac{2\beta_n D_s}{L^2} + \frac{1}{T_{1,m}} \right) t \right] + \phi_2 \exp\left[-\left(\frac{2\beta_n D_s}{(g/2-b)^2} + \frac{1}{T_{1,m}} \right) t \right] \right\} \tag{4.8}$$

where $\beta_n = (2n + 1)^2 \pi^2/8$, and $\phi_1 (= 2V_1/ (2V_1 + V_2))$ and $\phi_2 (= 1 - \phi_1)$ are the volume fractions of Ω_1 and Ω_2 domains, respectively. The summation in eq 4.8 converges quite

rapidly with n; numerical calculation using just two iterations yields errors less than 5% (see Figure 4.2). In typical PCNs with low clay concentrations (~5 wt %), ϕ_1 is much larger than ϕ_2 if $\Delta >> h$, indicating that the first term of the summation in equation 4.8 contributes much more to magnetization recovery than the second term.

Taking only the first term of the summation representing face-to-face interparticle domains, equation 4.8 can be recast:

$$\frac{M(t)}{M_o} = 1 - \frac{8}{\pi^2} f(t)\phi_1 \exp\left[-\left(\frac{\pi^2 D_s}{4L^2} + \frac{1}{T_{1,m}}\right)t\right]$$

(4.9)

where $f(t) = 1 + 1/9 \exp(-8B\,t) + 1/25 \exp(-24B\,t) + \ldots$, and $B = \pi^2 D_s/(4L^2)$. The value of $f(t)$ approaches 1 if $t > (8B)^{-1} = 2L^2/(\pi^2 D_s)$. Note that this approximation is valid when spin diffusion lengths, $(D_s \times 5T_1)^{1/2}$, are greater than interparticle separations, Δ. For instance, the interparticle distance is such that magnetization throughout the entire sample may equilibrate due to spin diffusion during the T_1-relaxation process. Thus, samples must be characterized by $T_1 > L^2/(5D_s)$. Since this is approximately $(8B)^{-1} = 2L^2/(\pi^2 D_s)$, eq 4.9 should sufficiently describe long-time relaxation behavior for $f(t) = 1$ (i.e., $n = 0$ in summation of eq 4.8). This was confirmed by numerically generating relaxation curves for the first four n values of the summation (n = 0, 1, 2 and 3) using parameter values similar to those for a PCN with 5 wt% MMT and a spin diffusion coefficient, D_s = 0.7 nm^2/ms. These are shown in Figure 4.2(a) and reveal no difference in the long-time relaxation behavior when t > ~180 ms $\approx 2L^2/(\pi^2 D_s)$. Although differences are observed in

the short-time behavior, Figure 4.2(b) shows that these do not significantly affect the overall T_1 values determined from plots of $\ln[\pi^2/8(1-M(t)/M_o)]$ versus recovery time. As a result, from eq 4.9 with $f(t) = 1$, the observed $1/T_{1,PCN}$ can be obtained

$$\frac{1}{T_{1,PCN}} \approx \frac{\pi^2 D_s}{4L^2} + \frac{1}{T_{1,m}} \tag{4.10}$$

Equation 4.10 can be compared to the semi-empirical equation used to compute the paramagnetic contribution to the spin-lattice relaxation rate[41-43,54]

$$R_{1,para} = 1/T_{1,para} = 1/T_{1,PCN} - 1/T_{1,polymer} \tag{4.11}$$

If the relaxation rate of the pure polymer, $1/T_{1,polymer}$, is taken to be the relaxation rate of the bulk polymer in the nanocomposite, $1/T_{1,m}$. In this case, after substituting $(\Delta - 2b)$ for $2L$, and recognizing that $\Delta >> 2b$, the paramagnetic contribution to the relaxation is

$$T_{1,para}^{-1} = R_{1,para} \approx \pi^2 D_s/\Delta^2 \tag{4.12}$$

which is consistent with the claim from VanderHart, et al. from their numerical calculations that $R_{1,para} \propto \Delta^{-2}$ in the diffusion-controlled time regime.[42] By measuring $R_{1,para}$, one can determine average interparticle spacing if a spin diffusion coefficient is

known. If the average interparticle spacing is known, for example, from a statistical analysis of TEM images, one can determine spin diffusion coefficients.

Average interparticle separations (Δ) determined from experimental $R_{1,para}$ values can be compared to idealized interparticle separations (Δ_i) calculated from clay content (e.g., eqs 4.2 and 4.3) and a measure of dispersion can be defined:

$$\alpha = \Delta_i / \Delta \tag{4.13}$$

Values for α depend on the degree of exfoliation, stratification and homogeneity of clay particle distribution. In general, dispersion decreases as α decreases and approaches 0. Incorporating α as a measure of dispersion, we can define the following scaling relation from eq 4.12:

$$R_{1,para} \propto \alpha^2 \Delta_i^{-2} \tag{4.14}$$

According to eq 4.14, plotting $R_{1,para}$ versus Δ_i^{-2} should yield straight lines when clay dispersion is of similar quality, that is, α is constant. Deviation from such lines will provide insight into how the dispersion quality changes with clay concentration. For fully exfoliated and highly dispersed clay, lines can be assigned slopes containing $\alpha = 1$. When aggregation of platelets leads to dispersions characterized by interparticle separations that are twice the size of the fully exfoliated case, that is, $\alpha = \Delta_i/\Delta = 1/2$, slopes of these plots will predictably decrease by $\alpha^2 = 1/4$. These plots should be useful for visualizing quality of clay dispersion as clay content increases.

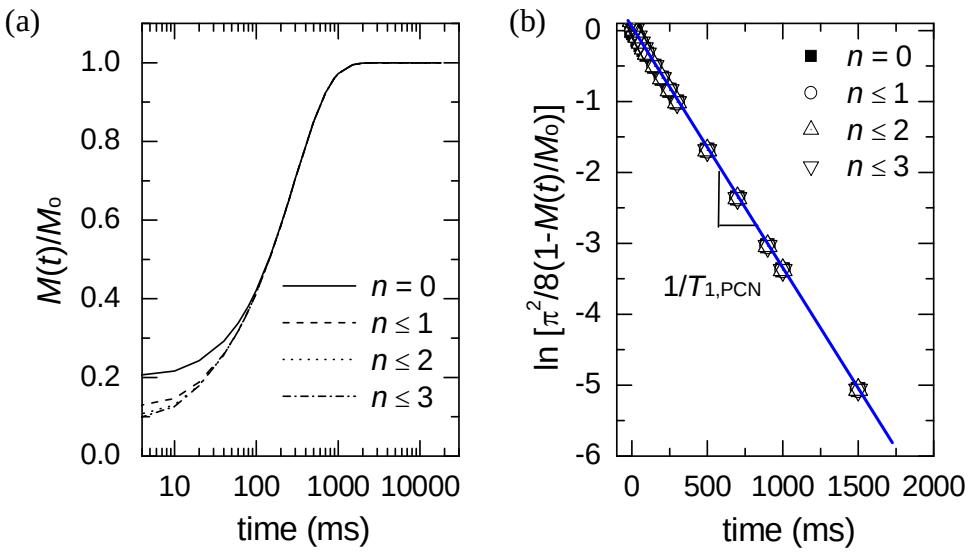

Figure 4.2. Relaxation curves numerically calculated using eq 4.8 and first four terms of $f(t)$, corresponding to eq 4.7 (first term of summation only) and $n = 0, \leq 1, \leq 2$ and ≤ 3: (a) $M(t)/M_o$, and (b) $\ln[\pi^2/8(1 - M(t)/M_0)]$ versus recovery time. The following parameters were used in the calculation: spin diffusion coefficient, $D_s = 0.7$ nm^2/ms, bulk polymer relaxation time, $T_{1,m} = 1.635$ s, $L = 25$ nm and recovery time range from 0.5 to 10000 ms. Calculated values of $T_{1,\,PCN}$ in (b), 296 ms ($n = 0$), 293 ms ($n \leq 1$), and 292 ms (n ≤ 2 and ≤ 3), are consistent with the relaxation constant of 296 ms determined by fitting the data points in (b) to a conventional exponential recovery

Alternatively, we can substitute equations 4.3 and 4.13 into eq 4.12 and combine constants to yield a direct relationship between $R_{1,para}$ and the clay weight fraction W_c:

$$R_{1,para} \approx AW_c^2/(1 - W_c)^2 \tag{4.15}$$

where the prefactor $A = \pi^2 h_0^{-2} D_s \alpha^2 (\rho_p/\rho_c)^2$. Plots of $R_{1,para}$ versus clay weight fraction should yield curves of constant dispersion quality, the relative magnitude of which is embodied in A ($\propto \alpha^2$). As dispersion quality increases, $R_{1,para}$ increases.

So far our model has naively neglected dependencies of $R_{1,\text{para}}$ on the concentration of paramagnetic impurities in the particles, and on the strength of the external magnetic field. The former is associated with the fluctuating electron magnetic field, while the latter changes the coupling constant between this electron field and nuclei of interest.[42] Both effects influence the relaxation behavior associated with the immediate area surrounding the clay nanoparticle therefore affecting the strength of the relaxation sink. Consequently, an additional proportionality factor K has to be introduced into equation 4.15 to account for the above effects:

$$R_{1,\text{para}} \approx \text{K}\, A W_c^2/(1 - W_c)^2 \tag{4.16}$$

Therefore, we are only able to calculate relative values KA for a given series of polymer/clay systems measured at one specific magnetic field. With independent knowledge of the dispersion state of a single sample obtained from another experimental method such as TEM, these NMR-determined relative dispersion values can be adjusted to provide absolute measures of the dispersion (i.e., α) for all of the samples. The advantage of this approach is that it precludes the need for conducting TEM, image analysis, and statistical analysis of the images on a large number of samples, which saves time. NMR results are naturally average values over the entire sample. In the following, we present NMR relaxometry data to demonstrate how the the scaling relations of eqs 4.14 and 4.16 can be used to explore and display dispersion quality in polymer/clay nanocomposites.

4.3.2. Poly(vinyl alcohol)/MMT Nanocomposites with Well Exfoliated MMT Prepared by Solution Intercalation

Figure 4.3 shows $R_{1,para}$ versus (a) Δ_i^{-2}, and (b) W_c for a series of six poly(vinyl alcohol) (PVA)/MMT nanocomposites (3.5 wt% Fe_2O_3 in the MMT). This series of samples is expected to contain clay that is fully exfoliated across a broad concentration range. Hence it is an ideal series of samples to use for comparing the predictions of our model. For the four samples with the lowest clay contents, $R_{1,para}$ is linearly proportional to Δ_i^{-2} (Fig 4.3a), consistent with eq 4.14, and consistent with the curve predicted by eq 15 when plotted versus W_c (Fig 4.3b). Both representations indicate that clay dispersion in these samples is of similar quality. X-ray diffraction (XRD) data show no basal peak (001) at scanning angles of $2\theta \leq 5°$, indicating full exfoliation, or at least a basal spacing larger than 1.8 nm.[201] Assuming these samples are fully exfoliated, we have labeled the straight line in Figure 4.4(a) as $\alpha^2 = 1$, and curve in Figure 4.4(b) as $\alpha = 1$, representing an average number of platelets/stack, $N_{ps} = 1$. We then used eqs 4.14 and 4.16 to predict the scaling of $R_{1,para}$ versus Δ_i^{-2} and W_c, respectively, for when the average interparticle distance is twice that shown for a fully exfoliated sample, in other words, when $N_{ps} = 2$. In Figure 4.4(a), this line is marked "2" (dot-dashed, $\alpha^2 = 1/4$) and in Figure 4.4(b) this curve is signified as $\alpha = 0.5$ (cf. eq 4.13). The two PVA/MMT samples with higher clay contents (100/8 and 100/10 w/w) diverge from the $\alpha^2 = 1$ line but remain distant from the line marked "2". Thus, even though these two samples also exhibit no basal peaks in their XRD patterns, their clay dispersions are of lower quality than that of the PVA/MMT samples with lower MMT contents. At the same time, they remain distant from the "2" line, which is consistent with the absence of stacks indicated by XRD. The divergence

from full exfoliation could be due to lower homogeneity at high clay content as compared to low clay content, which is often reported in PCNs. Such insights from plots of $R1$,para versus Δ_i^{-2} and W_c can be directly obtained for PCNs composed of a given clay and polymer measured at a given magnetic field strength.

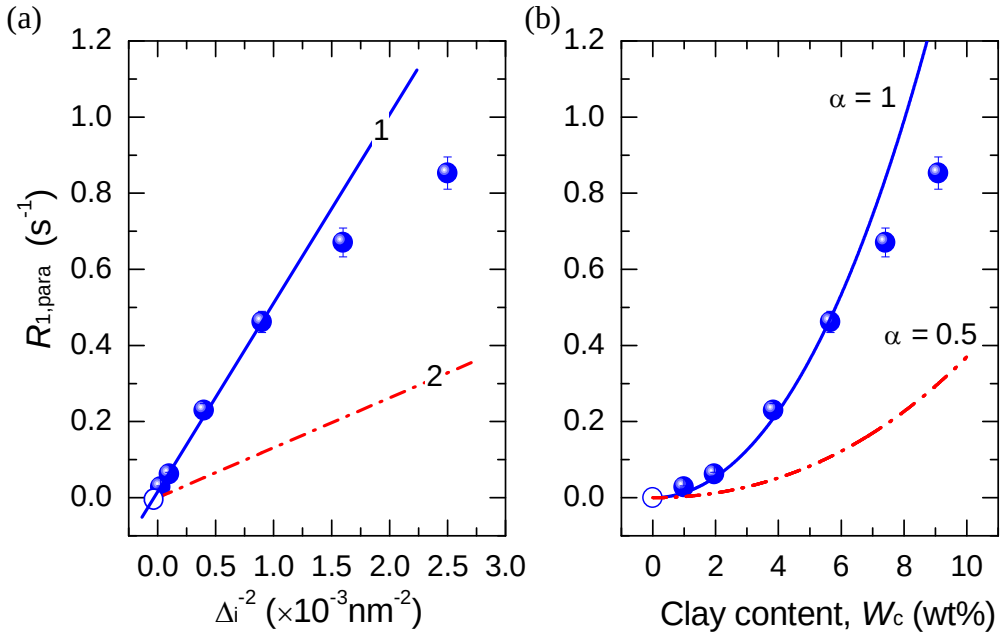

Figure 4.3. Paramagnetic contribution to the spin-lattice relaxation rate, $R_{1,para}$, versus (a) inverse ideal interparticle separation squared, Δ_i^{-2} (cf. eq 4.2), and (b) clay content, W_c (wt %) (cf. eq 4.3), for PVA/MMT nanocomposites with PVA/MMT weight ratio of 100/m where m = 1, 2, 4, 6, 8 and 10.[201] The MMT contains 3.5 wt% Fe^{3+} as Fe_2O_3. Relaxation rates were measured at 500 MHz. Numbers on lines denote average number of platelets/stack, N_{ps}. Solid line is (a) linear and (b) curvilinear fit through first four MMT concentrations; it represents fully exfoliated samples with N_{ps} = 1. Dot-dashed line in (a) was drawn by scaling its slope ($\propto \alpha^2$) by 1/4 (cf eq 4.15 or 4.16) and represents samples with N_{ps}= 2.

Now we turn to the scenario of the clay content dependence of $R_{1,para}$ in four series of PVA-MMT nanocomposites filled with four types of MMTs containing different Fe^{3+} concentrations. Three of them with higher Fe^{3+} concentrations were measured at 500 MHz by Asano et al.[201] while those with the lowest Fe^{3+} concentration were measured at

300 MHz. As described in the foregoing discussion, these PVA-MMT nanocomposites consist of well-exfoliated clay platelets or nanostructure with the basal spacing larger than 1.8 nm. Figure 4.4 shows that the experimental $R_{1,para}$ data in a certain series are well described by eq 4.16, except the two highest clay loadings. This indicates that, in a certain series samples show the similar dispersion. On the other hand, this result is to some degree consistent with XRD results on clay dispersion of all samples. Most importantly, our scaling model is in good accord with experimental $R_{1,\,para}$ values in these well-exfoliated PVA-MMT nanocomposites. This good match provides validation for our scaling model approach. In addition, these results also tell us that our scaling model can at least work for nanocomposites filled with MMT containing ≥ 1.2 wt% Fe_2O_3. Such MMT could produce fast relaxation of surface protons which can satisfy our assumption on the relaxation sink.

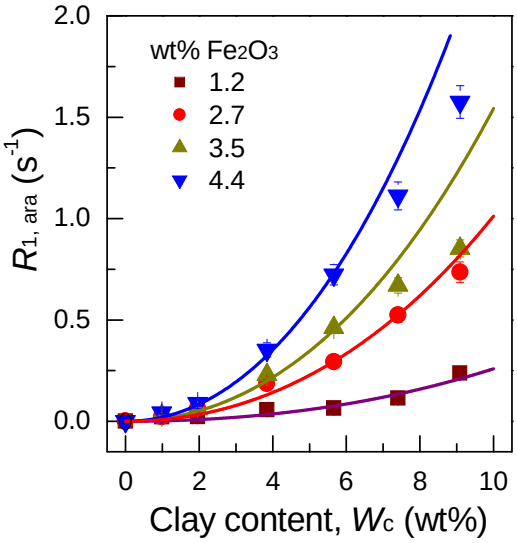

Figure 4.4. Paramagnetic contribution to the spin-lattice relaxation rate, $R_{1,\,para}$ as a function of clay content for poly(vinyl alcohol)/ montmorillonite (MMT) nanocomposites. These four series are filled with four types of MMTs containing the amounts of Fe^{3+} (as Fe_2O_3), 1.2 (PVA-MMT1.2, ■), 2.7(PVA-MMT2.7, ●), 3.5 (PVA-MMT3.5, ▲) and 4.4 wt% (PVA-MMT4.4, ▼). The simulated lines are calculated by eq 4.16.

4.3.3. Nylon 6/MMT Nanocomposites Prepared by Melt Compounding

In the following, we focus on an experimental data set for a technically relevant sample, nylon 6/MMT nanocomposites. The data for these samples exhibit trends far from the ideal scenario discussed above for poly(vinyl alcohol)/MMT nanocomposites; however, the samples are well characterized by various experimental methods. While XRD can be used to rapidly determine whether incorporated clay particles are exfoliated or not, statistical analysis of TEM images, costly in terms of time, can provide much more information. Such TEM data, along with NMR relaxation times, have been reported by van Es[117] and Bertmer et al.[41] for nylon 6/MMT nanocomposites with clay contents between 0.2 and 20 wt%. From their TEM data, they concluded that in the 5 wt% sample, "the majority of clay exists in groups consisting of two platelets still stuck together." [41] Thus, using this sample as the reference (platelets/stack = 2, $\alpha = 0.5$), we show $R_{1,para}$ versus Δ_i^{-2} in Figure 4.4. After calculating a reference line for the 5 wt % sample, lines marked 1, 3 and 4 were drawn with slopes ($\propto \alpha^2$) that are 4, 4/9, and 1/4 times the reference slope, respectively. From the plot it is directly revealed how the dispersion quality degrades with increasing clay concentration from full exfoliation at 1 wt % to larger particles with $N_{ps} > 3$ at 20 wt %. At 2.5 wt %, N_{ps} is about 1.5, entirely consistent with the reported analysis of TEM data that shows about half of the particles are fully exfoliated while the rest contain stacks of 2 − 3 platelets.[41,117]

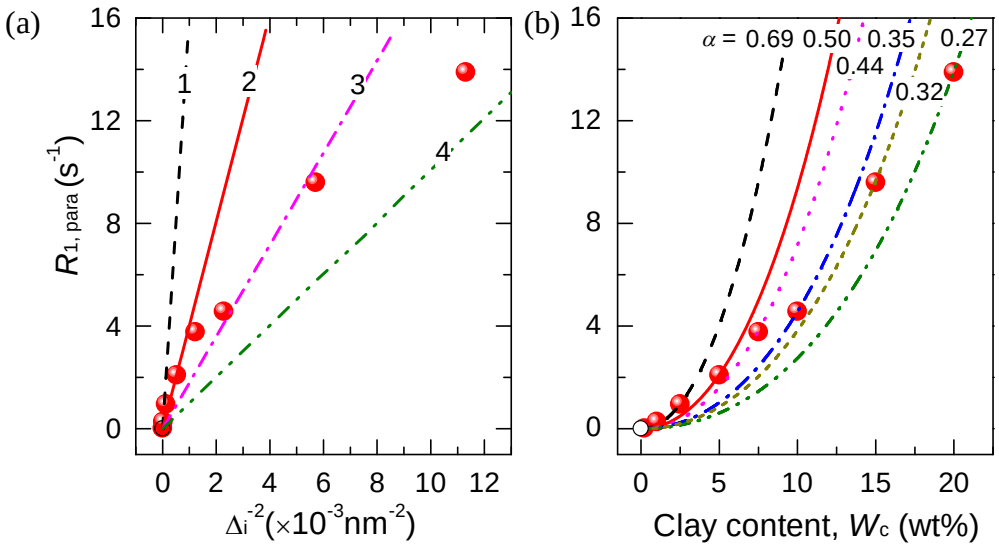

Figure 4.5. Paramagnetic contribution to the spin-lattice relaxation rate, $R_{1,para}$, versus (a) inverse ideal interparticle separation squared, Δ_i^{-2} (cf. eq 4.2), and (b) clay content W_c, for nylon 6/MMT nanocomposites with 0.2, 1, 2.5, 5, 7.5, 10, 15 and 20 wt % MMT containing Fe^{3+} (3.11 wt % as Fe_2O_3).[41,117] Relaxation times were measured at 500 MHz. Numbers on lines in (a) denote average number of platelets/stack, N_{ps}. The solid line (2) was chosen as the reference line for the 5 wt % sample since TEM data indicated the majority of clay particles consisted of 2 platelets/stack. Lines marked with 1, 3 and 4 were derived by scaling the slope ($\propto \alpha^2$) of the 2 line by 4, 4/9 and 1/4 (cf. eq 4.14), respectively. The α values in (b), which represent relative dispersion quality, were determined by matching individual data points to eq 4.16.

In Figure 4.5(b), $R_{1,para}$ is plotted versus W_c. Curves are calculated for each clay content $\geq$ 2.5 wt% MMT using eq 4.15. The KA values in eq 4.16 can be directly obtained from these predictions of the curves. As clay content increases, KA ($\propto \alpha^2$) values, which reflect the relative quality of clay dispersion, decrease. In using the 5 wt % sample as a reference for which we know contains predominantly 2 platelets/stack (α = 0.5), we can use the KA values to quantify the dispersion quality for all samples: $\alpha = (A/A_{ref})^{1/2}\alpha_{ref}$, where α_{ref} = 0.5. These α values are plotted in Figure 4.6 versus clay content. The most dilute samples (0.2 and 1 wt % MMT) are defined to have α = 1 since TEM indicates complete exfoliation and these samples do not satisfy the requirements of

the model, namely that the spin diffusion length, $(5T_{1,PCN}D_s)^{1/2}$, is greater than half the interparticle separation. For these two samples, the spin diffusion lengths are calculated using D_s = 0.7 nm^2/ms to be 74 and 63 nm, respectively, which are much smaller than half the calculated Δ_i (cf. eq 4.2) or reported Δ_{TEM} values. For the most concentrated systems, for example 15 and 20 wt%, surfactants in commercial MMT (38 wt%, or > 9 wt% of the PCN) may alter the relaxation behavior of the bulk polymer too much from that of the neat polymer for eq 4.11 to yield sufficiently accurate $R_{1,para}$ values.

Figure 4.6 shows that clay dispersion decreases with increasing clay content. This plot was constructed from the assumption that the paramagnetic contribution to the spin-lattice relaxation rate ($R_{1,para}$) is indirectly proportional to the average interparticle separation squared. Conversely, Bertmer et al.[41] claimed that $R_{1,para}$ is directly proportional to the surface-to-volume ratio of clay to polymer. Their assumption led to the appearance that dispersion quality slightly improved with increasing clay content (Figure 2 in reference[41]). In contrast, VanderHart et al.[44] showed that surface-to-volume ratios of clay to polymer are directly proportional to initial slopes of relaxation recovery curves. Since these initial slopes of relaxation recovery curves yield surface-to-volume ratios of clay to polymer they will also provide degrees of exfoliation.[42,44,146] Paramagnetic contributions to the overall spin-lattice relaxation rate provide information on the overall dispersion quality, which depends on both degree of exfoliation and distribution homogeneity. It is worthy of note that, for high clay content or small interparticle spacing, $R_{1,para}$ could be partially from the contribution of the relaxation-controlled region. In this region, nuclei exhibit faster relaxation due to the direct electron-nucleus interaction (see Chapter 6), when compared to the bulk nuclei in the diffusion-

controlled region. Thus, by using our scaling model focusing on the diffusion-controlled region, the calculated interparticle spacing in nanocomposites containing high content of clay apparently become smaller, which leads to overestimation of clay dispersion (e.g., 15 wt% and 20 wt% in Figures 4.5a and 4.6).

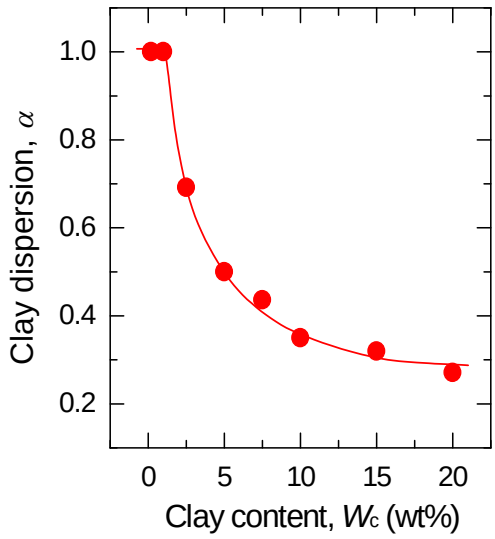

Figure 4.6. Clay dispersion, α, versus clay content, W_c, for nylon 6/MMT nanocomposites with 0.2, 1, 2.5, 5, 7.5, 10, 15 and 20 wt % MMT containing Fe^{3+} (3.11 wt % as Fe_2O_3) as extracted from the calculation in Figure 4.5.[41] The most dilute samples (0.2 and 1 wt% MMT) are defined to have $\alpha = 1$ since TEM shows that these samples are completely exfoliated.[41,117]

4.3.4. Poly(ε-caprolactone)/MMT Nanocomposites with Different Chemically Modified MMTs Prepared by Melt Compounding

Experimentally and theoretically, clay dispersion in PCNs is dependent not only upon clay content (e.g., Section 4.4.3) but also upon processing conditions (e.g., Chapter 2) and type of clay, clay surface modification and polymer characteristics. In our model, the change of clay dispersion can be monitored by the prefactor, K*A* in eq 4.16. In this section, we compare clay dispersion in poly(ε-caprolactone) (PCL)/MMT

nanocomposites with two different MMTs prepared by melt compounding. Lepoittevin et al.[60] reported the details about preparation and characterization of PCL nanocomposites filled with Cloisite 25A and Cloisite 30B. These two organically modified MMTs contain dimethyl-2-ethylhexyl ammonium cation (Cloisite 25A) and methyl bis(2-hydroxyethyl) ammonium cation, respectively (Cloisite 30B) (both from Southern Clay Products, Inc. TX). Fe^{3+} (as Fe_2O_3) concentrations in Cloisite 25A and Cloisite 30B are 3.14 wt% and 3.51 wt%, respectively. In considering the content of surface ammonium cation (Cloisite 25A: 34 wt%; Cloisite 30B: 30 wt%), the corresponding pure silicates marked by MMT_25A and MMT_30B, contain 5.17 wt% and 5.01 wt% Fe_2O_3, respectively. The resulting nanocomposites are designated as PCL_M25A for the former and PCL_M30B for the latter. Calberg et al.[43] measured proton relaxation times of these nanocomposites at 400MHz.

Due to the Fe^{3+} concentration dependence of $R_{1,\,para}$, it is impossible to compare clay dispersion in PCL_M25A and PCL_M30B directly using clay dispersion descriptors, K*A* or the scaled α in our model. For instance, K is partially dependent on the Fe^{3+} concentration. In Chapter 5, we will present our finding on the Fe^{3+} concentration (C_{Fe}) dependence of $R_{1,\,para} \propto C_{Fe}^{1.9}$. For a convenient comparison to PCL_M25A, we correct $R_{1,para}$ of PCL_M30B by multiplying $[(C_{Fe})_{MMT\_25A} / (C_{Fe})_{MMT\_30A}]^{1.90} = (5.17 / 5.01)^{1.90}$. In doing so, we can compare clay dispersion from $R_{1,para}$ under the same influence of C_{Fe}.

Figure 4.7 shows $R_{1,\,para}$ of PCL_M25A and the corrected $R_{1,\,para}$ of PCL_M30B as a function of clay content. It should be noted that the before C_{Fe} correction, PCL_M30B exhibits larger $R_{1,\,para}$ than PCL_M25A. Calberg et al.[43]attributed this to the higher C_{Fe} in MMT_30B than MMT_25A. In fact, we should consider Fe^{3+} concentration

in the pure silicate of organoclay. As discussed before, C_{Fe} in the pure silicate of MMT_30B is lower than that of MMT_25A. After C_{Fe} correction, PCL_M30B exhibits larger $R_{1,\ para}$. This result clearly suggests a better dispersion in PCL_M30B. This observation could be explained with respect to the interfacial interaction between PCL and clay. The modifier of MMT_30B contains hydrophilic hydroxyl groups that facilitate the access of PCL chains to silicate surface. These are helpful to exfoliate clay particles into PCL matrix. In contrast, hydrophobic modifiers with long alkyl chains cover the surface of MMT_25A, which hampers the interaction between PCL and silicates.[43,60] Hence, PCL_M25A shows a poorer dispersion.

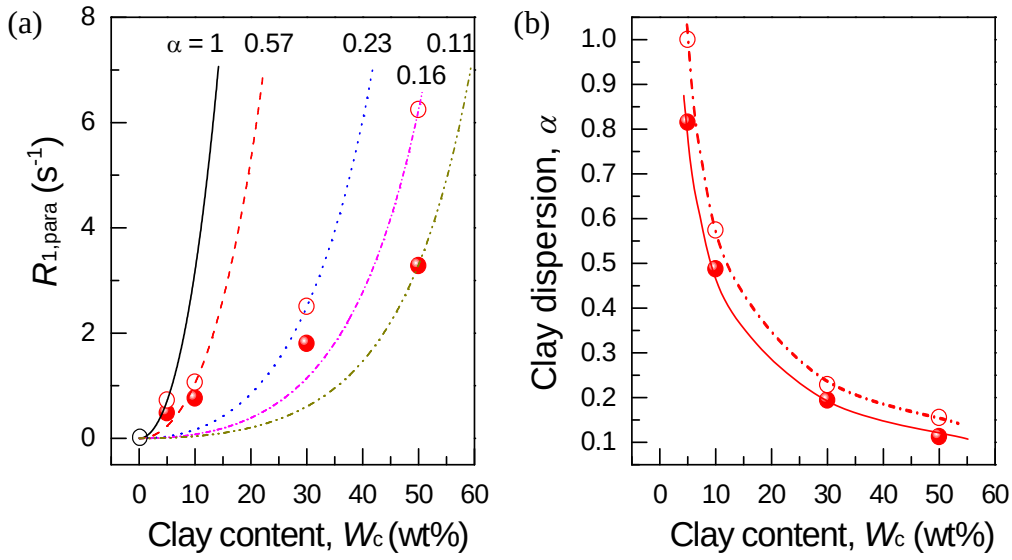

Figure 4.7. Paramagnetic contribution to the spin-lattice relaxation rate, $R_{1,\ para}$ and the relative quality of clay dispersion as a function of clay content in poly(ε-caprolactone)/clay nanocomposites prepared by melt compounding. (a) Comparison of $R_{1,\ para}$ of PCL_M25A (●) and corrected R_{para} of PCL_M30B (○). The lines are calculated using eq 4.16. (b) Relative quality of clay dispersion as extracted from (a). The α values in (b), which represent relative dispersion quality, were determined by matching individual data points to eq 4.16. PCL_M30B containing 5 wt% MMT was chosen as a reference and its quality of clay dispersion was arbitrarily defined as α = 1 since XRD indicates that this sample shows the best dispersion in these samples.

Using eq 4.16, we calculate the curves through each individual experimental point and zero (see Figure 4.7a). PCL_M30B containing 5 wt% MMT was chosen as a reference and its quality of clay dispersion was arbitrarily defined as α = 1. Using the calculated K*A* values of the curves in Figure 4.7(a) and following the procedure in Figure 4.6, we can quantitatively describe the quality of clay dispersion as a function of clay content. PCL_M30B with 5 wt% MMT_30B is chosen as a reference material, in which the quality of dispersion is arbitrarily defined as α_{ref} = 1, since XRD indicates that this sample shows the best dispersion in these samples. α values for PCL-MMT nanocomposites are shown as a function of clay content in Figure 4.7(b). It can be seen that clay dispersion becomes worse quickly with increasing clay content. The quality levels off until 50 wt% silicates. PCL_M30B samples show better dispersion than PCL_M25A samples, in particular at low clay contents. Hence, MMT_30B could be more easily exfoliated than MMT_25A when mixed with PCL melts. Clearly, our scaling model is demonstrated in comparing clay dispersion in nanocomposites filled with different organically modified clay particles.

4.3.5. Poly(lactic acid)/MMT Nanocomposites with Different Molecular Weight Matrices

In this section, effects of polymer characteristics on clay dispersion will be investigated using our model. Polylactic acid (PLA)/MMT nanocomposite (PLA-MMT) cast films were prepared using two types of PLAs: high molecular weight (HMW PLA) and low molecular weight (LMW PLA). NMR relaxation times of these cast-films were measured in a magnetic field of 0.54 T (23 MHz). Figure 4.8(a) shows that $R_{1,\,para}$ of

PLA-MMT nanocomposites increases with addition of MMT. HMW PLA nanocomposites increase faster than LMW PLA nanocomposites at 2.51 and 3.84 wt% MMT. It suggests that the former exhibits a better dispersion of MMT than the latter.

However, XRD curves of both systems hardly provide such information (see Appendix A). XRD patterns display no basal reflection at 1.30 wt% MMT and a weak bump at ~ 5.5°. A broad peak at 2.8° is present at the higher MMT contents, corresponding to a basal spacing of 3.2 nm. Taking into account the base spacing of 1.85 nm in MMT_30B, these features of XRD patterns indicates that PLA nanocomposites exhibit intercalated/exfoliated structures. The basal peak becomes sharper with increasing MMT content up to 3.84 wt%, indicating that highly ordered clay particles present at high clay contents. However, both systems show very similar XRD patterns.

On the other hand, our NMR results indicate that the MMT platelets are better dispersed in HMW PLA than LMW PLA. This observation can be attributed to effects of matrix molecular weight on clay exfoliation. XRD and TEM as well as mechanical properties and rheological measurements observed by Paul et al.[84,116] indicate that HMW nylon 6 nanocomposites exhibit higher clay exfoliation than LMW ones. They attributed this observation to a higher melt viscosity in the HMW system, which leads to more effective stress transfer from polymer to clay particles. The transfer of shear stress from polymer to clay was believed to shear the particles into smaller stacks and peel platelets apart.[84,116]

The relative degree of clay dispersion in both PLA nanocomposite series was extracted following the method used in nanocomposites discussed before. For a semi-quantitative analysis, the reference material is chosen as the nanocomposite containing

1.3 wt% MMT. This reference is arbitrarily assumed to have α = 1, since the same $R_{1,\,para}$ is observed in these two systems at 1.3 wt% MMT. Figure 4.8(b) shows the relative α values. The quality of clay dispersion in both systems decreases as increasing MMT content, which is to some degree consistent with XRD results. Within the experimental error, Figure 4.8(b) indicates that a degree of exfoliation in the HMW PLA nanocomposites is higher than the LMW PLA samples.

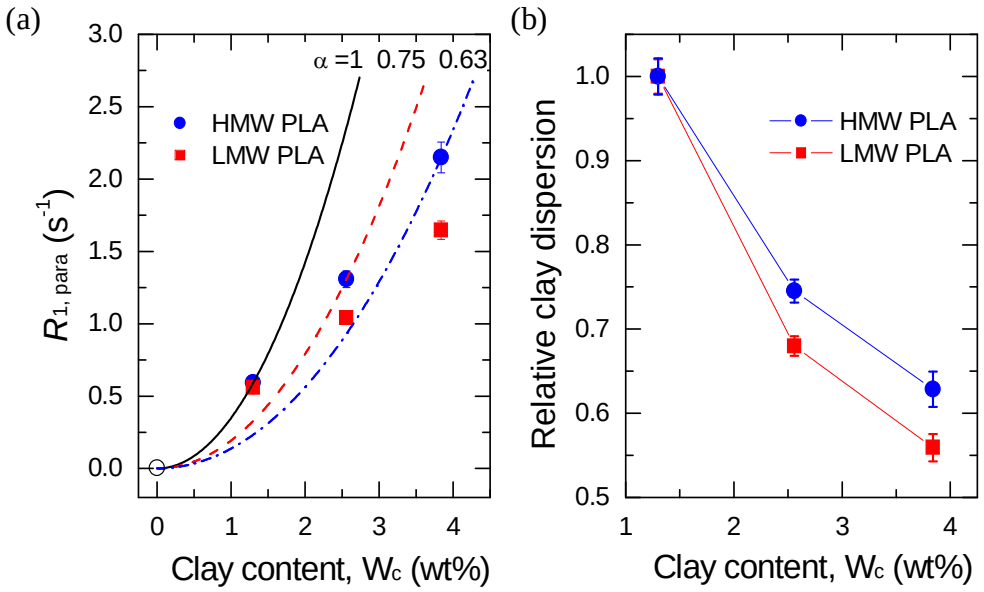

Figure 4.8. Comparison of clay dispersion in poly(lactic acid)/MMT (PLA-MMT) nanocomposites as cast films using $R_{1,para}$. (a) $R_{1,para}$, versus clay content W_c. The lines were calculated using eq 4.16. The relative quality, $\alpha = [KA/(KA)_{ref}]^{1/2}\ \alpha_{ref}$, where $\alpha_{ref} = 1$ for the sample containing 1.3 wt% MMT as a reference material. (b) The relative quality of clay dispersion for two series of LMW PLA and HMW PLA nanocomposites. Relaxation times were measured at 23 MHz.

4.3.6. Polypropylene/MMT Nanocomposites

Figure 4.9 shows that increasing MMT content in polypropylene nanocomposites leads to decreasing dispersion quality (aggregation/heterogeneity). XRD patterns of PP-MMT nanocomposites (see Appendix A) show that the intensity of the basal peak

increases with an increase of clay content. A reference material, PP-MMT nanocomposite containing 2.7 wt% MMT (PP-MMT2.7) has f = 0.38 (see Chapter 2), which was obtained from TEM data. Using $\alpha = f = 0.38$ in PP-MMT2.7, the value of α for each content was determined following the method used for Figure 4.6.

Nanocomposite containing 5.51 wt% MMT (PP-MMT5.5) shows $\alpha = 0.28 \pm 0.02$, which is lower than the TEM-scaled NMR value, $f = 0.44$ (± 0.09) from the initial slope measured at 300 MHz (see Chapter 6). As discussed before, α reflects an overall quality of clay dispersion reflecting both of clay exfoliation and distribution, whereas f reflects the degree of exfoliation converted from the interfacial surface area. The heterogeneous dispersion contributes to lower α than the degree of exfoliation in PP-MMT5.5. Thus, these results indicate that PP-MMT5.51 exhibits heterogeneous dispersion. The dilute samples apparently show higher quality of clay dispersion, although these samples could not fit our model.

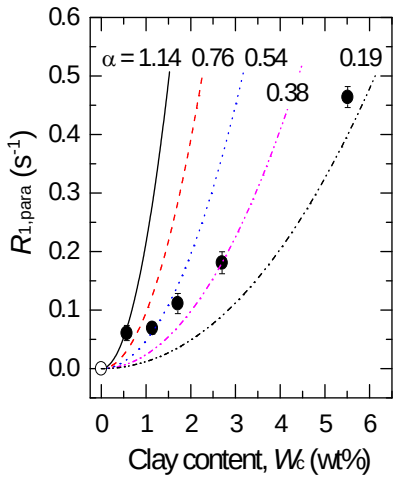

Figure 4.9. Paramagnetic contribution to the spin-lattice relaxation rate, $R_{1,para}$ vs clay content in polypropylene/MMT nanocomposites. The line at 2.7 wt% MMT is calculated to give KA_0 using eq 4.16. Lines were drawn to represent the quality of clay dispersion α, by scaling their KA values with KA_0 of a reference with 2.7 wt% MMT. The reference shows α = 0.38, obtained from TEM data.

4.3.7. Comparison of Clay Morphology from Initial Slope and Relaxation Time

From the foregoing discussions, we gain information on clay morphology in polymer nanocomposites from the spin-lattice relaxation behavior: the initial relaxation (Chapters 2 and 3) and $R_{1,\,para}$. The former is related to the degree of exfoliation by the effective interfacial area between polymer and clay particles, while the latter is with regard to overall quality of clay dispersion including the degree of exfoliation and clay distribution In this section, we will compare these two methods for characterizing clay morphology in PVA-MMT, PP-MMT and PLA-MMT nanocomposites.

Figure 4.10 shows initial slopes and relaxation times as a function of clay content in PVA-MMT1.2 films measured at 300 MHz. These PVA-MMT1.2 samples were prepared by the solution-intercalation film-casting method as described by other researchers.[73] Figure 4.10(c) and (d) summarize the results from initial slopes in (a) and $R_{1,\,para}$ in (b), respectively. The initial slopes increase linearly with an increase of clay content, suggesting that the degree of exfoliation is same for all these samples (see Chapter 3). As shown in Figure 4.4, $R_{1,para}$ values of PVA-MMT1.2 increase with clay content described by eq 4.16. In another way, Figure 4.10(d) indicates that $R_{1,para}$ increases almost linearly with inverse ideal interparticle separation squared, Δ_i^{-2} (c.f. eq 4.14). $R_{1,para}$ results reveal that the quality of clay dispersion is similar in PVA-MMT1.2 nanocomposites. In this case, both methods reach the same conclusion on clay morphology, although they are based on different aspects of clay morphology. This consistence could be attributed to the similar clay dispersion including exfoliation and distribution in all PVA-MMT1.2 samples.

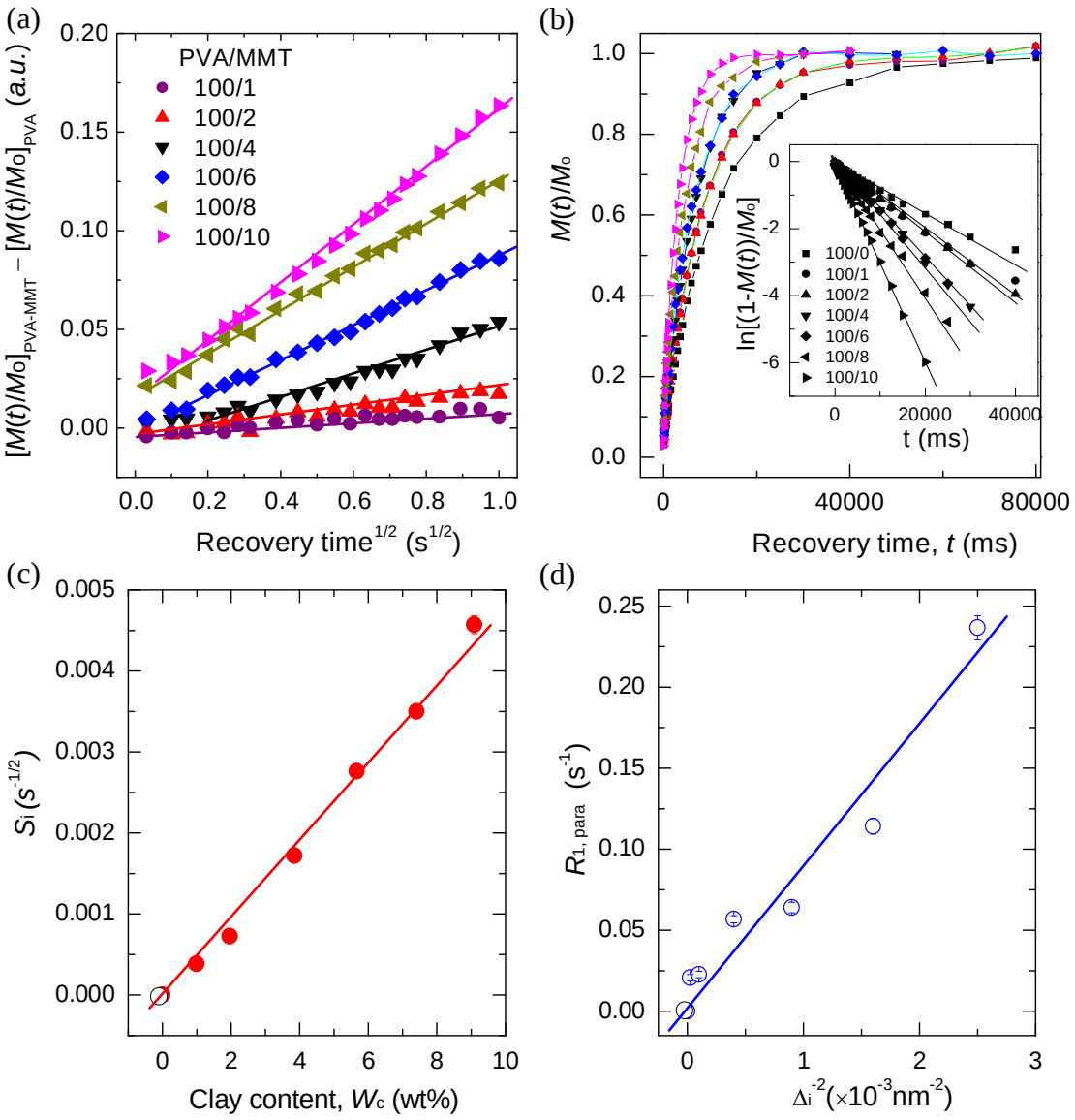

Figure 4.10. Relaxation behavior of initial slopes and relaxation times as a function of clay content in poly(vinyl alcohol)/montmorillonite (PVA-MMT1.2) nanocomposites films, measured at 300 MHz. (a) Normalized and corrected magnetization, $[M(t)/M_o]_{PVA\text{-}MMT} - [M(t)/M_o]_{PVA}$, versus the square root of recovery time. Weight ratios of PVA/MMT from 100/1 to 100/10, The experimental data are vertically displaced to prevent overlap. Lines are linear least-square fits. (b) Normalized magnetization, $M(t)/M_o$, versus recovery time. The inset in (b) displays the same data plotted as $\ln[1 - M(t)/M_o]$ versus recovery time, the slopes of which reflect the inverse T_1s. (c) slopes of lines in (a), S_i vs clay content. (d) Paramagnetic contribution to the spin-lattice relaxation rate, $R_{1,para}$ versus inverse ideal interparticle separation squared, Δ_i^{-2} (cf. eq 4.2).

Different from PVA nanocomposites with well exfoliated and dispersed clay, some nanocomposites prepared by melt compounding could exhibit more complicated clay morphology. In the following, we investigate two different systems prepared by melt compounding. Results for PP-MMT nanocomposites treated by different processes are shown in Figure 4.11. For PP-MMT pellets, initial slopes for PP-MMT nanocomposites with 1.14, 1.70 and 2.7 wt% MMT are almost on the line 2, which indicates $N_{p,eff} = 2$. The most dilute sample is on the line 1, suggestive of full exfoliation, namely, $f = 1$. PP-MMT5.51 shows slight lower degree of exfoliation than $f = 1/ N_{p,eff} = 1/2 = 0.5$. The quality of clay dispersion from $R_{1,para}$ shown in Figure 4.11(b) is $\alpha = 1/ N_{p,eff} = 1/2 = 0.5$ for PP-MMT1.14, PP-MMT1.7 and PP-MMT2.7. The same value, $\alpha = f$ indicates the similar clay distribution in these three samples. Similar to Section 4.4.6, $\alpha < f$ suggests that clay distribution in PP-MMT5.5 is quite inhomogeneous. PP/MMT nanocomposites prepared by melt compounding are often observed to exhibit inhomogeneous dispersion.[95,127,203-205]

Interestingly, the PP-MMT2.7 film (□) with the stretch ratio of $\lambda = 3.5$ shows smaller $N_{p,eff}$ (= 1.3) from surface area than $N_{p,eff}$ (= 2) from interparticle spacing; in other words, $f > \alpha$. Following the foregoing discussion, this result definitely indicates that the clay distribution contributes to the quality of dispersion, α. As shown in Figure 2.4, the $R_{1,para}$ values tends to level off after $\lambda = 2.5$, which suggests that the quality of dispersion is leveling off; that is, the interparticle spacing keeps constant. However, the increase of initial slopes indicates an increase of degree of exfoliation with the stretch ratio (see Figure 2.3). In such a case, the method of $R_{1,para}$ could be not effective enough to observe sliding apart of platelets in PCNs where interparticle spacing has no change. Therefore,

we can contribute the new surface area to sliding apart of platelets as we did in Chapter 2 (see Figure 2.7). For such a case, combination of these two methods will help to better understand the evolution of clay morphology in PCNs.

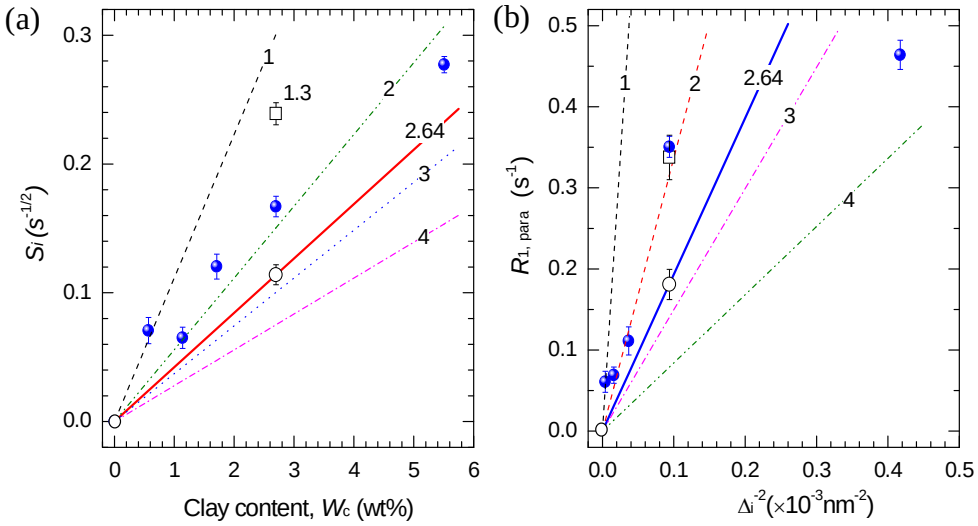

Figure 4.11. Comparison of dispersion descriptors, S_i vs clay content (a) and $R_{1,para}$ vs Δ_i^{-2} (b) in PP-MMT nanocomposite pellets (●), a compression-molded PP-MMT nanocomposite sheets (○) and the PP-MMT2.7 film (□) with the stretch ratio of λ = 3.5 (shown in Figure 2.3). PP-MMT nanocomposite sheets with 2.7 wt% MMT is defined as a reference with $N_{p,eff}$ = 2.64, obtained from TEM data. The solid lines through PP-MMT2.7 and zero were used to scale other lines with the numbers indicating average number of platelets/stack, N_{ps}. The slopes of lines in (a) were scaled by $S_i = (S_i)_{ref} \times (N_{p,eff})_{ref} / N_{ps}$, while the lines in (b) were drawn by scaling its slope ($\propto \alpha^2$) by $[(N_{p,eff})_{ref} / N_{ps}]^2$. The numbers on lines $N_{ps} = 1/\alpha$, which can be compared with N_{ps} from initial slopes in (a). All relaxation data were measured at 300 MHz.

PP-MMT2.7 pellets show $f = \alpha$, indicating that there is homogeneous clay distribution in this sample. After compression molded, $N_{p,eff}$ (or smaller particle size) of PP-MMT2.7 sheet increases in both plots. This result suggests that the compression molding changes clay dispersion. There are two possibilities contributing to this observation. One is about the collapsed interlayer spacing (d_{001}) produced by degradation

of surfactants and the resulting de-intercalation of polymer chains when PP-MMT2.7 pellets experience compression molding. Another is associated with the re-clustering of clay particles. Contrary to PP-MMT2.7 films by biaxially stretching, the platelets peeled off by shear stress during extrusion could reunite into the original particles. This leads to a decrease of surfaces area.

Figure 4.12 shows comparison of exfoliation from S_i vs W_c, and the quality of dispersion from $R_{1,para}$ vs Δ_i^{-2} for a series of HMW PLA/MMT nanocomposites as cast films. The initial slope increases almost linearly with an increase of clay content (Figure 4.12a). This result indicates that the degree of clay exfoliation is almost the same except the sample with the highest clay content showing slightly low exfoliation. On the other hand, the quality of clay dispersion obviously become worse with increasing clay content (Figure 4.12b), reflected by the downward curvature of $R_{1,para}$ vs Δ_i^{-2}. Taking the same exfoliation into account, this downward curvature is attributed to clay distribution becoming poorer as an increase of clay content.

Figure 4.13 schematically depicts a nanocomposite having stacks consisting of one, two, or three platelets for illustrating relationships between clay dispersion and NMR observables we proposed above. High exfoliation provides large interfacial surface area, small interparticle spacing and small thickness of particles (or fewer platelets per stack). Correspondingly, NMR observes large initial slopes and high $R_{1,para}$. The above arguments are based on the homogeneous distribution of particles. For heterogeneous systems, the quantitative information on clay morphology from the degree of exfoliation obtained from initial slopes could not be consistent with that from quality of dispersion obtained from $R_{1,para}$. The former of NMR descriptors is sensitive to clay exfoliation,

whereas the latter is sensitive to exfoliation and distribution. In order to gain a whole picture of clay dispersion, both NMR descriptors should be comparably considered.

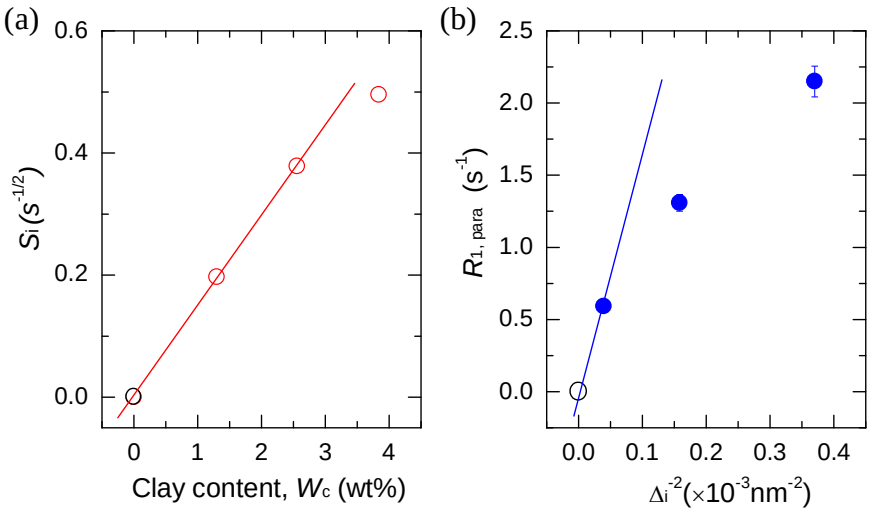

Figure 4.12. Comparison of dispersion by S_i vs W_c (a) and $R_{1,para}$ vs Δ_i^{-2} (b) in a series of PLA4-MMT nanocomposites as cast-films. All relaxation data were measured at 23 MHz. The lines were drawn through the first data point and zero.

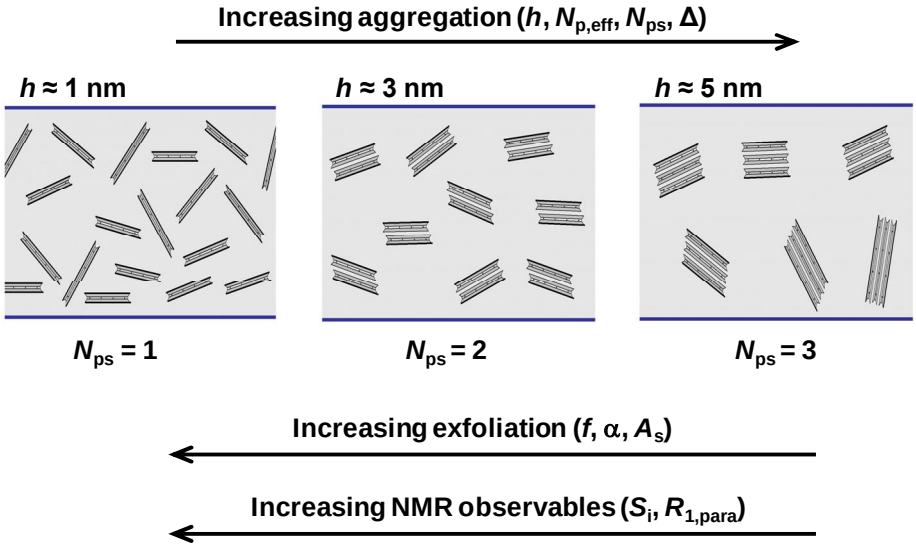

Figure 4.13. Schematic illustration of the relationship between morphological descriptors (particle thickness, h; average number of platelets/stack, N_{ps}; effective number of paramagnetic centers, $N_{p,eff}$; interfacial surface area, A_s; interparticle spacing, Δ; exfoliation, f; quality of dispersion, α) and NMR observables (initial slopes, S_i; paramagnetic relaxation rate, $R_{1,para}$).

4.4. Conclusions

A lamella based model was developed for describing NMR longitudinal relaxation in polymer nanocomposites filled with paramagnetic clay. From an analytical solution of the model, the paramagnetic contribution to the relaxation rate, $R_{1,para}$ was found to be inversely proportional to the square of the interparticle spacing and directly proportional to a function of the weight fraction squared, namely, $R_{1,para} \propto W_c^2/(1- W_c)^2$. We defined a relative measure of clay dispersion, α, as the ratio of idealized interparticle separation to the real separation, and showed how α can be determined by scaling parameters found by calculating curves for $R_{1,para}$ versus clay content. The scaling depends on knowledge of the clay dispersion in at least one sample determined from an independent measurement such as TEM. Also, the proportionality of $R_{1,para} \propto W_c^2/(1- W_c)^2$ was also developed to semi-qualitatively observe evolution of clay dispersion as a function of clay content. The model and scaling relations were validated by comparison with data obtained for four series of well exfoliated poly(vinyl alcohol)/montmorillonite (PVA/MMT) nanocomposites, and for a series of nylon 6/MMT nanocomposites.

Applications of our model and scaling relations have been further developed to investigate three different nanocomposites: poly(ε-caprolactone)/MMT (PCL/MMT) nanocomposites filled with two different chemically modified MMTs, Cloisite 25A and Cloisite 30B; poly(lactic acid)/MMT (PLA/MMT) nanocomposites with two different molecular weight PLAs and polypropylene/MMT (PP/MMT) nanocomposites with different thermal treatments. The quality of dispersion from our model in PCL/MMT nanocomposites suggests that the more polar surfactant benefits clay dispersion in PCL.

Observations in PLA/MMT nanocomposites reveal that increasing PLA molecular weight leads to higher quality of clay dispersion.

Comparison of clay morphology gained from the initial slopes and relaxation rate has been systematically carried out in three different types of polymer/clay nanocomposites. The initial slope is related to the interfacial surface area and the resulting degree of exfoliation, and $R_{1,para}$ is related to average interparticle spacing and the resulting quality of dispersion. The two NMR observables show the same clay dispersion in the well exfoliated and dispersed PVA/MMT nanocomposites. Thermal treatments change the degree of exfoliation and the quality of dispersion in PP-MMT nanocomposite. $R_{1,para}$ reveals the heterogeneity in PLA-MMT nanocomposites with the same exfoliation. Combining these two NMR descriptors is believed to offer a whole picture of clay morphology in paramagnetic polymer/clay nanocomposites.

CHAPTER 5

Impurity Concentration Dependence of Paramagnetic Contribution to Spin-lattice Relaxation Rate

5.1. Introduction

Solid-state NMR paramagnetic relaxation enhancement (PRE) has been applied for structure elucidation and morphology detection in macromolecular systems.[196,199,206] The PRE originates from direct dipolar interactions of the unpaired electrons from paramagnetic centers with neighboring nuclei. A paramagnetic center changes the appearance of NMR spectra in several ways, most often via chemical shifts, line-broadening and relaxation rates. In static solids, the PRE effect rapidly builds up magnetization gradients around paramagnetic centers immediately following spin saturation of the sample. The PRE effect can thus be propagated to the remote nuclei by spin diffusion. This leads to a spin-diffusion-averaged T_1, which is shorter than that of the pristine polymer. The enhancement in the relaxation rate is defined as the paramagnetic contribution to the relaxation rate, $R_{1,para}$. The spin-diffusion-averaged PRE, $R_{1,para}$ could be employed to detect morphology of nanostructures.[41-42,44,146,200] For example, $R_{1,para}$ is larger in polymeric nanocomposites with good dispersion of clay particles when compared to that with poor dispersion or the unfilled polymer (see Chapters 2 & 4).

$R_{1,para}$ has been analytically related to dispersion of naturally Fe^{3+} doped clay and applied to quantitatively measure dispersion quality in Chapter 4. We found that $R_{1,para} = KAW_c^2/(1- W_c)^2$ (e.g., eq 4.16), where W_c is the weight content of clay, and the prefactor K*A* is dependent not only on clay dispersion but also on the magnetic fields (Chapter 6) and impurity concentration (C_{Fe}) (Figure 4.4). At a specific field and certain clay, K*A* can be related to clay dispersion, which has been applied to investigate several different nanocomposites. However, as illustrated in Figure 4.4, MMT containing different C_{Fe} (e.g., 1.2, 2.7, 3.5 and 4.4 wt%) provides different values of K*A* in PVA/MMT nanocomposites. The different values of K*A* are due to different C_{Fe} rather than clay dispersion. Thus, $R_{1,para}$ cannot be used to directly compare clay dispersion in nanocomposites filled with MMT containing different C_{Fe}. What is missing is that the relationship between $R_{1,para}$ and C_{Fe} is unknown. In this Chapter, we report the impurity-concentration dependence of the spin-diffusion averaged PRE. $R_{1,para}$. It will extend $R_{1,para}$ to quantify clay dispersion in nanocomposites filled with different types of clay.

5.2. Experimental

NMR measurements were conducted on a Bruker DSX 300 as described in Chapter 4.3. The preparation of poly(vinyl alcohol) nanocomposites filled with MMT containing 1.2 wt% Fe_2O_3 was described in Chapter 4.3. These samples were prepared by solution intercalation.

5.3. NMR results

Similar to Figures 4.3(a), Figure 5.1(a) shows $R_{1,para}$ versus Δ_i^{-2}, for six poly(vinyl alcohol) (PVA)/MMT nanocomposites (4.4 wt% Fe_2O_3 in the MMT). Solid line 1 was linear fit through the first four data points as well as zero, which presents clay morphology depicted in Figure 5.1(b). The samples on line 1 are believed to be well exfoliated and dispersed. The lines 2 and 3 scaled by 1/4 and 1/9– fold slope of line 1, imply states of clay dispersion: average two and three platelets per stack (Figure 5.1c and d), respectively. The data points of PVA-MMT4.4 are away from line 2 and line 3. These observations provide evidence that there are well exfoliated and dispersed clay particles in PVA-MMT4.4 samples, similar to PVA-MMT3.5 shown in Figure 4.3.

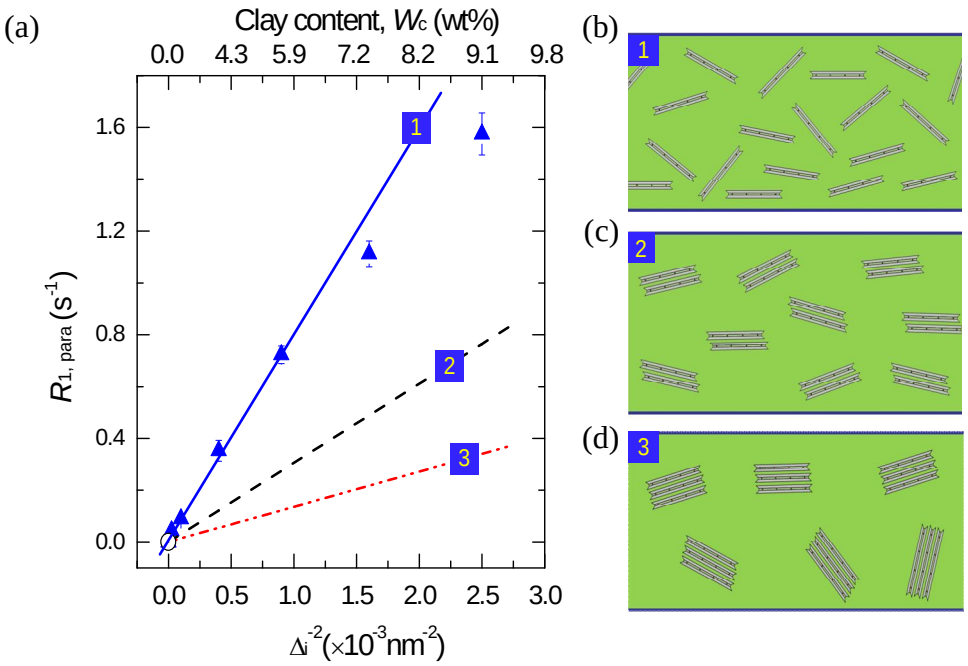

Figure 5.1. (a) Paramagnetic contribution to the spin-lattice relaxation rate, $R_{1,para}$, versus (a) inverse ideal interparticle separation squared, Δ_i^{-2}, for a series of PVA/MMT nanocomposites filled with MMT containing 4.4 wt% Fe^{3+} (as Fe_2O_3). Relaxation rates were measured at 500 MHz. Numbers on lines denote average number of platelets/stack, N_{ps}. Line 1 is linear fit trough first four MMT concentrations. Dashed and dot-dashed

lines in (a) were drawn by scaling its slope ($\propto \alpha^2$) by 1/4 and 1/9 (cf eq 4.14) and represents samples with N_{ps} = 2 and 3, respectively. (b), (c), (d) Schematic illustrations of three nanostructures: N_{ps} = 1 (b), 2 (c) and 3 (d) corresponding to the lines 1, 2 and 3 in (a), respectively.

Figure 5.2(a) shows that the $R_{1,\,para}$ is a function of Δ_i^{-2} for four series of PVA-MMT nanocomposites. Following the discussions in Figure 5.2(a), we argue that all PVA-MMT nanocomposites show the similar clay morphology containing well exfoliated and dispersed clay particles. As such, different values of $R_{1,\,para}$ between different series should be due to different C_{Fe} rather than due to the change of clay dispersion. It can be seen that higher impurity concentration produces larger $R_{1,\,para}$. All solid lines are fitted by the first four samples for each series as shown in Figure 5.2(a). Figure 5.2(b) depicts the logarithmic relationship between the slopes of these lines and C_{Fe}, indicating that $R_{1,para}$ is proportional to $C_{Fe}{}^{\beta}$, where $\beta = 1.90 \pm 0.08$.

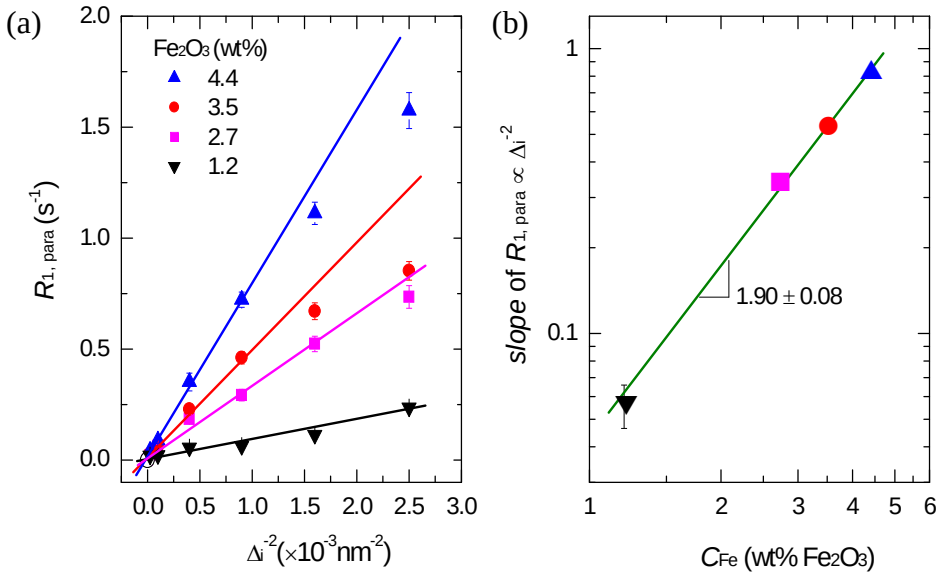

Figure 5.2. Impurity concentration (C_{Fe}) dependences of $R_{1,para}$ for PVA/MMT nanocomposites filled with four types of MMTs containing the amounts of Fe^{3+} (as wt% Fe_2O_3), 1.2(PVA-MMT1.2), 2.7(PVA-MMT2.7), 3.5(PVA-MMT.35) and 4.4 wt% (PVA-MMT4.4). (a) $R_{1,para}$ vs Δ_i^{-2}. (b) Slopes of $R_{para} \propto \Delta_i^{-2}$ shown in the lines in (a). This

slope value increases with increasing C_{Fe} by the power of β = 1.90 (± 0.08). These three series of PVA-MMT2.7, 3.5 and 4.4 give $R_{para} \propto C_{Fe}^{1.86 \pm 0.06}$ ($R^2 > 0.99$). Note that for 1.2 wt% Fe_2O_3, R_{para} was obtained under a magnetic field of 7.05 T, while others were measured at an 11.74 T magnetic field.

Figure 5.3(a) shows the prefactor K*A* values obtained in Figure 4.4 as a function of C_{Fe}. The exponent, β is calculated to be 1.88 ± 0.09, consistent with the β value in Figure 5.2(b) within fitting error. For samples of the weight ratio of PVA/MMT =100/6, $R_{1,para}$ increases linearly on a logarithmic scale with the concentration of Fe^{3+} (Figure 5.3b), giving the dependence of $R_{1,para}$ upon C_{Fe}^{β} with β = 1.88 ± 0.03 ($R^2 > 0.99$), whereas samples at all six different weight ratios display on average β = 1.46 ± 0.45. Due to the dilute clay content, the small $R_{1,para}$ could introduce larger error. In contrast, Figures 5.2(a) and 5.3(a) reflect dependence of $R_{1,para}$ upon N_p for all fully exfoliated samples. Taking these factors into account, we conclude that $R_{1,\,para} \propto C_{Fe}^{1.90}$.

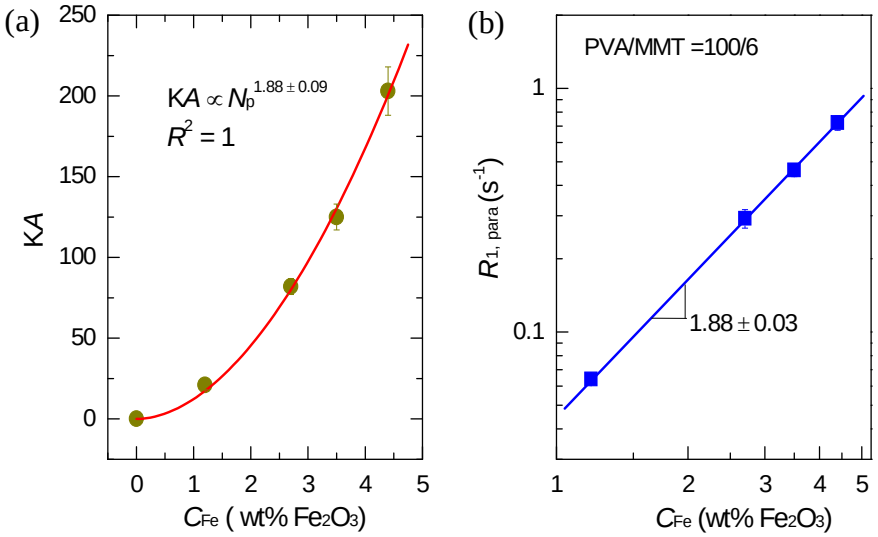

Figure 5.3. Impurity concentration dependence of $R_{1,para}$: (a) the prefactor, K*A* as a function of impurity concentration for poly(vinyl alcohol)/ montmorillonites (MMT) nanocomposites with four types of MMTs containing the amounts of Fe^{3+} (as Fe_2O_3), 1.2, 2.7, 3.5 and 4.4 wt%; (b) $R_{1,\,para}$ vs C_{Fe} for samples having the same weight ratio of

PVA/MMT =100/6. Note that for 1.2 wt% Fe_2O_3, $R_{1,para}$ was obtained at a magnetic field of 7.05 Tesla, while others reported in literature were measured at an 11.74 Tesla magnetic field.[201]

It is the first time, to our knowledge, to find analytical dependence of $R_{1,para}$ upon C_{Fe} in paramagnetic polymer/clay nanocomposites. It is worth noting that the spin-spin dipolar interaction among impurity ions could complicate this relationship. The interaction between Fe^{3+} ions in PCNs has been considered to investigate effects of these impurities on $R_{1,para}$[42] and ^{7}Li NMR line shape.[207] When the correlation time of the paramagnetic impurities were completely determined by spin changes of Fe^{3+} ions, β was theoretically predicted to vary from 5/4 to 2. The β value depends on the competition between direct relaxation and spin diffusion.[56-57] When the spin-diffusion process is dominated, β was predicted to be 2. Our finding of β, to some degree, coincides with the prediction of $\beta = 2$ in the spin-diffusion dominated case where the Fe^{3+}–Fe^{3+} interaction determines the correlation time. Keep in mind that Fe^{3+} ions here are in nature fixed within a central octahedral alumina layer sandwiched between two sheets of tetrahedral silica; this sandwich structure as a platelet is well dispersed in the host polymer matrix. In a platelet, the distance of Fe^{3+} ions is in the range of 2 nm up to 5 nm, which depends on C_{Fe}. The short Fe–Fe distance results in spin exchange interaction between Fe^{3+} ions, although clay particles in typical PCNs (1- 5 wt% clay) are separated by > 50 nm. An additional point should be addressed that Fe^{3+} ions in clay occur naturally, which could lead to Fe^{3+} ion clusters.[208] In the case of Fe^{3+} ion clusters, the dependence of $R_{1,para}$ could not be on $C_{Fe}^{1.90}$. MMT with 4.4 wt% Fe_2O_3 from Wyoming montmorillonite used here, shows an homogenous distribution of iron atoms[12], whereas the MMT (STx, 1.2 wt% Fe_2O_3) displays extensive iron clustering detected using an Fe K-edge X-ray absorption

spectroscopy.[208] Nevertheless, the dependence of $\beta = 1.90$ obtained from MMTs is close to the prediction of $\beta = 2$ by theories where the homogeneity of impurity dispersion was assumed.

5.4.Conclusions

In summary, we found the impurity-concentration (C_{Fe}) dependence of spin-diffusion averaged PRE, $R_{1,para}$, NMR observable useful for quantifying nanoparticle dispersion in a host polymer matrix. Our finding, compared to the theoretical prediction, suggests that the relevant mechanism of $R_{1,\ para}$ is associated with the spin-diffusion dominated case, suggesting spin exchange between Fe^{3+} ions in our systems. This finding has been applied in Chapter 4.4.4 to correct effects of C_{Fe} on $R_{1,para}$ for poly(ε-caprolactone)/MMT (PCL/MMT) nanocomposites filled with two different organo-MMTs, Cloisite 25A (C_{Fe} = 5.01 wt% Fe_2O_3 in silicates) and Cloisite 30B (C_{Fe} = 5.17 wt% Fe_2O_3 in silicates). It will be of great help to compare clay morphology in polymer nanocomposites containing MMTs with different C_{Fe}. As such, our finding extends the capacity of $R_{1,\ para}$ as a NMR observable that can be used to quantify dispersion of impurity-containing nanoparticle in nanocomposites.

CHAPTER 6

Field Dependence of Paramagnetic Contribution to Spin-lattice Relaxation

6.1.Introduction

Solid-state NMR paramagnetic relaxation enhancement (PRE) is a method for investigating distances in macromolecular systems as well as polymeric nanocomposites.[41-42,44,196,200,206] The origin of PRE is associated with electron–nucleus dipolar interaction (direct interaction) between nuclear spins and paramagnetic centers. Electron–nucleus dipolar interaction can enhance T_1 and T_2 relaxation rates, R (= C/r^6 , where r is the electron-nucleus distance, and the electron–nucleus coupling constant C[209] (e.g., eq 2.3)). As a result, the relaxation of the nuclei close to the impurity centers can be largely enhanced, which is called direct relaxation. The direct relaxation forms magnetization gradients around impurity centers and the magnetization can be propagated to the remote nuclei via spin diffusion (see Chapter 4). Most often, high magnetic field NMR spectrometers favor measurements of PREs due to their high sensitivity and resolution.

The electron-nucleus coupling constant, C is strongly dependent on the magnetic field strength, as indicated in eq 2.3. When $\omega_o\tau_c >> 1$ (ω_o, τ_c are Larmor frequency of nuclei, and correlation time of impurity centers, respectively), $C \propto B_o^{-2}$, then $R \propto B_o^{-2}$, suggesting that direct relaxation is inversely proportional to field strength (B_o). Thus, a

low field could increase the direction relaxation when compared to a high field, leading to different initial relaxation behavior. The magnetization gradient could be built up rapidly around the impurity centers, leading to a larger paramagnetic contribution to the relaxation rate. With this in mind, we explored the external field dependence of the ^{1}H relaxation in paramagnetic PCNs following spin saturation. In doing so, we have employed bench top NMR to detect ^{1}H relaxation from which quantitative information on clay morphology has been extracted using methods developed in Chapters 3 and 4.

In the first part, we focus on investigating the initial relaxation behavior in polypropylene nanocomposites filled with Cloisite 15A with an average Fe−Fe distance of 1.2 nm (4.96 wt% Fe_2O_3) (Chapters 2 and 4), and poly(lactic acide) nanocomposites filled with Cloisite 30B with an average Fe−Fe distance of 1.2 nm (5.01 wt% Fe_2O_3) (Chapters 4) in different static fields. Considering clay morphology in PCNs, the initial relaxation behavior of the neighboring ^{1}H nuclei could be attributed to PRE effects from direct interaction, the Curie spin relaxation as well as spin diffusion.

In the second part, we will examine the magnetic field dependence of paramagnetic contribution to relaxation rate, $R_{1,\,\mathrm{para}}$ via spin diffusion in nanocomposites. We concentrate on three external magnetic fields with the proton Larmor frequencies (ω_H) of 23, 300 and 400 MHz. Given a specific PCN, the quality of dispersion is expected to be somewhat consistent, measured at different fields. More importantly, magnification of paramagnetic rates at a lower magnetic field, as compared to a high magnetic field, could enhance the sensitivity and reliability of $R_{1,\,\mathrm{para}}$ as a measure of clay dispersion in PCNs.

6.2. Experimental

The systems chosen for this work are the extruded pellets of polypropylene (PP), PP/MMT nanocomposites as well as compression molded PP-MMT2.7. See Chapter 2 for the details on sample preparation. The relaxation data measured at 300 MHz field has been reported in Figure 4.9.

See Chapter 4 for full details about as-cast films of polylactic acid (PLA)−MMT nanocomposites. The NMR relaxation data at 7.05 T for HMW PLA and HMW PLA-MMT nanocomposites has been presented in Figure 4.8. ^{1}H saturation-recovery NMR experiments were performed in magnetic fields of 0.54 T, 7.05 T and 9.4 T.

^{1}H saturation-recovery NMR experiments were performed at room temperature on a magnetic resonance analyzer (MARAN 23 Ultra) using a permanent magnet of 0.54 T and two high-resolution NMR spectrometers operating at 7.05 T (Bruker DSX-300) and 9.4 T (Bruker AV3-400). The pellets of PP and PP-MMT nanocomposites and as-cast films of PLA-MMT nanocomposites were cut into small pieces and packed into magic-angle spinning (MAS) rotors for measurements at 7.05 and 9.1 T, and into a 10 mm NMR tube for measurements at 0.54 T. Details about saturation-recovery experiments were described in Chapter 2.4. At the two high fields, the 90^{o} pulse was 5 μs, dwell time was 1 μs, and recycle decay was 4 s.

In order to avoid any influence from an inhomogeneous field, similar weight and packing height of different samples in a 10 mm NMR tube were always maintained during measurement at 23 MHz, and the location of samples in this field was also kept the same. When focusing on initial relaxation, 2048 scans were measured for each relaxation delay at 0.54 T. At 0.54 T, the 90^{o} pulse was automatically calibrated to be 3.5

μs, and dwell time was 1 μs, recycle decay was 5 s. Plots of $M(t)/M_o$ versus t yielded the saturation recovery curves. The overall ^{1}H T_1 was obtained by fitting a single exponential function. The experimental error comes from the fitting error. Standard deviation, a positive square root of variance was calculated for the propagate error. The standard deviation of the resulting degree of exfoliation and quality of dispersion was computed.

Details on thermogravimetric analysis (TGA) and wide-angle X-ray diffraction are described in Chapter 2.

6.3. Initial Relaxation Behavior

6.3.1. Polypropylene/MMT nanocomposites

Paramagnetic contribution to the initial spin-lattice relaxation, M_c^n was calculated by subtracting of PP from that of PP/MMT nanocomposite with 2.7 wt% neat MMT (PP-MMT2.7). Figure 6.1(a) shows normalized magnetization (M^n) and M_c^n for PP and PP-MMT2.7 at short times in two fields of 0.54 T and 7.05 T. It is observed that ^{1}H relaxation depends on the magnetic field. PP-MMT2.7 exhibits faster magnetization recovery in 0.54 T than 7.05 T during the initial relaxation.

Particularly, during the first 1 ms PP-MMT2.7 gains 3.2 % magnetization at 0.54 T, while the pure PP almost recovers relatively quite small magnetization (~ 0.5%) (Figure 6.1b). 2.7 wt% pure MMT in PP-MMT2.7 indicates 2 wt% organic modifiers in PP-MMT2.7 (see Table 2.1). Taking into account detectable 64% protons of modifiers inside Cloisite 15A(see Chapter 2), we calculated 1.3% contribution from modifiers to 3.2% recovered magnetization at the first 1 ms at 0.54 T. XRD pattern of PP-MMT2.7 shows almost no intercalation of polymer chains into Cloisite 15A, since d_{001} of PP-

MMT2.7, 3.25 nm is slightly higher than 3.15 nm of Cloisite 15A. Thus, we deduce that 3.2% recovered magnetization is not only from protons inside particles but also from polymer protons around clay particles.

An average interparticle spacing in PP-MMT2.7 was estimated to be 176 ± 25 nm from TEM images. Assuming an alternating polymer/clay lamellar structure, protons between clay particles contribute to 100% magnetization, Thus, 3.2% magnetization is contributed to protons in a layer of (176 × 3.2%)/2 = 2.8 nm thickness on particle surface. It can be seen that the low magnetic field can detect the relaxation of neighboring nuclei at very short times.

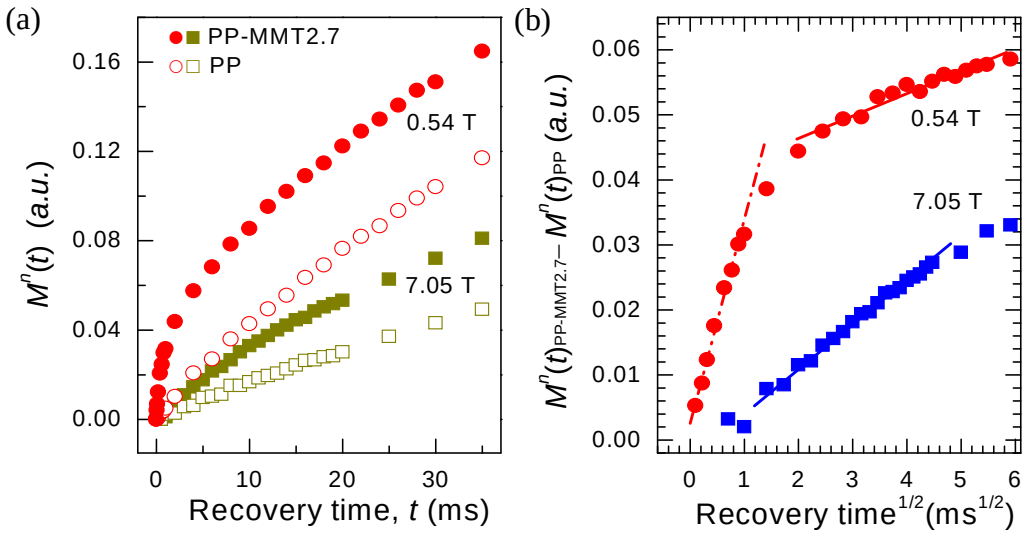

Figure 6.1. ^{1}H NMR magnetization recovery following saturation for pellets of PP and a representative nanocomposite with 2.7 wt% neat clay (PP-MMT2.7): (a) Comparison of normalized recovery curves (M^n) of PP-MMT2.7 (solid markers) and PP (open markers), collected at magnetic fields of Bo = 0.54 T (circle markers) and 7.05 T (rectangle markers); (b) Normalized and corrected magnetization, $M^n(t)_{PP\text{-}MMT2.7} - M^n(t)_{PP}$, versus the square root of recovery time at these two fields. Note that the first data points in (a) measured at both fields are vertically shifted to zero for comparison.

Theoretically the relaxation rate sharply decrease with r^{-6} (r is the electron-nucleus distance). The nuclei away from impurity centers show slow magnetization growth due to weak direct interaction. With increasing recovery time, more nuclei away from impurity centers will contribute to magnetization recovery.[191] This will lead to slow magnetization growth. Also, the relaxation rate is dependent on the electron-nucleus coupling constant, *C*. Thus, the enhanced magnetization in nanocomposites as a function of recovery time depends on the static fields. The enhancement ratio of magnetization of nanocomposites over the unfilled polymer, M^n_{PCN}/M^n_{PP} is introduced to reflect how the field contributes to the initial relaxation recovery under the influence of impurity centers. Figure 6.2(a) shows that the enhancement ratio of $M^n_{PP\text{-}MMT2.7}/M^n_{PP}$ decreases sharply with increasing time before 1 ms, and then levels off at 0.54T. The similar result is observed at 7.05 T. Note that the enhancement ratio before 1 ms is hard to be observed due to noise issue at 7.05 T.

Due to strong dipolar coupling between impurity centers inside our clay, the neighboring nuclei should experience the Curie spin relaxation besides direct interaction.[207] Thus, the coupling constant *k* including both factors, can be expressed as[209]

$$k = \frac{2}{5}\left(\frac{\mu_0}{4\pi}\right)^2 I(I+1)\left(\gamma_S\gamma_I\hbar\right)^2 \frac{\tau_c}{1+\omega_H^2\tau_c^2} + \frac{2}{15}\left(\frac{\mu_0}{4\pi}\right)^2 I^2(I+1)^2 \frac{\gamma_S^4\hbar^4}{k^2T^2}\frac{\omega_H^2\tau_r}{1+\omega_H^2\tau_r^2} \qquad (6.1)$$

where γ_S is the magnetogyric ratio of the electron, *I* is the spin number of the paramagnetic center, ω_H is the Larmor frequency of the proton, *T* is the absolute temperature, τ_c is the correlation time for the interaction of the impurity center with the

lattice, and τ_r is the rotational correlation time for molecular motion.[209] The first term on the right hand side of eq 6.1 is due to the direct relaxation, and the second term is due to the Curie relaxation (k_{Curie}).

In order to investigate which factor is dominant in the initial relaxation recovery, we calculate the ratio of the direct relaxation term to the Curie relaxation term at 7.05 T and at room temperature is give by

$$\frac{C}{k_{Curie}} = \frac{3k^2T^2\gamma_H^2\tau_r}{I(I+1)\left(\gamma_S\hbar\omega\right)^2\tau_c} \approx 333\tau_r/\tau_c \qquad (6.2)$$

The value of τ_r for polypropylene can be as high as 10^{-7} s,[210] and the single electronic relaxation correlation time, τ_c is $10^{-9} \sim 10^{-7}$ s, and then $\tau_r / \tau_c > 1$ to a reasonable approximation. It can be seen that the ratio is larger than 333. The ratio of C/ k_{Curie} at 0.54 T is $> 10^4$, even larger than the ratio at 7.05 T. Thus, in solid-state paramagnetic PCNs, The dipolar relaxation is dominant in the initial relaxation recovery. Owing to $\omega_H\tau_c > 1$ (see Chapter 2), the direct relaxation term, $C \propto B_o^{-2}$. As a consequence, the B_o dependence of the enhancement is expected, as illustrated in Figure 6.1.

Another equation is about what degree the low magnetic field can enhance the initial relaxation recovery when compared to the high field. We calculated the ratio of paramagnetic contribution to the initial relaxation recovery at 0.54 T to that at 7.05 T, $[M_c^n(t)]_{0.54T} /[M_c^n(t)]_{7.05T}$, as a function of recovery time (Figure 6.2b). In terms of the tendency plotted in Figure 6.2(b), the ratio can be predicted to be > 10 for the first 1 ms. Theoretically[54-55,58,172], $M_c^n(t) \propto C^{1/2}t^{1/2}$ for the dominant direct relaxation as claimed

above. When $\omega_H \tau_c >> 1$, $C \propto B_o^{-2}$. Then, we have $M_c^n \propto B_o^{-1}$. Therefore, the theoretical prediction of $[M_c^n(t)]_{0.54T} / [M_c^n(t)]_{7.05T}$ is expressed as

$$\frac{[M_c^n(t)]_{0.54\ T}}{[M_c^n(t)]_{7.05\ T}} = \left[\frac{(C)_{0.54T}}{(C)_{7.05T}}\right]^{1/2} = \frac{B_0(7.05\ T)}{B_0(0.54\ T)} \approx 13 \tag{6.3}$$

which is in good agreement with our observation at the first 1 ms in Figure 6.2(b). Note that the ratio cannot be measured before 2 ms at 0.75 T, owing to larger noise.

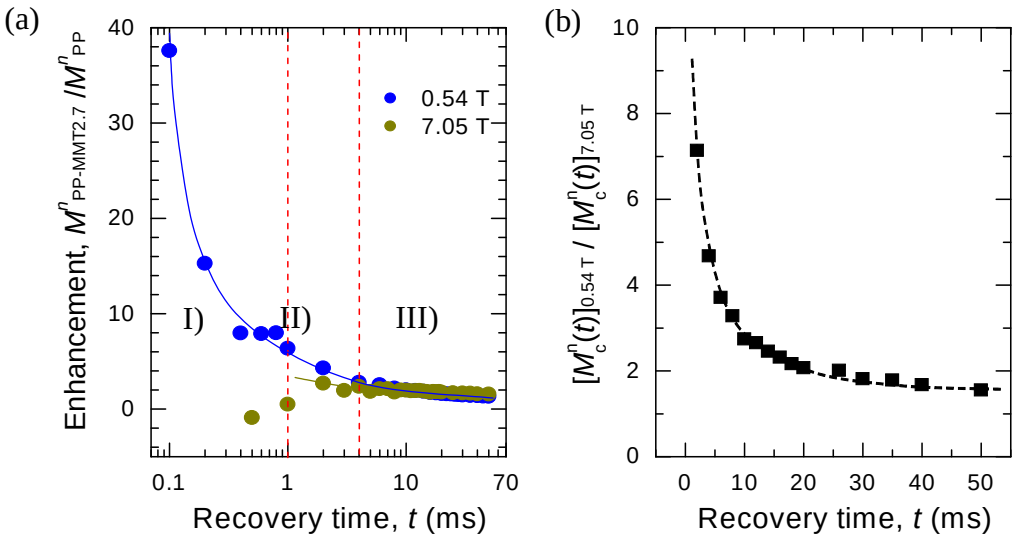

Figure 6.2. ^{1}H NMR magnetization recovery following saturation: (a) magnetization enhancement, $M^n(t)_{PP\text{-}MMT2.7}/M^n(t)_{PP}$ at two fields of 0.54 T and 7.05 T; (b) the ratio of enhancements, $[M_c^n]_{0.54\ T}/[M_c^n]_{7.05\ T}$. Paramagnetic contribution to the initial relaxation recovery, $M_c^n = M^n(t)_{PP\text{-}MMT2.7} - M^n(t)_{PP}$, at these two fields were shown in Figure 6.1b. The dashed lines at 1 ms and 4 ms distinguish relaxation process into three periods: (I) PRE by dipolar interaction for the first 1ms; (II) PRE by both of dipolar interaction and spin diffusion in the intermediate (III) PRE by spin diffusion after 4 ms.

Based on the foregoing discussions, we can distinguish the magnetization recovery process into three periods defined by the recovery time scale, as Figure 6.2(a) illustrates. In general, the magnetization gradient around clay particles is rapidly built up following saturation, because of strong electron-nucleus dipolar interaction. As magnetization gradient develops, spin-diffusion driven PRE is most prevalent. Large enhancement can be directly attributed to dipolar interaction before 1 ms following the saturation of the spin system (the first period, I). Owing to r^{-6} dependence of dipolar interaction relaxation, its contribution to magnetization recovery sharply decreases with recovery time. Leveling of enhancement is due to stable spin diffusion through which the polarization can be transferred into remote spins (the third period, III). The intermediate period, II, results from contributions from both dipolar interaction and spin diffusion to magnetization enhancement. The first and second periods disappear at 7.05 T owing to relatively slow build-up of magnetization gradients. Thus, we attribute this single stage of PRE to the combination of relatively weak dipolar interaction relaxation and slow spin diffusion at 7.05 T, which was claimed to be a diffusion-limited relaxation process in Chapter 2.

Figure 6.3 shows ^{1}H NMR magnetization recovery for pellets of PP-MMT nanocomposites with 0.57, 1.14, 1.70, 2.70 and 5.51 wt% MMT, measured at 0.54 T for the first 1 ms following saturation of the spin system. The pure PP only recovers a minor fraction of the magnetization, while all PP-MMT nanocomposites show fast initial relaxation recovery for the first 1 ms at 0.54 T.

Figure 6.4 exhibits the enhanced magnetization as a function of the square-root of recovery time ($t^{1/2}$) for PP-MMT nanocomposites with neat MMT contents (0.57, 1.14,

1.70, 2.70 and 5.51 wt%). The enhanced M_c^n at 0.54 T exhibits two stages that are linear with $t^{1/2}$, defined by two dashed lines. Figure 6.5(a) indicates that the slope of the $M_c^n \sim t^{1/2}$ law at the first stage is proportional to the clay content. Direct dipolar interaction, in principle, produces the $M_c^n \sim t^{1/2}$ law in the initial recovery stage, and the resultant proportionality has been related to the impurity concentration.[54-55,58,172,211] Assuming the homogeneous distribution of Fe^{3+} ions inside each platelet and homogeneous surface modification of MMT, all paramagnetic centers can contribute to M_c^n. Therefore, the slope of the first stage is expected to be linearly proportional to neat clay content. Our observation in Figure 6.5(a) is completely consistent with this expectation.

As we claimed in Figure 6.2(a), the second slope of $M_c^n \sim t^{1/2}$ is due to spin diffusion, which was related to effective surface-to-volume ratio of diffusive sources (see Chapters 2 & 3). The second slope of $M_c^n \sim t^{1/2}$ from 4 ms to 30 ms is directly correlated with effective interfacial surface area. Here, we use the pellets of PP-MMT2.7 as a reference sample. Its degree of exfoliation was measured to be f = 1/2 = 0.5 using the initial slope method at 7.05 T, as indicated in Figure 4.11. The value of f can be calculated using the slope and MMT content corrected with ones of the reference sample by

$$f = (\text{platelets/stack})^{-1} = S/\,[S_{ref} \times (\text{platelets/stack})_{ref}] \times\ [(\text{wt\%})_{ref}\ /\ (\text{wt\%})] \qquad (6.4)$$

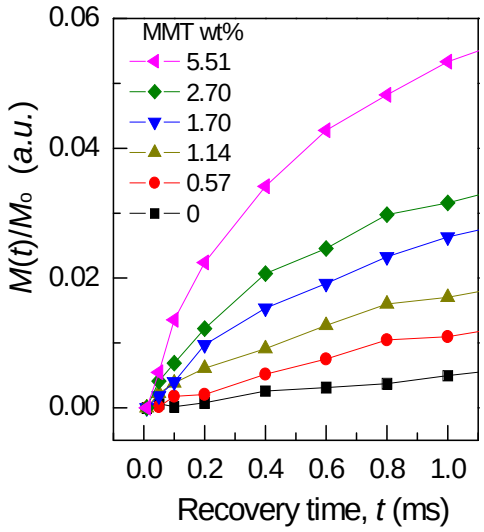

Figure 6.3. ^{1}H NMR magnetization recovery for pellets of PP and PP-MMT nanocomposites with 0.57, 1.14, 1.70, 2.70 and 5.51 wt% MMT, measured at 0.54 T for the first 1 ms following saturation of the spin system.

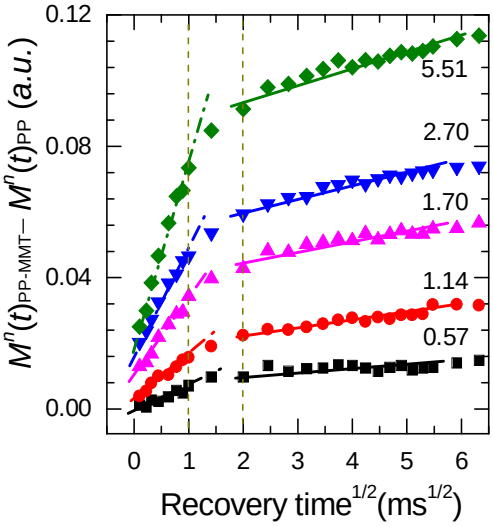

Figure 6.4. Paramagnetic contribution to the initial relaxation recovery, M_c^n (= $M^n(t)_{PP\text{-}MMT} - M^n(t)_{PP}$), versus the square root of recovery time for samples with neat MMT contents (0.57, 1.14, 1.70, 2.70 and 5.51 wt%) measured at 0.54 T. Each curve exhibits two stages of the $t^{1/2}$ law out of the three periods defined by two dashed lines, similar to Figure 6.2(a).

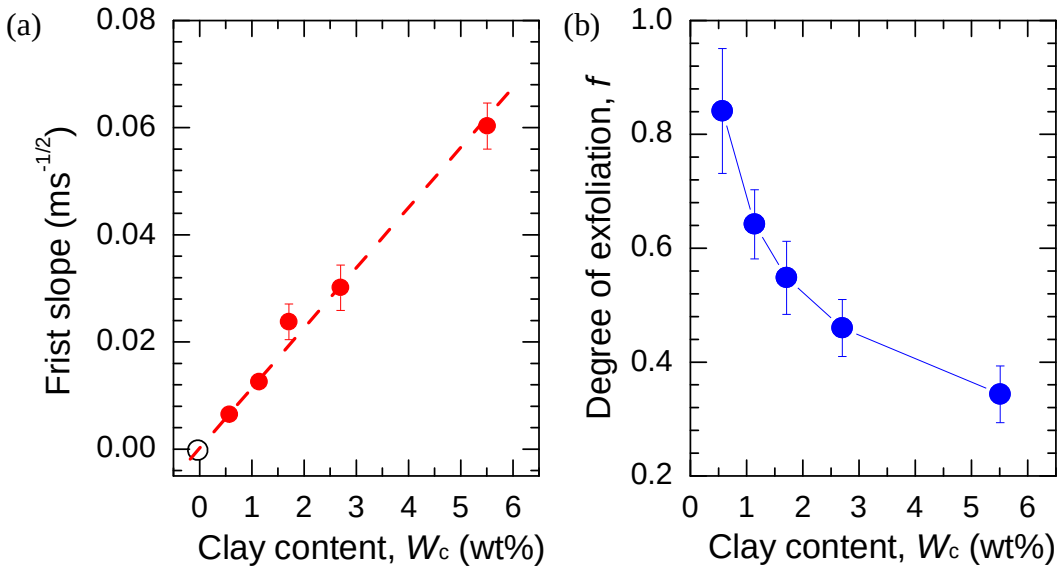

Figure 6.5. Each saturation-recovery curve of Figure 6.4 exhibits two stages of the $t^{1/2}$ law: (a) the slope of the first stage can be directly related to the total clay content, or neat MMT, (b) the slope of the second stage can be converted into a degree of clay exfoliation using eq 6.4. All slopes were scaled by that of a reference material, Compression molded PP-MMT2.7, which was also measured at 0.54 T. The reference material shows f = 0.38, obtained from TEM data (see Chapter 2).

Figure 6.5(b) shows the degree of exfoliation for all PP-MMT nanocomposites, indicating that the degree of exfoliation decreases with increasing MMT content. XRD curves (see Appendix A) exhibit the shift of the d_{001} peak into larger angles for higher MMT content as well as the stronger peak, suggestive of the existence of bigger stacks and lower degree of exfoliation.[44,70,150] The degree of exfoliation, f sharply decreases from 0.84 ± 0.10 of PP-MMT0.57 to 0.34 ± 0.03 of PP-MMT5.51. The results are roughly in agreement with those obtained by the initial slopes of these samples at 7.05 T (Figure 4.11a). It is important to note that PP-MMT5.51 apparently exhibits a higher exfoliation, f = 0.45 ± 0.02 at 7.05 T. 4.17 wt% surfactants were introduced with 5.51 wt% pure MMT into PP-MMT5.51, since Cloisite 15A contains 43 wt% surfactants (Table 2.1). As mentioned before, PP-MMT2.7 contains 2 wt% surfactant, Hence, this inconsistency

could be associated with more surfactants inside clay particles in PP-MMT5.51 relative to other samples. This would increase the initial slope of PP-MMT5.51 at 7.05 T. However, we argued before that the initial slope is only related to interfacial surface area. This argument could be correct for samples where protons inside particles have small contribution to the initial slope. If this contribution from protons inside particles becomes larger compared to a reference, we could overestimate the degree of exfoliation. Bearing these considerations in mind, Figure 4.11(a) gives the upper boundary to the degree of exfoliation in this most concentrated sample at 7.05 T. On the other hand, a low field of 0.54 T can avoid this problem by separating contributions from direct interaction and spin diffusion to initial relaxation recovery.

Figure 6.6(a) exhibits the enhanced magnetization as a function of $t^{1/2}$ for PP-MMT2.7 nanocomposite films with stretch ratios from $\lambda = 1$ (unstretched, compression molded sample) to 3.5, measured at 0.54 T. The enhanced M_c^n at 0.54 T exhibits two stages that are linear with $t^{1/2}$. The slope of the second stage is related to the degree of exfoliation using eq 6.4 and $f_{ref} = 0.38$ in the sample with $\lambda = 1$. Figure 6.6(b) shows the degree exfoliation as a function of stretch ratio, which is completely consistent with that from the single initial slope obtained at 7.05 T.

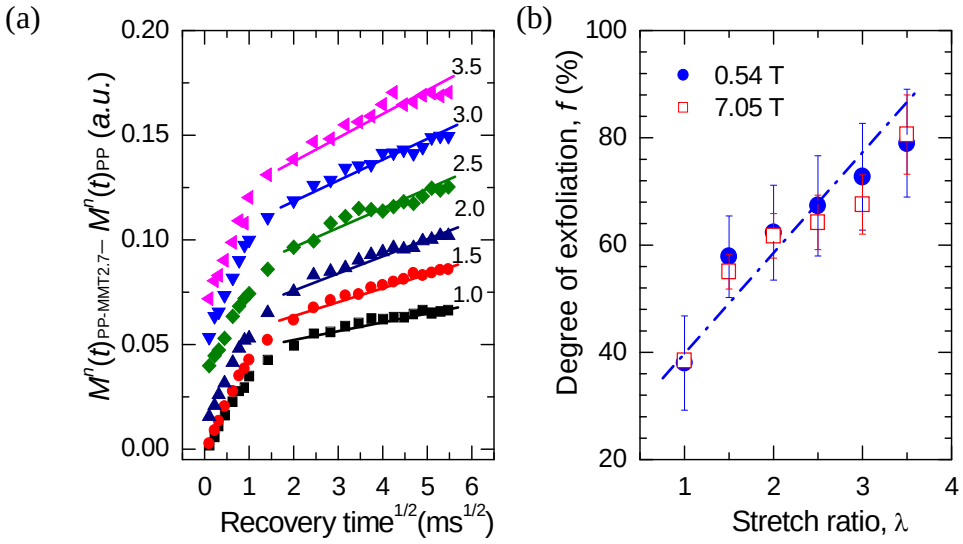

Figure 6.6. Paramagnetic contribution to the initial relaxation recovery, M_c^n (= $M^n(t)_{PP\text{-}MMT} - M^n(t)_{PP}$), versus the square root of recovery time for PP-MMT2.7 nanocomposite films with stretch ratios from λ = 1 (unstretched) to 3.5: (a) samples measured at the magnetic field of B_o = 0.54 T; (b) comparison of degree of exfoliation measured at magnetic fields of B_o = 0.54 and 7.05 T. Compressed molded PP-MMT 2.7 (λ = 1), as a reference material, shows f = 0.38, obtained from TEM data (Chapter 2).

6.3.2. Intercalated Poly(lactic acid)/MMT Nanocomposites

XRD spectra of PP-MMT nanocomposites show a slight change (± 0.2 nm), even a decrease for PP-MMT5.51 in the basal spacing relative to the pristine Cloisite 15A (see Appendix A). These results suggest that almost no PP chains intercalate into Cloisite 15A. In contrast, XRD spectra of PLA-MMT nanocomposites show expanded basal spacings by ~1.5 nm, indicating PLA intercalation into Cloisite 30B. These two different systems are two typical cases of PCNs, in particular prepared by melt compounding.[7,9,15-17,37-39] Therefore, investigations of such intercalated systems will be necessary to address our methods. Two molecular weight PLAs were filled to make PLA/MMT nanocomposites. First, we focus on the high MW PLA nanocomposites (HMW PLA-MMT). Then we

compare effects of the molecular weight (MW) on clay dispersion by initial relaxation and paramagnetic contribution to the relaxation rate.

Figure 6.7 compares ^{1}H NMR magnetization recovery for HMW PLA and HMW PLA-MMT nanocomposites containing 1.30, 2.56, and 3.84 wt% MMT, measured at 0.54 T (a) and 7.05 T (b) for the first 10 ms following saturation of the spin system. All HMW PLA-MMT nanocomposites recover magnetization intensity faster for the first 10 ms, in particular for the first 1 ms at 0.54 T, while HMW PLA recovers more slowly. It can be seen that nanocomposites recover magnetization intensity faster than HMW PLA at both fields, and magnetization recovery of these nanocomposites becomes slow at a higher field at a specific time. These observations would be interpreted by the fact that a low field allows a larger electron-nucleus coupling (C), leading to faster direct relaxation (see Section 6.3.1). The faster direction relaxation facilitates buildup of magnetization gradients around paramagnetic particles.

Figure 6.8 exhibits the enhanced magnetization as a function of the square-root of recovery time ($t^{1/2}$) for HMW PLA-MMT nanocomposites. M_c^n at 0.54 T exhibits two stages of the $t^{1/2}$ law. At 7.05 T M_c^n shows the first weak stage and the second strong stage. Compared to the first stage at 0.54 T, M_c^n is much weak for all nanocomposites at the first 4 ms at 7.05 T. We observed the same behavior of the initial relaxation at 9.4 T (not shown here) as 7.05 T; but magnetization recovery becomes slower at the higher field.

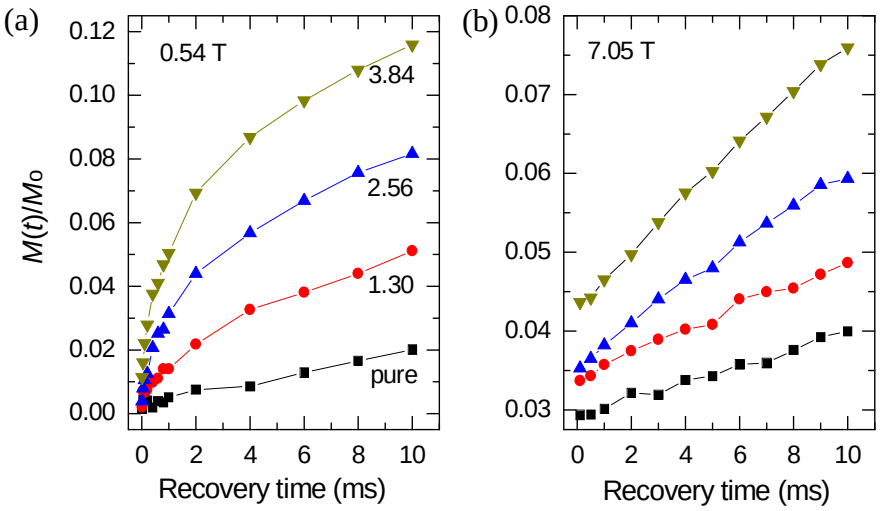

Figure 6.7. Comparison of ^{1}H NMR magnetization recovery for HMW PLA-MMT nanocomposites with 1.30, 2.56, and 3.84 wt%, measured at 0.54 T (a) and 7.05 T (b) for the first 10 ms following saturation of the spin system. Cloisite 30B filled here is the organo-MMT, containing 5.02 wt% Fe_2O_3 in the pure silicates.

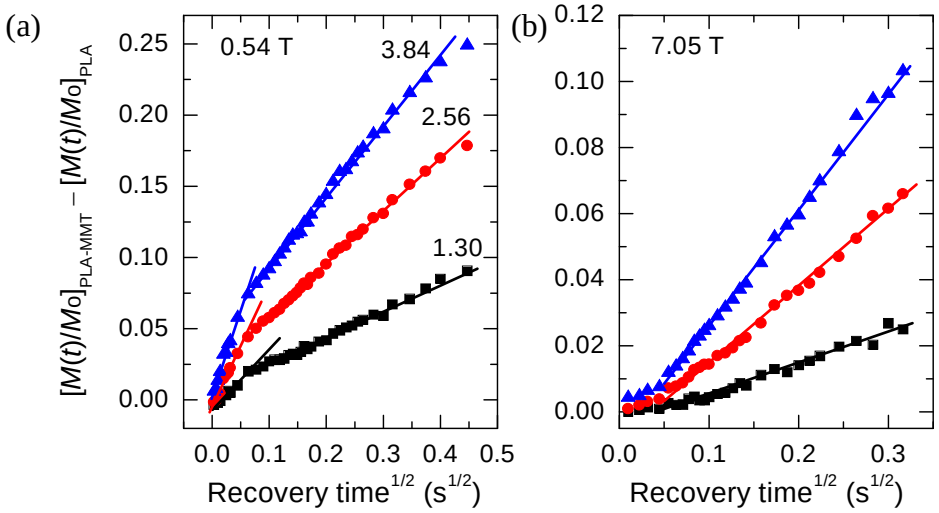

Figure 6.8. Normalized and corrected magnetization, M_c^n (= $M^n(t)_{PLA\text{-}MMT} - M^n(t)_{PLA}$), versus the square root of recovery time for HMW PLA-MMT nanocomposites with neat MMT contents (1.30, 2.56, and 3.84 wt%) measured at 0.54 T (a) and 7.05 T (b). Each curve exhibits two stages of the $t^{1/2}$ law. The solid lines are guides.

Figure 6.9 shows that the first slopes increase linearly with clay content in PLA-MMT nanocomposites as well as PP-MMT nanocomposites. These results indicate the

first slope is involved in direct interaction relaxation, which is directly related to clay content if all silicate surfaces are covered by surfactants. The first slopes of PLA-MMT nanocomposites (HMW PLA-MMT and LMW PLA-MMT) are in a complete agreement with those of PP-MMT nanocomposites. This is associated with two facts about organoclays involved here: (1) similar surfactants used in Cloisite 15A and Cloisite 30B, despite differences between dimethyl, dehydrogenated tallow, quaternary ammonium in the former and methyl tallow, bis-2-hygroxyethyl quaternary ammonium in the latter; (2) the similar impurity concentrations: 4.96 wt% Fe_2O_3 in Cloisite 15A and 5.02 wt% Fe_2O_3 in Cloisite 30B. Through the first slope of the spin-lattice relaxation at a low field, we could measure the clay content by a reference with a known content, and detect the impurity concentration.

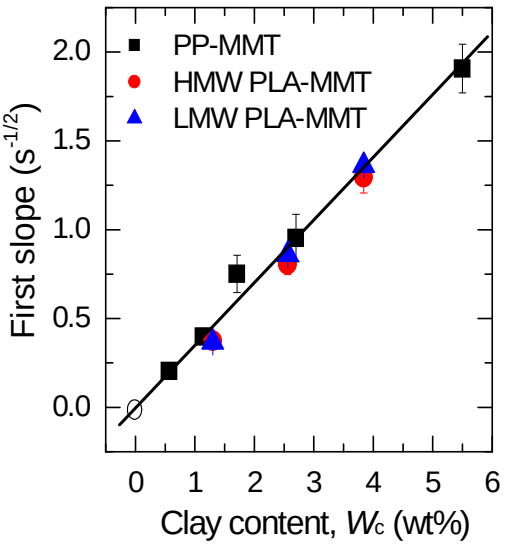

Figure 6.9. The first slopes in paramagnetic contribution to the initial relaxation recovery, M_c^n (= $M^n(t)_{PLA\text{-}MMT} - M^n(t)_{PLA}$) that is linear with $t^{1/2}$ for HMW PLA-MMT nanocomposites in Figure 6.8(a), and those of LMW PLA-MMT nanocomposites and PP-MMT nanocomposites. Cloisite 30B (C30B) is filled in PLA-MMT samples, which contains 5.02 wt% Fe_2O_3 in pure silicates; Cloisite 15A (C15A) in PP-MMT samples contains 4.96 wt% Fe_2O_3 in pure silicates. The solid lines are guides.

Figure 6.11 shows the second slopes of $M_c^n \sim t^{1/2}$ as a function of clay content at three fields. These slopes increase linearly with clay content in different fields. This indicates that all fields are consistent in detecting the similar information about clay dispersion in this series of nanocomposites. It can be also seen that the slopes are larger at a low field, and the slopes in two high fields of 7.05 T and 9.4 T are slightly different. This is due to the faster buildup of magnetization gradients around particles in a lower field, accelerating spin diffusion. Increasing the magnetic field strength leads to decreasing direct relaxation, and slowing spin diffusion. Theoretically, the electron-nucleus coupling constant, C decreases with increasing magnetic field strength (cf. eq 2.4). Therefore, the first slop due to the direct relaxation becomes weaker with increasing magnetic field strength. It would be expected that the protons contributing to the first slope cannot help the protons in the barrier to build up magnetization gradients, while the protons in spin-diffusion barrier acts as relaxation sinks. As such, the second slope could converge with increasing the magnetic field strength.

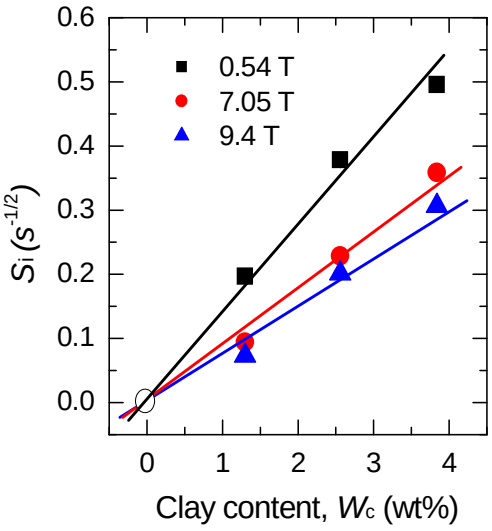

Figure 6.10. Comparison of the second slopes at 0.54T with the initial slopes at 7.05 T and 9.4 T as a function of clay content for HMW PLA-MMT nanocomposites.

In summary, two aspects of initial relaxation behavior was found at low fields that separate contributions from direct relaxation and spin diffusion to initial magnetization recovery: (1) the first slope due to direct relaxation can be used to determine clay content or detect impurity concentration; (2) the second slope due to spin diffusion can be related to quantify clay exfoliation. This would facilitate the quality control by monitoring clay exfoliation in manufacturing PCNs products using a bench-top NMR spectrometer in industry.

6.4. Paramagnetic Spin-lattice Relaxation Rate

In last section, we discussed the effects of magnetic fields on the initial behavior in the spin-lattice relaxation process in paramagnetic polymer/clay nanocomposites. In this section, we will investigate magnetic field dependence of paramagnetic contribution to relaxation rate ($R_{1,para}$).

Figure 6.11(a) shows that the lower field of 0.54 T provides large $R_{1,\,para}$, while the higher 7.05 T field gives rise to small $R_{1,\,para}$. This observation could be interpreted based on the initial magnetization recovery behavior under these two fields in last section. The magnetization recovery of the nearby nuclei at 0.54 T is much faster than at 7.05 T immediately following the saturation of these systems. The magnetization gradients around clay particles are built up more rapidly at the lower field, leading to the enhanced $R_{1,\,para}$ via spin diffusion.

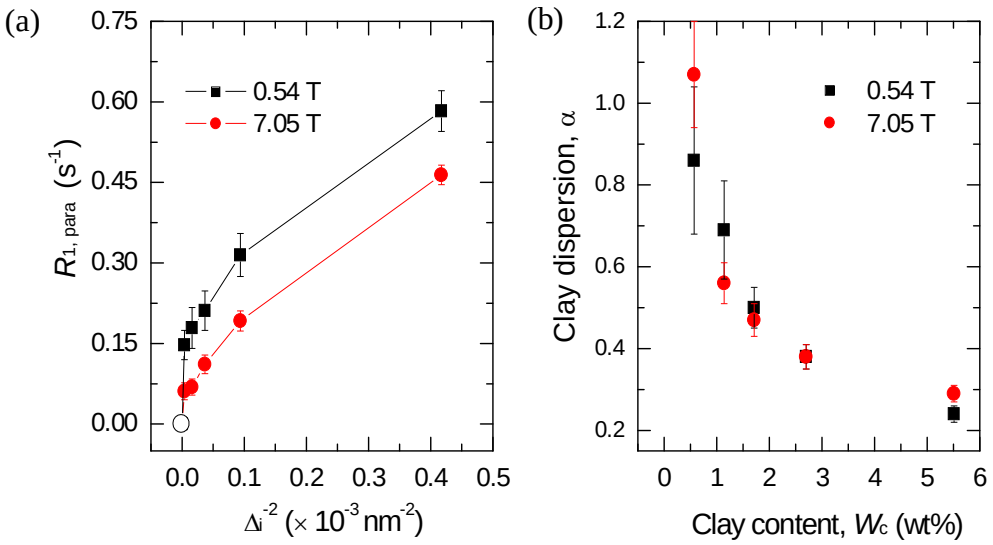

Figure 6.11. Effects of magnetic field stregnth on $R_{1,\,para}$ of PP-MMT nanocomposites and the resulting degree of clay dispersion as a function of MMT content: (a) $R_{1,\,para}$ versus clay content, collected in two magnetic fields of B_o = 0.54 T and 7.05 T; (b) Quantitative comparison of the quality of clay dispersion obtained using eq 4.16. Note that compression-molded PP-MMT2.7 was chosen as a reference material. Its degree of exfoliation, *f* is 0.38, obtained from TEM data (see Chapter 2).

In Chapter 4, it was described how $R_{1,\,para}$ can be employed to extract the quality of clay dispersion in PCNs. The values of *KA* in eq 4.16 can be computed for each PP-MMT nanocomposite (Figure 6.11a). Compression-molded PP-MMT2.7 is chosen as a reference material that shows α = 0.38, obtained by TEM data in Chapter 2. Thus, the quality of clay dispersion in other samples can be correlated with this reference by $\alpha = [(KA)/(KA)_{ref})]^{1/2}\ \alpha_{ref}$. The quality of clay dispersion is shown as a function of MMT content in Figure 6.11(b). The value of α obtained from two fields is similar within the experimental error, especially for samples which satisfy our model (e.g., eq 4.15 or 4.16). PP-MMT5.51 exhibits the almost same α value, obtained from these two fields (e.g., 0.24 ± 0.02 at 0.54 T and 0.28 ± 0.03 at 7.04 T). For the initial slope method, PP-MMT5.51 shows the degree of exfoliation, f = 0.34 ± 0.02 at 0.54 T (Figure 6.5), which is higher

than the quality of clay dispersion. As addressed in Figure 4.11, inhomogeneous clay distribution could lead to a lower quality of dispersion, α than the degree of exfoliation, f, since the quality of dispersion includes the clay distribution and exfoliation.

One may notice that the experimental error of $R_{1,\,para}$ is larger at 0.54 T than at 7.04 T, leading to the larger standard deviation of the resultant α values. In fact, a smaller difference in the T_1 values between nanocomposite and the pure polymer is detected at 0.54 T, thereby resulting in a possibility of the larger experimental error. On the other hand, through creating the difference in $R_{1,\,para}$ values between the nanocomposites and the reference material at a low field, the resulting standard deviation of f values could become smaller.

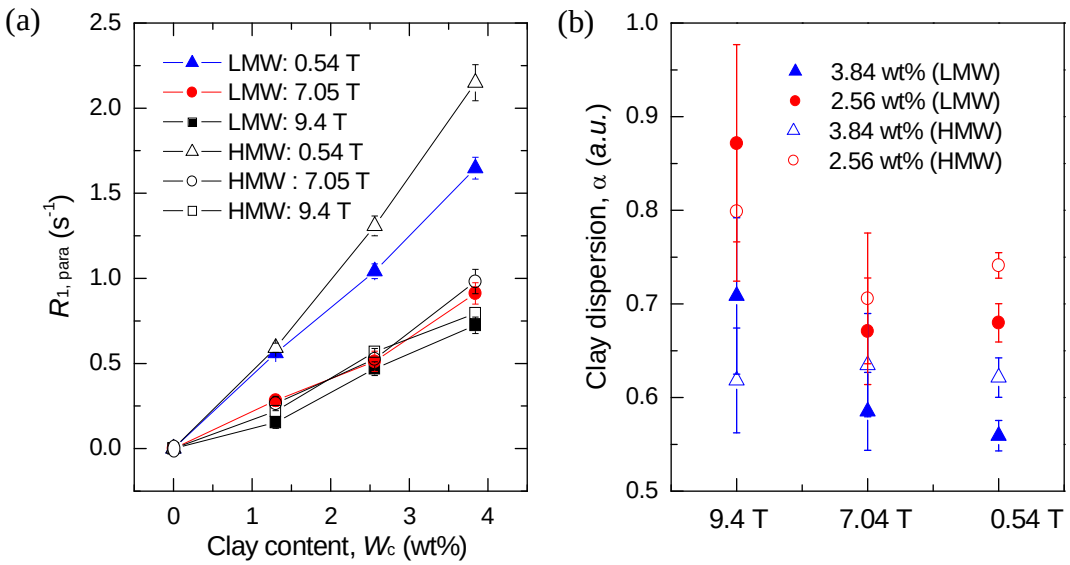

Figure 6.12. Static field dependence of $R_{1,\,para}$ as a function of clay content, W_c and the resulting relative degree of MMT exfoliation in LMW PLA-MMT (solid markers) and HMW PLA-MMT (open markers) nanocomposites. (a) $R_{1,\,para}$ versus W_c, measured in three fields of B_o = 0.54 T, 7.05 T and 9.4 T. (b) Semi-quantitative comparison of the quality of dispersion, calculated using eq 4.16. The samples with 1.30 wt% MMT is chosen as the reference material having α = 1, because their $R_{1,\,para}$ are same at a field. The relative degree of MMT exfoliation in other samples is correlated with the reference by eq 6.4.

PLA-MMT nanocomposites with LMW PLA and HMW PLA were measured in three magnetic fields of 0.54 T, 7.05 T and 9.4 T. Figure 6.12(a) shows the same trends for all measurements: $R_{1,\,para}$ increases with the addition of clay. There are magnified $R_{1,\,para}$ values of PLA nanocomposites detected at 0.54 T as compared to two high fields of 7.05 T and 9.4 T.

Figure 6.12(a) also shows that there is slight difference in $R_{1,\,para}$ values measured at 7.05 T and 9.4 T. In contrast, the low field of 0.54 T provides larger $R_{1,\,para}$ values. Moreover, it distinguishes larger $R_{1,\,para}$ values of HMW PLA nanocomposites from those of LMW PLA nanocomposites at 2.51 wt% and 3.84 wt% MMT. It suggests that, at a given MMT content HMW PLA nanocomposites show better dispersion than LMW PLA nanocomposites. However, XRD results of both systems (see Appendix A) hardly provide distinct difference in clay dispersion. On the other hand, our NMR results on $R_{1,\,para}$ from 0.54 T indicate that clay particles are better dispersed in the high MW PLA4 than the low MW PLA2. The explanation for this observation has been addressed in Section 4.4.5.

$R_{1,\,para}$ data are converted into the relative degree of exfoliation. The reference material is chosen as 1.30 wt% MMT filled composites assumedly having $\alpha = 1$ for a semi-quantitative analysis. The relative α values for all samples are shown as a function of magnetic field strength in Figure 6.12(b). The quality of clay dispersion in both systems decreases as increasing clay content. The standard deviation shown in Figure 6.12(b) was calculated using the T_1 error from fits of experimental relaxation curves by a single exponential function. Hence, the smaller difference in the $R_{1,\,para}$ data for PLA samples and the reference material at high fields introduces the relative bigger error to α.

The field of 9.4 T offers no difference in clay dispersion between PLA2 and PLA4 nanocomposites within the experimental error. On the contrary, the low magnetic field of 0.54 T introduces smaller errors via magnifying the $R_{1,\ para}$ values. Within the experimental error the data from 0.54 T can clearly tell one that better dispersion of clay is presented in the high MW PLA4 matrix. The results for PLA nanocomposites at 7.05 T are similar to those at 0.54 T.

6.5. Conclusions

In summary, we have shown that the nuclear paramagnetic enhancement depends upon the static NMR field in the initial relaxation recovery and the spin-lattice relaxation time. The magnetization enhancement in the initial relaxation recovery was consistent with the theoretical prediction. We demonstrated that the paramagnetic contribution to the initial relaxation recovery as a function of square root of time can be used to detect: (i) clay content or impurity concentration using the first initial slope due to direct relaxation; (ii) quantitative dispersion using the second slope due to spin diffusion.

We found the magnetic field dependence of the paramagnetic contribution to the spin-lattice relaxation rate in paramagnetic polymer/clay nanocomposites. The larger paramagnetic contribution to the relaxation rate in PCNs was observed in a lower field. This effect has been utilized to facilitate extracting more reliable information on clay morphology in paramagnetic PCNs.

CHAPTER 7

Measurement of Long-distance ^{1}H Spin Diffusion Coefficients in Paramagnetic Polymer/clay Nanocomposites

7.1. Introduction

Solid-state NMR spin diffusion techniques are known to be powerful and convenient tools for elucidating heterogeneous structures and multiphase miscibility in solid systems.[42,192-193,212-217] Large insights are gained about the domain size and the interfacial thickness without stringent requirements for sample preparation or modification. The spin diffusion behavior to microscopic morphology, a spin diffusion coefficient is required. Therefore, the choice of the spin-diffusion coefficient D_s plays a vital role in obtaining accurate information on domain size in a sample. To date several strategies have been developed for determining proton spin-diffusion coefficients in polymers.[186,193,195,214,218-220] The early scheme described by Clauss et al.[193] compared NMR results with TEM and SAXS data in the phase domain sizes to estimate the spin diffusion coefficient of poly(styrene)-poly(methyl methacrylate) block copolymer (PS-PMMA) as 0.8 ± 0.2 nm^2/ms for PS. This value has been employed in turn to scale D_s in other polymer systems using the static ^{1}H line width at half intensity ($\Delta\nu_{1/2}$), and establish a relation between D_s and ^{1}H spin-spin relaxation times (T_2).[186,214] The spin diffusion coefficient was also related to the second van Vleck moment of the NMR absorption line, which is a function of $\Delta\nu_{1/2}$ and an average square of interproton distance, $\langle r_{H-H} \rangle^2$.[214,218-219] Recently, two NMR methods have been proposed for measuring D_s in polymer. They

are associated with very local polarization transfer, which is detected using a two-dimensional heternuclear correlation sequence embedded with a spin-diffusion evolution period[219,221] and ^{13}C-^{1}H REDOR experiment,[195] respectively. These two methods, however, return inconsistent D_s values for polystyrene. A more recent paper[220] describes the measurement of D_s over larger distances (2 − 5 nm) for glassy polymers which are uniformly doped by paramagnetic centers. Such an approach is limited to amorphous glassy polymers due to restrictions on the choice of paramagnetic dopants and polymer proton intrinsic relaxation times.

In previous chapters, we described spin-diffusion averaged PRE for investigating clay morphology in paramagnetic polymer/clay nanocomposites. However, in these methods (e.g., eqs 3.15, 3.17 and 4.15), we need prior knowledge of a proton spin diffusion coefficient to calculate descriptors of clay morphology. On the other hand, we can measure long-distance ^{1}H D_s using our model and information on clay morphology (typically, interparticle spacing, > 10 nm). This would be of value to the characterization of clay morphology and heterogeneous structures as well. In this Chapter, we attempt to calculate this coefficient based on the known clay morphology.

In this contribution, we describe a strategy similar to that used with impurity-doped glassy polymers,[220] for measuring the spin-diffusion coefficient over a pretty large distance (10 nm up to 100 nm) in polymer/clay nanocomposites (PCN). The common PCN investigated typically contains ~ 5 wt% clay, exhibiting an interparticle spacing of $\Delta \sim 50$ nm for well dispersed and fully exfoliated structure. Clay particles can serve as the paramagnetic relaxation centers, which quickly build up a polarization gradient by saturating the polarization of the nearest neighboring nuclei (see Chapters 2, 3 and 4).

The resultant spin diffusion takes place around the particles, and throughout the interparticle spacing that could be the diffusion distance. Since highly oriented clay platelets of large aspect ratio (50 – 1000) could form lamellar structures, the slab model of the spacing Δ was assumed in describing spin diffusion (see Chapter 4). Therefore, the characterization of interparticle spacing Δ plays a central role, which has been achieved using TEM.[41,93,95,117,119] Two different methods for calculating the diffusion coefficient in polypropylene/montmorillonite (PP−MMT) samples will be discussed: one using analytical fits of the time-dependent magnetization recovery curves by analytical solution of the Fick's law governing the spin diffusion process in this slab unit, and the other based on a simplified solution which relates paramagnetic contribution to the spacing Δ. Our measurement should therefore provide an overall average D_s in the bulk polymer, which is comparable to the reported methods discussed above. In most cases, this measurement includes the spin diffusion steps along the chain, between different chains in the bulk, and even between the multi-domains (e.g. in semi-crystalline polymer).

7.2. Experimental

7.2.1. Materials and Measurements

The details on NMR measurements are described in Chapter 2. The isotactic polypropylene/montmorillonite nanocomposite samples used in this study are films subjected to equibiaxal stretching by ratios of $\lambda = 1$ up to 3.5 (Chapter 2) as well as the cast-film of poly(lactic acid)/MMT nanocomposite cast films are also studied (Chapter 6). All NMR experiments were conducted on a Bruker DSX-300 spectrometer. The

reported data on nylon 6[42,45,51,79,222], PS[44], PCL[43], PLA[223] and PBT[222] were taken from the literature (see Table 7.1).

7.2.2. TEM Statistics of Interparticle Spacing

In Chapter 1, we reviewed some techniques for measuring interparticle spacing in PCNs. We address a method that was descried to determine the platelet distance (Δ_{TEM}) from statistics on TEM images by van Es.[117] A test line (the inset of Figure 7.1a) is drawn, perpendicular to the orientation direction in a TEM image for a PP−MMT sample with $\lambda = 3.5$ (PP−MMT$_{3.5}$) as shown in Figure 7.1(a), then the average spacing from this test line is given by $\Delta_i = L/(N_L - 1)$, where L is the total length of the test line numbered by i, and N_L is the number of clay particles intersecting the test line or close to the test line within Δ_i ($N_L - 1$: the number of entities or units). A point we need to note is that the counted particles include nearby ones in addition to the intersected ones (e.g., marked by the red open rectangle in Figure 7.1a), because these nearby particles also affect the relaxation of nuclei around the drawn line. Another point is that two particles are considered one when separated by < 2 nm (the height of clay gallery, ~ 2 nm in the PP−MMT samples = the basal spacing, ~ 3.3 nm – the thickness of a single platelet, 1 nm). Also, we clearly see many platelets normal to the view direction of TEM. Such a clay structure could create difficulties in identifying the accurate value of N_L. Testing more lines and having more counted particles in several TEM images could improve the accuracy of Δ_{TEM}.

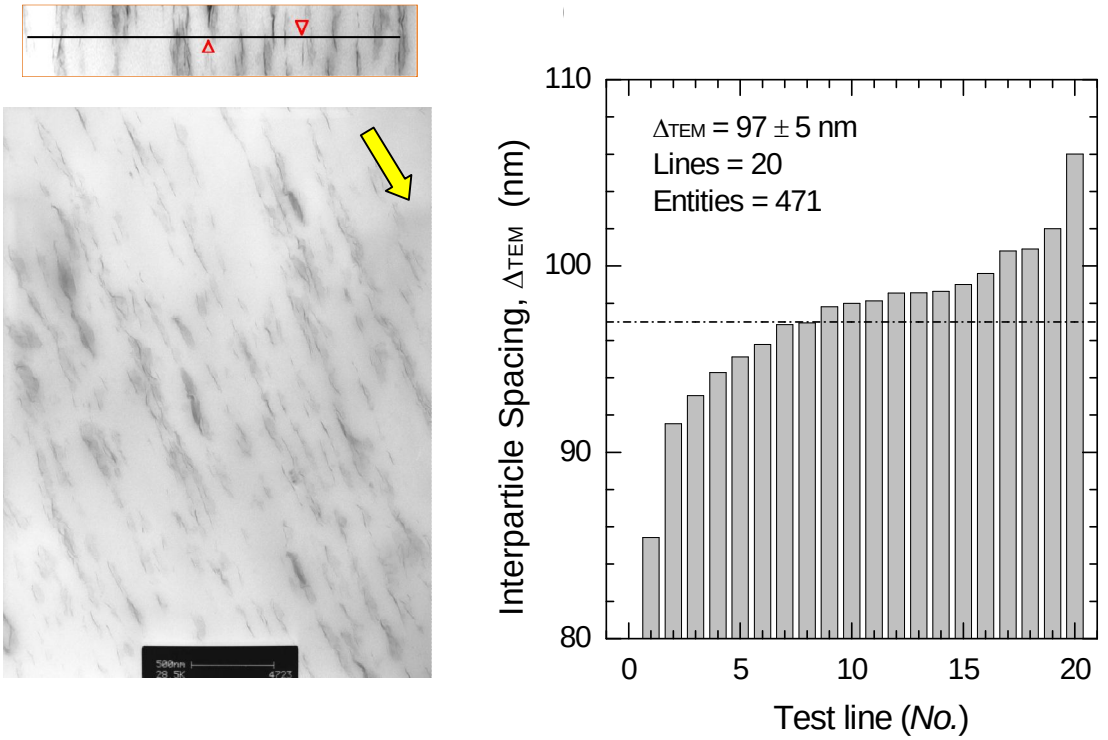

Figure 7.1. Microstructure of the PP-MMT nanocomposite film with a stretch ratio of λ = 3.5 (PP−$MMT_{3.5}$): (a) Representative image with a scale bar of 500 nm; (b) TEM statistics on average interparticle spacing (= line length /number of entities) as a function of test lines, which are sorted by the spacing from the smallest to the largest. The inset in (a) illustrates an example of the test line drawn perpendicular to the orientation direction of stacks and/or platelets in a specific magnified region of the TEM image; the triangle markers indicate the special platelets numbered as crossing ones when they are close to the line within < 50 nm. The total number of entities (sum of sample size) intersecting these twenty lines is 471. The dash-dotted line in (b) shows an average spacing of 97 ± 5 nm. Note that the arrow in (a) indicates the primary orientation direction of clay particles.

For the PP-MMT film with a stretch ratio of λ = 3.5 (PP−$MMT_{3.5}$), TEM data from 20 total lines that cover 471 entities are shown in Figure 7.1(b). The average value of TEM spacing in PP−$MMT_{3.5}$ can be calculated by

$$\Delta_{\mathrm{TEM}} = \sum_m \left[\Delta_m \times \frac{N-1}{\sum (N-1)} \right] \tag{7.1}$$

Here, for PP−$MMT_{3.5}$, Δ_{TEM} = 97 ± 5 nm. Following the same procedure, we determined Δ_{TEM} for all films with different stretch ratios, which are shown in Table 2.2.

7.3. Results and Discussions

Highly oriented and well-dispersed/exfoliated clay particles were achieved in PP−$MMT_{3.5}$ (Figure 7.1a). Proton T_1^H was measured to be 633 ms. T_1^H = 805 ms was measured for the neat $PP_{3.5}$ at λ = 3.5; T_1^H = 10 ms was measured for Cloisite 15A, which was filled in PP−MMT samples (see Table 2.1). The extremely short T_1^H of the modifiers in Cloisite 15A is much smaller than those of $PP_{3.5}$ and PP−$MMT_{3.5}$, thereby ensuring that these modifiers have less influence on calculation of the relaxation times (Figure 2.1). On the other hand, the 0.4 nm thick layer of nuclei on the surface of platelets can serve as the sources for the polarization transfer to the remote nuclei via spin diffusion (see Chapter 2). Considering these factors, we used a one-dimensional lamellar model to describe the diffusion process starting from the source (e.g., clay particles) and proceeding through their interparticle region of thickness, Δ_{TEM}, where a single spin-diffusion coefficient and spin density is assumed (see Chapter 4). The solution to the one-dimensional lamellar model for a combination of Fick's law diffusion description of spin diffusion process and ^{1}H spin-lattice relaxation was given by eq 4.9.

$$\frac{M(t)}{M_o} = 1 - \phi_1 \sum_{n=0}^{\infty} \beta_n^{-1} \exp\left[-\left(\frac{8\beta_n D_s}{\Delta^2} + \frac{1}{T_{1,m}} \right) t \right] \tag{7.2}$$

where $\beta_n = (2n + 1)^2\pi^2/8$, Δ is the interparticle spacing and $T_{1,m}$ is the apparent spin-lattice relaxation time of the matrix in the space without paramagnetic influence. It should be noted that the interparticle spacing, Δ in eq 7.2 does not include the 0.4 nm thickness of the undetectable nuclei layer. It is justified to approximate $\Delta \approx \Delta_{TEM}$, taking into account that 0.4 nm is much less than Δ. In practice, $T_{1,m}$ in eq 7.2 is generally assumed to be the same as the intrinsic relaxation time ($T_{1,polymer}$) of the corresponding neat bulk polymer.

The time-dependent magnetization recovery curve is fitted using the approximate analytical expressions, eq 7.2. A good fit to match the experimental data was established by using only the first 10 terms of the sum (n = 0 – 9). Fewer terms lead to larger discrepancy from the data points, especially at the short recovery times. The results of the fitting are shown in Figure 7.2(a) and the resulting D_s values are indicated by the open circle marks in Figure 7.2(b). The average D_s = 0.30 ± 0.02 nm^2/ms is found for spin diffusion coefficient in isotatic PP.

The paramagnetic contribution to the spin-lattice relaxation rate ($R_{1,para}$) can be calculated by $R_{1,para} = 1/T_{1,para} = 1/ T_{1,PCN} - 1/ T_{1,polymer}$) (see Chapter 4).. Furthermore, we have eq 4.10 as

$$\frac{1}{T_{1,PCN}} \approx \frac{\pi^2 D_s}{\Delta^2} + \frac{1}{T_{1,m}} \tag{7.3}$$

An expression for D_s in terms of measurable quantities is obtained by rearranging eq 7.3:

$$D_s \approx \Delta_{\mathrm{TEM}}^2 R_{1,\,\mathrm{para}} \Big/ \pi^2 \qquad (7.4)$$

where $\Delta_{\mathrm{TEM}} \approx \Delta$, and $R_{1,\mathrm{para}} = 1/\,T_{1,\mathrm{PCN}} - 1/\,T_{1,\mathrm{m}}$ by assuming $T_{1,\mathrm{m}} \approx T_{1,\mathrm{Polymer}}$. Here, for PP−MMT$_{3.5}$, $\Delta_{\mathrm{TEM}} = 97 \pm 5$ nm, $T_{1,\mathrm{PCN}} = 633 \pm 11$ ms, and $T_{1,\mathrm{polymer}} = 805 \pm 7$ ms, a value for the spin diffusion coefficient is calculated to be $D_{\mathrm{s}} = 0.32 \pm 0.06$ nm^2/ms. Following the same procedures, we obtained D_{s} values for a series of PP−MMT films as indicated by the solid circle makers in Figure 7.2(b). Except the unstretched sample with big error of Δ_{TEM}, the average value of D_{s} calculated by eq 7.4 is $D_{\mathrm{s}} = 0.32 \pm 0.04$ nm^2/ms. This result is completely consistent with that obtained by fitting magnetization recovery curves to eq 7.2, suggesting that the value of D_{s} calculated by eq 7.4 is not largely affected by the adopted simplifications and assumptions.

For isotactic polypropylene (iPP), the calculated spin-diffusion coefficients are in agreement with the published values. In particular, they are exactly the low limit of D_{s} (0.3 − 0.5 nm^2/ms) measured by Schmidt-Rohr et al.[195] The calculated effective diffusivities are multi-domain averaged, which reflect spin diffusion across the rigid, intermediate and mobile domains throughout samples.[184] Hence, the value of D_{s} measured by our method is largely dependent on the domain size and fraction in heterogeneous systems as well as the polymer dynamics.[186,192-193,215,218] An effective diffusivity in heterogeneous systems can be estimated by $D_{\mathrm{s,eff}} = 2\sqrt{(D_{\mathrm{mobile}}D_{\mathrm{rigid}})}/(\sqrt{D_{\mathrm{mobile}}} + \sqrt{D_{\mathrm{rigid}}})$,[186,215] where D_{mobile} and D_{rigid} are the spin-diffusion coefficients estimated by the static line-widths for the mobile and rigid domain, respectively. This method yields effective $D_{\mathrm{iPP}} \approx 0.50$ nm^2/ms for iPP having $D_{\mathrm{mobile}} \approx 0.13$ nm^2/ms and $D_{\mathrm{rigid}} \approx 0.62$ nm^2/ms at room temperature as reported by Hedesiu et al.[184] Following their procedure, we obtain exactly the same effective spin-diffusion

coefficients for our samples as their estimations. This may arise from the similar crystallinity of our samples as their iPP sample, which was tested by differential scanning calorimetry (DSC). It is clear that the value, ~ 0.3 nm^2/ms obtained by our model is smaller than the effective $D_{s,eff}$ calculated using the static line-width method. However, there have been indications that the static line-width method yields the upper limit for D_s that is consistent with the upper boundary of D_s = 0.5 nm^2/ms, reported by Schmidt-Rohr et al.[195] In fact, different D_s values estimated by different methods could be due to the origin of these two methods, as mentioned above.

We should emphasize that, the model of T_1^H relaxation described by a simple combination process of a Fick's law diffusion and ^1H spin-lattice relaxation would be incomplete, because there are multiple relaxation and spin diffusion processes in paramagnetic PCNs composed of semicrystalline polymers. The relaxation due to the direct interaction between neighboring nuclei and impurity centers may contribute to part of the initial magnetization recovery at short times.[45,200] Here, we limited ourselves to simulating the whole recovery process including the initial relaxation recovery. Equation 7.4 is associated with the relaxation time. Thus, estimation of D_s using eq 7.4 could be not influenced by the initial relaxation recovery. However, in order to calculate $R_{1,para}$, the similarity between the $T_{1,m}$ of matrix in PCN and the corresponding pure polymer is assumed. This assumption has been verified in some cases, such as nylon 6[42] and poly(vinyl alcohol).[201] These two methods for an estimation of D_s agree with each other to a degree (Figure 7.2b), suggesting that the initial relaxation recovery could not put too much into our estimations.

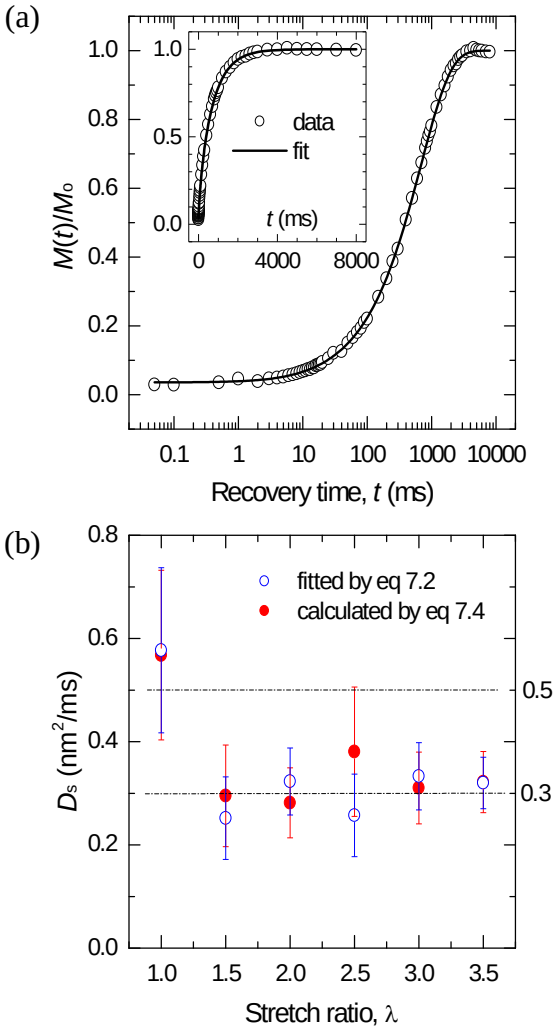

Figure 7.2. (a) ^{1}H NMR magnetization recovery curve following saturation, against recovery time for PP−MMT$_{3.5}$. The line through the experiential data is the best fit to the diffusion model, eq 7.2 having the first 10 terms of the summation (n = 0 to 9), where Δ = 97 nm for the interparticle spacing in PP−MMT$_{3.5}$. The best fit was obtained with D_s = 0.32 ± 0.02 nm^2/ms. (b) spin diffusion coefficients of PP−MMT films with stretch ratios from λ = 1.0 (unstreched) to λ = 3.5, obtained by the method in (a) and calculated using eq 7.4 with the interparticle spacing, Δ_{TEM} reported in Table 2.3. These D_s values from these two methods are comparable, consistent with the low limit of the range shown between the dot-dashed lines, D_s = 0.3 – 0.5 nm^2/ms for isotactic PP reported by Schmidt-Rohr et al.[195]

The foregoing results for iPP are comparable to the reported values. Thus, we are justified in the determination of D_s by eq 4, but we must certainly consider uncertainties

of the accuracy of D_s that arise from its dependence on the square of interparticle spacing. Now we estimate the spin diffusion coefficients for various polymers in the reported polymer/MMT nanocomposites directly using eq 7.4. The most important factor, the interparticle spacing is estimated according to the clay dispersion using the following methods. (a) TEM in case high-resolution TEM images are available, (b) The ideal spacing, Δ_i (= h_0 $(1/\phi_c - 1)$, see eq 4.2) is taken for the PCNs with well-dispersed and fully exfoliated clay structure (see Chapter 4). The whole picture on clay morphology can be acquired by the combination of TEM images showing the quality of clay dispersion with XRD or X-ray scattering assumedly indicating the full exfoliation by no presentation of the basal peak. (c) the NMR spacing proposed by Bourbigot et al.[44] This estimate could ignore the quality of platelet distribution.

The spin-diffusion coefficient, $D_s \sim 0.7$ nm^2/ms for nylon 6 estimated from T_1^H times of nanocomposites measured under two different static fields of 2.35 T and 7.05 T,[146] is completely consistent with the accepted values of 0.8 ± 0.2 nm^2/ms for rigid polymers.[193] The estimated values at the higher static fields of 9.4 T and 11.75 T, apparently decrease to 0.6 – 0.4 nm^2/ms. There are several potential factors contributing to this tendency in semicrystalline nylon 6: (a) uncertainty in estimation of the spacing; (b) fractions of domains; (c) Fe^{3+} concentration of clay, and (d) field dependence of $R_{1,para}$. We realize that the paramagnetic contribution, $R_{1,para}$ demonstrates the static-field dependence in our PP–MMT and poly(lactic acid)/MMT (PLA–MMT) samples (see Chapter 6). In these case except the sample from UBE Ltd. (Japan) in Ref. 79 , the concentration of Fe^{3+} as Fe_2O_3 is ~ 5 wt% in the neat MMT. Uncertainty in estimation of the spacing should be considered, because the error, ± 10 nm in the spacing of < 100 nm

for these nylon 6 cases produces ± 0.1 nm^2/ms in our estimations. Field dependence of $R_{1,para}$ should be considered as well. The determination of D_s for nylon 6 according to the static line-width method is possibly underestimated due to the disadvantage of this method. In addition, addition of ethylenemethyl acrylate copolymer (EMA, 5wt%) into nylon 6 /MMT could be one of reasons for a low spin-diffusion coefficient D_s, 0.25 ± 0.11 nm^2/ms for the nylon 6-EMA blend.[51] Within these considerations, our estimation of D_s for nylon6 is to some degree in agreement with literature values.

Estimations of D_s are shown in Table 7.1, including polystyrene (PS),[44] poly(ε-caprolactone) (PCL),[43] PLA[223] and poly(butylene terephthalate) (PBT).[222] It is clear that our evaluations are close to the values in literature or those calculated from the static line-width method. As described by Bourbigot, et al.[44] the exfoliated PS/MMT nanocomposite (PS–VB16) exhibits heterogeneities, that is, clay dispersion is inhomogeneous. TEM images with different magnified scales display that the average interparticle spacing is much larger than the locally-focusing spacing between 10 and 50 nm.[44] If we use the spacing obtained from TEM, it would cause erroneously smaller values of D_s for PS. In addition, the ideal spacing for this sample is not reasonable for our model to evaluate D_s of PS, because our model requires homogeneous distribution as well as high orientation for an accurate TEM-based spacing as mentioned above. Within these limits, it is justified to claim that our estimation for D_s of PS will be between 0.14 and 0.94 nm^2/ms. The PLA-MMT sample we investigate here gives the exactly same value of D_s for PLA as that reported by Bourbigot et al.[223] In addition, our value of D_s for PBT is close to the prediction for the similar polymer, poly(ethylene terephehalate) (PET).[224]

7.4. Conclusions

In this chapter, we have proposed a method to measure proton spin-diffusion coefficients in paramagnetic polymer/clay nanocomposites on a more than 10 nm scale. It is based on paramagnetic relaxation enhancement in spin-lattice relaxation, T_1^H of polymer matrices via spin diffusion. The paramagnetic clay particles generate the sharp magnetization gradient to transfer the polarization of neighboring nuclei to the remote nuclei. In this point, the neighboring nuclei with fast relaxation serve as a 'natural' dipolar filter, which generates the magnetization gradient around diffusion sources. With an average interparticle spacing Δ obtained by TEM, numerical fits on the saturation-recovery spin-lattice relaxation curve yield average value of spin-diffusion coefficients $D_s = 0.32 \pm 0.04$ nm^2/ms for isotactic polypropylene. A slightly smaller D_s value ($= 0.30 \pm 0.02$ nm^2/ms) is also obtained from direct calculation by the paramagnetic contribution to T_1^H relative to the square of the spacing Δ. We further estimate D_s values for several polymers by this direct calculation, which are fairly in agreement with those reported in the literature or predicted using other methods. Accurate evaluation of the interparticle spacing would ensure a good estimate of D_s. In semicrystalline polymers, the method described here provides the multi-domain averaged values of D_s over a distance of more than 10 nm, which is comparable to those obtained by other techniques on the $\leq$10 nm scale. Furthermore, our method may be used to study many more polymer systems if the preparation of their clay nanocomposites is successful and information on the resultant clay dispersion is available.

Table 7.1. Reported clay morphology, T_1^H, proton $R_{1,para}$ values and calculated spin diffusion coefficients for various polymers in paramagnetic clay nanocomposites.

Polymer Matrix	Clay dispersion description[a]	MMT wt%[b]	Spacing (nm)	T_1^H [g] (s)	Field strength (T)	$R_{1,para}$ [h] (1/s)	D_s (nm^2/ms)	D_s in literatures (nm^2/ms)
iPP	Highly orientated; well-dispersed; intercalated/exfoliated	2.7	97 ± 5[c]	0.63(0.81)	7.05	0.34 ± 0.03	0.32 ± 0.05	0.3–0.5[195]; 0.62[i]; 0.5[184i]
Nylon-6	No d_{001} peak; well-dispersed[42,45]	2.85	80[d]	0.60 (1.63)	7.05	1.05 ± 0.04	0.69 ± 0.03	0.7[42,45]
				0.33 (0.53)	2.35	1.16 ± 0.09	0.76 ± 0.06	
	Well-dispersed; exfoliated [79]	1.9	120 [d]	1.08 (2.06)	9.4	0.44	0.64	
	No d_{001}peak; well-dispersed[222]	3.5	86[e]	0.77 (1.67)	9.4	0.70	0.53	
	Orientated; well-dispersed[41]	2.5-20	74-19[f]		11.75		0.52 ± 0.01	0.15–0.17 [i]
	Well-dispersed[51]	3.5	64 [d]	0.62 (1.60)	11.75	0.96	0.40	
	Stacks; clay shells[51]	3.5	50 ± 10 [c]	0.63 (1.60)	11.75	0.99	0.25 ± 0.11	
PS	Exfoliated (PS-VB16)[44]	2.0	136 (346) [d]	9.72 (39)	7.05	0.08	0.14(0.94)	0.2–0.3; 0.6–1.0
PCL	Well-dispersed; exfoliated [43]	3.5	63 [d]	0.69 (1.27)	9.4	0.66	0.27	0.4–0.6
PLA	Well-dispersed; exfoliated [223]	2.5	102 [e]	0.98 (1.46)	9.4	0.34	0. 36	0.21 [31]
	Orientated; well-dispersed	2.56	81 [d]	0.56 (0.79)	7.05	0.52	0.35	0.48 [i]
PBT	Intercalated; big stacks [222]	3.5	113 [e]	1.32 (2.49)	9.4	0.36	0.46	0.5[j]

[a] from TEM and/or wide angle X-ray diffraction (WAXD). [b] from thermogravimetric analysis (TGA). [c] obtained by TEM using the method shown in Figure 7.1. [d] calculated as the spacing in an ideally stratified structure (Δ_i). [e] Taken as the spacing (Δ_f) introduced by Bourbigot et al.[44] [f] values scaled by NMR method from sample with 5% MMT using eq 4.12 (see Chapter 4); an average spin diffusion coefficient for these samples is calculated. [g] Proton spin-lattice relaxation times of nanocomposites ($T_{1,PCN}$) and the unfilled polymer (in the parenthesis) ($T_{1,polymer}$). [h] Calculated by $R_{1,para} = 1/T_{1,PCN} - 1/T_{1,polymer}$. [i] calculated for the rigid phase following the method reported by Demco et al.[214] using the spin-spin relaxation time, T_2^H = 11 – 12 μs; average value of D_s in semicrystalline polymer calculated as sum of the individual D_s times proton fractions in multi-domains. [j] This value taken as that of poly(ethylene terephthalate).[224]

CHAPTER 8

In situ Observation of Polypropylene/Montmorillonite Nanocomposite upon Uniaxial Deformation

8.1. Introduction

The general pattern on work in polymer/clay nanocomposites is as follows: material preparation, characterization of morphology, and property measurement. The effect of a large variety of parameters has been examined within this framework. Using this information, structure-property-processing relationships have been constructed. However, despite this knowledge base, there is no generic model that guides one to design a nanocomposite with any given set of properties. What is missing is a thing: how morphology develops during processing and deformation. It is known what types of morphologies can be formed from a large variety of starting recipes, and what kinds of properties these nanocomposites exhibit. However, relatively little is known about how nanocomposite morphologies reach their characteristic forms during processing as well as how these structures behave under large-scale deformation to fracture. This knowledge, needed to complete comprehensive modeling, can be provided by conducting *in-situ* studies of nanocomposite processing and deformation. In Chapter 2, we attempted to address the evolution of clay morphology in polypropylene/clay nanocomposites upon biaxially stretching. In this Chapter, we will explore *in situ* observation of nanocomposites under mechanical deformation.

To date *in situ* deformation of PCNs has been observed using several techniques, in particular real-time X-ray techniques (WXAS and SAXS). Wang et al.[126] investigated maleated polyethylene/Cloisite 20A nanocomposite (PEMA/20A) under tensile deformation using the real-time X-ray scattering. They found that the 20A particles inhibit orientation of polyethylene crystals in the tensile direction. Similar phenomena were observed in polypropylene/organically modified montmorillonite nanocomposites by Kim et al.[225] On the other hand, results from SAXS/SANS experiments by Finnigan et al.[124] showed that clay platelets do not affect the morphology of thermoplastic polyurethanes (TPUs) upon deformation. They also found that the smaller particles in the nanocomposites are easily aligned along the direction of strain to improve the tensile properties, while big tactoids are unable to orientate, leading to void formation and reduced tensile properties. More recently, Tang et al.[137] studied polyethylene/MMT with strong interfacial interaction by X-ray scattering. They claimed that good mobility of MMT platelets can assist in improving the tensile properties during tensile deformation.

In this Chapter, we will present preliminary work on *in-situ* deformation of PP-MMT nanocomposites under mechanical stress in a home-made magnetic field. The preliminary data suggest that our experimental design could work for such observations. These investigations would offer new insights into the response of nanocomposites to deformation and provide a better understanding of mechanical behavior for nanocomposites.

8.2. Experimental

8.2.1. Materials

The extrusion-cast sheets of polypropylene and nanocomposites were provided by Dr. Harkin-Jones. These samples were prepared by melt compounding in Colin ZK25 twin screw extruder of 30:1 length-to-diameter (L/D) ratio and screw diameter 25 mm. The die gap is 1.2 mm and the extruded sheet was cooled on a pair of chilled rolls rotating at 1 m/min at 70 ^{o}C. The resultant sheets are ~ 1.0 mm thick. Some features of these sheets were characterized as shown in Table 8.1. DSC tests show no change in the crystallinity and melting temperature upon addition of clay particles, while the crystallization temperature decreases. It could be associated with the formation of a clay network which retards mobility of chains during the crystallization process. Specimens of extruded sheets in 200 mm length and 5 mm width were cut by a chopping machine to match the size of a probe in a home-made NMR.

Table 8.1. Characteristics of the tested samples.

	sample		
	PP	PP-MMT5	PP-MMT10
montmorillonite (wt%)		2.70	5.51
PP-g-maleic anhydride (wt%)	3	3	3
DSC crystallinity (wt%)[a]	44.1	44.7	44.3
T_m (T_c) (^{o}C)	168.4 ± 0.2 (120.1 ± 0.1)	168.6 ± 0.4 (117.8 ± 0.1)	168.2 ± 0.2 (117.3 ± 0.1)
XRD basal peak (d_{001})[b]		weak (3.21 nm)	strong (2.68 nm)
T_1^H (ms) [c]	368 ± 14	325 ± 8	303 ± 7
Degree of exfoliation, f [d]		0.46 ± 0.05	0.34 ± 0.03
Quality of dispersion, α[e]		0.46 ($\alpha = f$)	0.24 ± 0.02

[a] was based on the melting enthalpy, 165 J/g of perfect iPP crystals;[226-227] [b] Basal spacing of organically modified MMT is 3.15 nm. [c] Measured using saturation recovery at 0.54 Tesla for samples before stretching. [d] Measured at 0.54 Tesla following the method reported in Chapter 6. [e] measured at 0.54 T.

8.2.2. Step-strain Stress Deformation

The step-strain stress experiments were carried out on an Instron 5566 universal machine at room temperature. Bone-shaped samples with a central width of 3.18 mm were cut out of ~ 1.0 mm thick extruded sheets aligned parallel to the extrusion direction. A procedure of ten step strains was designed. During the procedure, the specimens were stretched by each stain of 4 mm at the cross-head speed of 0.8 mm/min (5 min), and then held for 30 min stress relaxation measurements. The sides of the central part of samples were carefully grand a little using sandpaper before any tensile test to influence the location of necking propagation. After deformation, the central necked surface of the stretched specimens was observed using scanning electron microscopy (SEM). SEM images were obtained using a LEO 1530 FEG field-emission instrument equipped with a thermally assisted field emission gun operating at 5 keV. The samples were sputter-coated with gold for a period of 5 min with current at 20 mA in vacuum at 0.7 Torr.

A procedure of ten tensile steps was carried out on the Instron machine, which is similar to the deformations experiences in the NMR probe. Each extension by a certain distance took ~ 5 minutes and was held for ~ 15 minutes before the NMR measurement. Each measurement for the spin-lattice relaxation time took ~ 50 min. At the end of each extension, the load on samples was supported to hold a constant deformation.

8.2.3. Home-made Magnetic Field and Mechanical Deformation System

A portable NMR system (Figure 8.1a) was design by Dr. Ulrich Scheler of the Institute for Polymer Research Dresden, Germany. The permanent bar magnets wre

arranged in a Halbach layout to offer a homogeneous field at the center of a magnet stack.[228] The resultant NMR spectrometer exhibits a magnetic field of 0.75 Tesla, operating at a frequency of 32 MHz. The NMR data acquisition and processing system, NTNMR was bought from Tecmag, Inc.

The mechanical stretch system was designed as shown in Figure 8.1(b). One end of the specimen is fixed in the frame and the other is connected with beams which can allow for vertically stretching the sample. Grinding a certain part of the specimen makes sure that this part experiences the deformation in the coil (Figure 8.2). Two stretched samples, PP and PP-MMT5.51, are displayed (Figure 8.2).

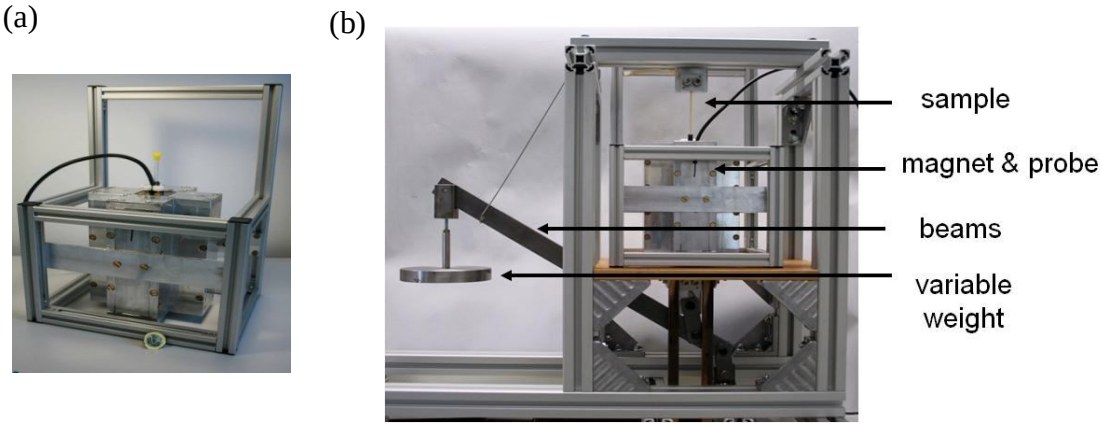

Figure 8.1. Photographs of the magnet with a probe (a), and the stretching system incorporated with the NMR magnet (b). Pictures were provided by Dr. Ulrich Scheler.

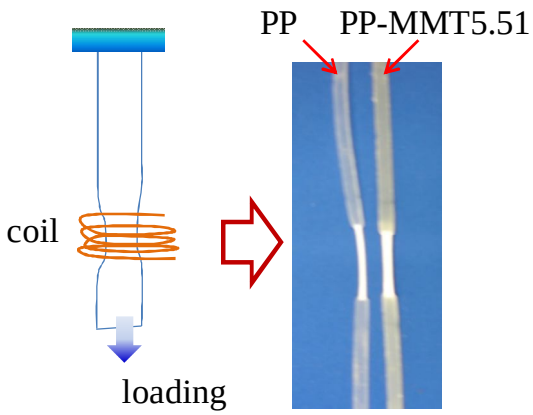

Figure 8.2. Schematic for the deformation of specimens with the grand part inside a coil of the probe in NMR. One end of the specimen is fixed in the frame, and the other is connected with beams which can allow for vertically stretching the sample when loaded. The grand part of a sample experiences the deformation in the coil. Two samples, PP and PP-MMT5.51, are displayed after deformation.

A saturation-recovery pulse program was employed for collecting the ^{1}H T_1 data. A train of 90^{o} pulses was used in the saturation stage, followed by a Hahn echo to record the recovered magnetization. The value of τ between 90^{o} and 180^{o} pulses was optimized to observe the maximum intensity of the Hahn-echo peak. 1024 scans were measured for each relaxation delay.

8.3. Results and Discussions

8.3.1. Effect of stretching on Paramagnetic Spin-lattice Rate

Figure 8.3 shows ^{1}H NMR magnetization recovery following saturation for PP-MMT5.51 before stretching. It can be seen that some noise peaks appear in 2D spectra, which are not attributed to the sample. During the relaxation process, the intensity of these peaks remains constant, while the intensity of the peak from the sample grows

(Figure 8.3a). Figure 8.3(b) displays the magnetization recovery curves based on sample peaks by the maximum values of peaks and areas of peaks. Both set of experimental data give the same relaxation time, T_1^H = 417.7 ± 10.5 ms (fitting_1 for the peak intensity data) and T_1^H = 418.7 ± 5.6 ms (fitting_2 for the peak area data). In the following sections, the peak area is used to build up the magnetization recovery curve in the saturation-recovery experiments.

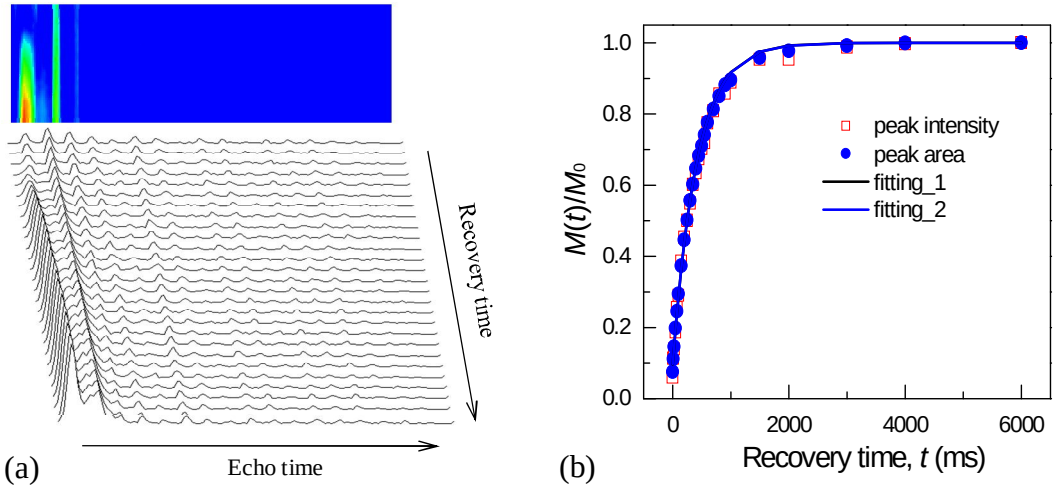

Figure 8.3. ^{1}H NMR magnetization recovery following saturation for PP-MMT5.51 before stretching: (a) two-dimensional spectra: the upper with the intensity-colored pattern and the bottom with echo slices at recovery times, and (b) Normalized magnetization, $M(t)/M_0$, as the intensity of the first peak (square marker) and the peak area (circle marker). The experimental data were fitted by a single exponential as shown in (b).

The T_1 values of PP and nanocomposites measured at 0.75 T are comparable to those at 0.54 T (Table 8.1, Figure 8.3 and Figure 8.4). Figure 8.4 shows the spin-lattice relaxation times of the pure PP and PP-MMT2.7 and PP-MMT5.51 nanocomposites upon extension. T_1^H of the pure PP slightly decreases first upon stretching. The tensile-strain curves of these samples show that the plastic deformation happens during 10 mm ~ 20

mm strain. This could be related to a decrease of T_1^H. When stretched more, T_1^H of the pure PP increases slightly due to stretching polymer chains. T_1^H of PP-MMT2.7 first decreases to reach a minimum at ~ 10 mm extension, and then increases. PP-MMT5.51 also shows the decrease of T_1^H at the early stage of deformation, and then no changes in T_1^H. The decrease of T_1^H in nanocomposites upon stretching could be attributed to two factors, the emergence of the new interfacial surface and shorten interparticle spacing. Figure 8.5(a) shows that the initial slope of $M^n(t) \sim t^{1/2}$ slightly increases at the early stage of extension in nanocomposites, while Figure 8.6(b) shows no change of the initial slope for PP.

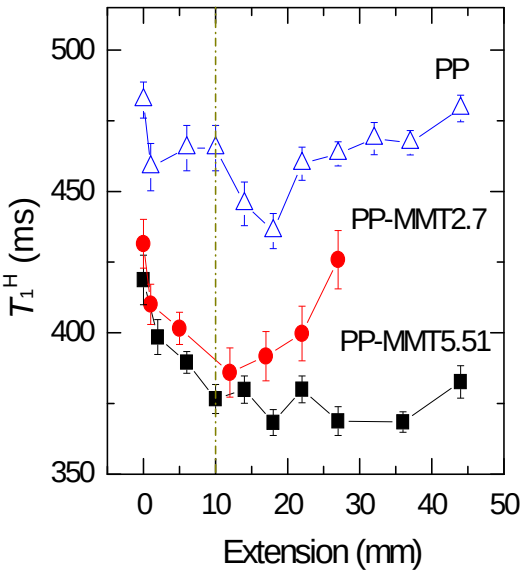

Figure 8.4. Proton spin-lattice relaxation time, T_1^H, as a function of extension for PP, PP-MMT2.7 and PP-MMT5.5 upon strain, measured at 0.75 T.

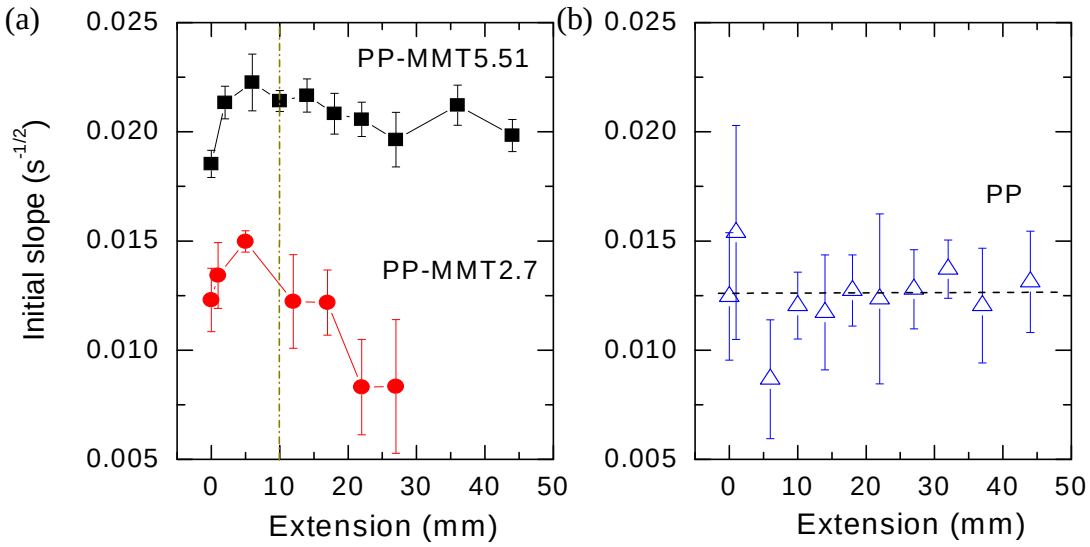

Figure 8.5. The initial slope of normalized magnetization proportional to the square root of recovery time, as a function of strain for PP, PP-MMT2.7 and PP-MMT5.5 upon strain, measured at 0.75 T. Due to low signal-to-noise rato, we directly calculate the initial slope in the first 20 ms without removing the contribution of PP intrinsic relaxation. Note that the initial slope between 1 ms and 50 ms is computed for the pure PP.

Figure 8.5(a) shows that the initial slope of nanocomposites decreases after a certain extension. This suggests that nanocomposites lose the effective surface after a certain extension. At a large extension, the voids and cavities on the polymer/clay interface have often been observed due to the de-bonding between particles and polymer.[126,137-138] Formation of these defects should decrease effective interfacial surface area in PP-MMT nanocomposites.

8.3.2. Mechanical Behavior and Morphology

A similar deformation to that in the probe of NMR was carried out on an Instron machine, in order to better understand the preliminary NMR results. Figure 8.6 shows

the stress relaxation behavior for the pure PP, PP-MMT2.7 and PP-MMT5.51. The addition of clay leads to an increase in the stress relaxation rate, independent of the clay content. The increase of stress relaxation rate is associated with the network formation of polymer and clay particles.[229-231] Also, Figure 8.6 indicates that the stress relaxation is fast in the beginning, and then become slow. Our NMR measurements were started 900 s after each strain. Thus, we detected NMR signal from polymer chains that have been mostly relaxed. The remaining stress during NMR detection is higher in nanocomposites than in pure PP, due to the clay particles interacting with polymer chains.

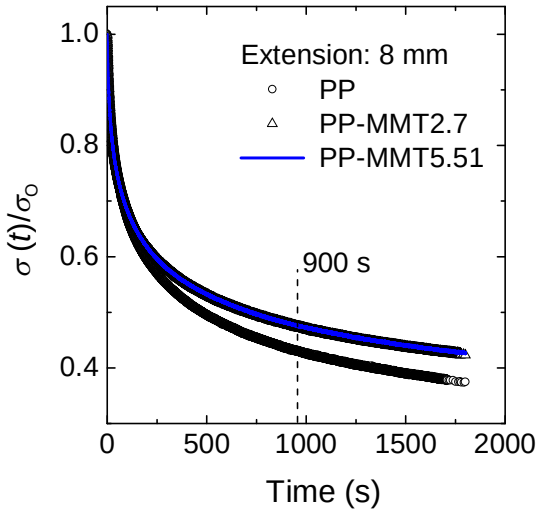

Figure 8.6. External deformation on Instron machine for PP, PPCN2.7 and PPCN5.5: representative stress-relaxation curves, given as $\sigma(t)/\sigma_0$ versus time by the extension of 8 mm. σ_0 is the initial stress during the relaxation. Note that the dashed line marks the time we started to collect NMR signal.

Figure 8.7 shows scanning electron micrographs of central necked surfaces of PP, PP-MMT2.7 and PP-MMT5.51, deformed by ten step strain of 40 mm extension. It is clear to see homogeneous surface morphology without any voids in the pure PP upon

deformation. Figure 8.7(c) shows that the breakups and deep elongated cavities as well as cracks in PP-MMT5.51. It is known that clay particles, in particular large aggregates with weak interfacial interaction, initiate the formation of cavities.[104,126,137-138] In contrast, besides the small cavities, PP-MMT2.7 exhibits fibrillar morphology that is composed of the stretched polymer chains. The fine nanoparticles and stronger interfacial adhesion in PP-MMT2.7 could inhibit the growth of cavities and aid in stretching polymer chains.

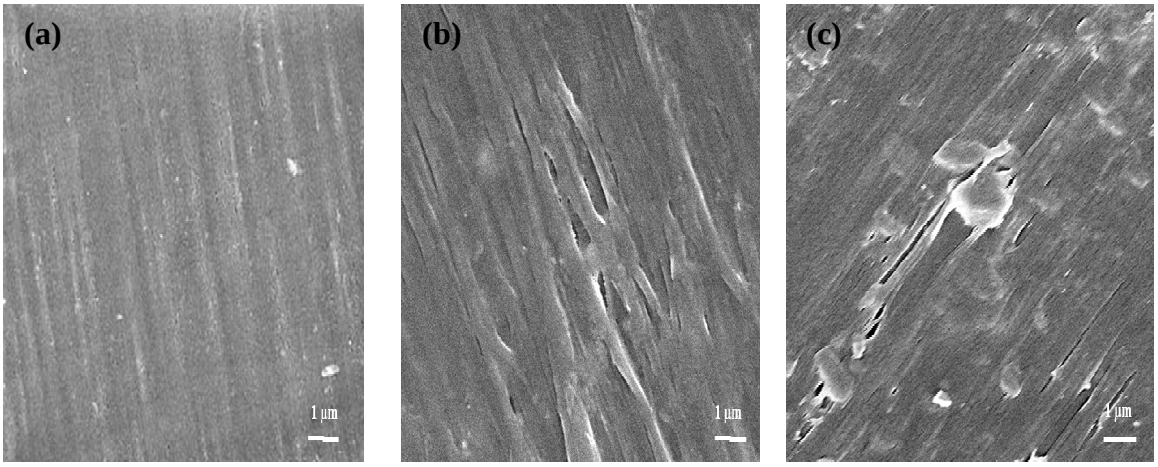

Figure 8.7. Scanning electron micrographs of central necked surfaces of PP (a), PP-MMT2.7 (b) and PP-MMT5.51 (c), after being deformed by ten step strain of 40 mm extension.

8.4. Discussion

PP/MMT nanocomposites were mechanically deformed in a home-made NMR spectrometer with magnetic field of 0.75 T. Spin-lattice relaxation times for PP-MMT nanocomposites tested at 0.75 T are comparable to those collected with commercial NMR spectrometers operating at 0.54 T and 7.05 T. We compare NMR relaxation times

and initial slopes in two nanocomposites: one is PP-MMT2.7 containing fine clay particles and strong interfacial adhesion, and the other is PP-MMT5.1 with big clay stacks and weak adhesion.

Upon deformation, nanocomposites show decreased proton spin-lattice relaxation times (T_1^H) and slightly increased initial slopes before a certain extension. The shortening of T_1^H indicates a decrease in the interparticle spacing (Chapter 4); the increase in the initial slope suggests an increase in effective interfacial surface area (Chapters 2 and 3). Upon elongation of the PCNs, clay particles have been observed to peel apart, align and approach each other (Figure 8.8a).[124,126,225,232] These transformations of clay particles lead to decreased interparticle spacing and increased interfacial surface, consistent with NMR results.

Interfacial adhesion and particle size play central roles in the response of nanocomposites to deformation.[104,126,137-138] Considering addition of 3 wt% PP-g-MA compatibilizer into these two samples, more PP-g-MA chains can cover the clay surface at a low content, which enhance compatibility between PP and MMT. Thus, more PP-g-MA provides the stronger interfacial adhesion between PP chains and clay surface at a low content than at a high content. Strong surface adhesion in PP-MMT2.7 would enable the formation of polymer-clay network (Figure 8.8b), and assist in orientation and alignment of chains as well as particles under the external deformation.[135,137,225] In the network, polymer chains can be easily stretched (Figure 8.8b). This might explain that T_1^H in PP-MMT2.7 increases after certain extension. SEM images show fibrillar morphology related to stretched polymer chains on the surface of PP-MMT2.7 (Figure 8.7b).

Bigger particles easily initiate the formation of voids, cavities and cracks between platelets inside particles due to weak adhesion.[104,126,137-138] The resultant breakup of particles could not change polymer-clay interface. Upon this motion of particles, particles effectively dissipate the energy for the external force, which hinders the further stressing of polymer chains and decreases the debonding between clay and matrix (Figure 8.9). As a consequence, PP-MMT5.51 exhibits no increase in T_1^H even after a large extension (Figure 8.4a). The formation of cracks and deep cavities can be clearly observed in the SEM image of PP-MMT5.51 (Figure 8.7c). At the same time, PP-MMT5.51 shows relatively small loss of effective interfacial surface relative to PP-MMT2.7 (Figure 8.5a). In contrast, the initial slope of PP-MMT2.7 containing fine clay particles decreases more (Figure 8.5a). It is associated with the loss of effective interface surface, as illustrated in Figure 8.9(a). The strong interfacial adhesion in PP-MMT2.7 assists in stretching polymer chains after ~ 10 mm extension, leading to an increase in the tension between clay and matrix. Upon further extension, this increasing surface tension would create the de-bonding between clay and matrix to lose more effective interfacial surface.

In this chapter, our preliminary results offer a rough picture on evolution of clay morphology in nanocomposites upon deformation by *in situ* NMR observations. It should be emphasized that more experiments need to be carried out in different deformation conditions, including strain rate, extension, and temperatures. Incorporation of the NMR into an Instron machines will help one to observe the mechanical performance at the same time the NMR signal can be collected. This combination as well as visualized morphology characterization will provide a complete picture on the evolution of morphologies in PCNs upon deformation.

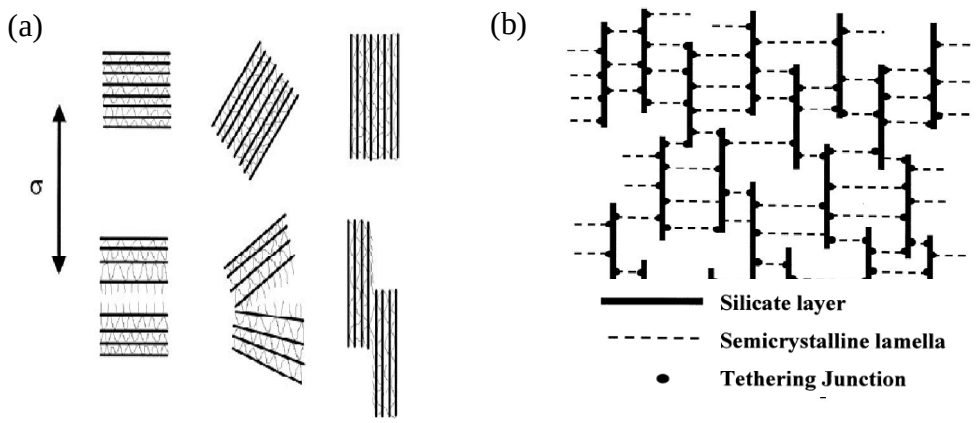

Figure 8.8. Proposal for structural and morphological responses of polymer/clay nanocomposites to deformation[138]: (a) splitting, opening and sliding of the silicate platelets inside stacks and (b) network of polymer and clay particles that are strongly bonded to each other.

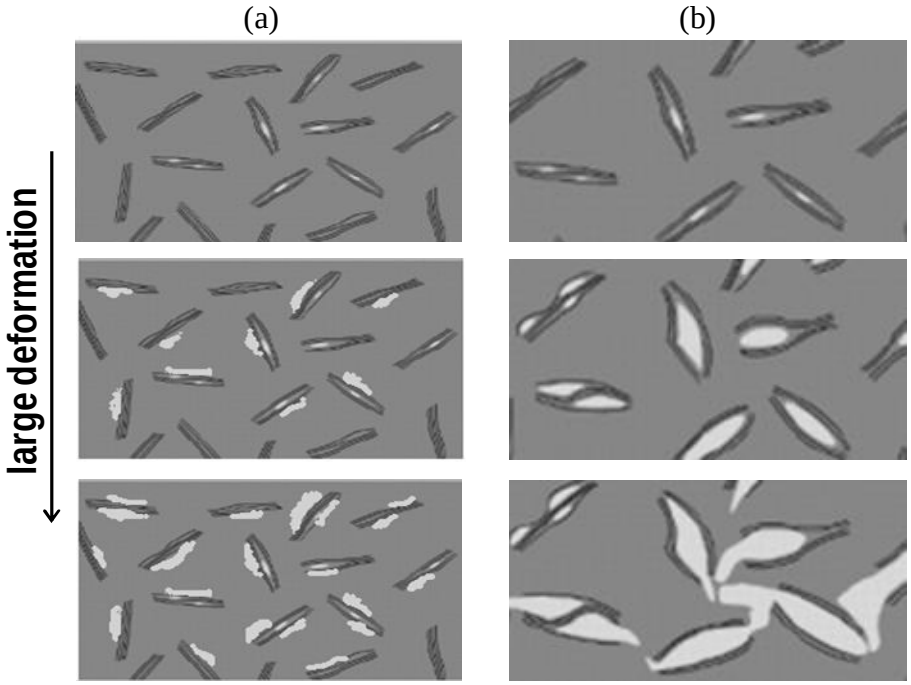

Figure 8.9. Schematics for the evolution of microvoids, cavities and cracks around fine clay particles (a) or inside clay big stacks (b) in nanocomposites upon large deformations.[104] Note that the white regions indicate the microvoids, cavities and cracks.

CHAPTER 9

Proton Relaxation in Organically Modified Clays

9.1. Abstract

Proton spin-lattice relaxation in organically modified clays was investigated using solid state NMR. Experiments using proton Bloch decay and spin-lattice relaxation revealed that the paramagnetic impurities largely broaden the line width. Increasing temperature improves the line narrowing but rather limitedly. Magnetization growth in paramagnetic organoclays was well described by a stretched exponential with the power of ~ 0.85, which is close to a theoretical prediction, 5/6. We found the field and temperature dependences of paramagnetic contribution to the relaxation time ($T_{1,para}$) in paramagnetic organoclays. The correlation time of impurity centers was estimated to be 1.4×10^{-9} s < τ_C < 9.6×10^{-8} s. The exponent dependence of $T_{1,para}$ on the field strength is close to 1, which is theoretically predicted in the diffusion-vanishing case. EPR spectra of two paramagnetic organoclays show two resonances from isolated Fe^{3+} ions and Fe^{3+} ion clusters. The peak-to-peak line-width of isolated Fe^{3+} ions resonance provides the spin-spin relaxation time of impurities, $\tau_S = 3.6 \times 10^{-9}$ s, consistent with our estimation from proton spin-lattice relaxation.

9.2. Introduction

The importance of the spin-lattice relaxation of nuclear spin in paramagnetic polymer/clay nanocomposites has been stressed in characterizing their clay morphology

in previous Chapters. The paramagnetic enhanced spin-lattice relaxation strongly depends on the relaxation sink - organically modified clay. In Chapter 2, the spin-diffusion barrier was found to be 0.4 nm thick around the clay platelets. In this barrier region, relaxation of nuclei is extremely disturbed by the strong fluctuating electron magnetic field produced from impurity centers inside clay platelets. The neighboring protons could not be observable due to a large line-broadening. The neighboring protons just beyond the barrier region, which are still under the electron magnetic fields, exhibit the fast spin-lattice relaxation due to their coupling with electrons. The relaxation rate due to the dipolar electron-nucleus coupling increases with the distance as r^{-6}. The signal from these neighboring protons collected at a low magnetic field can be used to correlate with clay content as well as impurity concentration inside clay (see Chapter 6). The magnetization gradient around particles built by these protons facilitates transferring the polarization of the neighboring nuclei to the remote via spin diffusion. These paramagnetic effects lead to the initial relaxation behavior (Chapters 2, 3 and 6) and spin-diffusion averaged paramagnetic contribution to the relaxation rate (Chapter 4). The initial relaxation behavior has been correlated to polymer/clay interfacial surface area and the exfoliation (Chapters 2 & 3); the latter can be employed to quantify average interparticle spacing and the quality of clay dispersion (Chapter 4). As a result, investigating the spin-lattice relaxation of the organically modified clay will be of value to understand paramagnetic enhanced NMR relaxometry in polymer nanocomposites. In the present Chapter, we focus on investigating spin-lattice relaxation of organoclay before filled in polymer matrix as a function of magnetic fields and temperature.

In order to increase the compatibility of hydrophilic silicate platelets with organic polymer, the cationic surfactants are normally exchanged with the interlayer cations.[9,62,84,137,233] The surface of the modified clay (organoclay) covered by hydrophobic alkyl chains shows reduced surface energy.[67-69] Such a surface can be more easily accessed by organic polymers by interacting with silicate and/or surfactants.[67,84,136] Surfactant chains in galleries of clay prefer to exist in an ordered arrangement like 'paraffinic' structure, or in a disordered liquid-like arrangement, which depends on the exchange content, alky chain number, alkyl chain length and temperature.[234-236] The protons of surfactant chains experience the different electron-nucleus interaction. In addition, the electron-nucleus coupling constant depends on the correlation time of impurity center, as indicated in eq 2.3. It is affected by the spin exchange between electron spins from the nearest Fe^{3+} ions in the same platelets and in two nearest platelets.[207] As a consequence, the details on the spin-lattice relaxation of the neighboring protons and the correlation time of impurity center could be of value to a better understanding of paramagnetic characteristic of clay particles. However, so far few such studies have been reported. In this chapter, two kinds of organoclays were investigated: one with paramagnetic impurities; the other without any impurities.

9.3. Experimental

Measurements were carried out on three organoclays shown in Table 9.1. The details on these two organoclays, Cloisite 15A and MAE-100 refer to Table 2.1. Cloisite 30B (Southern Clay Products Inc. TX) was also investigated, which was filled in PLA and PCL nanocomposites (Chapters 4 & 6). Before any measurements the samples were

dried under vacuum at 110 ^{o}C for 48 hrs and cooled for 72 hrs at room temperature. Differential scanning calorimetry (DSC) runs were performed on a Seiko 220C at a heating rate of 10 °C/min to 150 °C.

Table 9.1. Structural Characteristics of Organically Modified Clays[a]

	Montmorillonite		Fluorohectorite (FH)
Mean formula unit[b]	$Na_{0.65}[Al,Fe]_4Si_8O_{20}(OH)_4$		$Na_{0.66}Mg_{2.68}(Si_{3.98}Al_{0.02})O_{10.02}F_{1.96}$
Commercial name	Cloisite 15A	Cloisite 30B	Somasif MAE-100
DSC, T_m (^{o}C)	45.6	n/a	49.2
Fe_2O_3 content (wt %)	2.83[c]	3.51[c]	0
CEC (meq/100 g)[d]	125	90	85 ~ 120
Weight loss on ignition (%)	43	30	42
Basal spacing (nm)	3.2	1.85	3.4
Organic modifier[e]	2C18	C18	2C18
Area per cation (nm^2)[f]	~1.51	~1.48	~1.35
T_1^H (n) at 7.05 T (ms)[g]	10 (0.87)	5.7 (0.84)	290 (0.94)

[a,b,d,f] see Table 2.1.[c]determined by elemental analysis and corresponds to 4.96 wt % Fe_2O_3 and 5.02 wt% Fe_2O_3 in the pure clay of Cloisite 15A, and Cloisite 30B, respectively. [e] Cloisite 15A with tallow-sourced dimethyl dialkyl ammonium chlorides, and Cloisite 30B with methyl tallow bis-2-hydroxyethyl ammonium chlorides in which the alkyl tails consist of ~ 65 wt % C_{18}, ~ 30 wt % C_{16} and ~ 5 wt % C_{14}, and ~ 25 wt % C_{18}, ~ 74 wt % C_{16} and ~ 1 wt % other for FH. [g] fits of a stretched exponential (e.g., eq 3.4) to magnetization recovery curves in saturation-recovery experiments at 7.05 T; the exponent n is shown in the parenthesis.

The saturation-recovery sequence was used for collecting magnetization recovery at four magnetic fields with the field strength of 0.54 T, 7.05 T, 9.4 T and 14.1 T. To see details in Chapters 2 and 6. Bloch decay spectra were recorded at 7.05 T using 5 μs 90^0 pulse, 1 μs dwell time and 128 scans. Solid state 13C direct polarization MAS experiments at room temperature are referred to the details in Chapter 2.4.

X-band electron paramagnetic resonance measurements were recorded with a X-band Bruker EMX spectrometer operating at 9.868 GHz. A Bruker HS4119 high sensitivity cavity was operated with a microwave power of 3.181 mW, modulation

frequency 100 kHz, time constant 163.8 s, conversion time 81.9 s, modulation amplitude 2 G, sweep time 84 s and scans 5.

9.4.Results and Discussions

9.4.1. Line Broadening by Paramagnetic Impurities in Organoclay.

The effects of paramagnetic impurities on the line broadening have been well documented in the impurity-doped bio-macromolecules and polymer/Fe^{3+} -containing montmorillonite nanocomposites. The line broadening in Bloch-decay proton spectra for organically modified paramagnetic MMT (Cloisite 15A) is detected with comparison to the diamagnetic fluorohectorite (MAE-100) as indicated in Figure 9.1. The corresponding time-domain free induction decays (FIDs) are displayed with variable temperature in Figure 9.2. As seen in plots, paramagnetic impurities broaden the line shape of proton Bloch-decay spectra so much that FIDs show one Gaussian component at all temperatures, apparently showing no transition around melting temperature. In contrast, MAE-100 obviously exhibits a melting transition from two components with fast and low decays to one. Upon further heating, the change in dynamics of the modifiers becomes slow. This could be associated with liquid-crystalline modifiers in the galleries showing incompletely disordered arrangement above the melting temperature.[234]

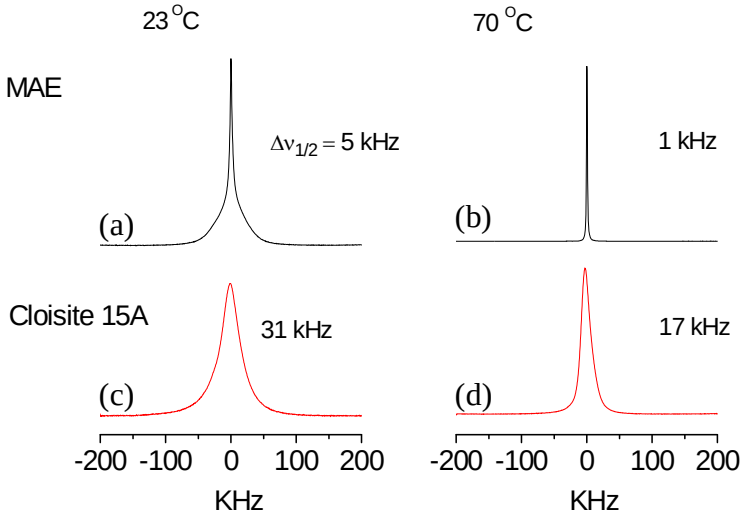

Figure 9.1. Proton Bloch-decay spectra of MAE without impurities (a, b) and paramagnetic Cloisite 15A (c, d) at 23 °C (left side) and 70 °C (right side). The line-width at the half intensity, $\Delta\nu_{1/2}$ is shown beside the corresponding spectrum.

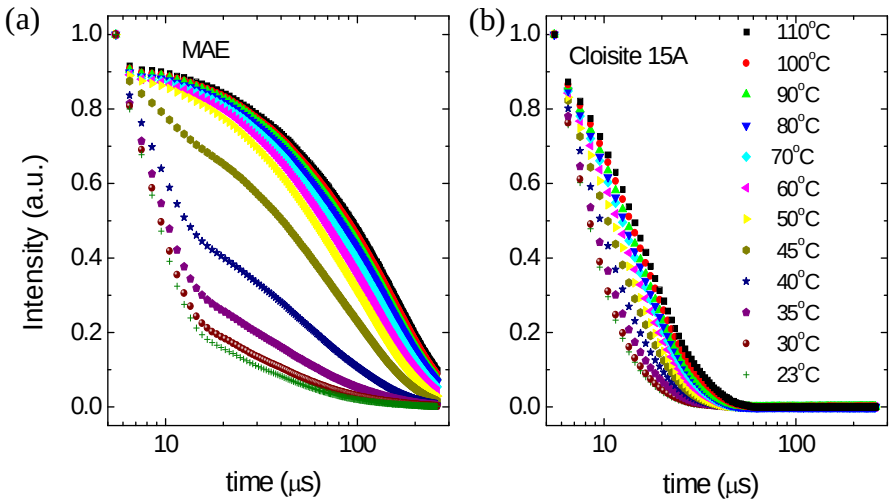

Figure 9.2. Experimental proton NMR free-induction decays converted from the Bloch decays for MAE (a) and Cloisite 15A (b) at the temperature from 23 °C up to 110 °C.

It can be clear that increasing the temperature produces a modest amount of line narrowing. This can be also confirmed by Figure 9.3 relative to Figure 2.1, where high temperature provides relatively sharp line shapes of solid state ^{13}C direct polarization spectra. In addition, with an undetectable barrier of 0.4 nm thickness on the silicate

surface, the observable ^{1}Hs were found to be 0.9 − 1.1 nm from the impurities in Cloisite 15A (see Figure 1.1).

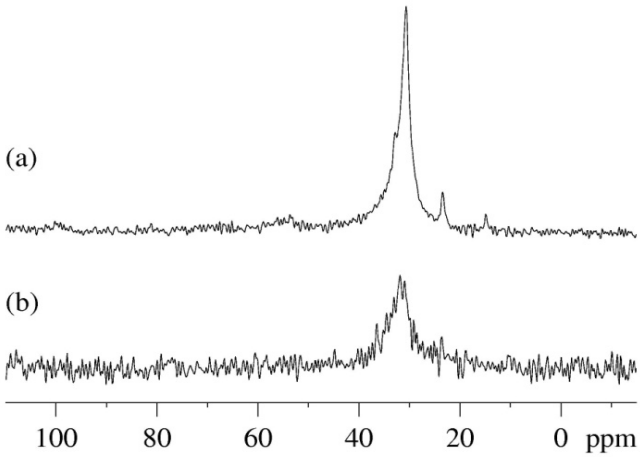

Figure 9.3. Solid-state ^{13}C direct polarization MAS spectra of organically modified diamagnetic MAE-100 (a) and paramagnetic Cloisite 15A (b), collected at 23 ^{o}C. As comparison, similar spectra collected at 70 ^{o}C are shown in Figure 2.1.

9.4.2. Spin-lattice Relaxation Rate as a Function of Temperature

The stretched exponential function, $\exp[-(t/T_1^{H})^{n}]$ has been successfully utilized to describe the growth of the proton magnetization in the impurity-doped systems.[188-189,237-238] The power of n ranges between 1/3 and 1. Here, the stretched exponential function can describe magnetization growth curves of organically modified clays. Table 9.1 shows the fitting results at room temperature under 7.05 T. These results indicate that the proton magnetization growth in diamagnetic MAE-100 is close to the exponential, owing to n = 0.94, while those of paramagnetic organoclays are stretched more. Discrepancy of the magnetization growth from the exponential for the diamagnetic MAE-100 may be related to the spatial distribution and arrangement of interlayer protons. The

more stretched behavior in paramagnetic organoclays should be associated with paramagnetic impurity centers. With comparison to Cloisite 15A, Cloisite 30B with similar impurity concentration shows smaller basal spacing, smaller n and shorter T_1^H. The smaller basal spacing indicates that the interlayer protons are closer to paramagnetic centers. This leads to stronger direct interaction (r^{-6}), which contributes to more stretched growth and faster relaxation.

Figure 9.4 shows normalized proton magnetization as a function of the recovery time such as t, $t^{1/2}$, $t^{2/3}$, and $t^{5/6}$. The relation between $1–M(t)/M_o$ and t for Cloisite 15A is close to $t^{5/6}$, reflected by their linearity. The value of n = 5/6 is the same as a theoretical prediction by Furman et al.[188-189] This result is consistent with the feature of the organoclays and impurity distribution. The calculated value, n = 0.87 for Cloisite 15A, however, is slightly higher than 5/6. Increasing temperature leads to slight decreases of n down to 0.85 rather down to 5/6.

The variable- temperature spin-lattice relaxation times, T_1^H in MAE-100 and Cloisite 15A are investigated at four magnetic fields of 0.54 T, 7.05 T, 9.4 T and 14.1 T (Figure 9.5). The field dependent T_1^H in MAE-100 suggests that the chain correlation time, $(\tau_c)_{chain} > 1/\omega_0 = 1/(2\pi \times 23MHz) = 6.9 \times 10^{-8}$ s > 1 nanosecond. The T_1^H values of MAE-100 sharply decrease upon heating to the melting temperature, 49.2 ^oC. Upon further hearting, T_1^H levels off. This result suggests that the dynamics of the interlayer modifiers experiences almost no change above melting temperature, consistent with the results from Bloch spectra.

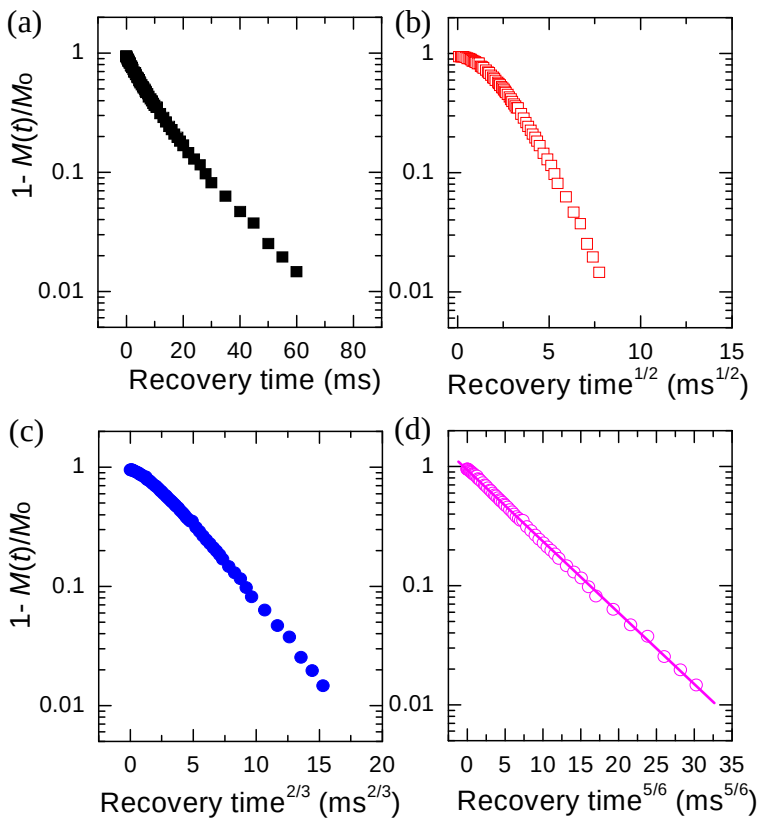

Figure 9.4. Semi-logarithm plots of normalized proton magnetization, $M(t)/M_o$ in Cloisite 15A at room temperature as a function of recovery time, t (a), $t^{1/2}$ (b), $t^{2/3}$ (c), and $t^{5/6}$ (d), measured at 7.05 T.

T_1^H values of Cloisite 15A clearly show almost no melting transition in Figure 9.5(b). The paramagnetic contribution to T_1^H in Cloisite 15A is calculated as shown in Figure 9.6, where T_1^H in Cloisite 15A is completely overlapped with the paramagnetic contribution, $T_{1,\,para}$. This result reveals that the paramagnetic contribution is dominated in the nuclear spin-lattice relaxation. The field- and temperature-dependence of $T_{1,\,para}$ implies that the correlation time of the paramagnetic center, $\omega_0\tau_c > 1$, and $\tau_c > 1/\omega_0 = 1/(2\pi \times 300\text{MHz}) = 5 \times 10^{-10}$ s.

An order of magnitude to the correlation time of the paramagnetic center, τ_c can be estimated as follows. First, $T_{1,\,para}$ values of Cloisite 15A were measured at room

temperature to be 0.57 ms, 10.3 ms and 24.6 ms under 0.54 T, 7.04 T and 14.1 T, respectively. The observable protons are located in the distance range of r = 0.9 nm and 1.6 nm away from paramagnetic impurities. If relaxation of protons is predominately affected by single paramagnetic center, for example, the proton at 7.04 T should have $T_{1,\,para}$ < 10.3 ms at r = 0.9 nm, and $T_{1,\,para}$ >10.3 at r = 1.6 nm. Thus, in terms of eq 2.3 and $1/T_{1,\,para} = Cr^{-6}$, we have

$$1 > T_{1,para}(2/5)(\gamma_{el}\gamma_n\hbar)^2 S(S+1)\left(r^{-6}\right)\left(\frac{\mu_0}{4\pi}\right)^2 \frac{\tau_c}{1+(\omega_n\tau_c)^2}$$

(r = 0.5 nm, T_1^H = 10.3 ms)

$$1 < T_{1,para}(2/5)(\gamma_{el}\gamma_n\hbar)^2 S(S+1)\left(r^{-6}\right)\left(\frac{\mu_0}{4\pi}\right)^2 \frac{\tau_c}{1+(\omega_n\tau_c)^2}$$

(r = 1.7 nm, T_1^H = 10.3 ms)

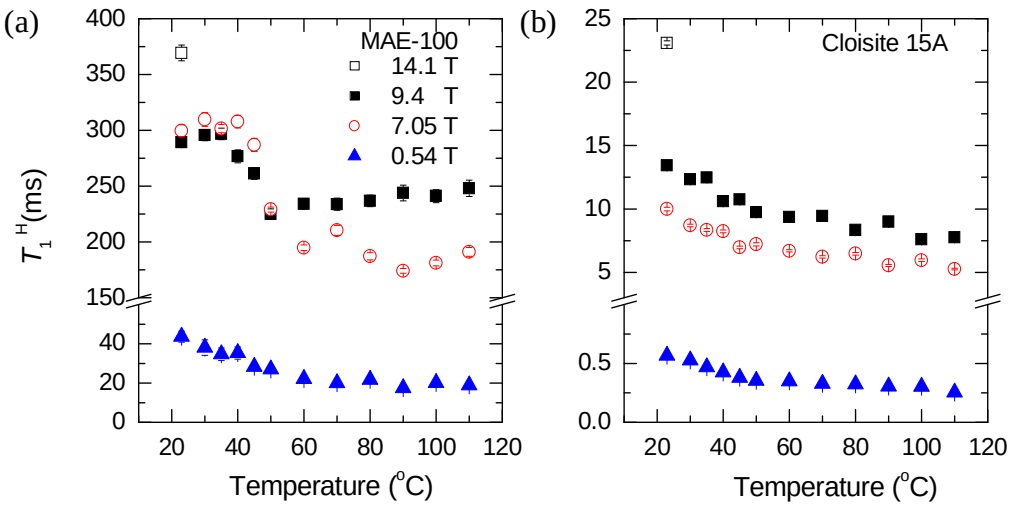

Figure 9.5. Proton spin-lattice relaxation time, T_1^H, as a function of temperature for MAE-100 (a) and Cloisite 15A (b), measured in four magnetic fields of 0.54 T, 7.05 T, 9.4 T and 14.1 T.

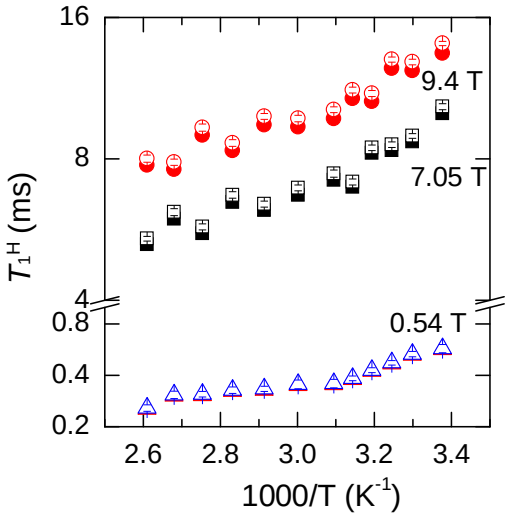

Figure 9.6. Proton spin-lattice relaxation time, T_1^H (open circles) and the paramagnetic contribution to T_1^H (solid circles), $T_{1,\,para}$ as a function of temperature for Cloisite 15A, measured under four magnetic fields of 0.54 T, 7.05 T and 9.4 T. $T_{1,\,para}$ is calculated as following: $1/T_{1,\,para} = 1/(T_{1,\,para})_{Cloisite15A} - 1/(T_1)_{MAE\text{-}100}$, assuming the intrinsic spin-lattice relaxation in Cloisite 15A is same as that of MAE-100

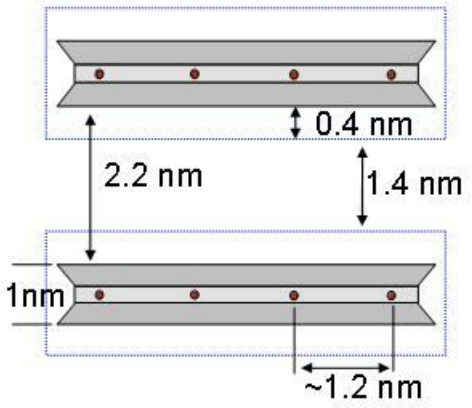

Figure 9.7. Cartoon illustrating ideal structures within Cloisite 15A: gallery height, 2.2 nm from the basal spacing, d_{001} =3.2 nm minus the platelet thickness, 1 nm; the barrier layer on the surface, 0.4 nm; detectable proton thickness, 1.4 nm; impurity distance, 1.2 nm. The blue frame presents the barrier region where the protons are unobservable by NMR. Note that the distance of detectable protons is located in the region between 0.9 nm and 1.7 nm away from impurities. The red spheres present the paramagnetic centers, Fe^{3+} ions.

Based on the above inequalities, we can obtain 1.5×10^{-10} s < τ_C < 1.1×10^{-7} s at 7.05 T. Following the same procedure, we can estimate 1.4×10^{-9} s < τ_C < 1.1×10^{-6} s for $T_{1,\,para}$ = 0.57 ms at 0.54 T, 1.2×10^{-10} s < τ_C < 8.3×10^{-8} s for $T_{1,\,para}$ = 14.1 ms at 9.4 T, and 8.9×10^{-11} s < τ_C < 6.7×10^{-8} s for $T_{1,\,para}$ = 24.6 ms at 14.1 T. Combining these estimations, we can conclude the range of τ_C, 1.4×10^{-9} s < τ_C < 6.7×10^{-8} s.

9.4.3. Spin-lattice Relaxation Rate as a Function of Static Fields

Blumberg,[54] and Lowe and Tse[58] theoretically predicted magnetic field dependence of relaxation rate for different relaxation cases by solving eq 3.5. As indicated in Table 3.1, when $\omega_0\tau_c >> 1$, exponent dependence of $T_{1,\,para}$ on the field strength, B_o is 2 for the rapid diffusion case (e.g., direct relaxation rate is small, and spin diffusion is dominate), 0.5 for the diffusion-limited cases (e.g., direct relaxation rate is large, spin diffusion become small), and 1 for the diffusion-vanishing case (e.g., direct relaxation rate is dominate). Figure 9.8 shows the paramagnetic relaxation time as a function of the field strength with varying temperature. The exponent dependence of $T_{1,\,para}$ on B_o ranges from 1.1 to 1.2, with an average value, 1.15 ± 0.02. This result implies that our system is close to the diffusion-vanishing case. Cloisite 30B also shows the similar field dependence of T_1^H, as indicated in Figure 9.9.

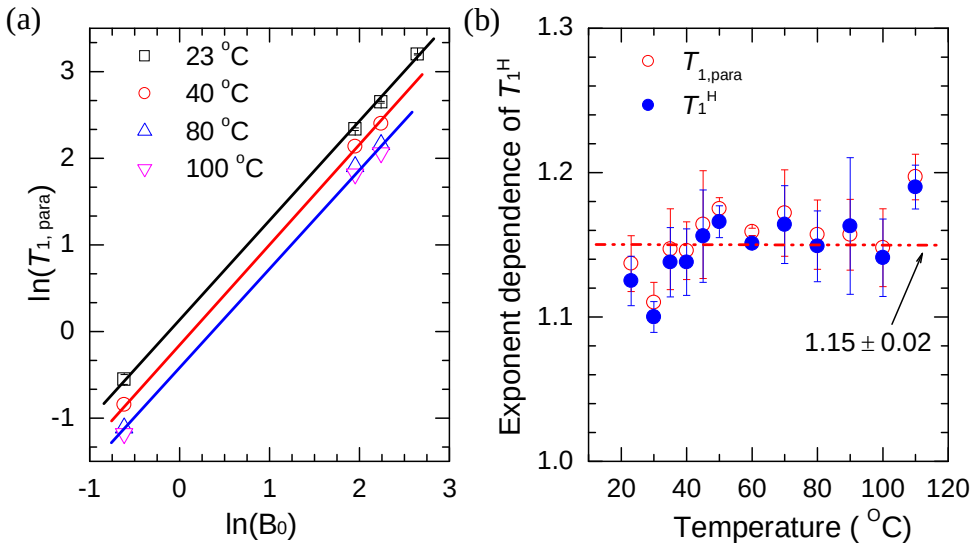

Figure 9.8. Magnetic field dependence of $T_{1,\,para}$ with varying temperature in Cloisite 15A: (a) ln($T_{1,\,para}$) vs ln(B_o); (b) exponent values of $T_{1,\,para}$ and T_1^H at temperatures. Note that the dashed line in (b) shows an average of exponent, 1.15 ± 0.02.

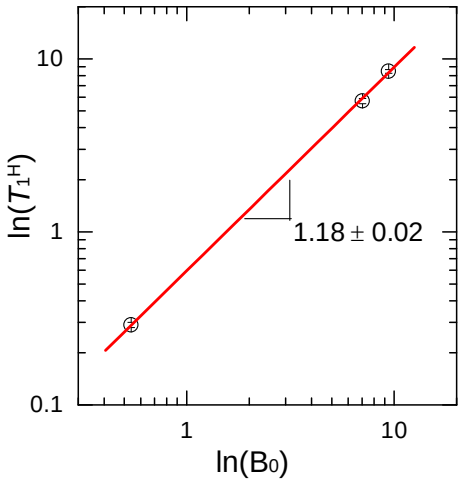

Figure 9.9. Magnetic field dependence of T_1^H in Cloisite 30B.

9.4.4. Correlation Time of Fe^{3+} in Montmorillonite

The distance between Fe^{3+} ions in a platelet of Cloisite 15A is ~ 1.2 nm in a cubic array. Following the estimation method of Yang and Zax,[207] we calculate that the correlation between a pair of electron spins from the nearest Fe^{3+} ions theoretically shows

the exchange coupling constant of ~ 190 MHz. The spin-spin exchange time is ~ 5.3×10^{-9} s. The electron spin interaction accelerates the electron spin-spin relaxation. The spin-spin relaxation time of impurity centers can be given by the peak-to-peak width of an electron paramagnetic resonance (EPR). EPR spectra of Cloisite 15A and Cloisite 30B in Figure 9.10 show two features: a $g = 4.2$ sharp signal and a broad resonance at $g \sim 2.0$. The former can be attributed to isolated Fe^{3+} ions and the latter can be due to exchange interactions between clusters of Fe^{3+} ions.[239] The peak-to-peak linewidth, ΔB_{pp} is ~ 207 G for isolated Fe^{3+} ions. Regardless of inhomogeneous broadening in a EPR spectrum, the spin-spin relaxation time of impurities can be calculated as[240]

$$\tau_s = \frac{4\pi}{\gamma_e \Delta B_{pp}} \tag{9.1}$$

We obtain $\tau_S = 3.6 \times 10^{-9}$ s, which is of the same order of amplitude as the theoretical prediction of the spin-spin exchange time, ~ 5.3×10^{-9} s. This value is also within a range of τ_C, 1.4×10^{-9} s < τ_C < 9.6×10^{-8} s estimated in last section.

The peak-to-peak linewidth, ΔB_{pp} for Cloisite 30B is almost same as that for Cloisite 15A. This may be due to their almost same impurity concentration and similar impurity distribution. It can be seen in eq 9.1 that these two paramagnetic clays exhibit the same spin-spin relaxation time of Fe^{3+} ions. There is possibly the electron spin-spin interaction between Fe^{3+} ions from two nearest platelets besides from the same platelets, when the basal spacing is comparable to the Fe-Fe distance in the same platelets. The basal spacing of Cloisite 30B (d_{001} = 1.85 nm) is largely smaller than 3.15 nm of Cloisite

15A; the distance between Fe^{3+} ions in a platelet of these two organoclays is d_p ~ 1.2 nm. As a result, the EPR results suggests that, if d_p is smaller than d_{001}, the electron spin interaction between impurities from the same platelet is predominate, while that from different platelets could be neglected. This result is consistent with the consideration from Yang and Zax[207] on neglecting the Fe-Fe interaction from the nearest platelets. In addition, Cloisite 15A filled polypropylene nanocomposites (PP-MMT2.7, see Chapter 2) shows the similar EPR spectrum as Cloisite 15A. The weak intensity is due to the dilute Cloisite 15A in the nanocomposite. The nanocomposite shows the slight narrower line from the isolated Fe^{3+} ions than that of Cloisite 15A. This difference could be due to noise issue from the inhomogeneous broadening and dilute clay in the nanocomposite.

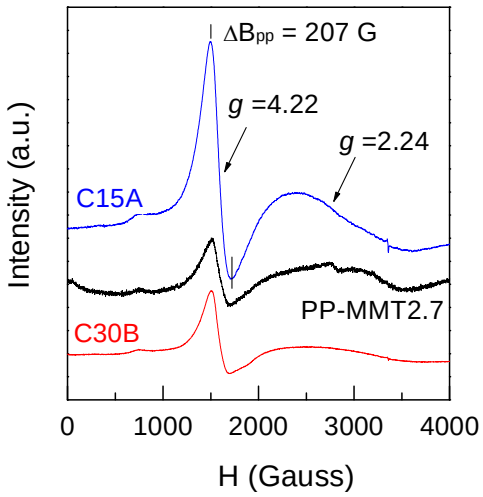

Figure 9.10. EPR spectra of Cloisite 15A (C15A), Cloisite 15A filled polypropylene nanocomposites (PP-MMT2.7), and Cloisite 30B (C30B) from 0 to 4000 Gauss. Note that a g = 4.2 signal is attributed to isolated Fe^{3+} ions and a broad resonance at g ~ 2.0 can be due to exchange interactions between clusters of Fe^{3+} ions

9.5. Conclusions

In summary, we investigated proton spin-lattice relaxation in a diamagnetic organoclay and two paramagnetic organoclays with varying temperature in different fields. The paramagnetic impurities broaden the line width so largely that the relaxation behavior can not disclose a transition of chain dynamics as revealed in the diamagnetic organoclay. Increasing temperature improves the line narrowing but rather limitedly. A stretched exponential was used to describe the magnetization growth in paramagnetic organoclays, and the power of the stretched exponential is close to a theoretical value, 5/6. The magnetic field and temperature dependence of the relaxation time, $T_{1,para}$ in paramagnetic clays were observed and utilized to estimate the correlation time of impurity centers, 1.4×10^{-9} s $< \tau_C < 9.6 \times 10^{-8}$ s. The exponent dependence of $T_{1,para}$ on the field strength, B_o reveals that proton spin-lattice relaxation is close to the diffusion-vanishing case for these two paramagnetic organoclays.

EPR spectra of paramagnetic organoclays show a $g = 4.2$ sharp signal attributed to isolated Fe^{3+} ions and a broad resonance at $g \sim 2.0$ related to Fe^{3+} ions clusters. The linewidth of the peak-to-peak distance at $g = 4.2$ is used to obtain the spin-spin relaxation time of impurities, $\tau_S = 3.6 \times 10^{-9}$ s, consistent with the amplitude of correlation time, τ_C estimated from proton spin-lattice relaxation.

CHAPTER 10

Conclusions and Future Work

Overall Conclusions

The purpose for investigating clay dispersion is driven by its impact on understanding and designing polymer/clay nanocomposites (PCNs). In spite of great efforts expended in characterizing clay dispersion, effective, simple and quantitative techniques are still needed. The groundwork for quantifying clay dispersion in PCNs using ^{1}H solid-state NMR (SS NMR) was outlined in this dissertation. Prior to this work, a handful of exploratory studies have been conducted in correlating nuclear spin-lattice relaxation with clay dispersion in paramagnetic PCNs. The lack of analytical relations between nuclear spin-lattice relaxation and clay dispersion, however, limited this utility of SS NMR. Our immediate goals were targeted to reveal their analytical relation along with accurate data interpretation. The developed methods and the acquired knowledge will be of great benefit to elucidate clay morphology in paramagnetic PCNs using SS NMR.

Two detailed models and thorough analyses were proposed to describe ^{1}H spin-lattice relaxation under the influence of paramagnetic clays in PCNs. Two features of this process were analytically correlated to clay dispersion. One is that the initial slope of the paramagnetic contribution to magnetization growth (M_c^n) with a square root of recovery time ($t^{1/2}$) was related to the interfacial surface area and the degree of clay exfoliation. The other is that the paramagnetic contribution to the spin-lattice relaxation rate ($R_{1,para}$) was connected with the interparticle spacing and the quality of clay dispersion. These two

features were employed to quantitatively observe the evolution of clay morphology in poly(propylene)/clay (PP/MMT) nanocomposites upon equibiaxial stretching, as well as upon *in situ* uniaxial deformation. Furthermore, the initial slope was independently utilized to determine the interfacial surface area in PCNs, which is comparable to TEM data. We demonstrated the capabilities of our models in quantitatively investigating several materials, including poly(vinyl alcohol), nylon 6, poly(ε-caprolactone) (PCL), poly(lactic acid) (PLA) and PP nanocomposites. These results were used to examine the dependence of clay morphology upon processing (strain ratio, strain rate, temperature), deformation (extension), component characteristics (polymer molecular weight, clay surface modification) and clay content. NMR relaxometry has been demonstrated to provide comparable but more thorough and quantitative results on clay morphology relative to other techniques.

Effects of paramagnetic Fe^{3+} concentration (C_{Fe}) and magnetic field strength on ^1H spin-lattice relaxation in PCNs were investigated and discussed. It was found to be $R_{1,para} \sim C_{Fe}^{1.9}$, and it extends our model to investigate PCNs filled with clays containing different C_{Fe}. In particular, low magnetic field separates the initial relaxation recovery into two stages: one related to clay content and the other related to polymer-clay interfacial surface area. The low field was also observed to enhance $R_{1,para}$, increasing its sensitivity to clay morphology in PCNs.

In addition, measurements of long-distance spin diffusion coefficients for a variety of polymers were explored using our model. The spin-lattice relaxation in organically modified clays was also investigated. It reveals that the relaxation in paramagnetic clays is close to the diffusion-vanishing case. These investigations will be

of value to understand the initial relaxation behavior and spin diffusion in nanocomposites.

Recommendations for Future work

The primary aim of this work was to correlate NMR relaxometry with clay morphology in paramagnetic PCNs, and to apply these relationships to investigate effects of processing, deformation, component characteristics and clay content on clay morphology. There are several items that could be studied further:

(1) The relation between $R_{1,\text{para}}$ and clay weight content has been found. Using the scaling method, we exclude the factors of the magnetic field strength, impurity concentration and spin diffusion coefficient into our analytical solution to the simplified polarization transfer equation (eq 4.4). A numerical simulation could be carried out to compute the exact polarization transfer equation (eq 3.5) for PCNs.

(2) Preliminary results for observing *in situ* deformation of PCNs in a home-made NMR shows that the nuclear spin-lattice relaxation could offer information on the response of clay particles to deformation. Thorough investigations and more stable measurements should be carried out. PCNs can be chosen or designed, such as composites with very different interfacial adhesions, or composites containing particles of quite different sizes, to investigate some very basic questions. Moreover, incorporation of the NMR into an Instron tensile machine will help one to observe the mechanical performance at the same time the NMR signal can be collected. This combination as well

as visualized morphology characterization will provide the complete picture on the evolution of morphologies in PCNs upon deformation.

(3) The initial slope in the spin-lattice relaxation has been analytically related to the surface area of paramagnetic particles with different shapes (Appendix B). This analytical relationship could be used to study other systems with particles in various shapes.

(4) The first slope during the initial nuclear relaxation in a low magnetic field has been attributed to the neighboring protons under direct electron-nucleus interaction. By detecting the intensity of magnetization at a short time, the content of surface protons could be estimated. For example, upon annealing a polymer/montmorillonite system, more polymer melts will access to the clay surface via melt intercalation. By monitoring the surface protons, the melt intercalation process can be detected so that the study of chain dynamics during polymer intercalation would be possible.

APPENDIX A

X-ray Diffraction Spectra of Nanocomposites

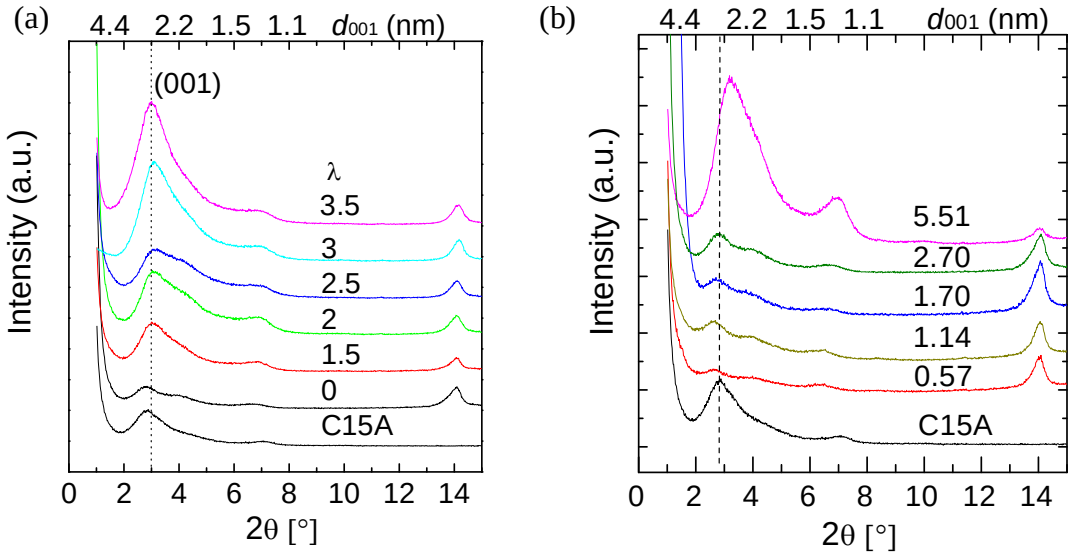

Figure A.1. XRD patterns for Cloisite 15A (C15A) and polypropylene/C15A nanocomposites (PP-MMT): (a) PP-MMT nanocomposite films with stretch ratios from λ = 1 (unstretched) to λ = 3.5 (reported in Chapters 2 & 3); films contain 2.7 wt% MMT; (b) PP-MMT nanocomposites containing 0.57, 1.14, 1.70, 2.7 and 5.51 wt% MMT (reported in Chapters 4 & 6).

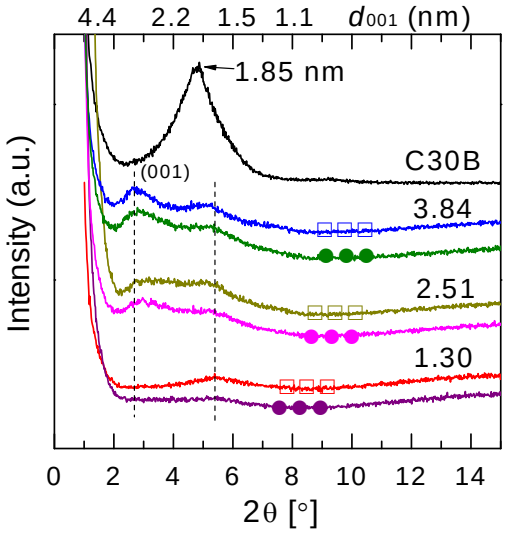

Figure A.2. XRD patterns for PLA-MMT nanocomposites and Cloisite 30B powder (C30B). Two PLA matrices, LMW PLA (□) and HMW PLA (●) were mixed with C30B to make nanocomposites containing 1.3, 2.51 and 3.84 wt% MMT.

APPENDIX B

Modeling Initial Spin-lattice Relaxation around Spherical and Rod-like Particles

We established a lamella-based model for describing the initial spin-lattice relaxation in the saturation-recovery experiment in Chapter 3. In general, there are the diverse shapes of clay particles dispersed in polymer matrices. Here, the spherical and rod-like models are also considered in this appendix. These models would work for materials containing paramagnetic nanoparticles with these shapes.

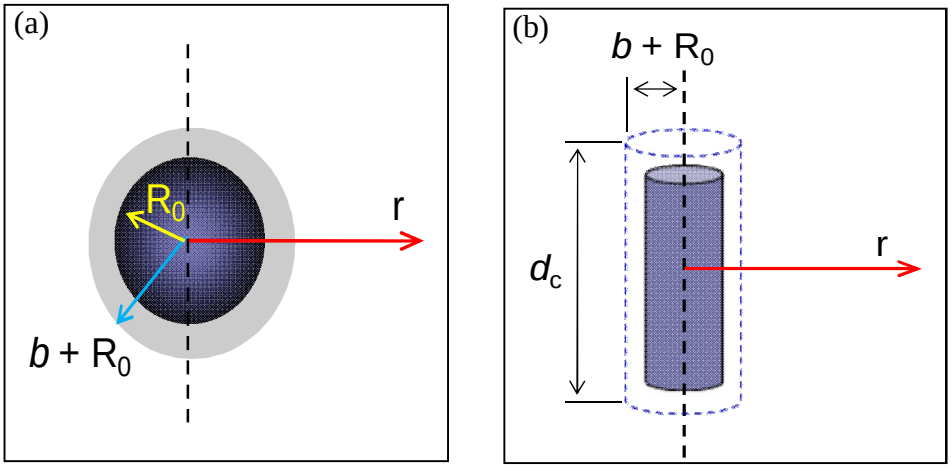

Figure B.1. Schematic of the spherical particle with radius R_0 and barrier b (a), and the rod-like particle with radius R_0, barrier b and length d_c (b). In the region of $r_0 = b + R_0$, there is no magnetization contribution to NMR signal in saturation recovery experiments.

The following calculation method, approximations and assumptions are same as those we proposed in the lamellar model. In a spherical model (Figure C.1a), we can obtain

$$\frac{M(t)}{M_0} = \frac{2D^{1/2}A_s}{\pi^{1/2}V_d}t^{1/2} + \left[\frac{D_0A_s}{V_d(b+R_0)} + \frac{1}{T_{1,m}}\right]t \tag{B.1}$$

where $D = D_0^2/D_s$.

In a rod-like model (Figure C.1b), we can have

$$\frac{M(t)}{M_0} = \frac{2D_0A_s}{V_d\sqrt{\pi D_s}}t^{1/2} + \left[\frac{D_0A_s}{2(b+R_0)V_d} + \frac{1}{T_{1,m}}\right]t - \frac{2D_0A_s}{3V_d\sqrt{\pi D_s}}\left[\frac{2}{T_{1,m}} + \frac{D_s}{4(b+R_0)^2}\right]t^{3/2}... \tag{B.2}$$

More about rod-like model

The Laplace solution of the typical diffusion equation for rod-like particles as shown in Figure C.1b can be found[194]

$$\overline{m} = \frac{m_0K_0(qr)}{pK_0(qr_0)} \tag{B.3}$$

Here, $\overline{m}$ is the Laplace transform of $m(r, t)$ and is a function of p which is a number of the standard Laplace transform, and $q = (p/D_s)^{1/2}$. In the surface of particles, the

polarization of the nuclei is m_0 at $r_0 = b + R_0$. The function of K_0 is the modified Bessel function of the second kind.

Substituting eq B.3 into the Laplace transform of eq 3.12 becomes

$$\bar{M} = \frac{A_s D_0 m_0}{D_s}\left(\frac{K_1(qr)}{pqK_0(qr_0)}\right)\Bigg|_{r=a} + \frac{1}{T_{1,m}}\left(\frac{M_0}{p^2} - \frac{\bar{M}}{p}\right) \tag{B.4}$$

The flux of magnetization at the surface can be obtained

$$f_M = -D_0 A_s\left[\frac{\partial m}{\partial r}\right]_{r=r_0} = \frac{4m_0 D_0 A_s}{r_0 \pi^2}\int_0^\infty e^{-D_0 u^2 t}\frac{du}{u[J_0^2(r_0u) + Y_0^2(r_0u)]} \tag{B.5}$$

where J_0 and Y_0 are the Bessel function of the first kind and the second kind, respectively. More information about the Bessel function is shown in the Appendix C.

Equation 3.12 can be rewritten as

$$\frac{\partial M(t)/M_0}{\partial t} = \frac{4D_0 A_s}{V_d r_0 \pi^2}\int_0^\infty e^{-D_0 u^2 t}\frac{du}{u[J_0^2(r_0u) + Y_0^2(r_0u)]} + \frac{1 - M(t)/M_0}{T_{1,m}} \tag{B.6}$$

The solution of eq B.6 can be obtained

$$\frac{M(t)}{M_0} = \frac{4D_0 A}{V_d r_0 \pi^2}\int_0^\infty \frac{1}{D_0 u^2 - 1/T_{1,m}}(1 - e^{-D_0 u^2 t})\frac{du}{u[J_0^2(r_0u) + Y_0^2(r_0u)]} \tag{B.7}$$

Here we consider the case of the approximate for the small values of time, *t*. Taking eq B.3 and using Appendix C, we have

$$\frac{K_1(qr_0)}{pqK_0(qr_0)} = \frac{1}{pq}\left\{\frac{1+\frac{3}{8qr_0}-\frac{15}{128q^2{r_0}^2}+O[e^{-2qr_0}]}{1-\frac{1}{8qr_0}+\frac{9}{128q^2{r_0}^2}+O[e^{-2qr_0}]}\right\}$$
$$= \frac{1}{pq}\left(1+\frac{1}{2r_0q}-\frac{1}{8{r_0}^2q^2}+\ldots\right) \tag{B.8}$$

Thus, eq B.4 can be rewritten as

$$\bar{M} = \frac{A_s D_0 m_0}{D_s}\frac{1}{pq}\left(1+\frac{1}{2r_0q}-\frac{1}{8{r_0}^2q^2}+\ldots\right)+\frac{1}{T_{1,m}}\left(\frac{M_0}{p^2}-\frac{\bar{M}}{p}\right) \tag{B.9}$$

Then, we obtain,

$$\frac{M(t)}{M_0} = \frac{D_0 A}{V_d D_s}\left\{\frac{2D_s^{-1/2}}{\sqrt{\pi}}t^{1/2}+\frac{1}{2r_0}t-\frac{D_s^{1/2}}{6r_0^2\sqrt{\pi}}t^{3/2}+\ldots\right\}+\frac{1}{T_{1,m}}\left(t-\frac{1}{M_0}\int_0^t M(\xi)\xi\right) \tag{B.10}$$

Following the calculation procedure in the lamellar mode, we can solve eq B.10 to give the approximated solution, eq B.2 ($r_0 = b + R_0$).

APPENDIX C

Error functions and Bessel functions

The error function, its complement and integral error function complement which are present in the can be referred to other references.

$$erf\ (x) = \frac{2}{\sqrt{\pi}} \int_0^x e^{-t^2} dt \tag{C.1}$$

where erf(0) = 0, and erf(∞) = 1.

$$erfc(x) = \frac{2}{\sqrt{\pi}} \int_x^\infty e^{-t^2} dt = 1 - erf(x) \tag{C.2}$$

where erfc(0) = 1, and erfc(∞) = 0.

$$ierfc(x) = \int_x^\infty erfc(t)dt = \frac{1}{\sqrt{\pi}} \exp(-x^2) - xerfc(x) \tag{C.3}$$

where ierfc(0) = $\pi^{-1/2}$ and ierfc(∞) = 0.

$$\frac{d}{dx}[i^n erfc(x)] = (-1)^{n-1} erfc(x) \qquad (n = 0, 1, 2, 3\ldots) \tag{C.4}$$

Some properties of Bessel functions are collected,[194] which have been required in Appendix B.

$$K_0'(z) = -K_1(z); \qquad J_0'(z) = -J_1(z); \qquad Y_0'(z) = -Y_1(z) \tag{C.5}$$

$$J_v(z)Y_v'(z) - Y_v(z)J_v'(z) = \frac{2}{\pi z} \tag{C.6}$$

For large values of z

$$K_1(z) = \left(\frac{\pi}{2z}\right)^{1/2} e^{-z} \left\{1 + \frac{4v^2 - 1^2}{1!8z} + \frac{(4v^2 - 1^2)(4v^2 - 3)}{2!(8z)^2} + O\left(\frac{1}{z^3}\right)\right\} \tag{C.7}$$

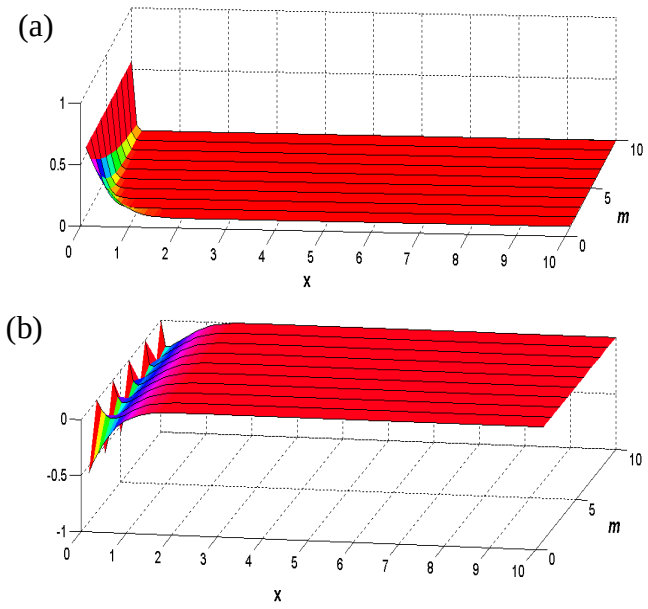

Figure C.1. Numerical value for ierfc(mx) (a) and $\sum_m (-1)^m$ierfc(mx) (b). m is 1, 2, 3… $\sum_m$ ierfc(mx) function converges fast as x increases. $2\sum_m$ ierfc(2.0) ≈ – 0.010 is much less than $\pi^{-1/2}$ (= 0.564).

Table C.1. Numerical values for $\sum_m (-1)^m$ierfc(mx) using a MatLab program

x	m					
	1	10	20	25	50	…
0	-0.5642	0	0	-0.5642	0	0
0.1	-0.4698	-0.2359	-0.2567	-0.2571	-0.2571	
0.2	-0.3866	-0.2318	-0.2321	-0.2321		
0.3	-0.3142	-0.2071	-0.2071			
0.4	-0.2521	-0.1821				
0.5	-0.1996	-0.1571				
1.0	-0.0503	-0.0493				
1.5	-0.0086	-0.0086				
2.0	-9.7802e-4					
2.5	-7.1762e-5					
3.0	-3.3550e-6					
3.5	-9.8869e-8					
4.0	-1.8221e-9					

APPENDIX D

Surface Area of Particles with Shapes of Disc, Rectangle and Hexagon

Table D.1. Surface area A_s and average $< A_s >$

clay platelet		dimensions	surface area, A_s	average, $< A_s >$
	disc	radius, r thickness, w	$\frac{2\pi\sum_i r_i^2 + 2\pi\sum_i r_i w_i}{1/\rho_p + (1-d)\pi\sum_i r_i^2 w_i}$	$\frac{2W_c(1/h_c + 1/r_0)}{d + W_c(1-d)}$
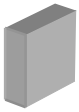	rectangle	edges, l_1, l_2, l_3	$\frac{2\sum_i (l_1 l_2 + l_2 l_3 + l_3 l_1)_i}{1/\rho_p + (1-d)\sum_i (l_1 l_2 l_3)_i}$	$\frac{2W_c(1/h_c + 2/l_0)}{d + W_c(1-d)}$
	hexagon	edge, l	$\frac{3\sqrt{3}/2\sum_i l_i^2 + 6\sum_i l_i w_i}{1/\rho_p + (1-d)3\sqrt{3}/2\sum_i l_i^2 w_i}$	$\frac{2W_c(1/h_c + 2.31/l_0)}{d + W_c(1-d)}$

[a] W_c: mass fraction of particles; d: ratio of densities of clay (ρ_c) and polymer (ρ_p); w: cumulative thickness of a paticle; h_c: average cumulative thickness of a particle (average radius r_0, and average edge l_0).

REFERENCES

(1) Wong, H. C.; Cabral, J. T. *Phys. Rev. Lett.* **2010,** 105, (3), 038301.

(2) Capadona, J. R.; Shanmuganathan, K.; Tyler, D. J.; Rowan, S. J.; Weder, C. *Science* **2008,** 319, (5868), 1370-1374.

(3) Rozenberg, B. A.; Tenne, R. *Prog. Polym. Sci.* **2008,** 33, (1), 40-112.

(4) Miaudet, P.; Derre, A.; Maugey, M.; Zakri, C.; Piccione, P. M.; Inoubli, R.; Poulin, P. *Science* **2007,** 318, (5854), 1294-1296.

(5) Allegra, G.; Raos, G.; Vacatello, M. *Prog. Polym. Sci.* **2008,** 33, (7), 683-731.

(6) Podsiadlo, P.; Kaushik, A. K.; Arruda, E. M.; Waas, A. M.; Shim, B. S.; Xu, J. D.; Nandivada, H.; Pumplin, B. G.; Lahann, J.; Ramamoorthy, A.; Kotov, N. A. *Science* **2007,** 318, (5847), 80-83.

(7) Kiliaris, P.; Papaspyrides, C. D. *Prog. Polym. Sci.* **2010,** 35, (7), 902-958.

(8) Paul, D. R.; Robeson, L. M. *Polymer* **2008,** 49, (15), 3187-3204.

(9) Pavlidou, S.; Papaspyrides, C. D. *Prog. Polym. Sci.* **2008,** 33, (12), 1119-1198.

(10) Giannelis, E. P. *Adv. Mater.* **1996,** 8, (1), 29-35.

(11) Kropka, J. M.; Pryamitsyn, V.; Ganesan, V. *Phys. Rev. Lett.* **2008,** 101, (7),075702.

(12) Sen, S.; Xie, Y. P.; Kumar, S. K.; Yang, H. C.; Bansal, A.; Ho, D. L.; Hall, L.; Hooper, J. B.; Schweizer, K. S. *Phys. Rev. Lett.* **2007,** 98, (12), 128302.

(13) Salaniwal, S.; Kumar, S. K.; Douglas, J. F. *Phys. Rev. Lett.* **2002,** 89, (25), 258301.

(14) Anastasiadis, S. H.; Karatasos, K.; Vlachos, G.; Manias, E.; Giannelis, E. P. *Phys. Rev. Lett.* **2000,** 84, (5), 915-918.

(15) Garces, J. M.; Moll, D. J.; Bicerano, J.; Fibiger, R.; McLeod, D. G. *Adv. Mater.* **2000,** 12, (23), 1835-1839.

(16) Okamoto, M. *Mater. Sci. Technol.* **2006,** 22, (7), 756-779.

(17) Hussain, F.; Hojjati, M.; Okamoto, M.; Gorga, R. E. *J. Compos. Mater.* **2006,** 40, (17), 1511-1575.

(18) Kim, H.; Abdala, A. A.; Macosko, C. W. *Macromolecules* **2010,** 43, (16), 6515-6530.

(19) Xu, H. P.; Dang, Z. M.; Jiang, M. J.; Yao, S. H.; Bai, J. *J. Mater. Chem.* **2008,** 18, (2), 229-234.

(20) Leng, J. S.; Huang, W. M.; Lan, X.; Liu, Y. J.; Du, S. Y. *Appl. Phys. Lett.* **2008,** 92, (20), 204101.

(21) Yoon, H. G.; Kwon, K. W.; Nagata, K.; Takahashi, K. *Carbon* **2004,** 42, (8-9), 1877-1879.

(22) Bradley, R. H.; Sheng, E.; Sutherland, I.; Freakley, P. K.; Ismail, H. *J. Mater. Chem.* **1994,** 4, (8), 1189-1193.

(23) Tsai, L.; Yuan, F. P.; Prakash, V.; Dandekar, D. P. *J. Appl. Phys.* **2009,** 105, (9), 93526.

(24) Kaynak, I.; Sen, F.; Sayman, O. *J. Reinf. Plast. Compos.* **2008,** 27, (11), 1117-1134.

(25) Gunduz, G.; Erol, D.; Akkas, N. *J. Compos. Mater.* **2005,** 39, (17), 1577-1589.

(26) Pang, H.; Zhang, Y. C.; Chen, T.; Zeng, B. Q.; Li, Z. M. *Appl. Phys. Lett.* **2010,** 96, (25), 251907.

(27) Piven', N. P.; Muradyan, V. E.; Babenko, S. D.; Allayarov, S. R.; Sokolov, E. A. *High Energ. Chem.* **2010,** 44, (4), 351-352.

(28) Chen, D. L.; Yang, H. M. *J. Appl. Polym. Sci.* **2010,** 115, (1), 624-634.

(29) Lee, S. Y.; Kang, I. A.; Doh, G. H.; Yoon, H. G.; Park, B. D.; Wu, Q. L. *J. Thermoplast. Compos. Mater.* **2008,** 21, (3), 209-223.

(30) Ariffin, A.; Mansor, A. S.; Jikan, S. S.; Ishak, Z. A. M. *J. Appl. Polym. Sci.* **2008,** 108, (6), 3901-3916.

(31) Collar, E. P.; Areso, S.; Laguna, O.; Garcia-Martinez, J. M. *J. Polym. Mater.* **1998,** 15, (3), 237-242.

(32) Maiti, S. N.; Sharma, K. K. *J. Mater. Sci. - Mater. Electron.* **1992,** 27, (17), 4605-4613.

(33) Peng, H. S.; Sun, X. M.; Cai, F. J.; Chen, X. L.; Zhu, Y. C.; Liao, G. P.; Chen, D. Y.; Li, Q. W.; Lu, Y. F.; Zhu, Y. T.; Jia, Q. X. *Nature Nanotechnology* **2009,** 4, (11), 738-741.

(34) Stankovich, S.; Dikin, D. A.; Dommett, G. H. B.; Kohlhaas, K. M.; Zimney, E. J.; Stach, E. A.; Piner, R. D.; Nguyen, S. T.; Ruoff, R. S. *Nature* **2006,** 442, (7100), 282-286.

(35) Ramanathan, T.; Abdala, A. A.; Stankovich, S.; Dikin, D. A.; Herrera-Alonso, M.; Piner, R. D.; Adamson, D. H.; Schniepp, H. C.; Chen, X.; Ruoff, R. S.; Nguyen, S. T.; Aksay, I. A.; Prud'homme, R. K.; Brinson, L. C. *Nature Nanotechnology* **2008,** 3, (6), 327-331.

(36) Cao, Q.; Kim, H. S.; Pimparkar, N.; Kulkarni, J. P.; Wang, C. J.; Shim, M.; Roy, K.; Alam, M. A.; Rogers, J. A. *Nature* **2008,** 454, (7203), 495-U4.

(37) Ray, S. S.; Okamoto, M. *Prog. Polym. Sci.* **2003,** 28, (11), 1539-1641.

(38) Balazs, A. C.; Emrick, T.; Russell, T. P. *Science* **2006,** 314, (5802), 1107-1110.

(39) Ginzburg, V. V.; Gendelman, O. V.; Manevitch, L. I. *Phys. Rev. Lett.* **2001,** 86, (22), 5073-5075.

(40) Lan, T. Polymer-Clay Nanocomposites - Better Plastics http://www.epa.gov/opptintr/nano/p2docs/casestudy2_lan.pdf (October 6, 2010).

(41) Bertmer, M.; Wang, M. F.; Kruger, M.; Blumich, B.; Litvinov, V. M.; van Es, M. *Chem. Mater.* **2007,** 19, (5), 1089-1097.

(42) Vanderhart, D. L.; Asano, A.; Gilman, J. W. *Chem. Mater.* **2001,** 13, (10), 3796-3809.

(43) Calberg, C.; Jerome, R.; Grandjean, J. *Langmuir* **2004,** 20, (5), 2039-2041.

(44) Bourbigot, S.; Vanderhart, D. L.; Gilman, J. W.; Awad, W. H.; Davis, R. D.; Morgan, A. B.; Wilkie, C. A. *J. Polym. Sci., Part B: Polym. Phys.* **2003,** 41, (24), 3188-3213.

(45) VanderHart, D. L.; Asano, A.; Gilman, J. W. *Macromolecules* **2001,** 34, (12), 3819-3822.

(46) Grandjean, J. *Clay Minerals* **2006,** 41, (2), 567-586.

(47) Hou, S. S.; Bonagamba, T. J.; Beyer, F. L.; Madison, P. H.; Schmidt-Rohr, K. *Macromolecules* **2003,** 36, (8), 2769-2776.

(48) Hou, S. S.; Beyer, F. L.; Schmidt-Rohr, K. *Solid State Nucl. Magn. Reson.* **2002,** 22, (2-3), 110-127.

(49) Harris, D. J.; Bonagamba, T. J.; Schmidt-Rohr, K. *Macromolecules* **1999,** 32, (20), 6718-6724.

(50) Lorthioir, C.; Laupretre, F.; Soulestin, J.; Lefebvre, J. M. *Macromolecules* **2009,** 42, (1), 218-230.

(51) Brus, J.; Urbanova, M.; Kelnar, I.; Kotek, J. *Macromolecules* **2006,** 39, (16), 5400-5409.

(52) Urbanczyk, L.; Hrobarikova, J.; Calberg, C.; Jerome, R.; Grandjean, J. *Langmuir* **2006,** 22, (10), 4818-4824.

(53) Bloembergen, N. *Physica* **1949,** 15, (3-4), 386-426.

(54) Blumberg, W. E. *Phys. Rev.* **1960,** 119, (1), 79-84.

(55) Rorschach, H. E. *Physica* **1964,** 30, (1), 38-44.

(56) Lowe, I. J.; Tse, D. *Phys. Rev.* **1968,** 166, (2), 279-291.

(57) Tse, D.; Lowe, I. J. *Phys. Rev.* **1968,** 166, (2), 292-302.

(58) Tse, D.; Hartmann, S. R. *Phys. Rev. Lett.* **1968,** 21, (8), 511-514.

(59) Abragam, A., *The principles of nuclear magnetism.* Clarendon Press: Oxford,, 1961; pp 19-389.

(60) Lepoittevin, B.; Devalckenaere, M.; Pantoustier, N.; Alexandre, M.; Kubies, D.; Calberg, C.; Jerome, R.; Dubois, P. *Polymer* **2002,** 43, (14), 4017-4023.

(61) Lepoittevin, B.; Pantoustier, N.; Devalckenaere, M.; Alexandre, M.; Kubies, D.; Calberg, C.; Jerome, R.; Dubois, P. *Macromolecules* **2002,** 35, (22), 8385-8390.

(62) Alexandre, M.; Dubois, P. *Mater. Sci. Eng. R: Reports* **2000,** 28, (1-2), 1-63.

(63) Tamura, K.; Yokoyama, S.; Pascua, C. S.; Yamada, H. *Chem. Mater.* **2008,** 20, (6), 2242-2246.

(64) Nakas, G. I.; Kaynak, C. *Polym. Compos.* **2009,** 30, (3), 357-363.

(65) Yeh, J. M.; Liou, S. J.; Lin, C. Y.; Cheng, C. Y.; Chang, Y. W. *Chem. Mater.* **2002,** 14, (1), 154-161.

(66) http://www.nanoclay.com (October 6, 2010).

(67) Fu, Y. T.; Heinz, H. *Chem. Mater.* **2010,** 22, (4), 1595-1605.

(68) Vaia, R. A.; Giannelis, E. P. *Macromolecules* **1997,** 30, (25), 7990-7999.

(69) Vaia, R. A.; Giannelis, E. P. *Macromolecules* **1997,** 30, (25), 8000-8009.

(70) Vaia, R. A., Structural Characterization of Polymer-Layered Silicate Nanocomposites. In *Polymer-Clay Nanocomposites*, Pinnavaia, T. J.; Beal, G. W., Eds. John Wiley & Sons: New York, 2000; pp 229-266.

(71) Chang, J. H.; Jang, T. G.; Ihn, K. J.; Lee, W. K.; Sur, G. S. *J. Appl. Polym. Sci.* **2003,** 90, (12), 3208-3214.

(72) Ogata, N.; Kawakage, S.; Ogihara, T. *J. Appl. Polym. Sci.* **1997,** 66, (3), 573-581.

(73) Strawhecker, K. E.; Manias, E. *Chem. Mater.* **2000,** 12, (10), 2943-2949.

(74) Sengwa, R. J.; Choudhary, S.; Sankhla, S. *Compos. Sci. Technol.* **2010,** 70, (11), 1621-1627.

(75) Loiseau, A.; Tassin, J. F. *Macromolecules* **2006,** 39, (26), 9185-9191.

(76) Lim, S. T.; Choi, H. J.; Jhon, M. S. *J. Ind. Eng. Chem.* **2003,** 9, (1), 51-57.

(77) Shen, Z. Q.; Simon, G. P.; Cheng, Y. B. *Polymer* **2002,** 43, (15), 4251-4260.

(78) Shelley, J. S.; Mather, P. T.; DeVries, K. L. *Polymer* **2001,** 42, (13), 5849-5858.

(79) Miri, V.; Elkoun, S.; Peurton, F.; Vanmansart, C.; Lefebvre, J. M.; Krawczak, P.; Seguela, R. *Macromolecules* **2008,** 41, (23), 9234-9244.

(80) Yano, K.; Usuki, A.; Okada, A.; Kurauchi, T.; Kamigaito, O. *J. Polym. Sci., Part B: Polym. Phys.* **1993,** 31, (10), 2493-2498.

(81) Usuki, A.; Kojima, Y.; Kawasumi, M.; Okada, A.; Fukushima, Y.; Kurauchi, T.; Kamigaito, O. *J. Mater. Res.* **1993,** 8, (5), 1179-1184.

(82) Kojima, Y.; Usuki, A.; Kawasumi, M.; Okada, A.; Kurauchi, T.; Kamigaito, O. *J. Polym. Sci., Part A: Polym. Chem.* **1993,** 31, (4), 983-986.

(83) Rama, M. S.; Swaminathan, S. *J. Appl. Polym. Sci.* **2010,** 118, (3), 1774-1786.

(84) Fornes, T. D.; Hunter, D. L.; Paul, D. R. *Macromolecules* **2004,** 37, (5), 1793-1798.

(85) Cho, J. W.; Paul, D. R. *Polymer* **2001,** 42, (3), 1083-1094.

(86) Lee, K. M.; Han, C. D. *Macromolecules* **2003,** 36, (19), 7165-7178.

(87) Lapshin, S.; Swain, S. K.; Isayev, A. I. *Polym. Eng. Sci.* **2008,** 48, (8), 1584-1591.

(88) Lapshin, S.; Isayev, A. I. *J. Vinyl. Addit. Techn.* **2007,** 13, (1), 40-45.

(89) Aranda, P.; Mosqueda, Y.; Perez-Cappe, E.; Ruiz-Hitzky, E. *J. Polym. Sci., Part B: Polym. Phys.* **2003,** 41, (24), 3249-3263.

(90) Wang, Z.; Pinnavaia, T. J. *Chem. Mater.* **1998,** 10, (7), 1820-1826.

(91) Zhu, Z. K.; Yang, Y.; Yin, J.; Wang, X. Y.; Ke, Y. C.; Qi, Z. N. *J. Appl. Polym. Sci.* **1999,** 73, (11), 2063-2068.

(92) Drummy, L. F.; Wang, Y. C.; Schoenmakers, R.; May, K.; Jackson, M.; Koerner, H.; Farmer, B. L.; Mauryama, B.; Vaia, R. A. *Macromolecules* **2008,** 41, (6), 2135-2143.

(93) Vermogen, A.; Masenelli-Varlot, K.; Seguela, R.; Duchet-Rumeau, J.; Boucard, S.; Prele, P. *Macromolecules* **2005,** 38, (23), 9661-9669.

(94) Carastan, D. J.; Vermogen, A.; Masenelli-Varlot, K.; Demarquette, N. R. *Polym. Eng. Sci.* **2010,** 50, (2), 257-267.

(95) Xie, S. B.; Harkin-Jones, E.; Shen, Y. C.; Hornsby, P.; McAfee, M.; McNally, T.; Patel, R.; Benkreira, H.; Coates, P. *Mater. Lett.* **2010,** 64, (2), 185-188.

(96) Zhou, Q.; Wang, K.; Loo, L. S. *J. Appl. Polym. Sci.* **2009,** 113, (5), 3286-3293.

(97) McNally, T.; Murphy, W. R.; Lew, C. Y.; Turner, R. J.; Brennan, G. P. *Polymer* **2003,** 44, (9), 2761-2772.

(98) Bhattacharya, M.; Maiti, M.; Bhowmick, A. K. *Polym. Eng. Sci.* **2009,** 49, (1), 81-98.

(99) Samadi, A.; Kashani, M. R. *J. Appl. Polym. Sci.* **2010,** 116, (4), 2101-2109.

(100) Becker, O.; Varley, R.; Simon, G. *Polymer* **2002,** 43, (16), 4365-4373.

(101) Brocorens, P.; Benali, S.; Broekaert, C.; Monteverde, F.; Miltner, H. E.; Van Mele, B.; Alexandre, M.; Dubois, P.; Lazzaroni, R. *Langmuir* **2008,** 24, (5), 2072-2080.

(102) Simons, R.; Qiao, G. G.; Powell, C. E.; Bateman, S. A. *Langmuir* **2010,** 26, (11), 9023-9031.

(103) Bellair, R. J.; Manitiu, M.; Gulari, E.; Kannan, R. M. *J. Polym. Sci., Part B: Polym. Phys.* **2010,** 48, (8), 823-831.

(104) Wang, K.; Chen, L.; Wu, J. S.; Toh, M. L.; He, C. B.; Yee, A. F. *Macromolecules* **2005,** 38, (3), 788-800.

(105) Nishioka, H.; Niihara, K. I.; Kaneko, T.; Yamanaka, J.; Inoue, T.; Nishi, T.; Jinnai, H. *Compos. Interfaces* **2006,** 13, (7), 589-603.

(106) Nawani, P.; Desai, P.; Lundwall, M.; Gelfer, M. Y.; Hsiao, B. S.; Rafailovich, M.; Frenkel, A.; Tsou, A. H.; Gilman, J. W.; Khalid, S. *Polymer* **2007,** 48, (3), 827-840.

(107) Martin, Z.; Jimenez, I.; Gomez, M. A.; Ade, H. W.; Kilcoyne, D. A.; Hernadez-Cruz, D. *J. Phys. Chem. B* **2009,** 113, (32), 11160-11165.

(108) Martin, Z.; Jimenez, I.; Gomez, M. A.; Ade, H.; Kilcoyne, D. A. *Macromolecules* **2010,** 43, (1), 448-453.

(109) Ray, S. S. *Polymer* **2010,** 51, (17), 3966-3970.

(110) Usuki, A.; Hasegawa, N.; Kadoura, H.; Okamoto, T. *Nano Lett.* **2001,** 1, (5), 271-272.

(111) Strawhecker, K. E.; Manias, E. *Macromolecules* **2001,** 34, (24), 8475-8482.

(112) Chow, W. S.; Ishak, Z. A. M.; Karger-Kocsis, J. *J. Polym. Sci., Part B: Polym. Phys.* **2005,** 43, (10), 1198-1204.

(113) Luo, Z. P.; Koo, J. H. *Polymer* **2008,** 49, (7), 1841-1852.

(114) Dennis, H. R.; Hunter, D. L.; Chang, D.; Kim, S.; White, J. L.; Cho, J. W.; Paul, D. R. *Polymer* **2001,** 42, (23), 9513-9522.

(115) Fornes, T. D.; Paul, D. R. *Polymer* **2003,** 44, (17), 4993-5013.

(116) Fornes, T. D.; Yoon, P. J.; Keskkula, H.; Paul, D. R. *Polymer* **2002,** 43, (7), 2121-2122.

(117) Van Es, M. **2001,** Ph.D.

(118) Nam, P. H.; Maiti, P.; Okamoto, M.; Kotaka, T.; Hasegawa, N.; Usuki, A. *Polymer* **2001,** 42, (23), 9633-9640.

(119) Basu, S. K.; Tewari, A.; Fasulo, P. D.; Rodgers, W. R. *Appl. Phys. Lett.* **2007,** 91, (5), -.

(120) Kohjiya, S.; Katoh, A.; Shimanuki, J.; Hasegawa, T.; Ikeda, Y. *Polymer* **2005,** 46, (12), 4440-4446.

(121) Jinnai, H.; Spontak, R. J.; Nishi, T. *Macromolecules* **2010,** 43, (4), 1675-1688.

(122) Bafna, A.; Beaucage, G.; Mirabella, F.; Mehta, S. *Polymer* **2003,** 44, (4), 1103-1115.

(123) He, C. B.; Liu, T. X.; Tjiu, W. C.; Sue, H. J.; Yee, A. F. *Macromolecules* **2008,** 41, (1), 193-202.

(124) Finnigan, B.; Jack, K.; Campbell, K.; Halley, P.; Truss, R.; Casey, P.; Cookson, D.; King, S.; Martin, D. *Macromolecules* **2005,** 38, (17), 7386-7396.

(125) Perrin-Sarazin, F.; Ton-That, M. T.; Bureau, M. N.; Denault, J. *Polymer* **2005,** 46, (25), 11624-11634.

(126) Wang, K. H.; Chung, I. J.; Jang, M. C.; Keum, J. K.; Song, H. H. *Macromolecules* **2002,** 35, (14), 5529-5535.

(127) Benetti, E. M.; Causin, V.; Marega, C.; Marigo, A.; Ferrara, G.; Ferraro, A.; Consalvi, M.; Fantinel, F. *Polymer* **2005,** 46, (19), 8275-8285.

(128) Schaefer, D. W.; Justice, R. S. *Macromolecules* **2007,** 40, (24), 8501-8517.

(129) Masenelli-Varlot, K.; Vigier, G.; Vermogen, A.; Gauthier, C.; Cavaille, J. Y. *J. Polym. Sci., Part B: Polym. Phys.* **2007,** 45, (11), 1243-1251.

(130) Bandyopadhyay, J.; Ray, S. S. *Polymer* **2010,** 51, (6), 1437-1449.

(131) Reyna-Valencia, A.; Deyrail, Y.; Bousmina, M. *Macromolecules* **2010,** 43, (1), 354-361.

(132) Bousmina, M. *Macromolecules* **2006,** 39, (12), 4259-4263.

(133) Sun, L.; Ertel, E. A.; Zhu, L.; Hsiao, B. S.; Avila-Orta, C. A.; Sics, L. *Langmuir* **2005,** 21, (13), 5672-5676.

(134) Vaia, R. A.; Jandt, K. D.; Kramer, E. J.; Giannelis, E. P. *Macromolecules* **1995,** 28, (24), 8080-8085.

(135) Wang, K.; Liang, S.; Deng, J. N.; Yang, H.; Zhang, Q.; Fu, Q.; Dong, X.; Wang, D. J.; Han, C. C. *Polymer* **2006,** 47, (20), 7131-7144.

(136) Manias, E.; Chen, H.; Krishnamoorti, R.; Genzer, J.; Kramer, E. J.; Giannelis, E. P. *Macromolecules* **2000,** 33, (21), 7955-7966.

(137) Ren, C. Y.; Jiang, Z. Y.; Du, X. H.; Men, Y. F.; Tang, T. *J. Phys. Chem. B* **2009,** 113, (43), 14118-14127.

(138) Kim, G. M.; Lee, D. H.; Hoffmann, B.; Kressler, J.; Stoppelmann, G. *Polymer* **2001,** 42, (3), 1095-1100.

(139) Chen, J. S.; Poliks, M. D.; Ober, C. K.; Zhang, Y. M.; Wiesner, U.; Giannelis, E. *Polymer* **2002,** 43, (18), 4895-4904.

(140) Yang, H. M.; Song, Y. H.; Xu, B.; Zheng, Q. *Chem. Res. Chin. Univ.* **2006,** 22, (3), 383-387.

(141) Loo, L. S.; Gleason, K. K. *Polymer* **2004,** 45, (17), 5933-5939.

(142) Na, B.; Xu, W. F.; Lv, R. H.; Tian, N. N.; Li, Z. J.; Su, R.; Fu, Q. *J. Polym. Sci., Part B: Polym. Phys.* **2010,** 48, (5), 514-519.

(143) Xu, W. F.; Lv, R. H.; Na, B.; Tian, N. N.; Li, Z. J.; Fu, Q. *J. Phys. Chem. B* **2009,** 113, (29), 9664-9668.

(144) Witschnigg, A.; Laske, S.; Kracalik, M.; Feuchter, M.; Pinter, G.; Maier, G.; Marzinger, W.; Haberkorn, M.; Langecker, G. R.; Holzer, C. *J. Appl. Polym. Sci.* **2010,** 117, (5), 3047-3053.

(145) Davis, R. D.; Bur, A. J.; McBrearty, M.; Lee, Y. H.; Gilman, J. W.; Start, P. R. *Polymer* **2004,** 45, (19), 6487-6493.

(146) VanderHart, D. L.; Asano, A.; Gilman, J. W. *Chem. Mater.* **2001,** 13, (10), 3781-3795.

(147) Chen, K.; Wilkie, C. A.; Vyazovkin, S. *J. Phys. Chem. B* **2007,** 111, (44), 12685-12692.

(148) Xu, B.; Zheng, Q.; Song, Y. H.; Shangguan, Y. *Polymer* **2006,** 47, (8), 2904-2910.

(149) Stejskal, E. O.; Memory, J. D., *High resolution NMR in the solid state : fundamentals of CP/MAS*. Oxford University Press: New York, 1994; xii, 189 p.

(150) Morgan, A. B.; Gilman, J. W. *J. Appl. Polym. Sci.* **2003,** 87, (8), 1329-1338.

(151) Koo, C. M.; Kim, S. O.; Chung, I. J. *Macromolecules* **2003,** 36, (8), 2748-2757.

(152) Preschilla, N.; Sivalingam, G.; Rasheed, A. S. A.; Tyagi, S.; Biswas, A.; Bellare, J. R. *Polymer* **2008,** 49, (19), 4285-4297.

(153) Krishnamoorti, R.; Yurekli, K. *Curr. Opin. Colloid Interface Sci.* **2001,** 6, (5-6), 464-470.

(154) Bandyopadhyay, J.; Ray, S. S.; Bousmina, M. *Macromol. Chem. Phys.* **2010,** 211, (15), 1632-1639.

(155) Sheng, N.; Boyce, M. C.; Parks, D. M.; Rutledge, G. C.; Abes, J. I.; Cohen, R. E. *Polymer* **2004,** 45, (2), 487-506.

(156) Chen, B. Q.; Evans, J. R. G. *Macromolecules* **2006,** 39, (5), 1790-1796.

(157) Park, S. Y.; Cho, Y. H.; Vaia, R. A. *Macromolecules* **2005,** 38, (5), 1729-1735.

(158) Chen, B.; Evans, J. R. G.; Greenwell, H. C.; Boulet, P.; Coveney, P. V.; Bowden, A. A.; Whiting, A. *Chem. Soc. Rev.* **2008,** 37, (3), 568-594.

(159) Kim, D. H.; Fasulo, P. D.; Rodgers, W. R.; Paul, D. R. *Polymer* **2007,** 48, 5960-5978.

(160) Zhang, Q.; Wang, Y.; Fu, Q. *J. Polym. Sci., Part B: Polym. Phys.* **2003,** 41, (1), 1-10.

(161) Okamoto, M.; Nam, P. H.; Maiti, P.; Kotaka, T.; Nakayama, T.; Takada, M.; Ohshima, M.; Usuki, A.; Hasegawa, N.; Okamoto, H. *Nano Lett.* **2001,** 1, (9), 503-505.

(162) Cole, K. C.; Perrin-Sarazin, F.; Dorval-Douville, G. *Macromol. Symp.* **2005,** 230, 1-10.

(163) Rajiv, R. S.; Harkin-Jones, E.; Soon, K.; McNally, T.; Menary, G.; Armstrong, C. G.; Martin, P. J. *Eur. Polym. J.* **2009,** 45, 332-340.

(164) Abu-Zurayk, R.; Harkin-Jones, E.; McNally, T.; Menary, G.; Martin, P.; Armstrong, C. *Compos. Sci. Technol.* **2009,** 69, (10), 1644-1652.

(165) Eckel, D. F.; Balogh, M. P.; Fasulo, P. D.; Rodgers, W. R. *J. Appl. Polym. Sci.* **2004,** 93, 1110-1117.

(166) Monticelli, O.; Musina, Z.; Russo, S.; Bals, S. *Mat. Lett* **2007,** 61, 3446-3450.

(167) Samyn, F.; Bourbigot, S.; Jama, C.; Bellayer, S.; Nazare, S.; Hull, R.; Castrovinci, A.; Fina, A.; Camino, G. *Eur. Polym. J.* **2008,** 44, 1642-1653.

(168) Okamoto, M.; Nam, P. H.; Maiti, P.; Kotaka, T.; Hasegawa, N.; Usuki, A. *Nano Lett.* **2001,** 1, (6), 295-298.

(169) Wang, K.; Zhao, P.; Yang, H.; Liang, S.; Zhang, Q.; Du, R. N.; Fu, Q. A.; Yu, Z. Q.; Chen, E. Q. *Polymer* **2006,** 47, (20), 7103-7110.

(170) Perrin-Sarazin, F.; Ton-That, M.-T.; Bureau, M. N.; Denault, J. *Polymer* **2005,** 46, 11624-11634.

(171) Degennes, P. G. *J. Phys. Chem. Solids* **1958,** 7, (4), 345-350.

(172) Gosele, U. *Physica B & C* **1976,** 85, (2), 317-322.

(173) Martin, P. J.; Tan, C. W.; Tshai, K. Y.; McCool, R.; Menary, G.; Armstrong, C. G.; Harkin-Jones, E. M. A. *Plast. Rubber Compos.* **2005,** 34, (5-6), 276-282.

(174) Xie, W.; Xie, R.; Pan, W.-P.; Hunter, D.; Koene, B.; Tan, L.-S.; Vaia, R. *Chem. Mater.* **2002,** 14, (11), 4837-4845.

(175) Yang, J. H.; Han, Y. S.; Choy, J. H.; Tateyama, H. *J. Mater. Chem.* **2001,** 11, (4), 1305-1312.

(176) Schmidt, D. F.; Clement, F.; Giannelis, E. P. *Adv. Funct. Mater.* **2006,** 16, (3), 417-425.

(177) Osman, M. A.; Ernst, M.; Meier, B. H.; Suter, U. W. *J. Phys. Chem. B* **2002,** 106, (3), 653-662.

(178) Blum, A. E.; Eberl, D. D. *Clays Clay Miner.* **2004,** 52, (5), 589-602.

(179) Okuyama, K.; Soboi, Y.; Iijima, N.; Hirabayashi, K.; Kunitake, T.; Kajiyama, T. *Bull. Chem. Soc. Jpn.* **1988,** 61, (5), 1485-1490.

(180) Levin, E. M.; Hou, S. S.; Bud'ko, S. L.; Schmidt-Rohr, K. *J. Appl. Phys.* **2004,** 96, (9), 5085-5092.

(181) Labouriau, A.; Kim, Y. W.; Earl, W. L. *Phys. Rev. B* **1996,** 54, (14), 9952-9959.

(182) Quijada-Garrido, I.; Wilhelm, M.; Spiess, H. W.; Barrales-Rienda, J. M. *Macromol. Chem. Phys.* **1998,** 199, 985-995.

(183) Chen, Q.; Schmidt-Rohr, K. *Solid-State Nuclear Magn. Reson.* **2005,** 29, 142-152.

(184) Hedesiu, C.; Demco, D. E.; Kleppinger, R.; Vanden Poel, G.; Gijsbers, W.; Blumich, B.; Remerie, K.; Litvinov, V. M. *Macromolecules* **2007,** 40, (11), 3977-3989.

(185) Hedesiu, C.; Demco, D. E.; Kleppinger, R.; Buda, A. A.; Blumich, B.; Remerie, K.; Litvinov, V. M. *Polymer* **2007,** 48, (3), 763-777.

(186) Mellinger, F.; Wilhelm, M.; Spiess, H. W. *Macromolecules* **1999,** 32, (14), 4686-4691.

(187) Khutsishvili, G. R. *Soviet Physics Jetp-Ussr* **1957,** 4, (3), 382-384.

(188) Furman, G. B.; Kunoff, E. M.; Goren, S. D.; Pasquier, V.; Tinet, D. *Phys. Rev. B* **1995,** 52, (14), 10182-10187.

(189) Furman, G. B.; Kunoff, E. M.; Goren, S. D.; Pasquier, V.; Tinet, D. *Solid State Nucl. Magn. Reson.* **1995,** 4, (4), 255-258.

(190) Bloembergen, N.; Purcell, E. M.; Pound, R. V. *Nature* **1947,** 160, (4066), 475-476.

(191) Devreux, F.; Boilot, J. P.; Chaput, F.; Sapoval, B. *Phys. Rev. Lett.* **1990,** 65, (5), 614-617.

(192) VanderHart, D. L.; McFadden, G. B. *Solid State Nucl. Magn. Reson.* **1996,** 7, (1), 45-66.

(193) Clauss, J.; Schmidtrohr, K.; Spiess, H. W. *Acta Polym.* **1993,** 44, (1), 1-17.

(194) Carslaw, H. S.; Jaeger, J. C., *Conduction of heat in solids*. 2nd ed.; Clarendon Press; Oxford University Press: Oxford Oxfordshire New York, 1986; Chapters XII and XIII.

(195) Chen, Q.; Schmidt-Rohr, K. *Solid State Nucl. Mag. Reson.* **2006,** 29, (1-3), 142-152.

(196) Clore, G. M.; Iwahara, J. *Chem. Rev.* **2009,** 109, (9), 4108-4139.

(197) Nadaud, P. S.; Helmus, J. J.; Kall, S. L.; Jaroniec, C. P. *J. Am. Chem. Soc.* **2009,** 131, (23), 8108-8120.

(198) Bhowmik, A.; Ellena, J. F.; Bryant, R. G.; Cafiso, D. S. *J. Magn. Reson.* **2008,** 194, 283-288.

(199) Linser, R.; Fink, U.; Reif, B. *J. Am. Chem. Soc.* **2009,** 131, (38), 13703-13708.

(200) Xu, B.; Leisen, J.; Beckham, H. W.; Abu-Zurayk, R.; Harkin-Jones, E.; McNally, T. *Macromolecules* **2009,** 42, (22), 8959-8968.

(201) Asano, A.; Shimizu, M.; Kurotsu, T. *Chem. Lett.* **2004,** 33, (7), 816-817.

(202) Seif, S. Temporally Programmed Stretching of Polymer Films: Influence of Nanoparticles. . Ph.D. thesis, The University of Akron, Akron, 2009.

(203) Kim, D. H.; Fasulo, P. D.; Rodgers, W. R.; Paul, D. R. *Polymer* **2007,** 48, (18), 5308-5323.

(204) Manias, E.; Touny, A.; Wu, L.; Strawhecker, K.; Lu, B.; Chung, T. C. *Chem. Mater.* **2001,** 13, (10), 3516-3523.

(205) Gilman, J. W.; Jackson, C. L.; Morgan, A. B.; Harris, R.; Manias, E.; Giannelis, E. P.; Wuthenow, M.; Hilton, D.; Phillips, S. H. *Chem. Mater.* **2000,** 12, (7), 1866-1873.

(206) (a) Bertini, I. B., A.; De Paepe, G.; Griffin, R. G.; Lelli, M.; Lewandowski, J. R.; Luchinat, C. *J. Am. Chem. Soc.* **2010,** *132*, 1032-1040. (b) Balayssac, S.; Bertini, I.; Bhaumik, A.; Lelli, M.; Luchinat, C. *Proc. Natl. Acad. Sci. U.S.A.* **2008,** *105*, 17284-17289. (c) Buffy, J. J.; Hong, T.; Yamaguchi, S.; Waring, A. J.; Lehrer, R. I.; Hong, M. *Biophys. J.* **2003,** *85*, 2363-2373. .

(207) Yang, D. K.; Zax, D. B. *J. Chem. Phys.* **1999,** 110, (11), 5325-5336.

(208) Vantelon, D.; Montarges-Pelletier, E.; Michot, L. J.; Briois, V.; Pelletier, M.; Thomas, F. *Phys. Chem. Miner.* **2003,** 30, (1), 44-53.

(209) (a) Solomon, I. *P. R.*, *99*, 559-565. (b) Gueron, M. *J.Magn. Reson.* **1975,** *19*, 58-66. (c) Vega, A. J.; Fiat, D. *Mol. Phys.* **1976**, *31*, 347-355. (d) Koeing, S, H. *J. Magn. Reson.* **1982,** *47*, 441-453. .

(210) (a) Schaefer, D. S., H. W.; Suter, U. W.; Fleming, W. W. *Macromolecules* **1990**, *23*, 3431-3439. (b) Roland, C. M.; Ngai, K. L.; Santangelo, P. G.; Qiu, X. H.; Ediger, M. D.; Plazek, D. J. *Macromolecules* **2001**, *34*, 6159-6160.

(211) Mchenry, M. R.; Silberna.Bg; Wernick, J. H. *Phys. Rev. Lett.* **1971,** 27, (7), 426-&.

(212) Kumashiro, K. K.; Schmidt-Rohr, K.; Murphy, O. J.; Ouellette, K. L.; Cramer, W. A.; Thompson, L. K. *J. Am. Chem. Soc.* **1998,** 120, (20), 5043-5051.

(213) Wang, B. X.; Yi, X. S.; Pan, Y.; Shan, H. F. *J. Mater. Sci. Lett.* **1997,** 16, (24), 2005-2007.

(214) Demco, D. E.; Johansson, A.; Tegenfeldt, J. *Solid State Nucl. Mag. Reson.* **1995,** 4, (1), 13-38.

(215) Schmidt-Rohr, K.; Spiess, H. W., *Multidimensional solid-state NMR and polymers*. Academic Press: London, 1994; Charpter 13.

(216) Wang, J. H.; Jack, K. S.; Natansohn, A. L. *J. Chem. Phys.* **1997,** 107, (3), 1016-1020.

(217) Singla, S.; Beckham, H. W. *Macromolecules* **2008,** 41, (24), 9784-9792.

(218) Cheung, T. T. P.; Gerstein, B. C.; Ryan, L. M.; Taylor, R. E.; Dybowski, D. R. *J. Chem. Phys.* **1980,** 73, (12), 6059-6067.

(219) Jia, X.; Wolak, J.; Wang, X. W.; White, J. L. *Macromolecules* **2003,** 36, (3), 712-718.

(220) Meurer, B.; Weill, G. *Macromol. Chem. Phys.* **2008,** 209, (2), 212-219.

(221) Wang, X. W.; White, J. L. *Macromolecules* **2002,** 35, (10), 3795-3798.

(222) Samyn, F.; Bourbigot, S.; Jama, C.; Bellayer, S.; Nazare, S.; Hull, R.; Castrovinci, A.; Fina, A.; Camino, G. *Eur. Polym. J.* **2008,** 44, (6), 1642-1653.

(223) Bourbigot, S.; Fontaine, G.; Bellayer, S.; Delobel, R. *Polym. Test.* **2008,** 27, (1), 2-10.

(224) Havens, J. R.; Vanderhart, D. L. *Macromolecules* **1985,** 18, (9), 1663-1676.

(225) Kim, J. H.; Koo, C. M.; Choi, Y. S.; Wang, K. H.; Chung, I. J. *Polymer* **2004,** 45, (22), 7719-7727.

(226) Chaffin, K. A.; Bates, F. S.; Brant, P.; Brown, G. M. *J. Polym. Sci., Part B: Polym. Phys.* **2000,** 38, (1), 108-121.

(227) Mark, J. E., *Polymer data handbook*. Oxford University Press: New York, 1999; 782.

(228) Raich, H.; Blumler, P. *Magn. Reson. B: Magn. Reson. Eng.* **2004,** 23B, (1), 16-25.

(229) Hotta, A.; Clarke, S. M.; Terentjev, E. M. *Macromolecules* **2002,** 35, (1), 271-277.

(230) Xia, H. S.; Song, M.; Zhang, Z. Y.; Richardson, M. *J. Appl. Polym. Sci.* **2007,** 103, (5), 2992-3002.

(231) Gurtovenko, A. A.; Gotlib, Y. Y. *J. Chem. Phys.* **2001,** 115, (14), 6785-6793.

(232) Haraguchi, K.; Li, H. J. *Macromolecules* **2006,** 39, (5), 1898-1905.

(233) Wang, Z. M.; Nakajima, H.; Manias, E.; Chung, T. C. *Macromolecules* **2003,** 36, (24), 8919-8922.

(234) Vaia, R. A.; Teukolsky, R. K.; Giannelis, E. P. *Chem. Mater.* **1994,** 6, (7), 1017-1022.

(235) Lagaly, G. *Solid State Ionics* **1986,** 22, (1), 43-51.

(236) Zheng, Q.; Xu, B.; Song, Y. H.; Yang, H. M.; Pan, Y. *J. Mater. Res.* **2005,** 20, (2), 357-363.

(237) Hartman, J. S.; Narayanan, A.; Wang, Y. X. *J. Am. Chem. Soc.* **1994,** 116, (9), 4019-4027.

(238) Kunoff, E. M.; Goren, S. D.; Korn, C.; Gavra, Z.; Johnson, J. R.; Reilly, J. J. *Solid State Nucl. Magn. Reson.* **1994,** 3, (1), 23-27.

(239) Craciun, C.; Meghea, A. *Clay Minerals* **1985,** 20, (3), 281-290.

(240) vanWyk, J. A.; Reynhardt, E. C.; High, G. L.; Kiflawi, I. *J. Phys. D Appl. Phys.* **1997,** 30, (12), 1790-1793.